

Quantum metrology using tailored non-classical states

Von der QUEST-Leibniz-Forschungsschule
der Gottfried Wilhelm Leibniz Universität Hannover

zur Erlangung des akademischen Grades

Doktor der Naturwissenschaften
– Dr. rer. nat. –

genehmigte Dissertation von

M. Sc. Jonas Junker

2023

Referentin: Prof. Dr. Michèle Heurs
Korreferent: Apl. Prof. Dr. Benno Willke
Korreferentin: Asst. Prof. Dr. Georgia Mansell
Tag der Promotion: 21. Februar 2023

Author contributions

Parts of this thesis have been already published as peer-reviewed publications. Here, I list these works in order of the corresponding chapters and present my personal contribution to them. In order of the corresponding chapter they are:

Chapter 3

[P1] J. Junker, D. Wilken, E. Huntington, and M. Heurs. “High-precision cavity spectroscopy using high-frequency squeezed light”. In: *Opt. Express* 29.4 (Feb. 2021), pp. 6053–6068. DOI: [10.1364/OE.416713](https://doi.org/10.1364/OE.416713)

Short abstract: This publication deals with a particular high-frequency and phase-modulated squeezed state that can be applied to spectroscopy. We show that a small phase signal generated in a cavity can be resolved below shot noise by using our squeezed quantum state.

Author contribution: JJ, DW, and MH adapted the initial idea from EH and modified the exact approach. JJ calculated the theoretical expressions for the squeezer and the FP cavity. JJ and DW built the experiment, took the measurements, and analysed the data. JJ wrote the manuscript with significant contributions from DW and contributions from MH.

Chapter 4

[P2] J. Junker, D. Wilken, N. Johny, D. Steinmeyer, and M. Heurs. “Frequency-Dependent Squeezing from a Detuned Squeezer”. In: *Phys. Rev. Lett.* 129 (3 July 2022), p. 033602. DOI: [10.1103/PhysRevLett.129.033602](https://doi.org/10.1103/PhysRevLett.129.033602)

Short abstract: In this publication, we demonstrate that a detuned single-mode squeezer is capable of generating a frequency-dependent squeezed state. This particular squeezer could be used as an approximate effective-negative mass oscillator, e.g., for coherent quantum noise cancellation.

Author contribution: JJ formulated the theoretical derivation for the detuned squeezer with input from DS. JJ set up the experiment and took the measurements. JJ wrote the programs for data acquisition and reconstruction of the Wigner function. All authors contributed to the discussion and interpretation of the measurement results. The visualisation of the results was performed by JJ and NJ. JJ wrote the manuscript with contributions from all co-authors.

Chapter 5

[P3] J. Junker, D. Wilken, D. Steinmeyer, and M. Heurs. “Reconstructing Gaussian bipartite states with a single polarization-sensitive homodyne detector”. In: *Opt. Express* 30.19 (Sept. 2022), pp. 33860–33868. DOI: [10.1364/OE.465186](https://doi.org/10.1364/OE.465186)

Short abstract: This publication deals with a new approach to detecting and characterising a two-mode squeezed state using a single polarisation-sensitive homodyne detector. With our approach, it is possible to reconstruct the full covariance matrix, which fully characterises the entangled state.

Author contribution: DS came up with the initial idea of using a polarisation-sensitive homodyne detector to reconstruct two-mode squeezed states. JJ built the experiment, took the measurements, and performed the statistical analysis. JJ prepared the manuscript with contributions from all co-authors.

Abstract

Squeezed states of light play a significant role in various technologies ranging from high-precision metrology such as gravitational wave detection to quantum information. These quantum states are prepared to carry particular characteristics depending on their application. For instance, some applications require squeezing in one, others only in the combination of two distinct optical modes. Furthermore, squeezing can appear constant for all frequencies or frequency-dependently. In this thesis, novel quantum optical methods employing different, tailored non-classical light sources, are developed and described. The individual squeezed states are controlled and characterised, each tailored for a particular application.

In high-precision spectroscopy, the measurement sensitivity is often limited by technical noise at low frequencies. The first publication shows that small phase signals at low-frequency are resolvable without increasing the laser power. We use a phase-modulated field, shifting the signal to high frequencies where technical noise is circumvented. In addition, the field is squeezed by 6 dB at high frequencies to reduce shot noise arising from quantum fluctuations. Our approach resolves sub-shot-noise signals at 100 Hz and 20 kHz on a reduced noise floor.

In opto-mechanical sensors such as gravitational wave detectors, the fundamental measurement limitation arises from the combination of shot noise and quantum back-action noise induced by quantum radiation pressure noise. A conventional fixed-quadrature squeezed state generated by a resonant optical parametric oscillator (OPO) can only fight one of these two contributions simultaneously. To cancel both quantum noise contributions, a particularly frequency-dependent squeezed state is required. Our second publication shows that a detuned OPO generates frequency-dependent squeezing. It can be used as an approximate effective-negative mass oscillator in an all-optical coherent quantum noise cancellation scheme and is suitable to coherently cancel quantum noise. Our generated state, which is reconstructed by quantum tomography, rotating over megahertz frequencies, exhibits a rotation angle of 39° and a maximal squeezing degree of 5.5 dB.

Two-mode squeezed quantum states are resources required in modern applications such as quantum information processing. In the third publication, we address the challenge of determining the ten independent entries of a two-mode squeezed state's covariance matrix to fully characterise the quantum state. We demonstrate a full reconstruction of a 7 dB two-mode squeezed state using only a single polarisation-sensitive homodyne detector, which avoids additional optics and potential loss channels.

The findings of this thesis are relevant for experiments in high-precision quantum metrology, e.g. in spectroscopy or gravitational wave detectors operating at the standard quantum limit. The insights gained on the generating and handling non-classical states enable advances in quantum information technology.

Keywords: squeezed states of light, homodyne detection, quantum tomography, spectroscopy, bipartite entanglement

Kurzfassung

Gequetschtes Licht spielt eine wichtige Rolle für Gravitationswellendetektoren oder Anwendungen in der Quanteninformationstechnologie. Diese Quantenzustände werden je nach Anwendung speziell präpariert. Für einige Anwendungen ist beispielsweise die Quetschung in einer, für andere nur in der Kombination zweier verschiedener optischer Moden erforderlich. Außerdem kann die Quetschung für alle Frequenzen konstant oder frequenzabhängig auftreten. Im Rahmen dieser Arbeit werden neuartige quantenoptische Methoden entwickelt, die unterschiedlich angepasste nicht-klassische Lichtquellen verwenden. Die einzelnen gequetschten Zustände werden anwendungsbezogen erzeugt, stabilisiert und charakterisiert.

In der Spektroskopie ist die Messempfindlichkeit oft durch technisches Rauschen bei niedrigen Frequenzen limitiert. Die erste Publikation zeigt die Messung von kleinen, niederfrequenten Phasensignalen, ohne die Leistung des Lasers zu erhöhen. Unser phasenmoduliertes Lichtfeld verschiebt das Signal zu hohen Messfrequenzen und umgeht daher technisches Rauschen. Weil wir zusätzlich mit gequetschtem Licht arbeiten, kann dort auch Quantenrauschen um 6 dB verringert werden. Unsere Messmethode zeigt die Detektion von Signalen, die bei 100 Hz und 20 kHz oszillieren.

Die Messgenauigkeit von optomechanischen Sensoren wie zum Gravitationswellendetektoren ist fundamental begrenzt durch eine Kombination aus quantenmechanischem Schrot- und Strahlungsdruckrauschen. Ein Zustand mit konstanter Quetschquadratur, der von einem resonanten optisch parametrischen Oszillator (OPO) erzeugt wird, wirkt nur gegen einen dieser beiden Rauschbeiträge. Um beide Beiträge zu unterdrücken, ist ein besonderer frequenzabhängiger gequetschter Zustand erforderlich. Unsere zweite Publikation zeigt, dass ein von der Resonanzfrequenz verstimmt OPO frequenzabhängiges gequetschtes Licht erzeugt. Er kann annähernd als effektiver negativer Massen-Oszillator verwendet werden, um Quantenrauschen kohärent zu unterdrücken. Der von uns erzeugte Zustand, der durch Quantentomographie rekonstruiert wird und über Megahertz-Frequenzen rotiert, weist einen Rotationswinkel von 39° und eine maximale Quetschung von 5.5 dB auf.

Gequetschte Quantenzustände mit zwei Moden werden für moderne Anwendungen wie die Quanteninformationstechnologie benötigt. In der dritten Publikation befassen wir uns mit der Aufgabe, die zehn unabhängigen Einträge der Kovarianzmatrix eines um 7 dB gequetschten Zweimodenzustands zu bestimmen. Damit ist der Quantenzustand vollständig charakterisiert. Wir zeigen eine vollständige Rekonstruktion eines zweimodigen gequetschten Zustands unter Verwendung eines einzigen polarisationsempfindlichen Homodyn-Detektors, der zusätzliche Optiken und potenzielle Verlustkanäle vermeidet.

Die Erkenntnisse dieser Arbeit sind relevant für Experimente in der Quantenmetrologie, z.B. in der Spektroskopie oder bei Gravitationswellendetektoren, die mit Sensitivitäten am Standardquantenlimit arbeiten. Die gewonnenen Erkenntnisse über die Erzeugung und Handhabung nicht-klassischer Zustände ermöglichen Fortschritte in der Quanteninformationstechnologie.

Schlagwörter: gequetschtes Licht, Homodyn-Detektion, Quantentomographie, Spektroskopie, bipartite Verschränkung

Contents

Author contributions	iii
Abstract	v
Kurzfassung	vii
1 Introduction	1
2 Theoretical and experimental background	7
2.1 Classical description of an optical cavity	7
2.1.1 Electric fields in a cavity	8
2.1.2 Escape efficiency, free spectral range, linewidth, finesse	9
2.2 Characteristics of quantum states	11
2.2.1 Electromagnetic field quantisation and quadrature operators	12
2.2.2 Statistics of quantum states	13
2.2.3 Vacuum states, coherent states, squeezed states	15
2.2.4 Detection of quantum states	18
2.3 Cavities with non-linear crystals	21
2.3.1 General theoretical model	21
2.3.2 Second harmonic generation	23
2.3.3 Squeezing from optical parametric oscillation	25
2.4 Experimental view on the OPO, the detuned OPO and the NDOPO	30
2.4.1 Comparison of the squeezers	30
2.4.2 Setting up a two-mode squeezer	35
2.4.3 Squeezing characterisation – from generation to detection	37
3 Cavity spectroscopy enhanced with squeezed light	39
3.1 Introduction	39
3.1.1 Noise versus signals	40
3.1.2 Motivation for our method applied in spectroscopy	42
3.2 [P1]: High-precision cavity spectroscopy using high-frequency squeezed light	45
3.3 Preparation of the required quantum state	63
3.3.1 Phase-modulated amplitude quadrature squeezed state	63
3.3.2 Squeezing characterisation behind the OPO	64
3.4 Fabry-Pérot cavity as spectroscopic device	65
3.4.1 Design of the Fabry-Pérot cavity	65
3.4.2 Squeezing characterisation behind the Fabry-Pérot cavity	67
3.4.3 Experimental challenges	68
3.5 Discussion and conclusion	70

4	Detuning a squeezer to generate frequency-dependent squeezing	73
4.1	Introduction	73
4.1.1	The standard quantum limit of interferometry	74
4.1.2	Frequency-dependent squeezing	74
4.2	[P2]: Frequency-Dependent Squeezing from a Detuned Squeezer	77
4.3	Quantum tomography	85
4.3.1	Tomography: imaging by sections	85
4.3.2	Locking-free tomographic acquisition of a squeezed state	86
4.3.3	Quantum tomographic reconstruction	88
4.4	The single-mode resonant squeezer	89
4.4.1	Characterisation	89
4.4.2	Wigner function of a 9 dB squeezed state	90
4.5	The single-mode detuned squeezer	91
4.5.1	Stabilising the detuned OPO	92
4.5.2	The effective pump threshold	93
4.6	Discussion and conclusion	94
5	Reconstruction of two-mode squeezed bipartite states	97
5.1	Introduction	98
5.1.1	Quantum technologies for entangled bipartite states	98
5.1.2	Deciphering the covariance matrix of bipartite states	99
5.2	[P3]: Reconstructing Gaussian bipartite states with a single polarization-sensitive homodyne detector	100
5.3	Detection of two-mode squeezing	111
5.3.1	Dual balanced homodyne detection	111
5.3.2	Polarisation-sensitive single homodyne detection	112
5.4	Bipartite states generated with a two-mode squeezer	115
5.4.1	First characterisation of the two-mode squeezer	116
5.4.2	Stability problems	118
5.5	From the measurement to the reconstruction of the Wigner function	119
5.5.1	Preparing the polarisation-sensitive homodyne detector	119
5.5.2	Data acquisition and statistical data analysis	120
5.5.3	Cross-sections of the Wigner function	120
5.6	Discussion and conclusion	122
6	Discussion	127
7	Conclusion	129
	Bibliography	131
	Acknowledgements	151
	Curriculum Vitae	153

List of Figures

1.1	Structure of this thesis	4
2.1	Schematic of an optical cavity	8
2.2	Reflected modes of a single-ended cavity	10
2.3	The quantum state in phase space	15
2.4	Phase state representation of a vacuum state, a coherent state, a quadrature squeezed state, and a bright quadrature squeezed state	16
2.5	Schematic of a homodyne detection scheme	19
2.6	Schematic of an optical cavity containing a non-linear $\chi^{(2)}$ medium	22
2.7	CAD model of the new second harmonic generation cavity	25
2.8	Quantum sideband picture of an amplitude quadrature squeezed state in the rotating frame	29
2.9	The two squeezer topologies used in this thesis	31
2.10	Schematic of the oven and beam path in the wedged crystal	33
2.11	Constructing the oven and inserting the PPKTP crystal	35
3.1	Logarithmic power spectrum visualising the signal-to-noise ratio	41
3.2	Motivation for using a high-frequency phase-modulated and squeezed state in spectroscopy	43
3.3	Phasor pictures of phase-modulated laser fields	44
3.4	Squeezing slope of the OPO used for the spectroscopy experiment	65
3.5	New design of the Fabry-Pérot cavity	66
3.6	Squeezing slope behind the Fabry-Pérot cavity	68
3.7	Competing fields in the spectroscopy experiment	69
4.1	Strain sensitivity of a gravitational wave detector and the standard quantum limit	75
4.2	Quantum sideband representation for frequency-independently and -dependently squeezed states	76
4.3	The basic principle of tomography consisting of acquisition and reconstruction	86
4.4	Homodyne measurement of a squeezed state while tracing over the detection angle	87
4.5	Tomographic acquisition	88
4.6	Squeezing slope and squeezing spectrum for the single-mode squeezed state generated by a resonant OPO	90
4.7	Wigner function from a squeezed state	91
4.8	Temperature dependence of the polarisation degeneracy in the OPO	92
4.9	Simulated squeezing slopes for a resonant and a detuned OPO	94
5.1	Schematic of a (balanced) dual homodyne detection scheme	112
5.2	Shot and dark noise of the two high-frequency homodyne detectors	113

5.3	Squeezing slope and squeezing spectrum for the two-mode squeezed state	117
5.4	Cross-sections of the Wigner function for the two-mode squeezed state	121
5.5	Setup of the polarisation degeneracy lock for a two-mode squeezer . .	123
5.6	Error signal of the polarisation degeneracy lock for a two-mode squeezer	124

List of Tables

2.1	Overview of important parameters of the three used squeezers	32
2.2	Scattering and absorption losses in the coatings and substrates	37
3.1	Main differences between the old and the new Fabry-Pérot cavity design	67
5.1	Difference currents of the polarisation-sensitive homodyne detector . .	115

List of Acronyms

AOM	acousto-optic modulator
CQNC	coherent quantum noise cancellation
EBE	electron beam evaporation
EPR	Einstein-Podolsky-Rosen
FP	Fabry-Pérot
FWHM	full width at half maximum
IBS	ion beam sputtering
NDOPO	non-degenerate optical parametric oscillator
NPRO	non-planar ring oscillator
NTC	negative temperature coefficient thermistor
OPO	optical parametric oscillator
PBS	polarising beam splitter
PDH	Pound-Drever-Hall
PID	proportional–integral–derivative
POM	polyoxymethylene
PPKTP	periodically-poled potassium titanyl phosphate
PZT	piezoelectric transducer
RMS	root mean square
ROC	radius of curvature
SHG	second harmonic generation
SNR	signal-to-noise ratio
SQL	standard quantum limit of interferometry

Chapter 1

Introduction

Interferometry revolutionised the understanding and application of waves and light. The phenomenon of interference was first described by Hooke in 1665 [Hoo65] and later studied and published by Newton in 1704 [Na04]. Two centuries later, Michelson and Morley set up an optical interferometer using light waves in 1887 [MM87b]. This experiment first falsified the ether theory but also marked the hour of birth for many following interferometric approaches.¹ For instance, the two scientists observed the fine structure splitting for hydrogen using light interferometry [MM87a].

During the late 19th and early 20th century, light was subject to many exciting investigations. In 1899, Planck found that the accurate black body radiation spectrum model can only be obtained when light is assumed to be emitted in discrete units of energy [Pla00; Pla01].² A few years later, Einstein proposed a theory of the photoelectric effect [Ein05], which also built on the energy quantisation of light.³ In 1913, Bohr used the concept of quantisation to verify the spectral lines of the hydrogen atom [Boh13].⁴ Now, light was considered a stream of particles called photons, which marked the beginning of modern quantum mechanics and quantum optics.

A great milestone in optical metrology was the new field of laser science, which experimentally began with the development of the first laser by Maiman in 1960 [Mai60]. Lasers significantly enhanced the sensitivity in interferometry and opened the door to an increasingly more detailed discussion on the statistics of light. The concept of the *coherent state* was introduced by Glauber [Gla63b].⁵ It refers to a classical and maximally coherent state of the quantised electromagnetic field. The quantum theory of the coherent electromagnetic field was described by Glauber [Gla63a] and by Sudarshan, who related the classical and quantum mechanical descriptions of light in 1963 [Sud63]. The coherent state turned out to be a minimum uncertainty Gaussian wave packet, fulfilling the famous uncertainty relation Heisenberg formulated in 1927 [Hei27].

For some exotic states of light, the classical description did not hold anymore. The research on these non-classical states was pushed with the experimental demonstration that light consists of single photons by Kimble and co-workers in 1977 [KDM77]. The so-called *squeezed states* [Wal83] can be considered the first class of these new states. Squeezing was first generated by Slusher and co-workers in 1985 [Slu+85].

¹For his optical precision instruments and the spectroscopic and metrological investigations carried out with their aid, Michelson was awarded the Nobel Prize in Physics 1907 [N07].

²In recognition of the services he rendered to the advancement of Physics by his discovery of energy quanta, Planck was awarded the Nobel Prize in Physics 1918 [N18].

³For his services to Theoretical Physics, and especially for his discovery of the law of the photoelectric effect, Einstein was awarded the Nobel Prize in Physics 1921 [N21].

⁴For his services to Theoretical Physics, and especially for his discovery of the law of the photoelectric effect, Bohr was awarded the Nobel Prize in Physics 1922 [N22].

⁵Therefore, coherent states are also called *Glauber states*. For his contribution to the quantum theory of optical coherence, Glauber was awarded the Nobel Prize in Physics 2005 [N05].

In 1972, twelve years after the invention of the laser, Weiss suggested that laser interferometers should be able to detect gravitational waves [Wei72]. He already expected technical challenges such as thermal and laser amplitude or frequency noise. The search for gravitational waves by using high-precision laser interferometers had begun. Caves found that even quantum mechanical noise will be expected to influence the measurements in a gravitational wave detector [Cav80]. He proposed the usage of squeezed light to overcome this limitation [Cav81]. Unruh advanced this idea in 1983, and he suggested using a frequency-dependent squeezed state to achieve a broadband noise reduction [Unr83]. Many follow-up works were published presenting different approaches to beat the quantum noise in an interferometric gravitational wave detector in a broad frequency band [BS84; JR90; VZ95]. In 2001, it was again Kimble, together with co-workers, who showed how quantum non-demolition gravitational wave interferometers could be designed [Kim+01]. They suggested using a tailored squeezed state to compensate for the ponderomotively squeezed state generated by the interferometer.

In the meantime, the gravitational wave detectors' measurement sensitivity was gradually increased due to technical improvements. The application of non-classical states was not required for the first detection of gravitational waves in 2015, generated by a binary black hole merger [Abb+16a].⁶ This first detection event was a milestone in optical high-precision metrology and ignited the era of multi-messenger astronomy with gravitational waves [Abb+17]. These new times call for further improvement of the existing detectors and the construction of new detectors, such as the Einstein Telescope [Pun+10; Mag+20] or the Cosmic Explorer [Rei+19] with exceedingly high sensitivities. In any case, the goal is to beat the standard quantum limit of interferometry, which can be realised by the injection of squeezed states [Heu18].

Frequency-independent squeezing has been applied to other high-precision measurements, as in [XWK87; Gra+87; PCK92; Luc+16]. Recently, it has also significantly improved the sensitivity in gravitational wave detectors [Tse+19; Ace+19; Lou+21]. The stable generation of a tailored frequency-dependent squeezed state is subject to current research, which usually works with single-mode squeezing and filter cavities [Oel+16b; Zha+20; McC+20] or with two-mode squeezing [Ma+17; Yap+20; Süd+20].

Other high-precision opto-mechanical measurements have also been working near the standard quantum limit. As in gravitational wave detectors, in some cases, displacement is measured [Wil+15; Ros+18; Mas+19], in others, mass [Liu+19], or acceleration [Kra+12; Qva+18]. Opto-mechanical force measurements [Cav+80] were demonstrated with atomic clouds [Sch+14], Bose-Einstein condensates [Mot+19] or microdisks [BE+19]. However, it is possible to beat the standard quantum limit with particular quantum states, exhibiting squeezing [XT14; Mot+16; Cla+16; Møl+17; Sud+17; Kam+17] or entanglement [Ma+17].

In our working group, we investigate an idea called coherent quantum noise cancellation (CQNC) [TC10; Wim+14; Ste19; Sch+22]. In our all-optical approach of CQNC, we want to cancel quantum back-action noise generated by an opto-mechanical system. An effective negative-mass oscillator is required to achieve cancellation and beat the standard quantum limit. A beam-splitter and a two-mode down-conversion process can form this oscillator. Interestingly, this quantum state is equivalent to Kimble's suggested inversely input squeezed state [Kim+01]. In recent years, realisations of quantum back-action evasion noise reduction, analogous to CQNC, have been already realised with spin ensembles [Møl+17; Koh+18].

⁶For decisive contributions to the LIGO detector and the observation of gravitational waves, Weiss, together with Barish and Thorne, was awarded the Nobel Prize in Physics 2017 [N17].

In recent times, another species of quantum states is gaining increasing attention: entangled states. They form the basis for many modern technologies. In 1992, Ou and co-workers demonstrated the Einstein-Podolsky-Rosen paradox for continuous variables with two-mode squeezed states [Ou+92]. Quantum entanglement is not only used to increase the measurement sensitivity [DLPP01; T12] – it also lays the basis for modern technologies in quantum information.

With two-mode entangled states, quantum teleportation and quantum logic gates are possible. Quantum logic gates are required for quantum computing, which pinpoints the limitations of classical cryptography. The reaction to these limitations is quantum cryptography, which has the advantage of detecting passive eavesdropping and is considered a secure communication channel. Entangled states are also well suited to violate the Bell inequalities [AGR82; Wei+98]⁷ or to test local hidden-variable theories [Cla+69; FC72].

This thesis discusses the need for squeezed states for numerous applications. Thus, some questions are relevant and need to be addressed for each application. Is quantum entanglement needed? Is frequency dependence required? How much degradation of the squeezed state by vacuum noise is permissible? When these questions have been answered, then the required squeezed state can be defined and generated with care.

The aim of this thesis is to investigate particular squeezed states of light, each tailored for a specific application. First, a theoretical description of the squeezed state is essential. Since squeezed states are very fragile and susceptible to optical losses, care has to be taken when manipulating them. The squeezed states used in this thesis are generated by sub-threshold optical parametric oscillators (OPOs). Depending on the non-linear crystal used for the down-conversion process and the resonance condition of the OPO, the squeezing has specific characteristics. The squeezed state can be frequency-dependent or -independent. It can be located in a single or two orthogonally polarised modes, so separating the modes by polarisation optics is straightforward. Working with squeezed states requires precise phase stabilisation of different electric fields in the full optical setup. This thesis works with specific approaches to detect and characterise squeezed states. It employs various homodyne detector setups and quantum tomography.

The main research question of this thesis can be summarised as this: How can each required squeezed state be theoretically understood, generated with high fidelity, stably controlled and coherently detected? In this thesis, novel quantum optical methods employing different, tailored non-classical light sources, are developed. This thesis gives a better understanding of the applied quantum states and features significant technical improvements to previously existing systems used in our working group. It underlines the diverse usage of squeezed states, from high-precision spectroscopy to gravitational wave detection or quantum information.

⁷For experiments with entangled photons, establishing the violation of Bell inequalities and pioneering quantum information science, Aspect, Clauser and Zeilinger were awarded the Nobel Prize in Physics 2022 [N22].

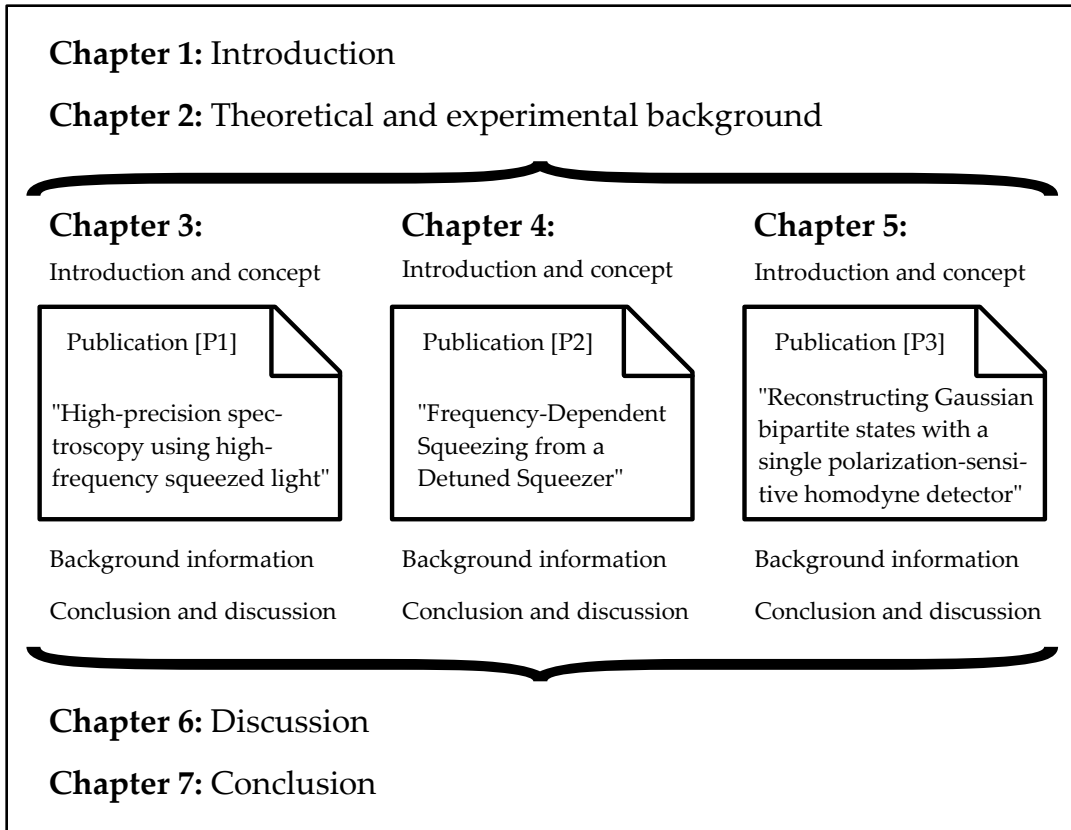


FIGURE 1.1: Structure of this thesis.

Structure of this thesis

This thesis is structured as shown in Fig. 1.1. The introduction is intentionally kept short. Chapter 2 treats general theoretical and experimental basics. This chapter serves as a background for the following three chapters. A central part deals with the properties of quantum states and how they are generated in non-linear optical cavities and measured by photodetectors. Also, classical cavities and second-harmonic generation cavities are discussed. Chapter 2 closes with a comparison of the three important squeezers used for the experiments.

Each of the following three Chapters 3, 4 and 5 is devoted to one particular experiment (symbolised by the rows in Fig. 1.1). The main results of these experiments have already been published as peer-reviewed publications. Chapter 3 deals with a particular high-frequency and phase-modulated squeezed state that can be applied to spectroscopy [P1]. The single-mode squeezer is again subject of Chapter 4 but now operated in a detuned resonance condition to generate frequency-dependent squeezing [P2]. Chapter 5 considers a two-mode squeezed state that is fully reconstructed by taking measurements with a single homodyne detector [P3]. The three Chapters 3, 4 and 5 are each organised as follows. First, a more general introduction is presented, including the context and the concept of the applied methods. Then, the original publications are reprinted. At the end of the chapters, detailed background information is given which is not included in the publications. This completion should deliver more general explanations and, in particular, more technical details and characterisations of the experiments, which are omitted in the papers. In the end, the three chapters each close with an individual conclusion and discussion. The papers stand for themselves, but potential open questions will hopefully be answered

by the supplements given in these chapters.

The thesis ends with an overall conclusion and discussion. Here, the three previous chapters are set in relation. In particular, the most relevant insights are highlighted and contextualised. Finally, the key research results are brought back into a larger framework.

Remarks on the nomenclature

Some remarks on the nomenclature should be noted first. Whenever the word *squeezer* is used, it implicitly means that both squeezers are addressed, the OPO and the non-degenerate optical parametric oscillator (NDOPO). Throughout this thesis, I often speak about *low-frequency* and *high-frequency*. If not stated otherwise, low-frequency refers to frequencies in the hertz to kilohertz range.⁸ High-frequency usually refers to frequencies in the order of the free spectral range of our squeezers which is approximately 200 MHz. This thesis uses different quantum mechanical operators. In most parts, it dispenses with using operator hats.

How to read this thesis

I recommend reading this thesis chronologically, starting with Chapter 2. The publications are smoothly included in the corresponding Chapters 3, 4 and 5, which are designed to be largely independent. Busy readers are advised to focus on the publications and selectively on the framework around them in the corresponding chapters.

⁸Note that we are not using one-to-one the definitions from the International Telecommunication Union [Lya16] here.

Chapter 2

Theoretical and experimental background

This chapter is devoted to presenting the basic theory, technical details and experimental methods applied in this thesis. It by no means covers everything in its entirety. Some theoretic aspects have been accurately discussed by other works, which are referenced at these points. The experimental content mentioned in this chapter is tailored to the following three Chapters 3, 4 and 5.

This chapter starts with the classical description of an optical cavity¹ in Sec. 2.1. We theoretically study the electrical fields interacting with a cavity and plot their intensities. The equations for the fields are the basis for an experimental method to characterise the intra-cavity losses of a single-ended cavity. The section ends with the definition of the escape efficiency, the free spectral range, the linewidth and the finesse of a cavity. Section 2.2 describes the basics of quantum optics and introduces the quadrature state operators defined for a light field. Different quadrature distributions are plotted in the phase state picture, and the Wigner function is defined. Subsequently, the homodyne detection technique is presented, which is used to measure quantum states of light. Section 2.3 deals with the generation of quantum states. It begins with the theoretical input-output formalism of an optical cavity containing a non-linear medium. This general formulation derives the output states of the second harmonic generation (SHG) cavity and the sub-threshold² optical parametric oscillator (OPO). Here, the SHG and the OPO are treated from a more experimental perspective. This chapter ends with Sec. 2.4 focussing on the experimental implementation of the three different squeezers used for this thesis. Namely, they are a resonant 6-mirror OPO, a detuned 4-mirror OPO and a 4-mirror non-degenerate optical parametric oscillator (NDOPO). In this thesis, the NDOPO is often called *two-mode squeezer*. This section illustrates how to set up a two-mode squeezer and ends with the method characterising a squeezing experiment, including the process of generation and detection.

2.1 Classical description of an optical cavity

In this thesis, optical cavities with different objectives play a major role in all the presented experiments. For instance, a mode cleaner cavity [Wil+98] spatially filters the Gaussian beam and a four-mirror SHG cavity generates pump light for the down-conversion process in the squeezers.

This section aims to describe the classical properties of an arbitrary optical cavity theoretically. In the experiment, this theoretical model strongly helps to characterise

¹Throughout this thesis, the term *cavity* is used instead of *resonator*.

²Throughout this thesis, the prefixed term *sub-threshold* is omitted.

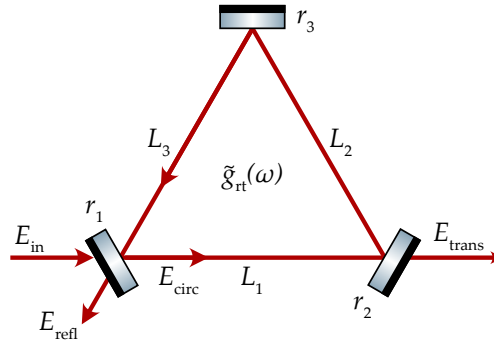


FIGURE 2.1: Schematic of an optical cavity with the electric input field E_{in} , the reflected field E_{refl} , the circulating field E_{circ} and the transmitted field E_{trans} . The parameter $\tilde{g}_{\text{rt}}(\omega)$ represents the frequency-dependent total intra-cavity gain per round-trip.

real cavities. One important parameter is the intra-cavity loss, which is directly related to the cavity's escape efficiency. Reaching a minimal loss is particularly important when working with squeezers.³

The section is distributed into two subsections. Subsection 2.1.1 derives the electrical fields inside, in transmission and reflection of an optical cavity. Subsection 2.1.2 defines the important parameters of the escape efficiency, the free spectral range, the linewidth and the finesse.

2.1.1 Electric fields in a cavity

The presented model is a scattering matrix formalism.⁴ We start with a resonant three-mirror travelling-wave cavity shown in Fig. 2.1. An electric field E_{in} is sent onto the input mirror with amplitude reflectivity r_1 .⁵ At this mirror, the reflected electric field is E_{refl} . The cavity consists of two more mirrors with amplitude reflectivities r_2 and r_3 . The mirror with r_2 is determined to be the output coupler, without loss of generality, where the transmitted field E_{trans} leaks out. In the cavity, a circulating field E_{circ} builds up, which is defined by⁶

$$E_{\text{circ}} = it_1 E_{\text{in}} + \tilde{g}_{\text{rt}}(\omega) E_{\text{circ}}. \quad (2.1)$$

Here, $\tilde{g}_{\text{rt}}(\omega)$ depends on the frequency ω and gives the net complex gain for a wave travelling one round-trip in the cavity. Note that in any passive optical cavity, this gain is less than unity, i.e. $|\tilde{g}_{\text{rt}}| < 1$.

Before \tilde{g}_{rt} is defined, the meaning of the mirror coefficients needs to be introduced. A convenient and general formulation, which holds for mirrors with arbitrarily high- and low-reflectivity mirrors,⁷ is the usage of *mirror coupling coefficients* δ . They are defined as

$$\delta_i = \ln \left(\frac{1}{R_i} \right) = 2 \ln \left(\frac{1}{r_i} \right). \quad (2.2)$$

³In this context, the term *squeezers* represents all cavities with non-linear crystals used for this thesis: OPO, detuned OPO and NDOPO.

⁴Here, I follow the model from [Sie86], Secs. 11.3 and 11.4.

⁵We assume lossless mirrors, meaning each mirror fulfils $1 = r^2 + t^2$, where t is the amplitude transmission. Any losses arising in the cavity are considered by δ_x later.

⁶Here, the symmetric beamsplitter convention is used.

⁷See [Sie86], Sec. 11.4.

In the limit of high reflectivities we use the approximations $\delta_i \approx T$, with T and $\delta_i \approx 1 - R$.⁸

Using the delta notation, the round-trip gain \tilde{g}_{rt} is defined as

$$\tilde{g}_{\text{rt}}(\omega) = e^{i\omega L_{\text{opt}}/c + \alpha - \delta_c/2}. \quad (2.3)$$

The exponent in Eq. (2.3) shows three different summands. The first represents the actual cavity resonance depending on the frequency ω , and the optical cavity length $L_{\text{opt}} = L_1 + L_2 + L_3$. Further, we can use the coefficient α for any active gain media. However, in the scope of this thesis, α is set to zero.⁹ The total cavity loss factor δ_c contains all losses arising in the cavity. Note that δ_0 includes not only the losses due to the mirrors $\delta_1, \delta_2, \delta_3$. Moreover, δ_0 also contains other arbitrary loss channels δ_x ,¹⁰ which may originate from stray light, absorption or lossy optical components in the beam path, e.g., crystals. Then, the total cavity loss factor reads

$$\delta_c = \delta_1 + \delta_2 + \delta_3 + \delta_x. \quad (2.4)$$

Equation (2.1) is solved for the circulating electric field E_{circ} which, after normalisation, reads

$$\frac{E_{\text{circ}}}{E_{\text{in}}} = \frac{it_1}{1 - \tilde{g}_{\text{rt}}(\omega)}. \quad (2.5)$$

From this result, the normalised transmitted and reflected fields are calculated:

$$\frac{E_{\text{trans}}}{E_{\text{in}}} = \frac{-t_1 t_2 \exp(-i\omega L_{\text{opt}}/c)}{1 - \tilde{g}_{\text{rt}}}, \quad (2.6)$$

$$\frac{E_{\text{refl}}}{E_{\text{in}}} = \frac{1}{r_1} \times \frac{r_1^2 - \tilde{g}_{\text{rt}}(\omega)}{1 - \tilde{g}_{\text{rt}}(\omega)}. \quad (2.7)$$

Equation (2.7) is an important result as it helps to characterise the intra-cavity losses of a single-ended cavity, which is often used in this thesis. In our experiments, usually, the power is measured, which is the integral of the intensity $I \propto |E|^2$ [ST19]:

$$P = \int dA I. \quad (2.8)$$

Using normalised modes, the power becomes also proportional to the intensity, with $P \propto I$ [Ste19].

2.1.2 Escape efficiency, free spectral range, linewidth, finesse

First, this subsection derives how the cavity escape efficiency is obtained from measurements of the reflected field. Then, the three important parameters, free spectral range, linewidth and finesse, are introduced.

⁸Here, R is the power reflection and T the power transmission of a mirror.

⁹Whenever we operate with cavities containing active gain media, we use the quantum-mechanical approach from Sec. 2.3.

¹⁰The index x refers to the fact that the origins of the intra-cavity loss, which can be, e.g. scattering loss or absorption are often unknown and not distinguishable when measuring the reflected modes.

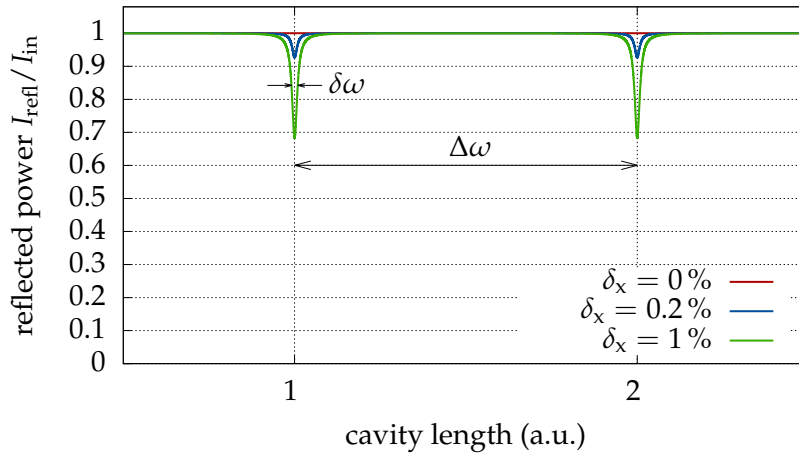


FIGURE 2.2: Reflected modes of a single-ended cavity with input/output mirror $R_1 = 90\%$ ($\delta_1 \approx 10.5\%$). Each trace corresponds to a specific intra-cavity loss δ_x .

We start with Fig. 2.2 where each trace shows the power of the modes in reflection of a ramped¹¹ cavity¹² for three different internal losses δ_x . Considering a single-ended cavity, it is convenient to rewrite Eq. (2.4) as

$$\delta_c = \delta_1 + \delta_x, \quad (2.9)$$

where δ_x simply includes all *bad losses*¹³ of the cavity, independent of their origins. In Fig. 2.2, the reflectivity of the input mirror is chosen to be $R_1 = 90\%$.¹⁴ Taking also the reflected powers on resonance P_{res} and anti-resonance P_{ares} into account, the intra-cavity power loss δ_x is calculated with the absolute squared of Eq. (2.7).¹⁵ We find

$$\delta_x \approx \frac{r_1 + \delta P}{1 + r_1 \delta P} \quad \text{with} \quad \delta P = \sqrt{\frac{P_{\text{res}}}{P_{\text{ares}}}}. \quad (2.10)$$

With δ_x being determined, the cavity's escape efficiency is calculated as

$$\eta_{\text{esc}} = \frac{\delta_1}{\delta_1 + \delta_x}. \quad (2.11)$$

Beneficially, the cavity does not have to be stabilised when using this method of studying modes in reflection. We also apply this method to optical cavities containing non-linear crystals.¹⁶ For such cavities, the dominating loss usually arises due to residual beam reflections on the crystal surfaces. For squeezers, minimising the intra-cavity loss is of high relevance.

¹¹Ramping the cavity means that the cavity phase is linearly changed.

¹²A full cavity transfer function for the electric field includes plots of the absolute $|E|$ and the phase given by $\arg(E)$.

¹³Later in Subsec. 2.3.2, also *good losses* will be defined arising from conversion in an SHG cavity

¹⁴In an experiment, this can be measured by the single-pass transmission.

¹⁵This approach assumes an ideal mode-matching of the input beam to the cavity eigenmode.

¹⁶In this case, we need to ensure that the conversion process is suppressed since it would manifest itself as a loss channel.

Figure 2.2 reveals further characteristic quantities of optical cavities. It shows the free spectral range of a cavity, defined by

$$\Delta\omega = \frac{c_0}{L_{\text{opt}}} \quad (2.12)$$

and the linewidths of the cavity's resonance peaks, defined by their full width at half maximum (FWHM)

$$\delta\omega = \frac{4c_0}{L_{\text{opt}}} \arcsin\left(\frac{1 - g_{\text{rt}}}{2\sqrt{g_{\text{rt}}}}\right). \quad (2.13)$$

Here c_0 is the speed of light in vacuum. In Fig. 2.2, the cavity linewidth $\delta\omega$ varies for the three different loss values δ_x . The finesse \mathcal{F} of a cavity indicates how narrow the resonances are in relation to their frequency distance. It is defined by

$$\mathcal{F} = \frac{\pi\sqrt{g_{\text{rt}}}}{1 - g_{\text{rt}}}, \quad (2.14)$$

with

$$g_{\text{rt}} = |\tilde{g}_{\text{rt}}|. \quad (2.15)$$

The current section focusses on the longitudinal resonance conditions for cavities since this part is most relevant to this thesis. Other aspects, such as the transversal resonance analysis of beams in cavities, mode-matching or the stability criteria, are intentionally omitted. However, they are also essential to consider when working with optical cavities. The interested reader is referred to, e.g. [KL66] or to doctoral theses [Thü09; Ste19]. In the scope of this thesis, the stabilisation of optical cavities is important and thus done with different methods: I used the Pound-Drever-Hall (PDH) technique [Dre+83; Bla01], the internal dither approach [Her+06], and the polarisation-based homodyne locking method [HC80; Heu+09].

Complex electric fields can be visualised in a sideband picture. It is helpful to present and understand phase or amplitude modulated electric fields by using sidebands. The sideband picture is thoroughly explained, e.g. in [Mal06; Kau18]. Moreover, Subsec. 2.3.3 introduces the quantum sideband picture.

2.2 Characteristics of quantum states

This section deals with the quantum-mechanical properties of light. It starts with describing the electromagnetic field and its quantisation in Subsec. 2.2.1, whose result is the quantised Hamilton operator. Next, the Hermitian quadrature operators are defined, which are thus observables playing a major role in the experiments in this thesis. In Subsec. 2.2.2, relevant terms such as the variance, the covariance matrix and the Wigner function are defined for a statistical description of quantum states. Different quantum states are discussed and compared in Subsec. 2.2.3. The phase-state picture is introduced to gain a better visualisation and understanding of these states. This section closes with Subsec. 2.2.4 explaining the homodyne detection technique used to measure quantum states.

2.2.1 Electromagnetic field quantisation and quadrature operators

The quantum-mechanical properties of light are not revealed by the classical description used in Sec. 2.1. This subsection deals with the quantisation of the electromagnetic field and introduces the quadrature operators as observables.¹⁷

Light can be described by electromagnetic fields. To find out how light propagates in free-space, the electromagnetic wave equation needs to be solved as derived by the Maxwell equations [Max65]. One solution of the wave equation can be written as the electric field vector consisting of discrete modes j

$$\mathbf{E}(\mathbf{r}, t) = i \sum_j \left(\frac{\hbar \omega_j}{2\epsilon_0} \right)^{1/2} \left(a_j \mathbf{u}_j(\mathbf{r}) e^{-i\omega_j t} - a_j^\dagger \mathbf{u}_j^*(\mathbf{r}) e^{i\omega_j t} \right). \quad (2.16)$$

Here, the normalisation factor contains the vacuum permittivity ϵ_0 , the angular mode frequency ω_j and the reduced Planck constant $\hbar = h/(2\pi)$. The vector \mathbf{u} describes the polarisation state and the spatial mode properties of the wave. For plane waves, Eq. (2.16) simplifies with $\mathbf{u}_j(\mathbf{r}) = e^{i\mathbf{k}_j \mathbf{r}}$. The complex field amplitudes a and a^\dagger are dimensionless in Eq. (2.16). For the canonical quantisation, they are converted into mutually adjoint operators via

$$a \rightarrow \hat{a}, \quad a^\dagger \rightarrow \hat{a}^\dagger. \quad (2.17)$$

With the same canonical quantisation, and by implementing the boundary conditions, the classical Hamiltonian for the electromagnetic field is converted via

$$H = \frac{1}{2} \int \left(\epsilon_0 \mathbf{E}^2 + \frac{\mathbf{B}^2}{\mu_0} \right) dV \quad \rightarrow \quad \hat{H} = \sum_j \hbar \omega_j \left(a_j^\dagger a_j + \frac{1}{2} \right), \quad (2.18)$$

into the quantum mechanical *Hamilton operator* \hat{H} .¹⁸ It means that the state in each mode is described by a state vector $|\psi\rangle_j$ in the Hilbert space. Below, all operator hats are omitted to increase readability. After the quantisation, the electric field becomes a superposition of individual and independent modes of harmonic oscillators, which all have a different frequency ω_j . For a specific mode j , $a_j^\dagger a_j = n_j$ represents the number of photons and corresponds to the energy of the vacuum fluctuations $\hbar \omega_j$.

The concept of a *mode* is essential for this thesis. Different parameters, e.g. the frequency, the polarisation, the spatial shape¹⁹ and the direction of propagation, determine a distinct mode. Hence, all these parameters are well defined for a mode [Sch17]. In this thesis, we deal with different modes that are well distinguishable. For instance, two orthogonally polarised modes do not interfere with each other since the orthogonal polarisation states are basis functions.²⁰

For any experimental work, it is beneficial to work with observables. Thus, we define the Hermitian quadrature operators as²¹

$$X_1 = X^+ = a^\dagger + a, \quad (2.19)$$

$$X_2 = X^- = i(a^\dagger - a). \quad (2.20)$$

¹⁷This subsection is geared to [WM08].

¹⁸Here, μ_0 is the vacuum magnetic permeability.

¹⁹More details can be found in literature, for basic definitions, e.g. the Rayleigh range, the beam waist and the Gouy phase, see [Sie86], Sec. 17.1.

²⁰For the polarisation, other basis functions are possible, e.g. left circular and right circular polarised states.

²¹The quadratures are normalised for a unitary vacuum variance.

fulfilling the commutator relation

$$[X_1, X_2] = 2i, \quad (2.21)$$

and translating the Hamilton operator from Eq. (2.18) into

$$H = \frac{\hbar\omega_j}{4} (X_1^2 + X_2^2). \quad (2.22)$$

We call X_1 the amplitude quadrature and X_2 the phase quadrature of a specific quantum state.

In quantum optics, an often-used linearisation facilitates working with operators. Mode operators can be decomposed into a complex number $\alpha = \langle a \rangle$ representing the mean field and into the operator δa containing the time dependent-fluctuations. This linearisation is valid for bright, steady-state electric fields, namely fields with amplitudes much larger than their fluctuations [Whi97]. We write them as

$$\begin{aligned} a &= \alpha + \delta a, \\ a^\dagger &= \alpha^* + \delta a^\dagger. \end{aligned} \quad (2.23)$$

Subsequently, the linearisation is analogously applied to Eqs. (2.19) and (2.20)

$$X_1 = \alpha + \alpha^* + \delta a^\dagger + \delta a = \langle X_1 \rangle + \delta X_1, \quad (2.24)$$

$$X_2 = i(\alpha - \alpha^* + \delta a^\dagger - \delta a) = \langle X_2 \rangle + \delta X_2. \quad (2.25)$$

These linearisations are used several times throughout this thesis.

Before continuing to the statistics, we should first clarify what a *quantum state* is. In classical physics, we can accurately determine the state of an object, e.g., by determining its specific position x_0 and momentum p_0 . However, in quantum mechanics, we do not know in which exact *state* a quantum particle is. We can only describe the wave function of a particle's trajectory. The wave function gives the probability of measuring quadratures X_1 and X_2 of the particle.

2.2.2 Statistics of quantum states

Since a quantum state is always determined by a probability distribution, it is useful to use statistics for its description. For any two arbitrary operators X and Y , the covariance is defined as

$$\text{cov}(Y, X) = \text{cov}(X, Y) = \frac{1}{2} \langle XY + YX \rangle - \langle X \rangle \langle Y \rangle. \quad (2.26)$$

Additionally, for any arbitrary operator X , the variance is defined as

$$\text{var } X = \text{cov}(X, X) = \langle X^2 \rangle - \langle X \rangle^2, \quad (2.27)$$

and the standard deviation as

$$\Delta X = \sqrt{\text{var } X}. \quad (2.28)$$

This thesis mostly discusses Gaussian states, which are related to normal distributions. A Gaussian quantum state is fully characterised by the first two statistical moments [SSM87]. The first moments d are the mean values defined by

$$d_i = \langle X_i \rangle. \quad (2.29)$$

The second moments are represented in the covariance matrix σ , which is a real, symmetric, positive definite matrix. It contains information about the quantum noise and fully characterises the state. The covariance matrix σ uses the definitions from Eq. (2.27) and Eq. (2.26). For any N -mode state with $2N$ canonical quadratures $\mathbf{X} = \{X_1, \dots, X_{2N}\}$, it has a dimension of $2N \times 2N$ and is entry-wise defined by

$$\sigma_{i,j} = \text{cov}(X_i, X_j). \quad (2.30)$$

When measuring the quadratures of a quantum state, the result cannot be predicted with arbitrary precision. In the simple scenario of a single-mode state, this is expressed in the famous Heisenberg uncertainty, which is here formulated for the standard deviations of the quadrature operators:

$$\Delta X_1 \Delta X_2 \geq 1. \quad (2.31)$$

If the equality is fulfilled in Eq. (2.31), the quantum state is a minimum uncertainty state or pure state. This is true, e.g. for a vacuum state or a coherent state, as will be seen in the next Subsec. 2.2.3. Before discussing different quantum states, the phase state picture is explained.

The phase space picture²² is used to visualise a quantum state and represents possible measurement outcomes of the state. Often only an ellipse is drawn. The ellipse is defined for any N -mode Gaussian state by a cross-section's contour line of the Wigner quasi-probability²³ distribution or Wigner function [Wig32; ASI04]

$$W(\mathbf{X}) = \frac{1}{\pi^N \sqrt{\det(\sigma)}} e^{-(\mathbf{X}-d)^\top \sigma^{-1} (\mathbf{X}-d)}. \quad (2.32)$$

The ellipse's major and minor axes represent the standard deviations ΔX_1 and ΔX_2 of the state, see Fig. 2.3a). The Wigner function is normalised:

$$\int_{-\infty}^{\infty} W(\mathbf{X}) d\mathbf{X} = 1. \quad (2.33)$$

We also can use the phase space picture to obtain the variance of a quantum state in an arbitrary quadrature rotated by an angle θ

$$X_\theta = a e^{-i\theta} + a^\dagger e^{i\theta} = X_1 \cos \theta + X_2 \sin \theta. \quad (2.34)$$

Now, we can also determine the widths ΔY_1 and ΔY_2 of the quantum state in the new coordinates $Y_1 = X_\theta$ and $Y_2 = X_{\theta+\pi/2}$, as shown in Fig. 2.3b).

The phase state picture is a powerful tool to represent a quantum state. However, it only shows the situation at a specific measurement frequency Ω . The frequency Ω refers to modes that are measured at $\omega_0 \pm \Omega$ around a reference state oscillating at ω_0 . Thus, to fully describe a frequency-dependent²⁴ quantum state, the phase state

²²The phase state picture originates from [Wey27; Wig32] and was further developed by [Gro46; Moy49]. Here, the *optical* phase state picture is used, where the two quadrature operators X_1 and X_2 are plotted instead of momentum and position operators.

²³A quasi-probability distribution does not need to fulfil the first axiom of probability. Thus, it can, e.g. contain negative values.

²⁴In reality, all quantum states are frequency-dependent. For instance, in the case of squeezing generated by an OPO, the cavity itself and the down-conversion process have limited bandwidths, which is limited by the phase-matching condition, as can be seen, e.g. in [Whi97], Sec. 2.4.2.

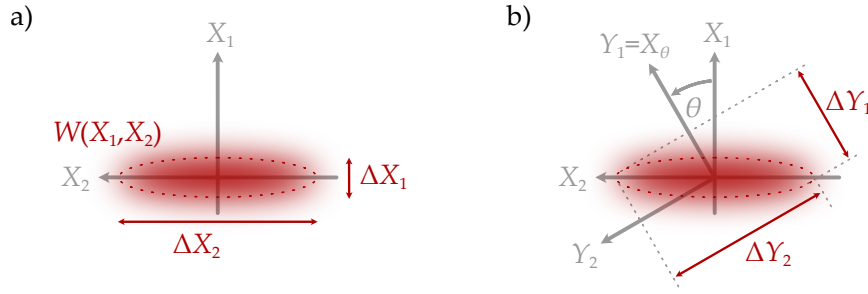


FIGURE 2.3: a) The phase space picture presents a quantum state described by its distribution $W(X_1, X_2)$. The widths of the quantum state correspond to the standard deviations ΔX_1 and ΔX_2 . b) In the new coordinate system rotated by θ , the quantum state has widths of $\Delta Y_1 = \Delta X_\theta$ and $\Delta Y_2 = \Delta X_{\theta+\pi/2}$.

picture must be drawn at all frequencies of interest.²⁵

The basic principles of quantum states visualised by the phase space picture were introduced. Next, we will discuss different quantum states.

2.2.3 Vacuum states, coherent states, squeezed states

This section is devoted to presenting some Gaussian quantum states that are important for this thesis.²⁶ It starts with vacuum and coherent states and will be continued explaining by squeezed states. Finally, the influence of optical loss on these kinds of states is discussed.

Vacuum and coherent states

Before analysing the coherent states, the *Fock states* or *number states* $|n_j\rangle$ are introduced. They are eigenstates of the number operator $N_j = a_j^\dagger a_j$ with

$$a_j^\dagger a_j |n_j\rangle = n_j |n_j\rangle. \quad (2.35)$$

The Fock states are orthogonal and form a complete set of basis vectors for a Hilbert space.

For our experiments, the most important Fock state is the ground state representing the vacuum state $|0\rangle_j$ of the field mode j , see its phase space representation in Fig. 2.4a). This is an exceptional Fock state since it is the only Gaussian one. It has no defined phase and thus equal variances for any quadrature X_θ . Even though this state contains zero photons, it has a zero point energy of $\hbar\omega_j/2$.

The coherent state can be seen as the most classical²⁷ quantum state and is created by letting the displacement operator $D(\alpha_j) = \exp(\alpha_j a_j^\dagger - \alpha_j^* a_j)$ act on the vacuum state:

$$|\alpha_j\rangle = D(\alpha_j) |0\rangle. \quad (2.36)$$

We see that in the phase space picture in Fig. 2.4b), the coherent state is created by displacing the vacuum state by $|\alpha_j|$. The parameter α_j is the complex eigenvalue of

²⁵In Subsec. 2.3.3, the quantum sideband picture is introduced, which elaborates more on the frequency dependence. A detailed presentation can be found in [Che07], Sec. 2.10.

²⁶A more detailed explanation of different quantum states can be found in [WM08], Chapter 2, or in [GK04], Chapter 3 and 7.

²⁷For instance, a field emitted by a laser can be described as a coherent state for high Fourier frequencies, where quantum noise dominates over technical noise sources.

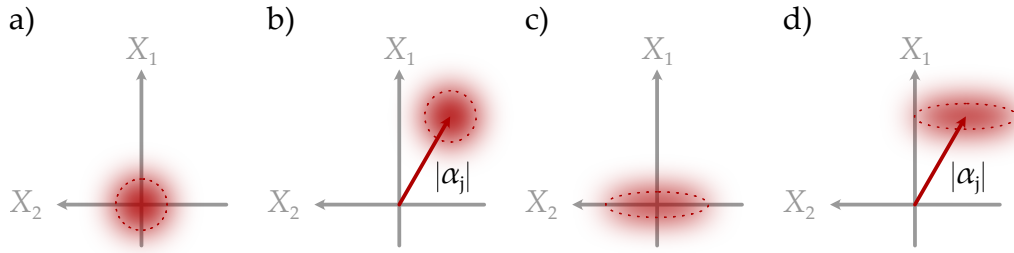


FIGURE 2.4: Representation of a) vacuum state, b) coherent state, c) quadrature squeezed state, d) bright quadrature squeezed state in the phase space picture. The dashed error ellipses show the widths of the variances for each state, and the arrow indicates a coherent amplitude with length $|\alpha| = 1/2\langle X_1 + iX_2 \rangle$.

the annihilation operator a_j :

$$a_j |\alpha_j\rangle = \alpha_j |\alpha_j\rangle. \quad (2.37)$$

Physically, it's absolute squared refers to the average photon number of the field $\bar{n}_j = |\alpha_j|^2$. The vacuum state and the coherent state both have a unitary variance in all arbitrary quadratures and are, thus, states with minimum uncertainty.

Single-mode squeezed vacuum and bright squeezed states

The next class of quantum states to discuss are single-mode quadrature squeezed states.²⁸ We distinguish between vacuum squeezing and bright squeezing, which can be seen in analogy to vacuum and coherent states. A squeezed state has less noise in one quadrature (squeezed) and increased noise in the orthogonal quadrature (anti-squeezed).

Squeezed vacuum states do not have a coherent amplitude, as shown in Fig. 2.4c). They are generated by applying the squeezing operator

$$S(\xi) = \exp\left(\frac{1}{2}(\xi^* a^2 - \xi a^\dagger)\right) \quad (2.38)$$

to the vacuum state

$$|\xi\rangle = S(\xi) |0\rangle, \quad (2.39)$$

which is a Bogoliubov transformation [BL04]. The argument of the squeezing operator is defined as $\xi = r e^{i\theta}$ with squeezing factor r fulfilling $0 \leq r < \infty$ and squeezing angle θ fulfilling $0 \leq \theta < 2\pi$.

Bright squeezed states are squeezed vacuum states displaced by $|\alpha_j|$, as presented in Fig. 2.4d). They are generated by applying the squeezing operator and the displacement operator to a vacuum state:

$$|\alpha, \xi\rangle = D(\alpha)S(\xi) |0\rangle. \quad (2.40)$$

Even though the standard deviation in one quadrature can fall below unity for a squeezed state, the uncertainty relation from Eq. (2.31) is always fulfilled.

The four states presented in Fig. 2.4 are fully defined by the covariance matrix $\sigma(X_1, X_2)$ according to Eq. (2.30). Since they are single-mode states ($N = 1$ in

²⁸The terms *quadrature squeezed* states should not be mixed with *squeezed* states. The latter class is not relevant to this thesis. Amplitude squeezed states are shown in [GK04], Fig. 7.13, or in [BLZ19], Fig. 3.1. They were generated, e.g. in [Yam+87]. However, throughout this thesis, the term *squeezed states* always implicitly stands for *quadrature squeezed states*.

Eq. (2.30)), the covariance matrix is 2×2 -dimensional:

$$\sigma = \begin{pmatrix} \text{var } X_1 & \text{cov } X_1, X_2 \\ \text{cov } X_2, X_1 & \text{var } X_2 \end{pmatrix}. \quad (2.41)$$

For the vacuum and the coherent state, the covariance matrix reads

$$\sigma_{\text{vac}} = \sigma_{\text{coh}} = \begin{pmatrix} 1 & 0 \\ 0 & 1 \end{pmatrix}. \quad (2.42)$$

For the single-mode squeezed states, the covariance matrix is [FOP05; ARL14]

$$\sigma_{1\text{ms}} = \begin{pmatrix} \cosh(2r) + \sinh(2r) \cos(\theta) & \sinh(2r) \sin(\theta) \\ \sinh(2r) \sin(\theta) & \cosh(2r) - \sinh(2r) \cos(\theta) \end{pmatrix}, \quad (2.43)$$

which takes a diagonal form for $\theta = 0$ or $\theta = \pi$. Then the state is squeezed/anti-squeezed only along the X_1 - respectively X_2 -axis.

After considering a single mode a , next, two-mode squeezed states are introduced.

Two-mode squeezed states

In analogy to the single-mode quadrature squeezed state discussed before, for the two-mode squeezed state, a new squeezing operator is required with

$$S_2(\xi) = \exp\left(1/2(\xi^* a_s a_p - \xi a_s^\dagger a_p^\dagger)\right). \quad (2.44)$$

To create a two-mode squeezed state, this operator is applied to a two-mode vacuum

$$|\xi\rangle_2 = S_2(\xi) |0_s, 0_p\rangle. \quad (2.45)$$

The two-mode squeezed state is entangled and exhibits correlations between the two modes a_s and a_p .²⁹ Hence, squeezing is not visible in the individual modes but rather in a superposition of the two modes, e.g. in one of the quadratures³⁰

$$X_\Sigma = (a_s + a_s^\dagger + a_p + a_p^\dagger) = X_1^s + X_1^p, \quad (2.46a)$$

$$X_\Delta = -i(a_s - a_s^\dagger + a_p - a_p^\dagger) = X_2^s + X_2^p. \quad (2.46b)$$

Two other combinations are possible with

$$X_\Gamma = X_1^s - X_1^p, \quad (2.47a)$$

$$X_\Lambda = X_2^s - X_2^p, \quad (2.47b)$$

For a fixed squeezing angle, we find that the operators X_Σ and X_Λ are squeezed and X_Δ and X_Γ are anti-squeezed. Hence, X_Σ and X_Λ are Einstein-Podolsky-Rosen (EPR) variables.³¹ They can be used to demonstrate the EPR paradox as they are measured with arbitrary precision at the same time [EPR35; Ou+92].

For the two-mode squeezed state, we also calculate the four-dimensional Wigner function using Eq. (2.32) with $N = 2$. Now, the covariance matrix σ is a 4×4 matrix

²⁹The indices s and p already refer to the two orthogonal polarisations used in Chapter 5. However, any other mode distinction is valid here.

³⁰In the other one, anti-squeezing is visible. For more details, see, e.g. [GK04], Sec. 7.7.

³¹For a different squeezing angle, also X_Δ and X_Γ can be EPR variables.

and reads for $\theta = 0$ ³²

$$\sigma_{2\text{ms}} = \begin{pmatrix} \cosh 2r & 0 & \sinh 2r & 0 \\ 0 & \cosh 2r & 0 & -\sinh 2r \\ \sinh 2r & 0 & \cosh 2r & 0 \\ 0 & -\sinh 2r & 0 & \cosh 2r \end{pmatrix}. \quad (2.48)$$

Chapter 5 shows an experiment, where two-mode squeezed states are generated and detected. There, the meaning and visualisation of the 4×4 covariance matrix is visualised.

Influence of loss on quantum states

Up to this point, all considered states were treated as pure states with minimum uncertainty according to Eq. (2.31). Next, the influence of optical losses on quantum states is considered. Optical loss is described as mixing the state with vacuum on a beamsplitter. The electric field operator changes according to

$$a_{\text{out}} = \sqrt{\eta}a_{\text{in}} + \sqrt{1-\eta}a_{\text{vac}}, \quad (2.49)$$

where the efficiency depends on the power loss factor L via $\eta = 1 - L$. Any variance V_{in} that is affected by optical loss can be written by

$$V_{\text{out}} = \eta V_{\text{in}} + (1 - \eta). \quad (2.50)$$

Sometimes it is more helpful to see how the full covariance matrix changes due to optical loss because it directly presents all required information and can be used to create a phase space picture of the state. For a single-mode squeezed state with efficiency η , the covariance matrix from Eq. (2.43) changes to

$$\sigma_{1\text{ms}} = \begin{pmatrix} 1 - \eta (1 - \cos(\theta) \sinh(2r) - \cosh(2r)) & \eta \sin(\theta) \sinh(2r) \\ \eta \sin(\theta) \sinh(2r) & 1 - \eta (1 - \cos(\theta) \sinh(2r) - \cosh(2r)) \end{pmatrix}. \quad (2.51)$$

For a two-mode squeezed state, the covariance matrix changes from Eq. (2.48) to [Ste19]

$$\sigma_{2\text{ms}} = \begin{pmatrix} 1 - \eta_s + \eta_s \cosh 2r & 0 & \sqrt{\eta_s \eta_p} \sinh 2r & 0 \\ 0 & 1 - \eta_s + \eta_s \cosh 2r & 0 & -\sqrt{\eta_s \eta_p} \sinh 2r \\ \sqrt{\eta_s \eta_p} \sinh 2r & 0 & 1 - \eta_p + \eta_p \cosh 2r & 0 \\ 0 & -\sqrt{\eta_s \eta_p} \sinh 2r & 0 & 1 - \eta_p + \eta_p \cosh 2r \end{pmatrix}, \quad (2.52)$$

where η_p and η_s are mode-dependent efficiencies.

In conclusion, squeezed states are theoretically described by the covariance matrix, and they are visualised in phase space pictures. To experimentally benefit from squeezed states, they need to be detected. The next section deals with the homodyne detection of quantum states.

2.2.4 Detection of quantum states

The quadrature variances are utilised in quantum optical experiments to describe a quantum state. The characteristics of the state are usually analysed with a spectrum

³²For a derivation, see e.g. [ARL14] or [Ste19].

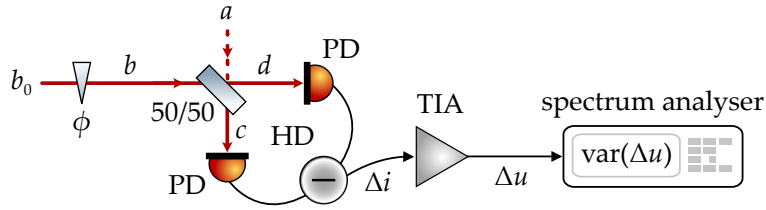


FIGURE 2.5: Schematic of a homodyne detection (HD) scheme. The local oscillator b interferes with the signal a on a 50/50 beamsplitter. The resulting modes c and d are detected by individual photodiodes (PDs). In the photodetector, the difference photocurrent Δi is generated and converted into a voltage Δu by a transimpedance amplifier (TIA). Finally, the voltage is applied to a spectrum analyser to measure its variance.

analyser measuring voltages. A photodetector is employed to change from the optical to the electronic regime. The photodetector consists of a photodiode converting the incident photons into a photocurrent. A transimpedance amplifier converts the photocurrent into a voltage. In the following, we call the quantum state under consideration *signal* field.

Photodetectors are deployed for different detection schemes. The most straightforward scheme is when the signal is directly detected on a photodetector. Then only the field's amplitude is measured for sufficiently high coherent amplitude signals. Using two photodetectors and a local oscillator field enables the advanced homodyne detection method. Various realisations are possible, from balanced homodyne detection to polarisation-based homodyne detection.³³ In this section, we want to focus on balanced homodyne detection because it is used in Chapter 3 and 4. In Chapter 5, two particular homodyne detection schemes are applied, which will be explained in Subsecs. 5.3.1 and 5.3.2.

The basic setup of homodyne detection is depicted in Fig. 2.5. Here, the local oscillator $b = b_0 \exp(i\phi)$ interferes with the signal a on a 50/50 beamsplitter. The resulting modes c and d are detected by individual photodiodes (PDs). The output modes are defined by³⁴

$$c = \frac{1}{\sqrt{2}}a + \frac{1}{\sqrt{2}}b, \quad (2.53)$$

$$d = -\frac{1}{\sqrt{2}}a + \frac{1}{\sqrt{2}}b. \quad (2.54)$$

In the photodiode, the n photons are converted into a photocurrent i . The performance of the process to detect photons can be ascribed by the quantum efficiency

$$\eta_{\text{qe}} = \frac{I}{P} \frac{hc_0}{e\lambda}, \quad (2.55)$$

with the wavelength of the light λ , the elementary charge e , the Planck constant h and the speed of light c_0 . The photocurrents from both photodiodes are subtracted, and the difference current Δi , proportional to the difference power ΔP , is $\Delta i \propto \Delta P \propto c^\dagger c - d^\dagger d$. Then, the transimpedance amplifier in the photodetector (TIA) generates a difference

³³A more detailed overview of different detection schemes is given, e.g. in [Che07; Den16].

³⁴Here, the asymmetric beamsplitter convention is used where one reflected (or transmitted) field, here a , experiences a phase shift of π .

voltage $\Delta u \propto \Delta i$.³⁵ Deploying the linearisations from Eq. (2.23), the two fields can be written as

$$a = \alpha + \delta a, \quad (2.56)$$

$$b = (\beta_0 + \delta b) \exp(i\phi). \quad (2.57)$$

We find the difference voltage³⁶

$$\Delta u \propto c^\dagger c - d^\dagger d \approx 2\alpha\beta_0 \cos(\phi) + \alpha\delta X_{-\phi,b} + \beta_0\delta X_{\phi,a}. \quad (2.58)$$

This equation is an approximation which neglects higher order terms going with δ^2 that are relatively small. Equation (2.58) shows that the signal's field fluctuations are amplified with the amplitude of the local oscillator. Further, the local oscillator's fluctuations scale with the signal's amplitude. Equation (2.58) is simplified when the two homodyne conditions

$$\beta_0 \gg \alpha, \quad (2.59)$$

$$\beta_0\delta X_{\phi,a} \gg \alpha\delta X_{-\phi,b} \quad (2.60)$$

are fulfilled.³⁷ Then the difference voltage reads

$$\Delta u \propto c^\dagger c - d^\dagger d \approx 2\alpha\beta_0 \cos(\phi) + \beta_0\delta X_{\phi,a}. \quad (2.61)$$

It means that the local oscillator's amplitude β_0 scales the signal's quadrature fluctuations $\delta X_{\phi,a}$. Depending on the relative phase ϕ ,³⁸ any arbitrary signal quadrature $\delta X_{\phi,a}$ can be read out.

Finally, the difference voltage is applied to a spectrum analyser to measure its variance³⁹

$$\text{var } \Delta u \propto \alpha^2 \langle \delta X_{-\phi,b}^2 \rangle + \beta_0^2 \langle \delta X_{\phi,a}^2 \rangle. \quad (2.62)$$

If the homodyne conditions from Eqs. (2.59) and (2.60) are fulfilled, Eq. (2.62) is, after shot noise normalisation, approximated to

$$\text{var } \Delta u' \propto \langle \delta X_{\phi,a}^2 \rangle. \quad (2.63)$$

The calculation of the homodyne detection assumes some idealisations. We implied the beamsplitter's reflectivity to be 50/50, equal quantum efficiencies of both diodes and that all optical fields are in the same spatial mode. In an experiment, an imperfect mode overlap has the most significant consequences for the homodyne detection. Then, the local oscillator field β_0 from Eq. (2.61) will amplify the signal's quadrature fluctuations $\delta X_{\phi,a}$ and a fraction of incoupling vacuum noise. The imperfect mode-overlap is covered by the visibility efficiency

$$\eta_{\text{vis}} = \mathcal{V}^2, \quad (2.64)$$

³⁵To calculate the exact voltage, use Eq. (2.55) and replace the current with Ohms law $u = Ri$, where R is the transimpedance resistance.

³⁶Remind the definition for an arbitrary quadrature X_ϕ from Eq. (2.34). A step-by-step derivation of Δu can be found in [Che07], Sec. 2.9.5.

³⁷For large quadrature fluctuations of the local oscillator, Eq. (2.60) might not be fulfilled anymore for a bright signal field ($a \neq 0$). Therefore, in this thesis, the homodyne detection is usually done at high Fourier frequencies, where the local oscillator is shot noise limited.

³⁸Often, ϕ is called the *detection angle*.

³⁹As can be seen e.g. in [Che07], Sec. 2.9.3.

where \mathcal{V} is the visibility. The visibility is measured by using equal amplitudes $a = b_0$, scanning the phase ϕ and detecting the maximal I_{\max} and minimal I_{\min} intensity measured on one photodiode of the homodyne detector:

$$\mathcal{V} = \frac{I_{\max} - I_{\min}}{I_{\max} + I_{\min}}. \quad (2.65)$$

In particular for detecting squeezed states, a good mode-matching and highly-efficient photodiodes are very crucial. Here, the goal is, to maximise the homodyne efficiency

$$\eta_{\text{hd}} = \eta_{\text{qe}}\eta_{\text{vis}}. \quad (2.66)$$

In this subsection we have seen that the homodyne detection technique is capable of detecting the quadrature fluctuations of a weak signal field, e.g. a squeezed state. The next Sec. 2.3 addresses the question how quantum states as squeezing can be generated by using optical cavities.

2.3 Cavities with non-linear crystals

The section is dedicated to the input-output formalism, which predicts the quantum mechanical noise behaviour of optical cavities. First, Subsec. 2.3.1 describes the general quantum model of an optical cavity with a $\chi^{(2)}$ -interaction.⁴⁰ In this subsection, all needed parameters are introduced, and the equations of motion are shown. The first application of these equations is made for an SHG in Subsec. 2.3.2. This subsection already links the experimental part because it explains the actual design of the SHG used for all three experiments in Chapters 3, 4 and 5. The section ends with the input-output formalism applied on an OPO in Subsec. 2.3.3. Here, a recipe is presented, including all steps to calculate the output variances of an OPO. After obtaining the output variance, important parameters such as the cavity escape efficiency and the pump parameter are defined.

2.3.1 General theoretical model

Here, the general quantum model is applied to optical cavities containing a non-linear $\chi^{(2)}$ medium. The quantum Langevin equations are used to describe these cavities. First, Gardiner and Collett used this approach in 1985, which is shown here [GC85].⁴¹ It is adapted from its original formulation developed by Langevin in 1908 [Lan08; LG97].

The considered cavity is shown in Fig. 2.6. It consists of a non-linear $\chi^{(2)}$ -crystal and three mirrors, all designed for the fundamental mode a . For now, we assume type-0 phase matching,⁴² meaning the fundamental a and the harmonic b are in the same polarisation state. We also assume, that a oscillates with frequency ω_f and b with frequency ω_p and that $2\omega_f = \omega_p$. For simplicity, the cavity does not exist for the harmonic mode b , which is experimentally legitimated due to anti-reflective coated mirrors for this wavelength. The following parameters are needed for the description:

⁴⁰The model can also be studied for *empty* cavities, as done e.g. in [WM08; Whe16; BR19].

⁴¹A general explanation of the input-output formalism, e.g., for an empty cavity and an optical parametric oscillator, can be found in [WM08], Chapter 7.

⁴²Basically, phase matching means that the interacting waves do not run out of phase along the propagation direction, eventually inverting the process. For more information regarding phase matching in squeezers, see [Boy20], Chapter 2.

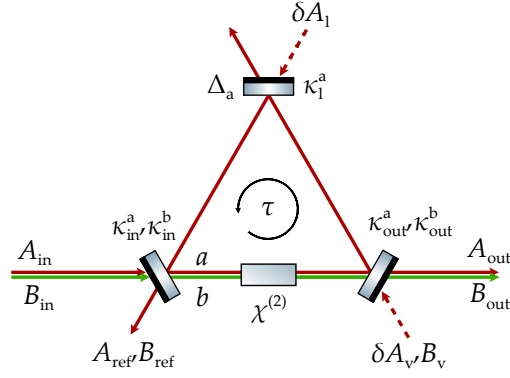


FIGURE 2.6: Schematic of an optical cavity containing a non-linear $\chi^{(2)}$ medium. We distinguish between the fundamental cavity mode a and cavity rates A and the harmonic mode b and cavity rates B . The cavity only exists for the fundamental field with detuning Δ and round-trip time τ . The coupling strengths of the mirrors are given by the decay rates κ .

- The intra-cavity modes a and b representing the photon numbers in dimensionless units.
- The input and output rates A_{in} , B_{in} , A_{out} and B_{out} in units of $\sqrt{\text{Hz}}$.
- The cavity round-trip time τ in units of second.
- The cavity decay rate⁴³ for the fundamental mode $\kappa_a = \kappa_{in}^a + \kappa_{out}^a + \kappa_1^a$ in units of Hz. The decay rate is connected to the absolute of the round trip gain g_{rt} from Eq. (2.15) via $\kappa = (1 - g_{rt})/\tau$ [Sie86; Lam98]. In the case of a single-ended cavity with the input coupler's power transmission of T and low internal losses, we can approximate $\kappa \approx T/(2\tau)$.⁴⁴
- The impinging vacuum rates δA_1 and δA_v in units of $\sqrt{\text{Hz}}$.
- The coupling strength χ , proportional to the second-order non-linear susceptibility in units of Hz. In the experiment, it also depends on the intensity distribution,⁴⁵ the mode-matching, the phase matching of the down-conversion process and imperfections of the crystal.
- The detuning of the cavity for the fundamental mode Δ in units of Hz.

The system is modelled by the Hamiltonian in the rotating frame of the pump field⁴⁶

$$H = \hbar\omega_f a^\dagger a + \hbar\omega_p b^\dagger b + \frac{i\hbar\chi}{2} (a^{\dagger 2} b - a^2 b^\dagger) + \text{driving and decay terms.} \quad (2.67)$$

⁴³Here, all cavity decay rates are defined as FWHM linewidths; This explains the factor of 1/2 in Eqs. (2.68) and (2.69). Note that in [P1] and in [P2], half width at half maximum values are used.

⁴⁴Moreover, different definitions for the decay rate exist as discussed in [Whi97], Sec. 2.2.2.

⁴⁵Highest coupling can be reached by using an optimally chosen beam waist in the crystal, see [BK68], Eq. (3.39).

⁴⁶This means: $a \rightarrow e^{-i\omega_p} a$ and $b \rightarrow e^{-2i\omega_p} b$ [DMW81; CG84; WM08].

For the single-mode case, the equations of motion for the intra-cavity modes a and b read⁴⁷

$$\dot{a} = -\frac{\kappa_a}{2}a + ia\Delta + \chi a^\dagger b + \sqrt{\kappa_{\text{in}}^a}A_{\text{in}} + \sqrt{\kappa_{\text{out}}^a}\delta A_v + \sqrt{\kappa_1^a}\delta A_1, \quad (2.68)$$

$$\dot{b} = -\frac{\kappa_b}{2}b - \frac{\chi}{2}a^2 + \sqrt{\kappa_{\text{in}}^b}B_{\text{in}} + \sqrt{\kappa_{\text{out}}^b}\delta B_v. \quad (2.69)$$

The change of the circulating mode amplitudes \dot{a} , \dot{b} depends on the modes themselves, scaled with the decay rates κ and the detuning Δ .⁴⁸ Furthermore, they change with all incoupling photon rates A and B . The two Eqs. (2.68) and (2.69) are coupled via the down-conversion coupling strength χ and the detuning Δ .

Equations (2.68) and (2.69) are the starting point for the theory that is applied in the publications [P1], [P2] and [P3]. In any case, the goal is to find an expression for the output fields of interest. To do so, first, the field operators are decomposed in a constant and a fluctuating term in the form $a = \alpha + \delta a$, as introduced in Eq. (2.23). Then, the equations are solved for the relevant intra-cavity mode a . Finally, the boundary conditions are applied to find expressions for the output rates [GC85].

The classical behaviour of the cavity can be studied by solving Eqs. (2.68) and (2.69) for the constant terms. Then, all fluctuating operators are omitted. The changes of the modes $\dot{\alpha}$ and $\dot{\beta}$ are set to zero to calculate the steady output of the cavity. Next, the output field rate can be calculated as described above. The quantum behaviour is considered when solving Eqs. (2.68) and (2.69) for the fluctuation operators δA and δB in the Fourier space.

2.3.2 Second harmonic generation

This subsection consists of two parts. First, the output field in the harmonic mode B_{out} is calculated for an SHG pumped with the fundamental mode A_{in} .⁴⁹ The ratio of the modes' powers define efficiency of the SHG. In the second part, this subsection makes the link to our experiments. We will discuss what is important when designing an SHG. Furthermore, the design and the performance of our developed SHG are presented.

We consider an SHG which has an input field in the fundamental mode A_{in} . The field of the harmonic mode B_{in} is zero. Assuming α is real, Eqs. (2.68) and (2.69) can be semi-classically written as⁵⁰

$$\dot{\alpha} = \frac{\kappa_a}{2}\alpha + \chi\alpha\beta + \sqrt{\kappa_{\text{in}}^a}A_{\text{in}}, \quad (2.70)$$

$$\dot{\beta} = \frac{\kappa_b}{2}\beta - \frac{\chi}{2}\alpha^2. \quad (2.71)$$

⁴⁷In these equations, the cavity is assumed to be resonant for mode a and b .

⁴⁸The detuning is $\Delta = 0$ except from Chapter 4.

⁴⁹The wavelengths for the harmonic and the fundamental modes are $\lambda_h = 532$ nm and $\lambda_f = 1064$ nm in our experiments.

⁵⁰For this subsection, a semi-classical description is sufficient. If the differential equations are solved for their fluctuating part, also squeezing could be observed in the harmonic mode [Per+88; Siz+90; LK94; Pas+94; WM08].

For a steady state, the two differential equations become a regular system of equations:

$$0 = \frac{\kappa_a}{2}\alpha + \chi\alpha\beta + \sqrt{\kappa_{\text{in}}^a}A_{\text{in}}, \quad (2.72)$$

$$0 = \frac{\kappa_b}{2}\beta - \frac{\chi}{2}\alpha^2. \quad (2.73)$$

Since most of the harmonic field leaves the cavity at the output port, we can assume $\kappa_b \approx \kappa_{\text{out}}^b$. Equations (2.73) and (2.72) are solved for β and the cavity boundary condition $B_{\text{out}} = \sqrt{\kappa_{\text{out}}^b}\beta$ is applied. Then the output field reads as

$$B_{\text{out}} = \frac{(-\sqrt[3]{6}\kappa_a\kappa_b\epsilon^2 + \tilde{A}(A_{\text{in}}))^2}{6\sqrt[3]{6}\sqrt{\kappa_b}\epsilon^3\tilde{A}(A_{\text{in}})}, \quad (2.74)$$

with

$$\tilde{A}(A_{\text{in}}) = \left(\sqrt{6}\sqrt{\kappa_b^2\epsilon^6 (54A_{\text{in}}^2\kappa_{\text{in}}^a\epsilon^2 + \kappa_a^3\kappa_b)} + 18A_{\text{in}}\sqrt{\kappa_{\text{in}}^a\kappa_b\epsilon^4} \right)^{2/3}. \quad (2.75)$$

Equation (2.74) looks cumbersome but accurately describes the conversion process in an SHG cavity. Often it is helpful to work with the conversion efficiency ζ defined as

$$\zeta = \frac{\hbar\omega_p B_{\text{out}}^2}{\hbar\omega_f A_{\text{in}}^2} = \frac{2B_{\text{out}}^2}{A_{\text{in}}^2} = \frac{P_{\text{out,B}}}{P_{\text{in,A}}}. \quad (2.76)$$

Here, P_A and P_B are the powers of the two fields, which relate to the photon rates

$$A = \sqrt{P_A/(2\pi\hbar\omega_f)} \quad \text{and} \quad B = \sqrt{P_B/(2\pi\hbar\omega_p)}. \quad (2.77)$$

The newly developed second harmonic generation cavity

In our experiment, the goal is to build a highly-efficient SHG cavity. This is often done by building a *single-ended* cavity, where one of the mirrors is defined as the input/output mirror for the fundamental field. To reach the best impedance matching, the accumulated loss in the cavity needs to equalise the input/output coupler's transmission. In an SHG, it is meaningful to distinguish between *good loss* and *bad loss*. The frequency conversion in the non-linear crystal accounts for the *good loss*. The *bad losses* consist, e.g. of scattering losses, absorption losses or residual transmissions of high-reflective cavity mirrors. If the cavity is impedance-matched, the reflected electric field is zero $A_{\text{ref}} = 0$. Then the cavity reaches the point of maximal conversion efficiency.

The intra-cavity loss δ_x , the non-linear interaction strength χ and the input/output mirror ($R_{\text{in/out}}$, respectively κ_{in}) for the second harmonic field play a big role when designing an SHG cavity. In general, δ_x cannot be reduced, and χ cannot be increased arbitrarily.⁵¹ A parameter that is free to choose is the reflectivity of the input/output coupler $R_{\text{in/out}}$. If the available input power is defined, we find the optimal reflectivity (given by κ_{in}^a) by maximising Eq. (2.76).

We have increased the performance of the SHG during the last years by changing its design. Compared to old SHGs [Den16; Wim16], the new cavity now has a six-axis alignment stage, see Fig. 2.7. This figure shows a CAD design of the new SHG with

⁵¹Note that χ can be changed, e.g. by modifying the cavity eigenmode and thus the waist size in the crystal or by changing the phase matching with temperature detuning.

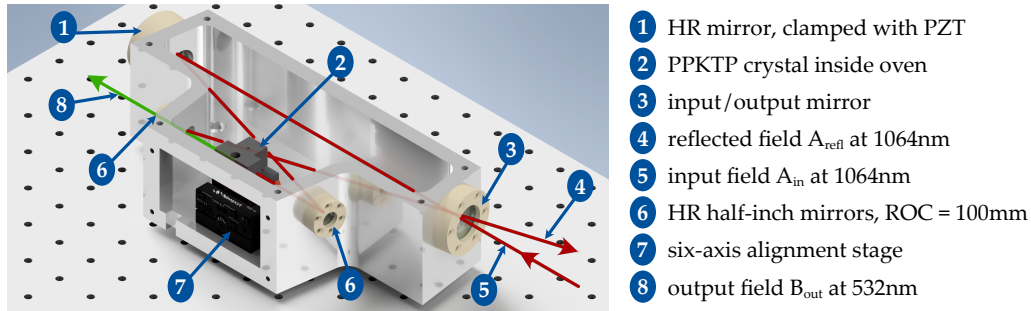


FIGURE 2.7: CAD model of the new SHG cavity including the six-axis alignment stage.

labelled components. In our experiments, the fundamental field has a wavelength of 1064 nm, and the harmonic has half the wavelength, which is 532 nm. With the six-axis alignment stage, the crystal can be precisely moved and tilted to the ideal position, where no beam clipping and best frequency conversion occurs. We could reduce the intra-cavity losses from $> 1\%$ to 0.2% . The non-linear interaction strength χ was increased from 115 Hz to a range from 179 Hz and 196 Hz. The old design reached a maximal conversion efficiency of 65 %. We measured conversion efficiencies of up to 94 % with the new design. A more detailed description of the new SHG cavity can be found in [Bar20], which also shows measurements and fits by using Eq. (2.76) in Fig. 5.7.

The demands for harmonic power are different for the three experiments set up in this thesis. Our fundamental laser source is a non-planar ring oscillator (NPRO) [Coherent Mephisto], with maximal 2 W of output power. For the experiment in Chapter 3, only roughly 300 mW of green pump power was used. This experiment was conducted with the old, low-efficient SHG. Anyhow, for the experiments in Chapters 4 and 5, powers of up to 800 mW were required. Here, it was necessary to use the new design of the SHG with a larger conversion efficiency of up to 94 %. The squeezers in these experiments have individual green power demands because of a lower input/output coupler or a different non-linear crystal. Each squeezer has its characteristic functionality, which will be presented in the following section.

2.3.3 Squeezing from optical parametric oscillation

In this section, the input-output formalism introduced in Subsec. 2.3.1 is applied to an OPO. The starting point for the calculations is the quantum-mechanical Hamiltonian for the parametric down-conversion process. The goal is to derive the quantum noise variances describing the output state of the OPO. In this subsection, we present a recipe including all computational steps performed to compute the variances.

First, some general remarks are relevant to be mentioned. To drive the parametric down-conversion process, we usually only need the harmonic input field B_{in} . Since we are considering the down-conversion process in a cavity that is only resonant for the fundamental wavelength, we assume that this pump field is undepleted. The consequence is that we replace $b \rightarrow \beta e^{i\theta}$, with real mean field β and the relative phase between squeezed fundamental and harmonic field θ . In the following, we work again with Fig. 2.6 depicting the system of consideration.

Calculating the noise variances is a straightforward analysis consisting of the following seven steps:⁵²

1. The Hamiltonian

The starting point is the Hamiltonian giving the energy distribution of the system. To describe the OPO, the interaction part of the Hamiltonian from Eq. (2.67) can be rewritten as

$$H = i\epsilon a^{\dagger 2} - i\epsilon^* a^2, \quad (2.78)$$

with the complex parameter $\epsilon = i\hbar\chi\beta e^{i\theta}/2$.

2. Equations of motion

Analogous to Eq. (2.68), the equations of motion for the fundamental field a are considered:

$$\dot{a} = \epsilon a^{\dagger} - \frac{\kappa_a}{2}a + \sqrt{\kappa_{\text{in}}^a}A_{\text{in}} + \sqrt{\kappa_{\text{out}}^a}\delta A_{\text{v}} + \sqrt{\kappa_1^a}\delta A_1. \quad (2.79)$$

3. Fourier transform

Equation (2.79) is transformed to frequency domain by using the Fourier transform $\mathcal{F}\{a(t)\}$:

$$\tilde{a}(\omega) = \mathcal{F}\{a(t)\} = \frac{1}{\sqrt{2\pi}} \int dt e^{i\omega t} a(t). \quad (2.80)$$

Thus, the field operators transform as $\tilde{a}(\omega) = \tilde{a}^{\dagger}(-\omega)$.⁵³ In the following we write: $\tilde{a}(\omega) \equiv \tilde{a}$ and $\tilde{a}^{\dagger}(-\omega) \equiv \tilde{a}^{\dagger}$.⁵⁴ Next, we obtain two equations of motion in the frequency domain, namely for \tilde{a} and its complex conjugated \tilde{a}^{\dagger} , which read as

$$-i\omega\tilde{a} = \epsilon\tilde{a}^{\dagger} - \frac{\kappa_a}{2}\tilde{a} + \sqrt{\kappa_{\text{in}}}\tilde{A}_{\text{in}} + \sqrt{\kappa_{\text{out}}^a}\delta\tilde{A}_{\text{v}} + \sqrt{\kappa_1^a}\delta\tilde{A}_1, \quad (2.81)$$

$$-i\omega\tilde{a}^{\dagger} = \epsilon^*\tilde{a} - \frac{\kappa_a}{2}\tilde{a}^{\dagger} + \sqrt{\kappa_{\text{in}}^a}\tilde{A}_{\text{in}}^{\dagger} + \sqrt{\kappa_{\text{out}}^a}\delta\tilde{A}_{\text{v}}^{\dagger} + \sqrt{\kappa_1^a}\delta\tilde{A}_1^{\dagger}. \quad (2.82)$$

4. Solution for cavity mode

Next, Eqs. (2.81) and (2.82) are solved for the intra-cavity mode fields \tilde{a} and \tilde{a}^{\dagger} .

5. Cavity output rate

Now, the boundary condition for the fundamental field $\tilde{A}_{\text{out}} = \sqrt{\kappa_{\text{out}}^a}\tilde{a} - \delta\tilde{A}_{\text{v}}$ is applied to calculate the cavity output rate \tilde{A}_{out} .

6. Output quadrature fluctuations

From the output field rates, the output quadrature operators X_{out}^{\pm} are calculated by using Eqs. (2.19) and (2.20) ($X^+ \equiv X_1$ and $X^- \equiv X_2$). Here, the quadrature operators are again decomposed into a constant \mathcal{X} and fluctuating term X : $\delta X = \mathcal{X} + \delta X$.

⁵²For the following theoretical remarks, I follow [CG84; BR19]. A similar overview was already given in [Whi97], Fig. 3.6.

⁵³This indicates that the electric field is the sum of its positive and negative frequency parts as in [Gla63b], Sec. II.

⁵⁴See e.g. [Ste19], Eqs. (1.37) and (1.38).

7. Output variance noise

The final step is to compute the output noise variances $V_{\text{out}}^{\pm}(\omega) = \langle |\delta X_{\text{out}}^{\pm}|^2 \rangle$:

$$V_{\text{out}}^{\pm} = 1 \pm \frac{8\kappa_{\text{out}}|\epsilon|}{4\omega^2 + (\kappa \mp 2|\epsilon|)^2}. \quad (2.83)$$

All incoming vacuum field rates have a unity variance ($V_{\text{v}}^{\pm} = V_1^{\pm} = 1$). In an experiment, relative squeezing and anti-squeezing values are usually used, which are normalised to vacuum noise. These values are obtained, by transforming Eq. (2.83) into decibels units via

$$\text{todB}(x) = 10 \log_{10}(x), \quad (2.84)$$

$$\text{fromdB}(x) = 10^{x/10}. \quad (2.85)$$

By following the recipe above, the output noise variances are calculated. Equation (2.83) can be written differently as

$$V_{\text{out}}^{\pm} = 1 \pm \eta_{\text{esc}} \frac{4x}{(1 \mp x)^2 + 4\Omega^2}. \quad (2.86)$$

Equation (2.86) reveals some important experimental parameters. We can identify the escape efficiency η_{esc} , which is compared to Eq. (2.11) now defined with decay rates κ as

$$\eta_{\text{esc}} = \frac{\kappa_{\text{out}}}{\kappa_{\text{in}} + \kappa_1 + \kappa_{\text{out}}}. \quad (2.87)$$

Further, we introduced the normalised linewidth of the cavity in Eq. (2.86), defined as

$$\Omega = \frac{\omega}{\kappa_{\text{in}} + \kappa_1 + \kappa_{\text{out}}}, \quad (2.88)$$

and the pump parameter

$$x = \frac{\epsilon}{\kappa_{\text{in}} + \kappa_1 + \kappa_{\text{out}}} = \sqrt{\frac{P}{P_{\text{thr}}}}, \quad (2.89)$$

which is connected to the pump power P and the pump threshold P_{thr} . The best squeezing can be obtained for a resonant cavity ($\Omega = 0$) with no losses ($\eta_{\text{esc}} = 1$). Then Eq. (2.86) gives the initial squeezing and anti-squeezing, which are only theoretical values.⁵⁵ We have seen how the squeezed output state of an OPO is calculated. In this thesis, we use the concept of homodyne detection from Subsec. 2.2.4 to detect the state.

Detecting a squeezed state with a homodyne detector

We want to briefly discuss how phase noise and optical loss spoil the homodyne measurement of a squeezed state. During the process from generation to detection, the squeezed state accumulates optical loss of L_{total} , which is converted into the total efficiency η_{total} .⁵⁶ A homodyne detector can detect the amplitude or phase quadrature of the state, as mentioned in Subsec. 2.2.4. The readout quadrature depends on the detection angle ϕ , as shown in Eq. (2.62). In the experiment, ϕ is usually locked for

⁵⁵These values are impossible to measure in an experiment due to optical losses.

⁵⁶In the publications [P1] and [P2], $\eta \equiv \eta_{\text{total}}$ is used. More details on efficiencies will be discussed in Subsec. 2.4.3.

lower frequencies.⁵⁷ Fast oscillating disturbances are not suppressed by the control loop and lead to a noisy detection angle. When fluctuations are present with a period of τ smaller than the measurement time T_{meas} , the detected variance V_{det}^{\pm} will be an average over a range of quadratures [Oel+16a]. The residual fluctuations in the detection angle are assumed to follow a normal distribution with standard deviation of $\Delta\phi$. Then, the effectively detected variance is [Zha03; ATF06; Sch18]

$$V_{\text{det}}^{\pm} = \eta (V_{\text{out}}^{\pm} \cos^2(\Delta\phi) + V_{\text{out}}^{\mp} \sin^2(\Delta\phi)) + 1 - \eta. \quad (2.90)$$

If phase noise is present ($\Delta\phi \neq 0$), mixing between the two variances occurs. Then, the squeezed state becomes a mixed state with non-Gaussian statistics.⁵⁸ For a constant amount of phase noise $\Delta\phi$, the observable squeezing can be optimised for the pump parameter x (see Eqs. (2.86) and (2.90)). The experiments in this thesis aim to operate near this optimised pump power.

A squeezed state in the quantum sideband picture

The squeezed probability distribution shown in Figs. 2.4c) and d) can be derived from a different, intuitive perspective using the quantum sideband picture.⁵⁹ There, the situation is only sketched for one measurement frequency, Ω .

In the following description, Ω is a representative for all frequencies inside the linewidth of the OPO. In the OPO, a pump photon with frequency $\omega_p = 2\omega_f$ decays into two photons at frequencies $\omega_f - \Omega$ and $\omega_f + \Omega$ inside the cavity's linewidth.⁶⁰ Both photons are created simultaneously and are correlated because of energy and momentum conservation. We study the situation for an amplitude quadrature squeezed state in Fig. 2.8. The quantum sideband picture shows the electric fields in the frame of reference rotating with ω_f in Fig. 2.8a). The blue arrows draw correlated electric fields at $\pm\Omega$. Uncorrelated fields at this frequency are depicted as blurred, red circles. The four pictures in Fig. 2.8a) demonstrate the situation at four arbitrary time stamps $t_1 - t_4$. Due to phase indetermination, the phasors do not follow a predictable trajectory as in the case of a classical modulation. Notwithstanding, they are always correlated and aligned parallel in the phase quadrature X_2 and anti-parallel in the amplitude quadrature X_1 .

The top picture of Fig. 2.8b) shows how the sideband pairs of the four different times add up at the measurement frequency Ω . For instance, correlated phasors in the X_1 direction interfere destructively, and correlated phasors in the X_2 direction add up. The uncorrelated phasors shown by the blurred red circles from a) will not cancel. The bottom part summarises the situation when not only four but all possible situations of correlated phasors are considered. The result is a squeezed state, exhibiting squeezing in X_1 and anti-squeezing in X_2 . In conclusion, the quantum sideband picture shows that squeezing will be visible due to correlations of sidebands.

⁵⁷Our control loop bandwidths typically go up to kilohertz frequencies, limited by the phase response of the piezoelectric transducer (PZT) used as the actuator.

⁵⁸A phase space picture of a phase-diffused squeezed state can be found in [Fra+06].

⁵⁹A more detailed view of the quantum sideband picture is given in [Che+05], Sec. 2.10.2 or in [Bon+17], Sec. 6.1.

⁶⁰The two photons can also be created at higher free spectral ranges (see Eq. (2.12)) of the OPO, e.g. at $\omega_f - \Delta\omega$ and $\omega_f + \Delta\omega$.

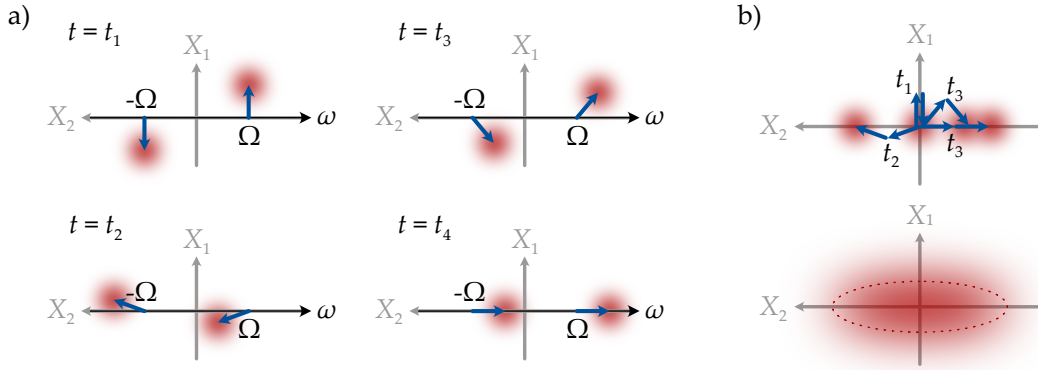


FIGURE 2.8: Quantum sideband picture of an amplitude quadrature squeezed state in the rotating frame. a) Correlated (blue arrows) and uncorrelated sidebands (blurred red circles) at frequency $\pm\Omega$ at different times t_1-t_4 . The correlated sidebands are always parallel in phase quadrature X_2 and anti-parallel in amplitude quadrature X_1 . b) The four cases are added in the top picture, only showing the situation at the measurement frequency Ω . In the bottom picture, the resulting squeezing ellipse is shown, squeezed in the amplitude quadrature X_1 .

Distinction between single- and two-mode squeezing

Above, we assumed the phase-matching process to be of type-0, which means that all contributing fields have the same polarisation. An NDOPO, which is a two-mode squeezer, requires the consideration of two orthogonally polarised modes.⁶¹ Then, Eq. (2.67) must be modified and exhibits the modes a^s and a^p . The equations of motion can be traced back to the equations for a single-mode OPO from Eqs. (2.81) and (2.82) and then solved accordingly. Here, I omit to present the theory of the NDOPO since it is not needed for this thesis. The interested reader can get more information, e.g. in [Ste19].

For completeness, we should discuss the distinction between single- and two-mode squeezed states more precisely. It seems to be terminological but is at least interesting to expound. Two-mode squeezing consists of two distinguishable modes. For *polarisation* two-mode squeezed states, the distinction is obvious. However, what is with squeezing where the correlated sidebands have the same polarisation but different frequency modes? From a nitpicking perspective, we can call this state a *frequency* two-mode squeezed state. Single-mode squeezing only occurs when both sidebands have the same polarisation *and* frequency of ω_f .

A different perspective is helpful to maintain our terminology of single- and two-mode squeezed states. In the experiment, the sideband distinction is only sometimes visible. In the example of a polarisation two-mode squeezed state generated by an NDOPO, the sidebands can easily be separated by any polarisation-sensitive beamsplitter because they occur in perpendicular polarisation modes. The simple distinction of perpendicular polarisations justifies the term *two-mode squeezing*. In case of an OPO, the correlated sidebands are created at $\omega_f - \Omega$ and $\omega_f + \Omega$. However, we are usually not susceptible to any two-mode character when the correlated sidebands at $\omega_f \pm \Omega$ stay in the same spatial mode. They stay indistinguishable when the mode is detected on a photodetector. For instance, in gravitational wave detectors with

⁶¹A two-mode squeezer does not necessarily deal with *polarisation modes*. Also, e.g. frequency modes at different colours are possible [Vil+05].

frequency-independent squeezing, it is reasonable to still treat the squeezed state from the OPO as single-mode squeezing.⁶²

In our experiments, we always measure squeezing at the first free spectral range of the squeezing cavity. Thus, we detect correlated sidebands with frequencies of $\omega_f \pm \Delta\omega$, where $\Delta\omega$ is the free spectral range frequency according to Eq. (2.12).⁶³

This section has explained two cavities with non-linear crystals. For the SHG, the equation for the harmonic output field was derived. Additionally, the design of the built SHG was presented, which we developed for the experiments in the publications [P2] and [P3]. Then, a recipe to calculate the output field of an OPO cavity was presented. This section closed with an introduction to the quantum sideband picture and a distinction between single- and two-mode squeezing. The following section links the theoretically described OPO to our three experimental squeezers.

2.4 Experimental view on the OPO, the detuned OPO and the NDOPO

In each of our publications [P1], [P2] and [P3], we used a different squeezer. Since Sec. 2.3 considered the squeezers mostly from a theoretical perspective, we want to bring this together with the experimental realisation. This Sec. 2.4 summarises various technical details and measurement methods employed in the publications.

The section starts with a comparison of the three squeezers in Subsec. 2.4.1: the resonant OPO from [P1], the detuned OPO from [P2] and the NDOPO from [P3]. I point out commonalities and differences in the squeezer topology and used components. An essential point for the comparison is the non-linear crystal and how the phase-matching conditions are reached. Subsection 2.4.2 precisely instructs how to set up the two-mode squeezer from [P3]. It elaborates on the beam path in the cavity and the construction of the oven for the crystal. Finally, Subsec. 2.4.3 explains how squeezing is usually characterised in the scope of this thesis. An important measurement that needs to be mentioned is a squeezing slope from which the total efficiency η of the squeezing process and the phase noise $\delta\phi$ can be derived.

2.4.1 Comparison of the squeezers

This subsection elaborates on the three different squeezer designs used for this thesis. Each squeezer produces a differently tailored squeezed quantum state. This subsection starts with a broader perspective and compares the squeezers as a whole which includes the squeezer topology. The most relevant parameters for the three systems are listed in Table 2.1. Next, the perspective is changed, and squeezer differences are pointed out. We zoom into different subsystems of the cavities. We discuss the cavity eigenmodes, the input/output coupler's choice and the oven designs enabling the phase-matching.

Squeezer topology

The three squeezers' topological commonalities are shown in Fig. 2.9. The figure's upper row shows the topology for the six-mirror OPO cavity used for the spectroscopy

⁶²In the case of single-mode squeezing with sidebands created at $\omega_f \pm \omega$ it is possible to create two-mode squeezing by using frequency dispersive components [Hun+05; HSS10].

⁶³Finding the maximum amount of squeezing/anti-squeezing is a sufficient method to determine the free spectral range of the squeezer cavity.

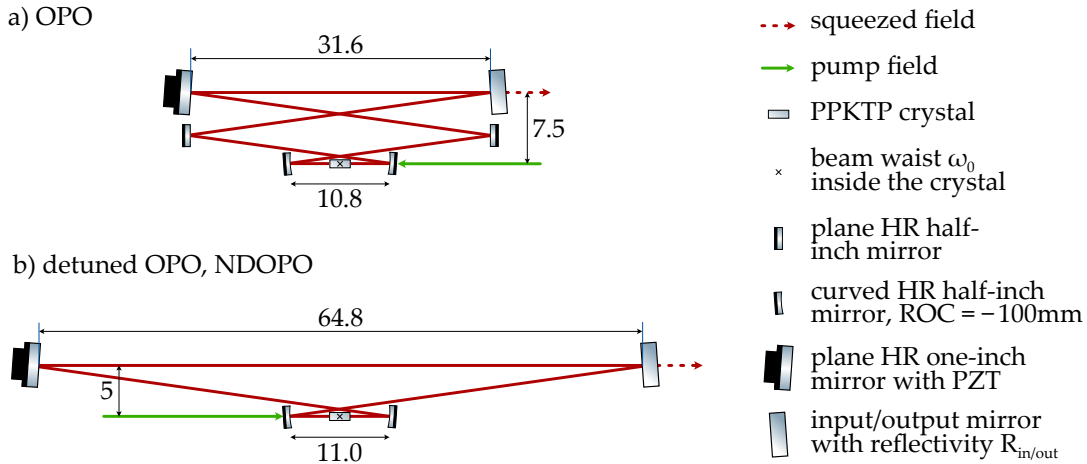


FIGURE 2.9: The two squeezer topologies used in this thesis. The cavities are only resonant for 1064 nm. Picture a) shows the OPO consisting of six mirrors used for the spectroscopy experiment in Chapter 3. Picture b) presents a squeezer with only four mirrors taken for the experiments presented in Chapters 4 and 5. Note that the two systems in b) are not identical since they use different crystals and input/output couplers, see Table 2.1. The numbers represent the geometric distances in centimetres.

experiment [P1] in Chapter 3. In the bottom row, a four-mirror squeezer is depicted employed for the frequency-dependent squeezing experiment [P2] in Chapter 4 and the Gaussian state estimation [P3] in Chapter 5. In all three cases, squeezing is generated by pumping a non-linear periodically-poled potassium titanyl phosphate (PPKTP) crystal sitting in a cavity. Then, the process of optical parametric oscillation is driven.⁶⁴ Depending on the squeezer, either a single- or a two-mode phase matching condition must be ensured. Hence the type of crystal differs for the detuned OPO and the NDOPO. All the squeezers were operated at a fundamental wavelength of 1064 nm and are pumped with 532 nm.

To give a clear overview, Table 2.1 compares the three systems' most important parameters. The individual points are discussed in the following.

The OPO cavity has a quasi-monolithic design, similar to the SHG cavity shown in Fig. 2.7. The mirrors are clamped to an aluminium spacer to make the cavity stable and robust. In operation mode, the cavity will be closed with a lid which decreases air fluctuations inside the cavity and thus reduces phase fluctuations. Notwithstanding, there are also disadvantages of the quasi-monolithic design. Since the mirrors can only be attached to a fixed position, the alignment procedure can be tenacious. Due to the static design, any quick changes, e.g. in cavity length and thus eigenmode, are hardly feasible. During this thesis, no measurable differences were identified regarding phase noise in the free space and the quasi-monolithic design.⁶⁵

Cavity eigenmode

The eigenmode in the cavity and, thus, the beam waist in the crystal affects the effective non-linear coupling strength. For a given pump power, the coupling strength

⁶⁴There are numerous other methods to generate squeezing, e.g. in opto-mechanical experiments [Pur+13; Agg+20], after frequency doubling [Per+88; Siz+90; LK94; Pas+94], or by using Kerr materials [SL99; Whi+00] or semiconductors [YIM86; MYI87; Kar+04].

⁶⁵A discussion on phase noise and other limitations is given in Chapter 6.

TABLE 2.1: Overview of important parameters of the three used squeezers. The beam waists are averages for the tangential and sagittal planes in the cavity. The pump threshold is highly prone to the current mode-matching of the pump beam into the squeezing cavity. Poling periods of the order of $9\ \mu\text{m}$ were already used by [Ari+97; Eng+97; Ari+98]. The manufacturing uncertainty of γ is given by the polishing company DDO Strichplatten und Dünnschicht GmbH to $\pm 0.08^\circ$.

	a) OPO	c) detuned OPO	b) NDOPO
number of mirrors	6	4	4
setup	quasi-monolithic	free-space	free-space
stability without crystal	no	yes	yes
large beam waist	$486\ \mu\text{m}$	$678\ \mu\text{m}$	$678\ \mu\text{m}$
small beam waist	$26\ \mu\text{m}$	$22\ \mu\text{m}$	$22\ \mu\text{m}$
input/output coupler $R_{\text{in/out}}$	90 %	80 %	95 %
pump threshold	368 mW	1.62 W	1.25 W
phase matching	type-0	type-0	type-II
poling period p	$9\ \mu\text{m}$	$9\ \mu\text{m}$	$458\ \mu\text{m}$
crystal polish angle γ	plane	wedged 0.5°	wedged 1°
temperature control crystal	single oven	dual oven	dual oven

can be optimised with respect to the beam intensity. For our 10 mm long crystals the optimal beam waist is $w_{\text{opt}} = 24.4\ \mu\text{m}$ according to [BK68]. For this beam waist, a squeezing cavity with optical round-trip length of $L_{\text{opt}} \approx 1.5\ \text{m}$ and curved cavity mirrors with radius of curvature of $\text{ROC} = -100\ \text{mm}$ is only marginally stable [Den16; Wim16; Ste19]. This comes with a drawback: The cavity without crystal becomes unstable due to the change of optical path length, which is observed in the six-mirror squeezing cavity used in Chapter 3.⁶⁶ In general, this is not a big problem, but it makes aligning the cavity more difficult. Therefore, for the experiments in Chapter 4 and 5, squeezers with different cavity eigenmodes were built. Due to the changed beam waist of $w = 22\ \mu\text{m}$ the squeezing cavity is even stable without the crystal but at the same time provides a good coupling strength. The required infrared power is increased by roughly 2 % to reach the same coupling strength as with an optimal beam waist w_{opt} [BK68].

The input/output coupler

For a constant intra-cavity escape efficiency η_{esc} and coupling strength χ , the input/output coupler choice determines the pump threshold of the squeezer. When dealing with single-ended squeezers, Eq. (2.89) simplifies with $\kappa_{\text{out}} = 0$ and $\kappa_{\text{in}} \equiv \kappa_{\text{in/out}}$. With increasing κ_{in} , the pump threshold P_{thr} increases with the square root. Before selecting an input/output coupler for the system, some technical questions need to be analysed. First, how much harmonic pump power is available? Second, how problematic are high beam intensities in the crystal regarding the integrity of the crystal [Bou+99], potentially causing other effects such as thermal lensing or thermal instabilities [Dou+99; TZL05; Wan+17]? For the OPO, the input/output coupler of $R_{\text{in/out}} = 90\ \%$ leads to a pump threshold

⁶⁶Here, the $w = 26\ \mu\text{m}$ beam size is differing from the optimal $w_{\text{opt}} = 24.4\ \mu\text{m}$ due to imprecisions in the spacer design.

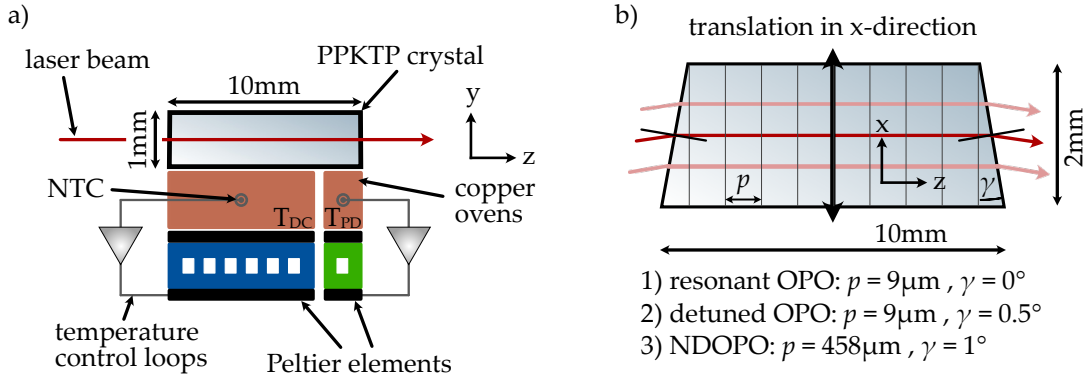


FIGURE 2.10: a) Schematic of the copper oven which holds the 10 mm long PPKTP crystal. I have implemented two temperature controls: to achieve phase matching for the down-conversion process and to adjust the polarisation degeneracy Δ in the squeezing cavity. b) The optical beam path in the wedged crystal can be changed by translating it perpendicular to the beam axis.

of $P_{\text{thr}} \approx 300 \text{ mW}$.⁶⁷ When the OPO is detuned, the effective pump threshold is increased depending on the amount of detuning, which is the reason for the 80% input/output coupler in this constellation.⁶⁸ The coupler of the NDOPO has a large reflectivity of 95%. Since the non-linear coefficient $\chi^{(2)}$ for the type-II phase matching is more than a factor of 4 less than for the type-0 phase matching⁶⁹ the pump threshold is still large with 1.62 W.⁷⁰

Phase matching and oven design

The efficiency of the down-conversion process in the squeezers depends on how well the phase-matching condition is met. For the OPO, only two electric fields are involved: The squeezed fundamental field, consisting of the degenerate signal and idler fields, and the harmonic pump field, all s-polarised. Three fields need to be considered in the NDOPO because signal and idler are orthogonally polarised and thus polarisation non-degenerate.

We use quasi-phase-matching for our squeezers, so that the crystal's non-linearity varies over its length periodically. Thus, the actual poling period p defines the *phase-matching temperature* T_{DC} . If this temperature is achieved, the squeezing process in the OPO works best. For the OPO and the NDOPO, the crystals are periodically poled, such that $T_{\text{DC}} \approx 30^\circ \text{C}$.⁷¹ Figure 2.10a) shows a simplified schematic of our oven used for the crystal.⁷² The actual temperature of the copper oven is sensed with a negative temperature coefficient thermistor (NTC). Depending on the resistance, the left Peltier element (blue) is driven to heat or cool the oven part for a chosen reference temperature. The unity gain frequency of the temperature control loops was in the order of 200 mHz.

⁶⁷Will be discussed in Subsec. 3.4.2.

⁶⁸Will be discussed in Subsec. 4.5.2.

⁶⁹For type-0 phase matching the non-linear coefficient $d = d_{33} \approx 17.4 \text{ pm V}^{-1}$ and for type-II phase matching $d = d_{24} \approx d_{32} \approx 3.7 \text{ pm V}^{-1}$ are employed [Mam+18]. Note that the coefficient we use is reduced by $d_{\text{eff}} = d \pi/2$ due to quasi-phase-matching, see [Boy20], Sec. 2.4.

⁷⁰Will be discussed in Subsec. 5.4.1.

⁷¹The temperature dependency of the conversion efficiency can be seen, e.g. in [Bar20], Fig. 5.5.

⁷²This design was only used for [P2] and [P3]. Only a single temperature control was employed in [P1].

Since the crystal is placed in a cavity, we also need to care about the accumulated phases in the cavity. We can neglect the pump field for this consideration because it does not see the cavity.⁷³ Subsequently, the OPO needs to be resonant only for the s-polarised squeezed field. In the NDOPO, the situation is more complicated. The idler and signal field generally accumulate different phases in the cavity. The reason for the phase difference Δ is twofold. First, all cavity mirrors generate a small non-degenerate phase shift for the reflected field depending on the polarisation state. Second and dominating, due to the crystal's birefringence, both fields collect different phases in the crystal. In the following, we will discuss how the polarisation degeneracy of the two orthogonally polarised modes can be adjusted in our experiment. We have implemented two options for adjusting the polarisation phase degeneracy Δ in the cavity.

I have installed a second temperature control for the fine adjustment (see Fig. 2.10a). It also works with a NTC and the right Peltier element (green). A small fraction of the right crystal side (roughly 2 mm) is controlled to the temperature T_{PD} . Because the beam intensity is very small compared to the centre of the crystal, changing the temperature here does not affect the strength of the down-conversion process much. However, this second temperature control facilitates changing the relative phases between s- and p-polarised fields propagating inside the crystal. The reasons for this behaviour are the photo-thermal and thermo-refractive effects of PPKTP. Temperature changes influence the effective optical path length difference between the s- and p-polarised fields.

The rough alignment of the polarisation degeneracy can be adjusted by changing the optical path length in the trapezoidally wedged crystals. It can be done manually by translating the crystal perpendicular to the beam axis in the cavity plane, see Fig. 2.10b). Then, due to the birefringent crystal, the relative phase between both polarisation contributions $\phi(\gamma)$ will change according to

$$\phi(\gamma) = \frac{2 \tan(\gamma)(n_z - n_y)}{\lambda_f} \approx \frac{2\gamma(n_z - n_y)}{\lambda_f}, \quad (2.91)$$

where γ is the angle of the crystal wedging, λ_f the fundamental wavelength and $n_y = 1.7455$, $n_z = 1.8297$ are the refractive indexes of PPKTP [KT02]. In Fig. 2.10b), shorter or longer optical beam paths are drawn by the light red arrows. For the two wedging angles used in this thesis, we find

$$\phi(\gamma_1 = 1^\circ) = \frac{1.74 \text{ rad}}{100 \mu\text{m}}, \quad (2.92)$$

$$\phi(\gamma_2 = 0.5^\circ) = \frac{0.87 \text{ rad}}{100 \mu\text{m}}. \quad (2.93)$$

The meaning of these values is that when displacing the 1° (0.5°) wedged crystal $100 \mu\text{m}$ along the x-axis, the polarisation phase degeneracy will change by 1.74 rad (0.87 rad). Using the wedge shape of the crystal allows for roughly adjusting the point of desired polarisation (non-)degeneracy.

In conclusion, the phase matching for the down-conversion is realised by T_{DC} . The polarisation degeneracy Δ is controlled by T_{PD} and the position of the wedged crystal. In the case of the resonant OPO needed in [P1], the polarisation degeneracy does not play a role, and the oven consists only of one part controlling T_{DC} . For the detuned OPO [P2] and the NDOPO [P3], we use the second temperature control

⁷³See again Fig. 2.9.

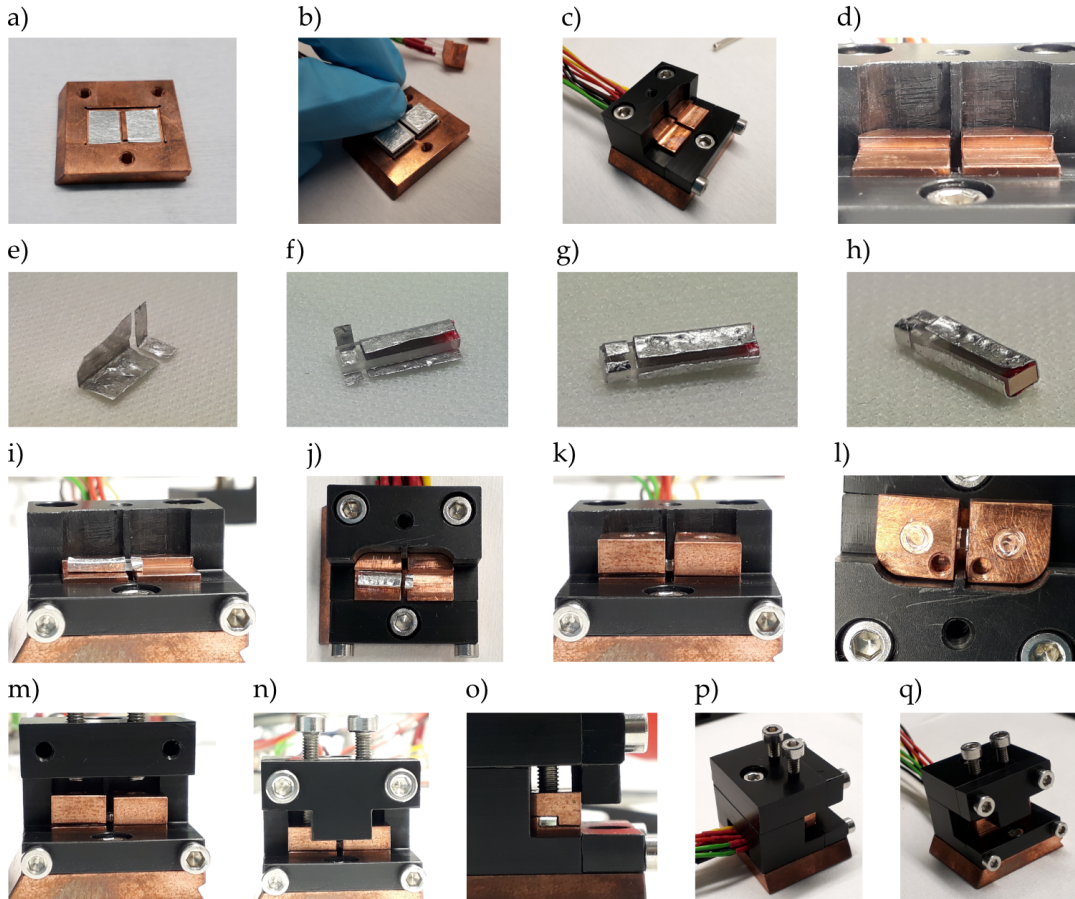


FIGURE 2.11: Constructing the oven and inserting the PPKTP crystal. a)–d) Preparation of the bottom part of the oven. e)–h) Wrapping the PPKTP crystal in two pieces of indium foil. i)–j) Crystal is placed on the bottom part of the oven. k)–o) The top part of the oven is fixed to bring the crystal to its final position. p)–q) Final pictures of the oven with built-in crystal.

T_{PD} and the wedged design of the crystal to change the polarisation degeneracy Δ between s- and p-polarised fields.⁷⁴

2.4.2 Setting up a two-mode squeezer

Setting up a two-mode squeezer consists of different steps and requires working with high accuracy. This subsection focuses on two main parts. First, it describes how the non-linear PPKTP crystal is mounted in the oven. Second, the most relevant steps for the cavity alignment procedure are explained.

As explained in Subsec. 2.4.1, the non-linear PPKTP crystal needs to be temperature controlled. For the case of an NDOPO (or a detuned OPO cavity), two different temperature locks are necessary; see Fig. 2.10 again. In the scope of this thesis, a new oven design compared to [Ste19] was developed that enables the independent temperature control of both crystal sides. The oven consists of individual elements that need to be stacked together.

The process of constructing the oven is visualised in Fig. 2.11. The pictures a)–d) show the preparation of the bottom stage of the oven. The symmetric copper base

⁷⁴The idea is to lock the cavity with a p-polarised field and set Δ as desired to get a detuned cavity for the s-polarisation. More information will follow in Chapter 4.

plate from a) has two rectangular notches for the two Peltier elements placed in b). Pieces of indium foil cover the heating plates of the Peltier elements to ensure better heat conductivity. In c), the bottom part of the polyoxymethylene (POM) hat, including the bottom oven parts, is put over the Peltier elements. Both copper parts must form a horizontally planar level, as seen in d).⁷⁵ Before the crystal is inserted, it needs to be carefully cleaned.⁷⁶ The pictures e)–h) depict how the crystal is covered in indium foil. First, two pieces of indium foil are prepared in e) such that they can be wrapped around the crystal in f). In the end, a small gap of roughly 1 mm separates the two indium regions g), h). Then, in i), the crystal is placed on the oven's bottom parts. The gap of the indium foil should match the gap of the bottom copper parts. Next, the two top copper parts are placed to cover the crystal in k) (side view) and l) (top view). Finally, the top POM hat is screwed on oven's top parts in m). The two holding screws, visible in n), o), are slowly and carefully screwed downwards to softly press the top oven parts against the bottom oven parts. The final oven, including the crystal, is seen in p), q).

When aligning an NDOPO cavity care has to be taken with respect to some critical points. Here, I want to list the most relevant points how to process.

1. **Align empty cavity:** The cavity is first aligned without crystal. The laser beam must hit all mirrors in the centre and, in particular, a planar cavity geometry⁷⁷ (at the standard beam height of 5 cm) should be ensured. The intra-cavity losses of the empty cavity are measured using the method from Subsec. 2.1.2.
2. **Prepare curved mirrors:** A wedged crystal will change the cavity eigenmode as indicated in Fig. 2.10b). Before inserting the crystal, the effect on the beam path must be calculated theoretically. Then, it can be compensated by carefully tilting the two curved mirrors by the pre-calculated angle. In this state, the cavity is misaligned and does not show light enhancement in a length scan.
3. **Insert crystal:** Now the oven with the crystal is inserted into the cavity. The crystal is moved to a position, such that the new cavity eigenmode corresponds to the mode of the input beam.
4. **Optimise crystal temperature:** Optimise T_{PD} with respect to the best single-pass SHG green light production. Adjust T_{PD} , such that $T_{PD} \approx T_{DC}$.
5. **Crystal fine alignment:** Minimise the intra-cavity loss when the cavity is ramped by changing the crystal position in translation and analysing the mode in reflection (see Subsec. 2.1.2 and Eq. (2.10)). The weaker the peak height of the reflected mode, the smaller the intra-cavity loss is. In the extreme case of a single-ended loss-less cavity, no modes are visible in reflection. Optimise the crystal's position in rotation for potential polarisation coupling.
6. **Eliminate polarisation degeneracy:** Eliminate the polarisation non-degeneracy by translating the crystal perpendicular to the beam axis, as shown in Fig. 2.10. Since beam clipping could occur when the crystal is moved too far, simultaneously check and preserve a small intra-cavity loss. Then, fine-tune to the point of polarisation degeneracy by changing T_{PD} .

⁷⁵If this is not ensured, the crystal can break . . .

⁷⁶This is usually done with a special polymer from Photonic Cleaning Technologies, LLC.

⁷⁷A non-planar geometry can cause polarisation coupling between the two resonant modes [SK96; GK97; DK87] which should be avoided.

TABLE 2.2: Left: Different coating techniques electron beam evaporation (EBE) and ion beam sputtering (IBS) produce coating losses due to absorption L_{abs} and due to scattering L_{sc} . Right: typical polishing losses depending on the roughness R_{q} .

Coating losses ⁷⁸			Substrate polishing losses	
			R_{q} (RMS)	L_{sc}
	L_{abs}	L_{sc}	< 0.1 nm	< 1 ppm
EBE	10 ppm	150 ppm	0.2 nm	6 ppm
IBS	3 ppm	negligible	0.3 nm	13 ppm
			0.5 nm	35 ppm
			1.0 nm	140 ppm

2.4.3 Squeezing characterisation – from generation to detection

This subsection explains how the squeezers used in this thesis are characterised. A complete characterisation always includes the squeezer itself and the detection scheme. For the squeezed state, the biggest opponent is optical loss. Thus, it is convenient to study different parts of the setup individually and assign efficiencies $\eta_i = 1 - L_i$ with each including the specific loss L_i of a subsystem. A squeezing slope is measured to evaluate the total optical loss L_{total} of the entire system and the phase noise $\Delta\phi$ at the detection.

Before measuring squeezing, the squeezer is characterised by its escape efficiency η_{esc} , which is related to the intra-cavity loss L_{cav} . In the experiment, this loss mainly originates from two contributions: First, the cleanness of the optical components (mirrors and crystal), second, the quality of the components. Table 2.2 gives an overview of expected losses arising from the coating quality and the substrate polishing quality. We further distinguish between losses due to absorption and scattering.

In the left Table 2.2, we see that the ion beam sputtering (IBS) coating technique is always recommendable for components used in squeezing experiments. Here, the expected absorption loss L_{abs} is small with 3 ppm, and the scattering loss L_{sc} is negligible.

The right Table 2.2 lists the expected scattering loss L_{sc} depending on the root mean square (RMS) roughness R_{q} ⁷⁹ of the substrate. The parameter R_{q} is related to the scattering loss L_{sc} via⁸⁰

$$L_{\text{sc}} = \left(\frac{4\pi R_{\text{q}}}{\lambda} \right)^2, \quad (2.94)$$

for an opaque coated substrate, where λ is the wavelength of the incident light. For squeezers, consistently high-quality polished optical components should be used.

However, the most dominating loss in our OPO is the residually reflecting surfaces of the crystal. Even though they are anti-reflective coated, they usually have a specified power reflectivity of less than 0.1 % per surface. The cavity loss is usually in the order of $L_{\text{cav}} = 0.2\%$ and is measured as pointed out in Subsec. 2.1.2. The loss is converted into an *escape efficiency* η_{esc} according to Eq. (2.11).

There are some more relevant parameters characterising the squeezer. From the obtained intra-cavity loss, the linewidth of the cavity is obtained, ignoring conversion in the crystal. The free spectral range is calculated from the cavity's optical round-trip

⁷⁸These are experience values received from LASEROPTIK GmbH.

⁷⁹The definition of R_{q} can be found in [Whi02], Sec. 3.2.1.2.

⁸⁰See [ERB83], Eq. (1b) who cite themselves [BP61; EBB79].

length. It can be easily verified when squeezing spectra are measured at higher free spectral ranges.

The squeezed state experiences optical losses along its propagation to a potential experiment and detection. These losses are measured by the power drop when a coherent beam travels the same path in the same optical mode. They are converted into the *propagation efficiency* η_{prop} .

At the homodyne detection, two optical loss factors play a role. These are the *visibility efficiency* η_{vis} from Eq. (2.64) and the *quantum efficiency* η_{qe} from Eq. (2.55). Subsection 2.2.4 already explained how η_{vis} and η_{qe} can be obtained. The visibility efficiency η_{vis} is usually measured with an accuracy of at least $\pm 0.1\%$. However, larger uncertainties are involved when analysing η_{qe} . By measuring the photodetector's transimpedance resistor, the electric gain in a photodetector, and thus the photocurrent, is accurately determined. However, accurately measuring the optical power is not that trivial. Often the used power meters have high measurement uncertainties of around $3\% - 7\%$ [Pow], which limits the determination of η_{qe} .

Now the total efficiency η_{total} consists of all individual efficiencies of the subsystems:

$$\eta_{\text{total}} = \eta_{\text{esc}}\eta_{\text{prop}}\eta_{\text{vis}}\eta_{\text{qe}}. \quad (2.95)$$

However, there is also an alternative method to determine the total efficiency.

The total efficiency η can also be obtained when measuring a *squeezing slope*.⁸¹ Then, squeezing and anti-squeezing values are measured for different pump powers at the homodyne detector. The measured data is compared to the theoretical model

$$V_{\text{det}}^{\pm} = \eta \left(\left(1 \pm \eta \frac{4x}{(1 \mp x)^2} \right) \cos^2(\Delta\phi) + \left(1 \pm \eta \frac{4x}{(1 \mp x)^2} \right) \sin^2(\Delta\phi) \right) + 1 - \eta, \quad (2.96)$$

which is basically Eq. (2.90), with $\Omega = 0$ (the measurement is taken for a resonant OPO). Note that Eq. (2.96) is power dependent because of the pump parameter $x = \sqrt{P/P_{\text{thr}}}$ (Eq. (2.89)). Also, note that P_{thr} depends on the actual mode-matching from the pump light into the crystal. Thus, sometimes this value might vary a little. Usually, during the measurement, squeezing and anti-squeezing values are monitored for different pump powers. Hence, each pump power corresponds to two measurement values. Therefore, a maximum logarithmic likelihood estimation is performed to fit the data to the model from Eq. (2.96).⁸² From the fit, the pump threshold P_{thr} , total efficiency η and phase noise $\Delta\phi$ are obtained as fitting parameters. Comparing Eqs. (2.95) and (2.96) is an elegant way accurately to determine η_{qe} .⁸³

This chapter presented theoretical and experimental points forming the background of this thesis. In the following three Chapters 3, 4 and 5 often subsections or important equations from this chapter will be cross-referenced.

⁸¹The efficiency η can also be obtained from the fit of a measured squeezing spectrum as done in [P1].

⁸²The fit was made by using the *Mathematica* [Wol] function *LogLikelihood*. A tutorial on maximum likelihood estimation can be found in [Myu03].

⁸³As done in [Vah+16].

Chapter 3

Cavity spectroscopy enhanced with squeezed light

Light does not *reveal* the colours of the world. Light *creates* them since it is absorbed or reflected depending on its wavelength, which determines an object's colour. Newton published this famous finding more than 300 years ago. It can be seen as one of the oldest experiments in spectroscopy [Na04].

Light can also be used as a carrier of information. The information is modulated on the light, which is sent over larger distances via a channel, and demodulated by the receiver. The first experiments on amplitude modulation were conducted by Mayer and Leblanc in the late 19th century [Czy18]. They set the basis for inventions such as the radio, television or modern digital modulation processes used in the internet.

Light can be used to perform high-precision phase measurements when it is prepared in a particular quantum state. This quantum state is called *squeezing* and was first generated in 1985 [Slu+85]. Nowadays, it is applied to high-sensitive instruments such as, e.g. gravitational wave detectors [Tse+19; Ace+19; Lou+21].

This chapter is dedicated to making use of a *modulation technique* and a particular state of *squeezed light*, applicable in the field of *spectroscopy*. Section 3.1 elaborates on the background and the motivation for our publication [P1]. This publication deals with a particular high-frequency and phase-modulated squeezed state that can be applied to a spectroscopy experiment. We show that a small phase signal generated in a cavity can be resolved below shot noise using our squeezed quantum state. We discuss current limitations in spectroscopic experiments, such as low-frequency technical and quantum shot noise. The important point is to define the difference between noise and signal. The idea of our method is illuminated in the intuitive sideband picture. Then, Sec. 3.2 reprints the publication [P1]. Next, Sec. 3.3 deals with the required quantum state, which is a high-frequency phase-modulated amplitude quadrature squeezed state. The preparation and characterisation of this state is explained here. Section 3.4 complements experimental details omitted in [P1]. Here, I want to highlight experimental challenges faced when working with the optical parametric oscillator (OPO) and the Fabry-Pérot (FP) cavity. This chapter ends with a discussion and conclusion of the conducted spectroscopy experiment in Sec. 3.5.

3.1 Introduction

The sensitivity of high-precision metrology devices as gravitational wave detectors is defined by the signal-to-noise ratio (SNR). To be sensitive to any potential signal, the SNR needs to be larger than one. Two straightforward ways exist to increase the SNR. Either the signal is increased, or the noise is decreased. The distinction between

noise and signals is the content of the first Subsec. 3.1.1. Then, Subsec. 3.1.2 deals with the motivation of our method from [P1] applied in spectroscopy. This subsection shows phasor pictures visualising how a low-frequency signal is detected at high frequencies.

3.1.1 Noise versus signals

This subsection discusses the two terms *noise* and *signals*. It starts with a famous historical example, demonstrating that sometimes assigning the signal or the noise is not trivial. This subsection emphasises that understanding and reducing noise sources is crucial to be sensitive to small signals of interest. The usual goal is to reach an SNR larger than one. Next, a more practical example of a laser beam susceptible to different types of noise is considered. We distinguish between quantum and classical technical noise. The subsection ends with comparing additive and multiplicative noise sources, which will be important for our method from [P1].

The key question is: How can we distinguish signal and noise? The simple answer is that a signal is relevant to an application (meaningful); contrarily, noise is irrelevant (meaningless). Moreover, the definition of a signal is highly dependent on the receiver, as shown by history. The astronomers Penzias and Wilson wanted to detect weak radio waves from satellites with the Holmdel Horn Antenna [CHH61] in 1965. Under their first impression, their measurements contained noise, which they could not eliminate. It turned out that they directly measured the cosmic microwave background for the first time, a radiation originating from the big bang of the universe [PW65]. For this discovery, Penzias and Wilson received the 1978 Nobel Prize in Physics [N78].

The discovery of the cosmic microwave background shows that depending on the perspective, one person's noise can become a future signal or be understood as a signal by another person. Noise can be interpreted as unwanted signals. Thus, noise can also contain information that is irrelevant to the receiver. Contrarily, a signal contains the information we are looking for.

Before the measurement, it is advantageous to predict the appearance of the signal, which is often done by simulating templates [Cam+06; Abb+16c; Abb+16b]. For instance, a simple signal can be modelled by a defined sinusoidal modulation. Additionally to the signal, the noise budget needs to be analysed by simulating models, estimation or direct measurements.

Understanding and characterising noise sources is crucial for their reduction in high-precision metrology. In general, stochastic noise is described by a stochastic process whose random variables do not follow a deterministic pattern.¹ Statistical parameters characterise the randomness of the process. Probability theory is used to determine the mean, variance, or covariance [VE06], as defined in Subsec. 2.2.1.

Another important parameter is the SNR, which is defined as

$$\text{SNR} = \frac{P_{\text{signal}}}{P_{\text{noise}}}, \quad (3.1)$$

where P_{signal} is the signal power and P_{noise} the noise power. Only when $P_{\text{signal}} > P_{\text{noise}}$, and thus $\text{SNR} > 1$, the signal can be resolved, as seen in the logarithmic power spectrum shown in Fig. 3.1. The figure shows a signal oscillating at Ω that peaks out of the noise floor.

¹*Deterministic* noise occurs when the process is too complex to model, which, e.g., is important in machine learning [AMMIL12].

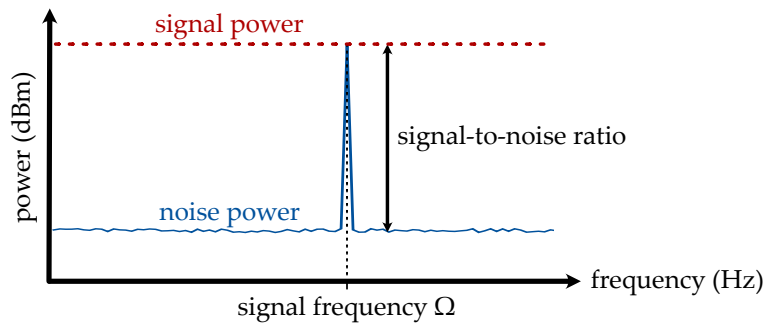


FIGURE 3.1: Logarithmic power spectrum of a signal peaking at frequency Ω out of the noise floor. The signal-to-noise ratio gives the power of the signal compared to the power of the noise floor.

Example: noise of a laser beam

Now, consider the example of an electric field emitted by a laser. To consider its noise, we can monitor the laser's power over a specific measurement time. We observe a randomly fluctuating quantity $P(t)$. It is not possible to predict the state of the laser field described by the random variable $P(t)$. Hence, we cannot attribute constant modulation coefficients or a fixed phase to describe the noise.

Often, the random signal is studied more conveniently in the frequency regime where we can assign specific noise powers to each frequency bin.² Stationary processes will create constant spectral densities. Noise can also be shown in the optical phase space picture introduced in Subsec. 2.2.1 by extending the picture with a third axis for the frequency.³ In the example of noise on a laser field, we need to distinguish between *amplitude* and *phase* noise.⁴ Another important discrimination is to consider the origin of the noise. It can be of *technical* and *quantum* nature.

Quantum noise originates from vacuum fluctuations and sets a fundamental classical limit for classical optical systems. Quantum noise on the laser field arises, e.g., from spontaneous emissions in the laser gain medium [HK96]. It also couples into the optical mode of interest at open ports, e.g. at non-perfect reflecting mirrors, as described in Subsec. 2.2.3. Quantum noise is white and occurs equally in the phase and amplitude quadratures. It occurs as photon shot noise if the laser power is measured with a photodetector. The signal-to-shot-noise ratio can be improved by increasing the laser power, as relative shot noise falls with the square root of the laser power [Kwe10]. Another option to fight quantum noise is the application of squeezed states of light.

Technical noise is caused by the technology, e.g. by the measurement instrument, the equipment or any unwanted environmental influences. For an optical experiment working with laser light, typical examples of technical noise sources are fluctuations in the pump current of the laser diode, beam pointing or polarisation fluctuations. These noise sources couple to the laser field's amplitude. Phase noise can be caused, e.g. by variations in the air current where the propagating laser light leads to fluctuations in the index of refraction.

²This is done by measuring power spectra (Fig. 3.1) or power spectral densities [SM05].

³Quantum noise is treated in the quantum noise sideband picture, as introduced in Subsec. 2.3.3. For more explanations on the representation of classical noise, see, e.g. [Kau18], Sec. 2.3.

⁴Phase noise is directly related to frequency noise since the frequency is the temporal derivative of the phase.

In principle, technical noise sources can be suppressed to arbitrarily low noise levels, depending on the time, effort, energy, cost, and corresponding technical sophistication invested in the experimental setup. All the mentioned noise sources can couple differently to the signal.

We will distinguish between multiplicative and additive noise, depending on how noise couples into the optical experiment. We again consider the stochastic process of the laser power described by the random variable $P(t)$.

Additive noise was first considered in [Kub62], and it arises if the influence of environmental fluctuations does *not* depend on the state variable of the system (the actual power $P(t)$) [Hor84]. Examples of additive noises can be found, e.g. at the photodetection because of stray light or electric noise originating, e.g. from dark current, or due to spontaneous emission in the laser [YAR89; BTW20]. Additive noise does not scale with the used laser power.

Multiplicative noise couples into state variables and thus changes the system dynamics [YS88]. It depends on the actual state of the system $P(t)$, i.e. on the used laser power. In the example of a laser beam, multiplicative noise sources are, e.g. vibrations on optical components or temperature fluctuations causing optical length changes. In the phasor picture, multiplicative noise scales with the size of the carrier.

3.1.2 Motivation for our method applied in spectroscopy

This subsection introduces publication [P1] by covering two points. First, it motivates our applied approach and accurately states when it becomes useful for experiments in spectroscopy. Second, it explains how we create and detect our spectroscopic signal.

Spectroscopic experiments frequently deal with inordinately small signals and call for high sensitivities [He+19; Ma+20]. Often, noise spoils the measurement and limits its sensitivity. We assume a scenario where the goal is to resolve a small signal expected at low frequencies. Furthermore, we assume that the signal is not visible due to two major limitations, as sketched in the two left blocks of Fig. 3.2: additive low-frequency noise and white photon shot noise. We use a modulation technique, so the signal also appears at high frequencies. Thereby, additive low-frequency noise, e.g. due to the electronics after the detection process,⁵ can be circumvented. Increasing the laser power is the conventional way to reduce relative shot noise. However, in some applications, the laser power must not be increased due to technical limitations [Den+06; Cas+20] as damage thresholds. Therefore, we want to follow an alternative approach to fight photon shot noise by using high-frequency squeezing.

By applying both, high-frequency modulation and high-frequency squeezing, we can increase the SNR and resolve a low-frequency signal. Next, we should consider the signal and its detection. In [P1], we apply a length modulation of an optical cavity to mimic a spectroscopic signal. The key question is: How can we detect this artificial signal created by the cavity's length modulation? In the following, two situations are discussed. First, a low-frequency phase modulation signal generated inside a cavity is investigated at low-frequencies. Second, a second phase modulation shifts the signal to high frequencies. We will see, that in both situations, the signal can be detected in the light's amplitude quadrature.

⁵Here, I do not mean photon detection noise (shot noise) but rather thermal noise in the resistors or photodiode dark noise. An extensive study regarding electronic noise is made in [Sei+06].

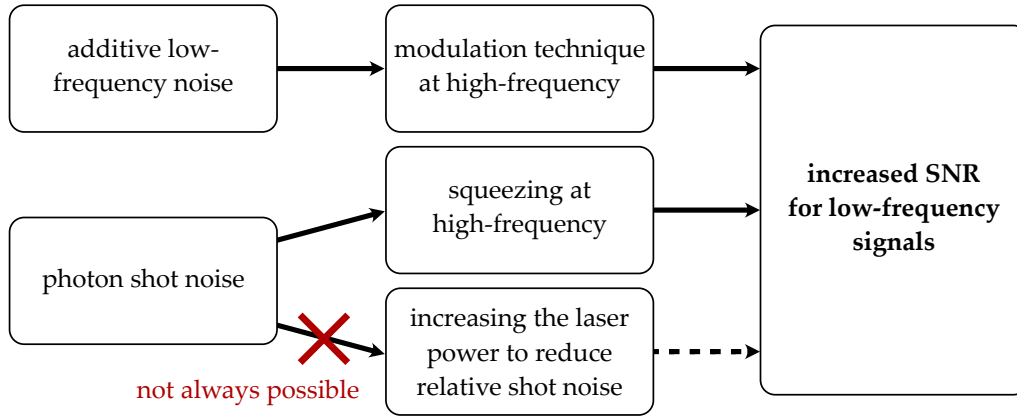


FIGURE 3.2: Motivation for our approach presented in [P1]. Assuming a low-frequency signal that is not resolvable due to additive technical low-frequency noise and photon shot noise. Our approach uses modulation and squeezing, both at high-frequencies to increase the SNR and make the low-frequency signal visible.

Single phase modulation

Assuming a mirror whose position is modulated at ω_m around x_0 . Then, the mirror position at $x_m = x_0 \cos(\omega_m t)$ will induce a phase shift $\phi_m = 2\omega x_m/c$ to an electric field upon reflection.⁶ This phase change also happens inside a cavity. If the position of a cavity mirror is modulated, the intra-cavity light will be phase-modulated.⁷ Thus, we need to measure the phase modulation to observe our signal, which is impossible with a direct detection on a single photodetector. However, a homodyne detector can measure a phase modulation imprinted on a light field.

For the following consideration, we work in the rotating frame of reference. We can write the phase-modulated classical field as

$$a = a_0 \exp(im_1 \cos(2\pi\omega_s t)) \quad (3.2)$$

and the local oscillator as $b = b_0 \exp(i\theta)$. Here, m_1 is the modulation index and ω_s the modulation frequency.

The homodyne detector measures the difference of the two powers, as seen in Eq. (2.58). The difference power ΔP depends on the relative phase θ between the two fields and reads

$$\Delta P(\theta) \propto 2b_0 \cos(\theta - m_1 \cos(2\pi\omega_s t)). \quad (3.3)$$

We would expect to see the phase modulation for a phase quadrature readout, i.e. for $\theta = \pi/2$ (see again Eq. (2.61)). However, due to the concatenated cosine function this is not easy to see. Hence, Eq. (3.3) is expanded for small modulation indices $m_1 \approx 0$:

$$\Delta P(\pi/2) \propto 2b_0 m_1 \cos(2\pi\omega_s t) + \mathcal{O}(m_1^3). \quad (3.4)$$

Now, the phase modulation can be directly seen oscillating with ω_s .

⁶For more details, see [Bon+17], Sec. 3.6.

⁷Assuming the modulation frequency ω_m is much smaller than the cavity linewidth.

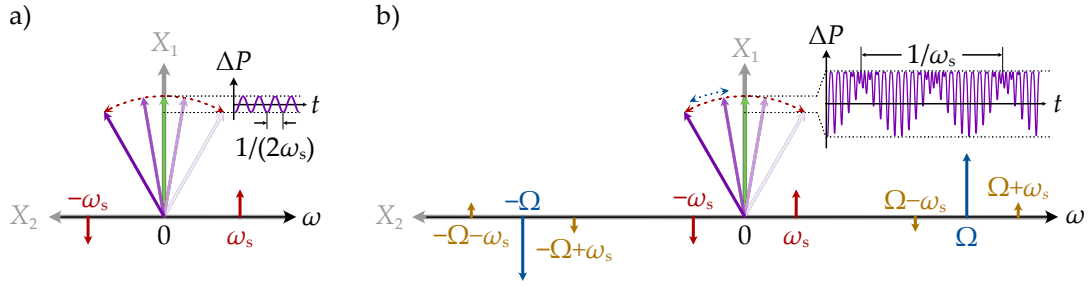


FIGURE 3.3: Phasor pictures of phase-modulated laser fields in the rotating frame of reference ($\omega \equiv 0$). In a) a single phase modulation is applied at ω_s (red phasors). If a homodyne detector reads out the amplitude quadrature, the purple sum phasor is projected onto the X_1 axis. The difference power is proportional to the change of X_1 and shows a $2\omega_s$ oscillation. In b) phase modulations are applied at ω_s (red phasors) and Ω (blue phasors). The resulting purple phasor follows a trajectory dominated by the beat notes $\Omega \pm \omega_s$. The pictures omit all higher-order phasors. Simulation parameters to compute ΔP : $m_1 = m_2 = 0.3$, $\Omega = 20\omega_s$.

When detecting the amplitude quadrature ($\theta = 0$), the analogous Taylor expansion as in Eq. (3.4) leads to

$$\Delta P(0) \propto 2b_0 - b_0 m_1^2 \cos(2\pi\omega_s t)^2 + \mathcal{O}(m_1^4) \quad (3.5)$$

$$= -\frac{1}{2}b_0 (m_1^2 \cos(2 \times 2\pi\omega_s t) + m_1^2 - 4) + \mathcal{O}(m_1^4). \quad (3.6)$$

According to Eq. (3.5) we also see a signal oscillation for $\theta = 0$, when we detect the amplitude quadrature.⁸ However, we find, that $\Delta P(0)$ predominantly oscillates with the double frequency $2\omega_s$ and the term scales with m_1^2 . This oscillation is a second-order effect, which is often neglected.⁹

The phase modulation at frequency ω_s detectable in the amplitude quadrature at $2\omega_s$ can also be understood in the phasor picture, as shown in Fig. 3.3a). The phase-modulated field from Eq. (3.2) is depicted by the purple phasor, which is the vectorial sum of the carrier (green phasor) and the rotating phase modulation sidebands (red phasors). According to Eq. (2.61), the homodyne detector always measures the actual projection of the purple phasor on the X_1 -axis since it measures the amplitude quadrature fluctuations. The measurement result is seen in the small diagram showing that $\text{var } \Delta P(t)$ oscillates with $2\omega_s$. This study concludes that a phase modulation applied with ω_s can be either detected in the phase quadrature at ω_s or, significantly smaller, in the amplitude quadrature at $2\omega_s$.

Two cascaded phase modulations

In our approach, we are not detecting the intra-cavity modulation at the oscillation frequency ω_s , which is assumed to be a low frequency. Instead, we are applying a high-frequency phase modulation at Ω to shift the signal originating from the cavity length modulation towards higher frequencies. We can write this cascaded phase modulation as

$$a = a_0 \exp(im_1 \cos(2\pi\omega_s t) + im_2 \cos(2\pi\Omega t)). \quad (3.7)$$

⁸Here, the difference between *amplitude* and *amplitude quadrature* becomes visible.

⁹The theoretical derivation in Sec. 2.1 in [P1] also neglects this second-order effect.

Again, we can calculate the Taylor expansions of the difference powers ΔP obtained from homodyne detection which read

$$\Delta P(\theta = \pi/2) \propto 2b_0 (m_1 \cos(2\pi\omega_s t) + m_2 \cos(2\pi\Omega t)) + \mathcal{O}(m^2), \quad (3.8)$$

$$\begin{aligned} \Delta P(\theta = 0) \propto & -b_0 m_1 m_2 \cos(2\pi(\Omega - \omega_s)t) \\ & + b_0 m_1 m_2 \cos(2\pi(\Omega + \omega_s)t) \end{aligned} \quad (3.9)$$

$$-2b_0 + \mathcal{O}(m^2). \quad (3.10)$$

These equations show an important result: To detect the intra-cavity phase modulation at high frequencies, we need to look at the amplitude quadrature given by Eq. (3.9), which is measured by a homodyne detector. Here, we find intermodulation products oscillating with $\Omega \pm \omega_s$.

For our experiment, we assume that the sidebands at $\pm\Omega$ act as a new carrier having an electric field proportional to m_1 . Measuring the beat notes at $\Omega \pm \omega_s$ is a first-order effect which is proportional to m_2 . Consequently, it does not matter if we detect the signal at ω_s or at $\Omega \pm \omega_s$ if we assume the same power in the sidebands at $\pm\Omega$ as in the carrier field at $\omega \equiv 0$.

The cascaded phase modulation is also presented in Fig. 3.3b). This phasor picture shows the first phase modulation at ω_s (red phasors), but also the second phase modulation at Ω (blue phasors) and the intermodulation sidebands (orange phasors). The cascaded phase modulation affects the resulting phasor (purple phasor). Now, the tilting of this phasor is dictated by a slow oscillation ω_s and a fast oscillation Ω . The phasor's projection onto the X_1 axis is seen in the difference photocurrent ΔP . The beat note from ΔP has contributing frequencies of $\omega_s - \Omega$ and $\omega_s + \Omega$ which corresponds to Eq. (3.9). In conclusion, two cascaded phase modulations can be observed in the amplitude quadrature of the light field.¹⁰

In the next section, the publication [P1] is reprinted.

3.2 [P1]: High-precision cavity spectroscopy using high-frequency squeezed light

This subsection reprints the following publication, which was accepted on 15 January 2021 and published on 10 February 2021 in Optics Express. The author contributions and a short abstract can be found on Page iii.

[P1] J. Junker, D. Wilken, E. Huntington, and M. Heurs. "High-precision cavity spectroscopy using high-frequency squeezed light". In: *Opt. Express* 29.4 (Feb. 2021), pp. 6053–6068. DOI: [10.1364/OE.416713](https://doi.org/10.1364/OE.416713)

¹⁰They could also be observed in the phase quadrature but weaker at different beat notes.



High-precision cavity spectroscopy using high-frequency squeezed light

JONAS JUNKER,^{1,*}  DENNIS WILKEN,¹  ELANOR HUNTINGTON,²  AND MICHÈLE HEURS¹ 

¹Max Planck Institute for Gravitational Physics (Albert Einstein Institute), and Institute for Gravitational Physics, Leibniz Universität Hannover, Callinstr. 38, 30167 Hannover, Germany

²Centre for Quantum Computation & Communication Technology and Research School of Engineering, The Australian National University, Canberra, ACT 2601, Australia

*jonas.junker@aei.mpg.de

Abstract: In this article, we present a novel spectroscopy technique that improves the signal-to-shot-noise ratio without the need to increase the laser power. Detrimental effects by technical noise sources are avoided by frequency-modulation techniques (frequency up-shifting). Superimposing the signal on non-classical states of light leads to a reduced quantum noise floor. Our method reveals in a proof-of-concept experiment small signals at Hz to kHz frequencies even below the shot noise limit. Our theoretical calculations fully support our experimental findings. The proposed technique is interesting for applications such as high-precision cavity spectroscopy, e.g., for explosive trace gas detection where the specific gas might set an upper limit for the laser power employed.

© 2021 Optical Society of America under the terms of the [OSA Open Access Publishing Agreement](#)

1. Introduction

Successful blue-sky experiments, such as the first direct detection of gravitational waves (GWs) in 2015 [1] require an intimidatingly high measurement sensitivity. In a GW detector the signal originates from the relative differential distance change caused by a GW, as measurable with a Michelson-type interferometer [1]. In this particular case of the GW event GW150914 a strain sensitivity of $\Delta L/L \approx 10^{-23}$ was required. Other types of high-precision metrology experiments detect other types of signals, but they have one requirement in common: All call for high sensitivity and detection with a sufficiently large signal-to-noise ratio (SNR).

As an example, in laser absorption spectroscopy [2,3] the concentration of a gas phase can be determined by measuring the interaction of a laser field with the gas molecules. The challenge here often lies in the fact that the spectroscopic signal to be detected is inordinately small - this makes its detection inherently difficult, but it additionally makes the signal highly susceptible to noise. These challenges can be generalized to the detection of any small signal.

The obvious way to maximize the SNR is to increase the signal and to decrease the noise. At low measurement frequencies, active feedback control often serves to suppress the dominant technical noise sources down to the fundamental shot noise limit [4–7]. In addition to noise reduction, the achieved signal-to-shot-noise ratio can be improved by increasing the laser power, as relative shot noise falls with the square root of the laser power.

In spectroscopic applications, amplifying the laser power increases the interaction strength and hence amplifies the signal. In some cases, however, the signal strength cannot be increased: for technical reasons such as damage thresholds [8,9], or for fundamental reasons, e.g. if the origin of the signal is astrophysical [10]. In other cases, the intrinsic noise of the measurement apparatus is already governed by quantum shot noise, making a further reduction of the noise floor seem initially unfeasible.

Technical noise is always present in experiments, in particular at low measurement frequencies in the Hz and kHz regions. Typical examples of technical noise sources include seismic noise

and mechanical vibrations, electronic noise, laser intensity and frequency noise, or fluctuations of air currents leading to variations in the index of refraction of the air through which light propagates. In principle, technical noise sources can be suppressed to arbitrarily low noise levels, depending on the time, effort, energy, cost, and corresponding technical sophistication invested in the experimental setup. Quantum noise, however, poses a more fundamental limit, which is expressed in the Heisenberg Uncertainty Relation. Quantum shot noise occurring in laser experiments originates from the Poissonian photon statistics of the coherent state [11], which is emitted by a technically well-stabilized laser.

The application of squeezed light [12] can reduce the relative shot noise and thus improve the SNR [13–15]. In this regard it acts like an increase in laser power, but without the drawbacks associated with higher optical power, such as increased absorption, higher thermal load, excess scattering, etc. Squeezed light first was experimentally demonstrated in 1985 [16] and has gained increasing relevance over the last decades. While the first squeezing experiment reduced the shot noise only by 0.3 dB, the highest achieved squeezing level to date lies at more than 15 dB [17]. The number of possible applications is too numerous to list, ranging from GW detection [14] over continuous variable quantum computing [18] to quantum imaging [19,20] and teleportation [21,22]. Squeezing generated at low frequencies (LFs) [23,24] always comes at the cost of considerable technical effort; in comparison, high-frequency (HF) squeezing [25–27] can drastically reduce these efforts.

Squeezing at base-band has been utilized to improve spectroscopic measurements [28,29], e.g. on atomic cesium [30]. Recently, a quantum enhancement of the SNR of 3.6 dB relative to the shot noise limited SNR was demonstrated in stimulated Raman spectroscopy [31]. In these experiments [28–31], a squeezed probe beam was transmitted through samples and then detected. However, an even higher signal strength can be achieved by enhancing the probe field in an optical resonator.

In this paper, we show in a proof-of-concept experiment the application of HF squeezing for cavity enhanced phase-sensitive spectroscopy. We report on a novel method that circumvents technical noise sources and improves the SNR without the need to increase the laser power and enables more advanced techniques such as noise-immune cavity-enhanced optical-heterodyne molecular spectroscopy (NICE-OHMS) [32]. We benefit from the advantages of HF squeezing by shifting the signal of interest (at Hz or kHz frequencies) to 200 MHz. We apply a small cavity length modulation as a signal that would conventionally be masked by quantum shot noise at HF. With our approach this signal can be revealed in a 6 dB squeezed noise floor. The results of our research are very promising for applications in high-precision metrology as in quantum spectroscopy, in particular for frequency modulation spectroscopy (FMS) [33] or trace gas detection [34,35] where the potentially explosive gas sets an upper limit for the employed laser power.

In Sec. II we provide a theoretical description of the effect of a cavity length modulation on a phase modulated laser field. We derive the variances, if the modulated field's amplitude quadrature is squeezed in an optical parametric oscillator (OPO) before it senses the cavity length modulation. Sec. III gives a detailed description of our experimental setup. In Sec. IV we present our results including the measurements that show cavity length modulation signals in the reduced noise floor around 200 MHz. In Sec. V we discuss our results, identify drawbacks and benefits of our method and give a brief outlook. We end with a conclusion in Sec. VI.

2. Theory

We detect artificial length variations of a cavity that are generated with a piezoelectric actuator at LFs. If we send a probe field through this cavity, a phase modulation (PM) is imprinted on the field that can be detected in transmission. In this section, we first calculate the variance of such a field. Second, we look at the case of a probe field that is phase modulated at the free spectral

range (FSR)-frequency. Third, we determine the output variance when using a probe field that is additionally squeezed. This allows an improvement of the SNR, when the classical measurement was shot-noise-limited.

2.1. Detecting a cavity length modulation

We start with the simple case of a Fabry-Perot (FP) cavity shown in Fig. 1. From the left, a classical laser field \hat{A}_{in} is sent into the impedance matched cavity with two loss-less mirrors with equal reflectivities R and detuning Δ . We want to determine the output field \hat{A}_{out} in transmission.

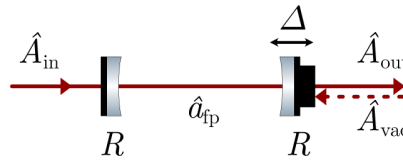


Fig. 1. Schematic of the length modulated FP cavity.

For the calculations we are following the approach in [11]. We can express the circulating cavity mode amplitude \hat{a}_{fp} after one cavity round-trip time τ_{fp} by

$$\hat{a}_{\text{fp}}(t + \tau_{\text{fp}}) = \exp(i\Delta) \left(R\hat{a}_{\text{fp}}(t) + \sqrt{T\tau_{\text{fp}}} (\hat{A}_{\text{in}}(t) + \hat{A}_{\text{vac}}(t)) \right). \quad (1)$$

The circulating mode amplitude after one cavity round-trip time depends on the initially circulating mode $\hat{a}_{\text{fp}}(t)$ and on the two input rates $\hat{A}_{\text{in}}(t)$ and $\hat{A}_{\text{vac}}(t)$. Next, we consider the cavity length modulation as phase modulation for the intra-cavity field. Therefore, we set $\Delta = d \sin(\omega_s t)$ where ω_s is the modulation frequency. After separating DC and fluctuating terms with $\hat{a}(t) = \bar{a} + \delta\hat{a}(t)$ and linearizing then, we can focus on the fluctuating part of Eq. (1) and find that

$$\begin{aligned} \delta\hat{a}_{\text{fp}}(t + \tau_{\text{fp}}) = & -\bar{a}_{\text{fp}} \left(1 - \exp(id \sin(\omega_s t)) \right) \\ & + \exp(id \sin(\omega_s t)) \left(\sqrt{T\tau_{\text{fp}}} (\delta\hat{A}_{\text{in}}(t) + \delta\hat{A}_{\text{vac}}(t)) + R\delta\hat{a}_{\text{fp}}(t) \right) \end{aligned} \quad (2)$$

The exponential expressions in Eq. (2) can be approximated using Bessel functions of the first kind. For small cavity length changes $d \ll 1$ we can approximate

$$\exp(id \sin(\omega_s t)) \approx 1 + \frac{d}{2} \left(\exp(i\omega_s t) - \exp(-i\omega_s t) \right) \quad (3)$$

and call the $\exp(\pm i\omega_s t)$ terms sidebands. Next, we can transform Eq. (2) to Fourier space analog to [25] by substituting $\hat{a}(t + \tau) \Leftrightarrow \tilde{a}(\omega) \exp(i\omega\tau)$. We can solve for the fluctuating part

$$\delta\tilde{a}_{\text{fp}}(\omega) = \frac{2(\delta\tilde{A}_{\text{in}} + \delta\tilde{A}_{\text{vac}})\sqrt{T\tau_{\text{fp}}} + \bar{a}_{\text{fp}}d(\delta_{\omega+\omega_s} - \delta_{\omega-\omega_s})}{2(\exp(i\tau_{\text{fp}}\omega) - R)}. \quad (4)$$

The cavity length modulation sidebands are now represented by the Dirac delta functions $\delta_{\omega \pm \omega_s} = \delta(\omega \pm \omega_s)$, both scaling with the modulation amplitude d and with the cavity mean field \bar{a}_{fp} .

We use the input-output theory from [36], including the quantum boundary conditions, to derive the field fluctuations leaving the FP cavity as

$$\delta\tilde{A}_{\text{out,fp}} = \sqrt{T/\tau_{\text{fp}}}\delta\tilde{a}_{\text{fp}} - \sqrt{R}\delta\tilde{A}_{\text{vac}}. \quad (5)$$

If we detect the output field, we can measure the amplitude (+) or phase quadrature (-) fluctuations

$$\delta\tilde{X}^+(\omega) = \delta\tilde{A}(\omega) + \delta\tilde{A}(-\omega)^\dagger, \quad (6)$$

$$\delta\tilde{X}^-(\omega) = i(\delta\tilde{A}(\omega) - \delta\tilde{A}(-\omega)^\dagger), \quad (7)$$

where $\delta\tilde{a}^\dagger(\omega) = \delta\tilde{a}(-\omega)^\dagger$ [37]. Finally, we are interested in the variances $V^\pm(\omega) = \langle |\delta\tilde{X}^\pm(\omega)|^2 \rangle$. Since the Dirac delta function δ is only an idealization and its square is not defined mathematically, below we replace them by Dirac delta-like functions $\tilde{\delta}$ with finite width, which are later defined in Eq. (23). Physically, the width of those sidebands corresponds to the technical noise present in the modulation sidebands. Assuming uncorrelated input fields \tilde{A}_{vac} and \tilde{A}_{in} , the output variances read

$$V_{\text{fp}}^+(\omega) = |A(\omega)|^2 V_{\text{in}}^+(\omega) + |B(\omega)|^2 V_{\text{vac}}^+(\omega) + V_{\text{n}}^+(\omega), \quad (8)$$

$$V_{\text{fp}}^-(\omega) = |A(\omega)|^2 V_{\text{in}}^-(\omega) + |B(\omega)|^2 V_{\text{vac}}^-(\omega) + \left| \frac{i\tilde{a}_{\text{fp}}d\sqrt{T}}{\sqrt{\tau_{\text{fp}}}(\exp(i\tau_{\text{fp}}\omega) - R)} (\tilde{\delta}_{\omega+\omega_s} - \tilde{\delta}_{\omega-\omega_s}) \right|^2 + V_{\text{n}}^-(\omega), \quad (9)$$

where $A(\omega)$ and $B(\omega)$ are cavity related pre-factors specified as

$$A(\omega) = \frac{T}{\exp(i\tau_{\text{fp}}\omega) - R} \quad (10)$$

$$B(\omega) = -\sqrt{R} + \frac{T}{\exp(i\tau_{\text{fp}}\omega) - R}. \quad (11)$$

Evidently, the two sidebands oscillating with $\omega \pm \omega_s$ originate from the cavity length modulation. They will only appear in the phase quadrature output variance V_{fp}^- . We use the term V_{n} to describe uncorrelated noise sources that add to the measured variance, e.g. electronic noise. Noise that is initially on the probe beam or noise sources that affect the probe beam at any point in the experiment (e.g. mechanical cavity resonances or an unstable cavity lock) are more comprehensive to describe and would overcomplicate the calculations shown here. We therefore neglect these noise terms but want to empathize that our approach is not immune to this type of noise. However, we elaborate on this in Sec. 5 and extend our idea to suppress these noise sources in Sec. 5.1.

2.2. Frequency up-shifting the signal

Typical noise sources occur primarily at LFs (<10 MHz). To circumvent the noise $V_{\text{n}}(\omega)$, we measure our signal at HFs. Therefore, we extend our setup according to Fig. 2. A PM at HF ($\Omega \gg \omega_s$) is imprinted by an electro-optic modulator (EOM) on the input field \hat{A}_{in} , before the field enters the cavity. To maximize the transmission of the modulation sidebands, the modulation frequency Ω should correspond to the FSR of the FP cavity ($\Omega = \text{FSR}_{\text{fp}} = 1/\tau_{\text{fp}}$).

Again, we assume a small modulation index β and use the Bessel approximation from Eq. (3). For the fluctuating part we get in frequency domain for the new input field

$$\tilde{\delta}\tilde{A}_{\text{in}}(\omega) = (\tilde{\delta}\tilde{A}_{\text{mod}}(\omega) + \frac{\beta}{2}\tilde{A}_{\text{mod}}(\tilde{\delta}_{\omega-\Omega} - \tilde{\delta}_{\omega+\Omega})) \exp(i\theta), \quad (12)$$

where \tilde{A}_{mod} corresponds to the field before the EOM. Here, we have dropped the $d\tilde{\delta}\tilde{A}$ terms assuming $d\tilde{\delta}\tilde{A} \ll d\tilde{a}_{\text{fp}}$. Then, the output variances of the cavity can be calculated analogously to

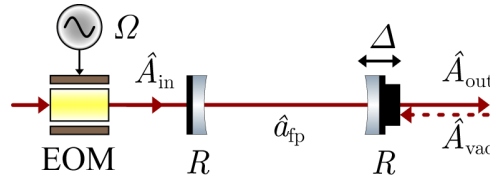


Fig. 2. Schematic of the length modulated FP cavity, with a phase modulated input field.

Sec. 2.1 yielding

$$V_{\text{fp,pm}}^+(\omega) = V_{\text{fp}}^+(\omega) + \left| \frac{\bar{A}_{\text{mod}} dT\beta}{2(\exp(i\tau_{\text{fp}}\omega) - R)} \right|^2 \times |(\delta_{\omega+\Omega-\omega_s} + \delta_{\omega-\Omega+\omega_s} - \delta_{\omega+\Omega+\omega_s} - \delta_{\omega-\Omega-\omega_s})|^2, \quad (13)$$

$$V_{\text{fp,pm}}^-(\omega) = V_{\text{fp}}^-(\omega) + \left| \frac{i\bar{A}_{\text{mod}} T\beta}{\exp(i\tau_{\text{fp}}\omega) - R} (\delta_{\omega+\Omega} - \delta_{\omega-\Omega}) \right|^2 \quad (14)$$

where V_{fp}^\pm corresponds to the results from the previous section derived in Eqs. (8) and (9). The terms oscillating with $\omega \pm \omega_s$ and $\omega \pm \Omega$ can be only seen in the phase quadrature V^- . The intermodulation terms oscillating with $\omega \pm \Omega \pm \omega_s$ can be detected only in the output amplitude quadrature V^+ , which is an important result. This result means that the cavity length modulation can also be resolved at HFs. External noise V_n , introduced in Eqs. (8) and (9) may still couple into the measurement. However, we can assume that there is negligible noise at hundreds of MHz.

Fundamentally, this measurement will be limited by the shot noise when technical noise sources on the probe beam are suppressed sufficiently. The relative shot noise level might be reduced by increasing the used laser power. However, this is often only possible in the limits of available and permissible power.

2.3. High-frequency phase modulated squeezing

One approach to further reduce noise and thereby improve the shot-noise-limited SNR is the usage of a squeezed probe field. In the following section we explain how such a field is generated and how its variances can be derived. The following calculations were similarly done for an unmodulated seed in [25].

We consider a singly resonant OPO that is operating below threshold at the fundamental frequency ω_0 as shown in Fig. 3. For simplification, we assume a cavity consisting of a partially reflective (PR) input mirror with $R_1 < 1$, a highly reflective (HR) mirror with $R_2 \approx 1$ and an ideal non-lossy mirror $R_3 = 1$ surrounding a non-linear $\chi^{(2)}$ medium. It is convenient to include the

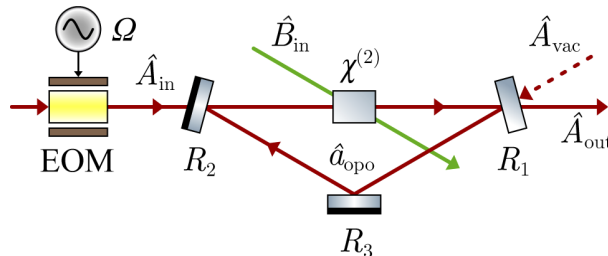


Fig. 3. Schematic of an OPO with a phase modulated seed as input.

effect of all intra-cavity losses in the reflectance of mirror 2. The nonlinear medium is pumped with the field \hat{B}_{in} at the second harmonic frequency $\omega_{\text{pump}} = 2\omega_0$. The cavity round-trip time is τ_{opo} and, ideally, should be identical to the round-trip time in the FP cavity ($\text{FSR}_{\text{opo}} = \text{FSR}_{\text{fp}}$). A vacuum field \hat{A}_{vac} is impinging on mirror 1 and the phase modulated seed field \hat{A}_{in} , identical to Eq. (12), is sent into the cavity on mirror 2. We are dealing with a single mode as we do not discriminate in frequency between the upper and lower sidebands. Thus we assume a single-mode interaction Hamiltonian with an undepleted pump field:

$$\mathcal{H} = \frac{i\hbar\chi}{2} (a^2 - a^{\dagger 2}). \quad (15)$$

As in subsections 2.1 and 2.2, the fundamental cavity mode \hat{a}_{opo} after a single cavity round-trip with round-trip time τ_{opo} can be expressed on resonance by

$$\begin{aligned} \hat{a}_{\text{opo}}(t + \tau_{\text{opo}}) = & -\chi\tau_{\text{opo}}\hat{a}_{\text{opo}}^{\dagger}(t) + \sqrt{R_1R_2}\hat{a}_{\text{opo}}(t) \\ & + \sqrt{R_1T_2\tau_{\text{opo}}}\hat{A}_{\text{in}}(t) + \sqrt{T_1\tau_{\text{opo}}}\hat{A}_{\text{vac}}(t). \end{aligned} \quad (16)$$

The solution for the fluctuating part $\delta\tilde{a}(\omega)_{\text{opo}}$ of the intra-cavity field in frequency domain can be computed similarly as above. Since the OPO is seeded with a phase modulated field, $\delta\tilde{A}_{\text{in}}$ is defined as in Eq. (12). To derive the desired fluctuations for the output field of the OPO, the boundary condition

$$\delta\tilde{A}_{\text{out,opo}} = \sqrt{T_1/\tau_{\text{opo}}}\delta\tilde{a}_{\text{opo}} - \sqrt{R_1}\delta\tilde{A}_{\text{vac}} \quad (17)$$

needs to be applied. We can now use $\delta\tilde{A}_{\text{out,opo}}$ for the OPO's output to substitute the FP cavity's input $\delta\hat{A}_{\text{in}}$ in Eq. (5). Then, the output variances of the FP cavity can be computed similarly to Eqs. (8) and (9)

$$V_{\text{fp}}^{\pm}(\omega) = V_{\text{cav}}^{\pm}(\omega) + |C^{\pm}(\omega)|^2 + V_{\text{n}}^{\pm}, \quad (18)$$

but become rather complex. The variance V_{cav}^{\pm} is specified as

$$\begin{aligned} V_{\text{cav}}^{\pm} = & \left| A(\omega) \left(-\sqrt{R} + \frac{T_1}{\exp(i\tau_{\text{fp}}\omega) - \sqrt{R_1R_2} \pm \tau_{\text{opo}}\chi} \right) + B(\omega) \right|^2 V_{\text{vac}}^{\pm}(\omega) \\ & + \left| \frac{\sqrt{R_1T_1T_2T}}{(\exp(i\tau_{\text{fp}}\omega) - R)(\exp(i\tau_{\text{fp}}\omega) - \sqrt{R_1R_2} \pm \tau_{\text{opo}}\chi)} \right|^2 V_{\text{in}}^{\pm}(\omega). \end{aligned} \quad (19)$$

It shows how the variances of the impinging vacua and the seed are transformed by the two cavities and thus defines the shot noise level. In fact, it is important to take a closer look onto C^+ . The situation is similar as before in Eqs. (13) and (14). C^+ represents the intermodulation sidebands we are interested in. We find

$$\begin{aligned} C^+(\omega) = & \frac{\bar{A}_{\text{mod}}dT\beta\sqrt{R_1T_1T_2}}{2(\exp(i\tau_{\text{fp}}\omega) - R)(\exp(i\tau_{\text{opo}}) - \sqrt{R_1R_2} - \tau_{\text{opo}}\chi)} \\ & \times (\delta_{\omega+\Omega-\omega_s} + \delta_{\omega-\Omega+\omega_s} - \delta_{\omega+\Omega+\omega_s} - \delta_{\omega-\Omega-\omega_s}). \end{aligned} \quad (20)$$

The sidebands oscillating with $\omega \pm \omega_s$ and $\omega \pm \Omega$ can be found in $C^-(\omega)$:

$$\begin{aligned} C^-(\omega) = & \frac{i\bar{A}_{\text{mod}}T\beta\sqrt{R_1T_1T_2}}{(\exp(i\tau_{\text{fp}}\omega) - R)(\exp(i\tau_{\text{opo}}) - \sqrt{R_1R_2} - \tau_{\text{opo}}\chi)} (\delta_{\omega+\Omega} - \delta_{\omega-\Omega}) \\ & + \frac{i\bar{a}_{\text{fp}}d\sqrt{T/\tau_{\text{fp}}}}{\exp(i\tau_{\text{fp}}\omega) - R} (\delta_{\omega+\Omega} - \delta_{\omega-\Omega}). \end{aligned} \quad (21)$$

Choosing amplitude quadrature squeezing by setting the phase of the seed $\theta = 0$ in Eq. (12), we achieve a reduced noise floor in the amplitude quadrature and an increased noise floor in

the phase quadrature in Eq. (18). Thereby, we improve the SNR measuring the cavity length modulation.

The variance in Eq. (18) is only an idealization. If the field is measured with a homodyne detector (HD) to access the phase quadrature, phase fluctuations between the signal and the local oscillator (LO) need to be taken into account. For small standard deviations of the normally distributed phase fluctuations, phase jitter with a root mean square of ϕ will affect the detection angle at the HD. Including the total efficiency η and thus optical loss, we can write the measured variances behind the FP cavity as [38]

$$V_{\text{fp,det}}^{\pm}(\omega) = \eta(V_{\text{fp}}^{\pm}(\omega) \cos^2(\phi) + V_{\text{fp}}^{\mp}(\omega) \sin^2(\phi)) + (1 - \eta). \quad (22)$$

Hence, the output variance will be a mixture of the amplitude and phase quadrature V^+ and V^- . In consequence, the squeezing level will be reduced and all existent sidebands, to some degree, will be visible in both measured variances. We will use Eq. (22) for fitting our experimental data in Sec. 4. However, we will first present our experimental setup in the next section.

3. Experimental setup

Our experimental setup shown in Fig. 4 can be divided into three subsystems. The first part is the preparation stage and consists of the OPO, our non-classical light source. Here, our probe beam is generated which is a phase modulated but amplitude quadrature squeezed field. This field is sent into our second subsystem, the FP cavity. Here, we apply a cavity length modulation to mimic a spectroscopic signal. Finally, our third subsystem consists of a balanced HD where we resolve the length modulation signal in a squeezed sub-shot-noise floor at HF.

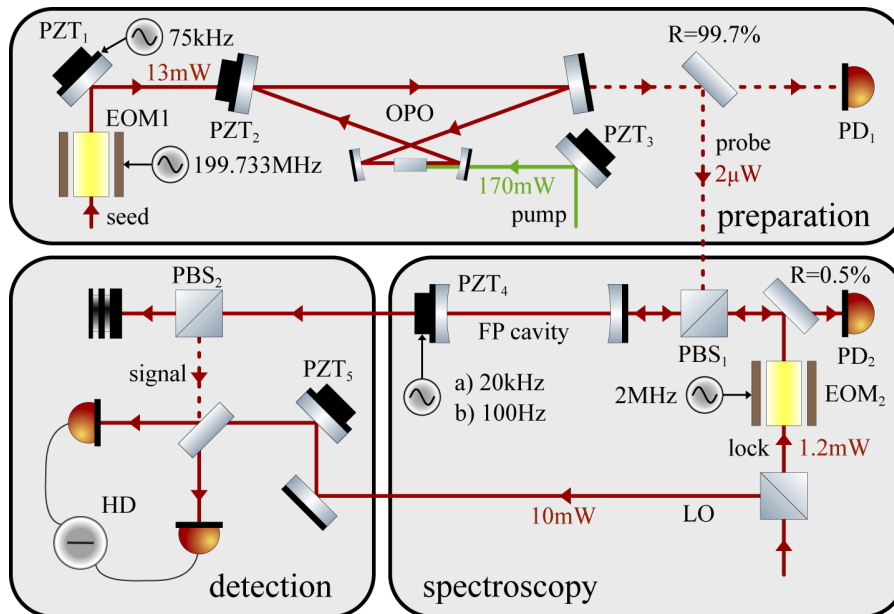


Fig. 4. The experimental setup consisting of the three subsystems: squeezed state preparation, spectroscopy and homodyne detection.

3.1. Non-classical light source

Our non-classical light source consists of a sub-threshold OPO, shown in the upper block of Fig. 4. In this block, all shown laser fields are s-polarized. The OPO has a comparably long

round-trip length of $L_{\text{opo}} \approx 1.5\text{m}$. This leads to a relatively small FSR of 199.66 MHz. Two curved mirrors with radius of curvature of -100 mm create a cavity eigenmode with beam waist of $25.6\ \mu\text{m}$ in the crystal. The OPO is seeded with a phase modulated classical laser field through an HR mirror (transmission $T = 0.01\%$) that is attached to a piezoelectric element (PZT₂) from the left side. The PM frequency of 199.733 MHz is chosen to match the FSR of the OPO and, in particular, of the FP cavity (see Sec. 3.2 and Table 1). This ensures that the PM sidebands are transmitted by the two cavities. The singly-resonant OPO cavity is held on resonance with PZT₂ for 1064 nm using a field in counter-propagating direction of the cavity. This field is not depicted in the Fig. 4 for simplicity. The $1\text{mm} \times 2\text{mm} \times 10\text{mm}$ nonlinear PPKTP crystal is pumped with 170 mW at 532 nm. To reach a stable production of amplitude quadrature squeezing in the probe beam, the squeezing angle needs to be locked: First, we modulate the phase of the seed with 73 kHz, by dithering the PZT₁ attached to a steering mirror. Second, 0.3 % of the probe's power are detected on the photodiode (PD₁) behind a PR mirror. Then, the detected signal is demodulated to generate an error signal which is sent back to PZT₃. The full characterization of our non-classical light source ("squeezing comb") and its performance is given in detail in a publication currently under preparation. The most important parameters characterizing the OPO are given in Table 1.

Table 1. Important parameters of OPO and FP cavity.

OPO	Value	Error	Unit
linewidth (FWHM)	4.5	± 0.1	MHz
FSR	199.66	± 0.01	MHz
pump power	170	± 12	mW
escape efficiency	97	± 1	%
FP cavity	Value	Error	Unit
linewidth (FWHM)	200	± 7	kHz
FSR	199.733	± 0.01	MHz
finesse	998	± 33	
round-trip-loss	90	± 10	ppm

3.2. Fabry-Pérot cavity for spectroscopy

The second subsystem is shown in the right bottom block of Fig. 4 including the FP cavity as the spectroscopic device. In the FP cavity the artificial signal is created by actuating PZT₄ which corresponds to a cavity length modulation. The FP cavity consists of two PR mirrors ($R = 99.69\%$, $\text{ROC} = 2\text{m}$) attached to an aluminum spacer in a distance of roughly 37.5 cm. The intra-cavity loss per round-trip is 90 ppm and the exact FSR of the FP cavity is 199.733 MHz. Hence, the cavity finesse is 998 and the linewidth at the full width at half maximum (FWHM) is 200 kHz. The output mirror is attached on PZT₄ to modify the cavity length.

We stabilize the FP cavity with the p-polarized lock beam, so that it is resonant for our s-polarized probe beam. This is possible because the cavity is radially symmetric and therefore degenerated for s- and p-polarization. The lock field is phase modulated with EOM₂ at 2 MHz and sent into the FP cavity. The part that is reflected is detected on PD₂, demodulated, low-pass-filtered and fed back to PZT₄ [39]. The s-polarized amplitude quadrature squeezed probe field coming from the OPO is reflected at PBS₁ and it is also injected into the resonant FP cavity. PBS₂ is used to separate the lock field from the signal field in transmission of the FP cavity.

In our approach we show that small phase signals created in the FP cavity can be resolved by the use of amplitude quadrature squeezing. In order to generate these signals, we can apply tiny length modulations with a) 20 kHz (amplitude $(9.8 \pm 1.0)\text{ pm}$) and b) 100 Hz (amplitude

(25.4 ± 1.0) pm) on PZT₄. The corresponding PZT amplitudes are obtained from the fits in Fig. 6, see Sec. 4.2, via the fitting parameter d . Both modulation frequencies are smaller than the linewidth of the FP cavity. We can easily modify the modulation strength by changing the voltage applied to the PZT₄. We summarize all important parameters in Table 1.

3.3. Balanced homodyne detection

The detection stage is the third subsystem of our setup, depicted in the bottom left corner of Fig. 4. In this stage we measure the phase and amplitude quadratures of the signal field. We use a balanced HD where the signal is interfered with the s-polarized LO. The detector has a low-noise AC output to access the signal's fluctuations. The detector's DC output is used to lock the detection angle. The relative phase information between LO and signal is encoded in the beat signal. The DC slope can be taken as error signal to lock the detection angle on phase quadrature. For an amplitude quadrature readout, we need to stabilize at an interference maximum. Therefore, we demodulate the signal at 73 kHz and low-pass filter it to obtain the corresponding error signal. In both cases, the error signal is applied to PZT₅. In the next section we present measurements of the signal's phase and the amplitude quadratures.

4. Results

In this section, we present, characterize and discuss our measurements. First, we quantify the performance of our non-classical light source after integration into the setup, behind the FP cavity. Second, we detect two different cavity length modulation signals. Finally, we discuss our approach and give a brief outlook.

4.1. Squeezing performance behind the FP cavity

We measured the noise spectrum of our amplitude quadrature squeezed state in transmission of the FP cavity with an unmodulated probe field (EOM₁ turned off in Fig. 4). For a full characterization, we measured squeezing (sqz) in the amplitude quadrature (blue trace) and anti-squeezing in the phase quadrature (red trace) in Fig. 5. The measurements are normalized to the shot noise which is measured classically when the pump of the OPO is turned off. Thus, the 0 dB level corresponds to the quantum shot noise limit. All presented measurements in this section are taken with a Keysight N9020a MXA signal analyzer.

Table 2. Fitting parameters plugged in Eq. (22) for creating the fits in Fig. 5.

Parameter	Value
R_1	90 %
R_2	99.99 %
FSR _{opo}	199.66 MHz
χ	7.39 MHz
R	99.69 %
FSR _{fp}	199.733 MHz
\bar{A}_{mod}	0
η	86 %
ϕ	38 mrad

On cavity resonance, we detected 6.7 dB squeezing and 14.7 dB anti-squeezing after subtracting the electronic DN, which is approximately 14.2 dB below the shot noise. For comparison, without the FP cavity 8.2 dB of squeezing and 15.1 dB of anti-squeezing were measured. This vertical

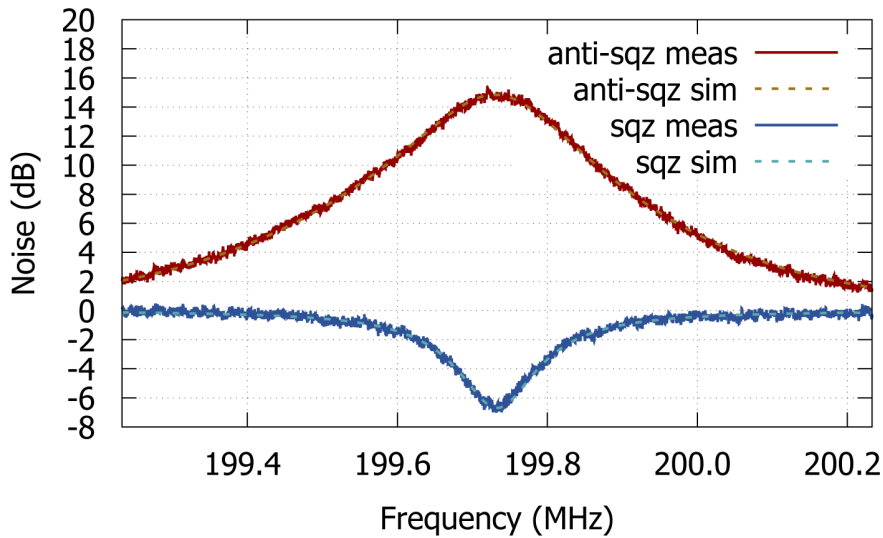


Fig. 5. Spectrum of the amplitude quadrature squeezed state behind the FP cavity. The simulation was obtained with Eq. (22). For the measurement, the detection angle is locked onto amplitude quadrature to observe squeezing and onto phase quadrature to see anti-squeezing. The spectrum was taken around the center frequency of 199.733 MHz which is equal to the FSR of the FP cavity, see Table 2. The dark noise (DN) of the HD was subtracted from the raw data. Further, it was normalized to the shot noise level, which was 14.2 dB above the dark noise (DN). Span 1 MHz, resolution bandwidth (RBW) 5.1 kHz, video bandwidth (VBW) 20 Hz, avg 10. For comparison, without the FP cavity 8.2 dB of squeezing and 15.1 dB of anti-squeezing with a phase noise of 30 mrad were measured.

asymmetry depends on the amount of optical loss and phase noise [17,40] and can be explained by Eq. (22). The FSRs of the OPO and the FP cavity were not perfectly matched and differed by 73 kHz (see Table 1), which corresponds to an optical round-trip length difference of 55 μm . Notwithstanding, the maximal squeezing degradation due to this mismatch is only 0.01 dB.

Our measured data agrees well with our theoretical model from Eq. (22), fitted by the dashed traces in Fig. 5. Table 2 gives an overview of the fitting parameters. The most relevant parameters to characterize the performance are the total efficiency $\eta = 86\%$ and the root mean square phase noise $\phi = 38\text{mrad}$. For comparison, without the FP cavity 30 mrad of phase noise was measured. In further measurements we determined the composition of η . The escape efficiency of our OPO was $\eta_{\text{esc}} = 97 \pm 1\%$. The total propagation efficiency including all optics and FP cavity was $\eta_{\text{prop}} = 94 \pm 1\%$. The efficiency of the detection process is determined by the homodyne visibility $\eta_{\text{vis}} = 98.5 \pm 0.5\%$. Thus the quantum efficiency $\eta_{\text{qe}} = 96 \pm 1\%$ of the HD was obtained as in [17], by using $\eta = \eta_{\text{esc}}\eta_{\text{prop}}\eta_{\text{vis}}\eta_{\text{qe}}$.

The linewidths of squeezing and anti-squeezing become unequal behind the FP cavity, see again Fig. 5. This linewidth asymmetry can be explained by the smaller linewidth of the FP cavity compared to the OPO. Frequency contributions outside of the linewidth of the FP cavity experience a significantly higher loss which degrades the squeezing far more than the anti-squeezing, see Eq. (22). To our knowledge, this created asymmetry has not been shown in previous publications.

4.2. Measuring a cavity length modulation

We turned on the PM applied on EOM₁ to acquire the length modulation signals of the FP cavity at the first FSR. As before, we generate an amplitude quadrature squeezed state, but additionally it is phase modulated at 199.733 MHz. The frequency is tuned to match the FSR of the FP cavity. We first demonstrate the general feasibility of our method by injecting a kHz cavity length modulation. Since external noise often increases with decreasing frequency, we secondly push the experiment to the LF limit. In each case we compare our results with the classical (class) case which corresponds to shot noise, when the pump of the OPO is turned off.

First, we apply a cavity length modulation at 20 kHz with an amplitude of 9.8 pm and measure the output variances plotted in Fig. 6(a)). We see two peaks in a frequency distance of 20 kHz to the EOM peak corresponding to the length modulation. The peaks maxima are located 2.9 dB below shot noise in the 5.7 dB squeezed noise floor. Again, the turquoise dashed trace was plotted with Eq. (22) and agrees well with the measured data. For comparison, we repeated the measurement for the classical case when the OPO's pump is blocked. This measurement is shown in red in Fig. 6. Here, we effectively cannot reveal the cavity length modulation. Our simulation (dashed orange trace) predicts a peak size of 0.08 dB above shot noise which would require significantly more averaging to resolve experimentally. In conclusion we see an effective SNR improvement of 5.7 dB. The parameters needed for the simulation can be found in Table 3. To plot the Dirac delta-like function from Eq. (22), we used a normalized Gaussian distribution, with

$$\tilde{\delta}_\omega = \tilde{\delta}(\omega) = \exp\left(-\frac{\omega^2}{2\sigma^2}\right) \quad \text{and} \quad \sigma = \text{RBW}. \quad (23)$$

Table 3. Parameters plugged in Eq. (22) for creating the fits in Fig. 6. Missing parameters are identical to Table 2.

Parameter	a)	b)
ω_s	20 kHz	100 Hz
Ω	199.733 MHz	
\bar{A}_{mod}	$3.3 \times 10^6 \sqrt{\text{Hz}}$	
β	3.3×10^{-5}	9.1×10^{-5}
d	5.8×10^{-5}	1.5×10^{-4}
ϕ	49 mrad	51 mrad

Finally, we demonstrate that our method can even resolve sub-kHz signals, that are presumably more affected by LF external noise. We have chosen a cavity length modulation of 100 Hz with an amplitude of 25.4 pm. The measured spectrum can be found in Fig. 6(b). We get similar results as in a): the two peaks originating from the length modulation have a maximum of 2.8 dB below shot noise in a 6.0 dB squeezed noise floor. Thereby, we improved the signal to noise ratio by 6.0 dB at this frequency compared to the classical case, where the length modulation cannot be effectively resolved. Again, the experimental data can be well fitted with our derived theory, shown by the dashed traces.

For the given set of seed power and modulation index of the EOM, we could resolve displacement signals with an amplitude down to 4 pm at 20 kHz and 14 pm at 100 Hz with signals 1 dB larger than the squeezed noise floor.

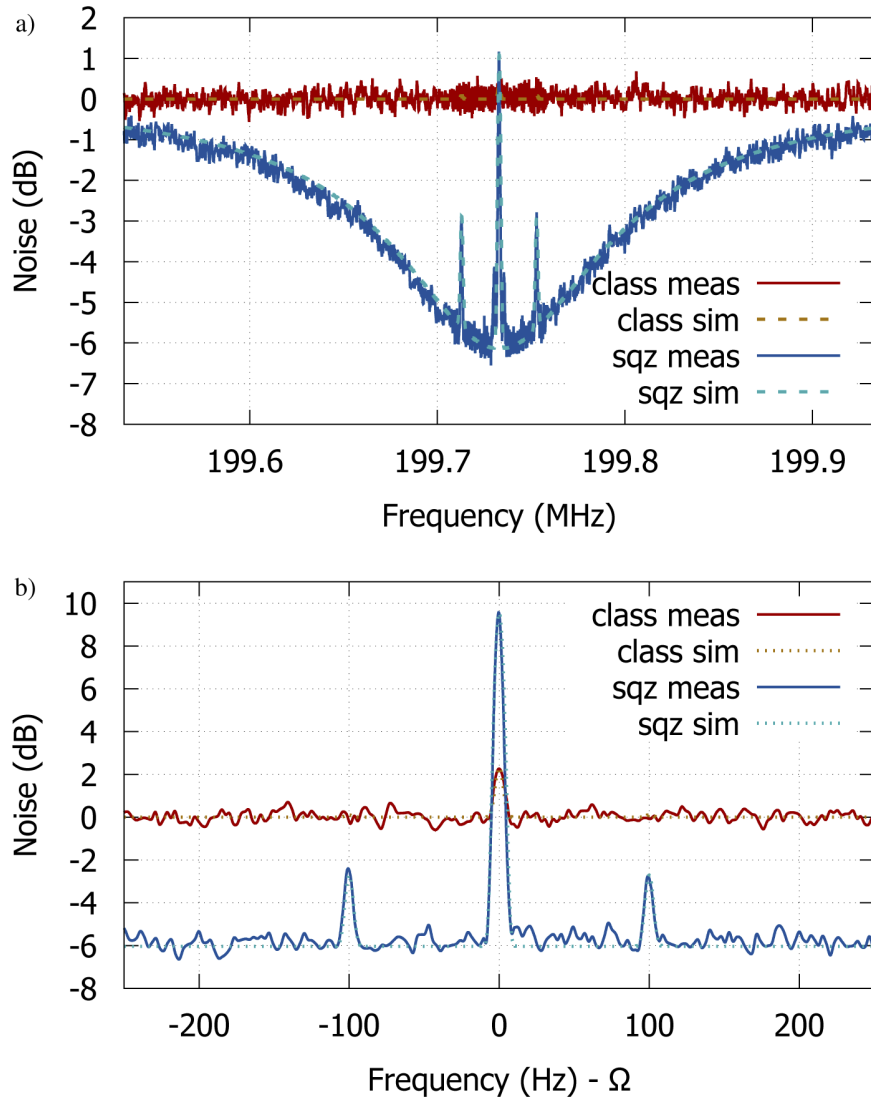


Fig. 6. Resolved cavity length modulation signals applied at a) 20 kHz and b) 100 Hz in the squeezed noise floor. The center frequency corresponds to $\Omega = 199.733$ MHz. The peaks located at this frequency are related to the PM sideband of the EOM and mainly originate from phase quadrature to amplitude quadrature coupling via phase noise, see Eq. (22). For the squeezed case, the peaks are enhanced compared to the classical case since the phase quadrature is amplified due to anti-squeezing. In a), the peaks at a distance of 2.6 kHz to the center peak originate from a FP cavity resonance. Parameters of the signal analyzer: a) two distinct measurements: span 400 kHz: RBW 1 kHz, VBW 10 Hz, avg 50; span 50 kHz: RBW 5.1 kHz, VBW 20 Hz, avg 10 (DN and SN avg 50), b) span 500 Hz: RBW 5.1 Hz, VBW 1 Hz, avg 300.

5. Discussion

We have demonstrated that our method is capable of resolving tiny signals otherwise masked by quantum shot noise, by using HF squeezed light and sophisticated modulation techniques. In comparison to previous spectroscopic experiments in literature employing base-band squeezed light [28–30], we have significantly improved the squeezing level while sending our probe beam through an optical resonator.

In contrast to base-band experiments, we need significantly less effort locking the squeezing angle. Even though it is possible to control the squeezing angle using a noise dither technique without a carrier [23,41], more stable locks can be achieved using bright optical fields that co-propagate with the squeezed vacuum [42,43]. However, for base-band measurements these fields need to be frequency shifted [24] to avoid excess noise caused by the LF laser noise. In our case of measuring at HFs, we can avoid this effort and use our seed field to control the squeezing angle.

Our experiment is sensitive to some types of noise and immune to others. It is not immune to any disturbances that act as phase or amplitude noise coupling into our laser field, similar to [30]. These disturbances cannot be differentiated from the cavity modulation signal we want to detect. This kind of noise might be caused by e.g. temperature fluctuations or vibrations that are affecting the stability of the laser resonator or optical components. These sources have in common that they will also appear around the EOM sideband at HF, since they all experience the modulation process. Contrariwise, any noise sources coupling into the measurement that do *not* add coherently on our laser field, are circumvented because they do not occur on the EOM sideband at HF. Those noise sources are predominantly at LFs. Examples for these kind of noises are electric or post processing noise, incoherent stray light like ambient light or infrared thermal radiation.

Our demonstrated approach has a number of advantages. Technical laser noise typically occurs at frequency ranges from Hz to 100 kHz and drops off for higher frequencies (\sim MHz). Therefore our LO does not exhibit technical noise around 200 MHz and is thus shot noise limited. Imperfections like a non-ideal common-mode rejection at the HD will have a much lower impact than at LF, where technical noise is present. Since our high-frequency squeezer is built in a bow-tie topology, back-scattered light is significantly suppressed in comparison to linear squeezers [44]. Furthermore, in our case of perfect frequency matching ($\text{FSR}_{\text{fp}} = \Omega$) all PM sidebands are transmitted by the cavity symmetrically in frequency. Therefore all sidebands experience frequency noise identically, such that frequency-to-amplitude noise coupling in the cavity is strongly suppressed. This feature is often referred to as *laser frequency noise immunity* [45] and is used e.g. in NICE-OHMS [32].

Our technique is not fundamentally limited to the detection of preferably LF signals. However, to resolve the cavity length modulation sidebands with high precision, two technical requirements need to be fulfilled: The spectrum analyzer needs a sufficiently high resolution, and the EOM must produce sufficient narrowband and stable sidebands. We used a network analyzer [Keysight E5061B] to generate the signal at 199.733 MHz. The generated signal has a measured bandwidth of <1 Hz, which is limited by the RBW of our spectrum analyzer. For further improvement towards measurements at lower cavity length modulation frequencies a better RBW is hence required.

5.1. Outlook

With our approach we have demonstrated the detection of small sub-shot-noise phase signals. In order to measure amplitude signals, merely the detection angle at the HD needs to be adjusted for readout of the orthogonal quadrature. For an improved common-mode rejection of phase fluctuations on LO and probe beam the two beams have to co-propagate in the FP cavity. This will lead to a significant reduction of phase noise imprinted by the FP cavity on the probe beam. To

achieve this, the LO has to be orthogonally polarized to the probe beam. The common-mode phase fluctuations do not affect our final measurement in transmission, where the probe's amplitude quadrature can be measured with a polarization based HD scheme [46].

As discussed before, our approach is still sensitive to technical noise sources that couple into our probe beam. We therefore propose to implement the spectroscopic FP cavity in one arm of a Michelson interferometer. A HF phase modulated field similar to our seed is coupled into the interferometer's input port. The HF squeezed field is sent into the interferometer's output port. For a specific interferometer design, the LF cavity length modulation sidebands will exit the interferometer at HF in the squeezed noise floor and will interfere with a coherent field at DC. This technique is similar to a gravitational wave detector operated with DC readout [47]. To reduce technical noise on the probe beam this is a promising approach which deserves further investigation.

6. Conclusion

We have presented a new method to significantly improve the signal-to-shot-noise level in high-precision spectroscopic measurements without increasing the laser power. Our approach circumvents technical noise sources such as low-frequency detection noise by applying a high-frequency PM. Additionally, the shot noise of the probe beam is squeezed by a sub-threshold OPO. With this prepared phase modulated, amplitude quadrature squeezed probe, we demonstrated a sub-shot-noise limited detection of small spectroscopic phase signals. In our experiment, we were able to resolve tiny cavity length modulations at 20 kHz (100 Hz) on a squeezed noise floor of 5.7 dB (6.0 dB). The derived theory confirms the measurements very well.

Our approach is interesting for spectroscopic applications, e.g. for FMS [33]. Experiments where the probe under investigation (e.g. a gas) may set a certain laser power limit can also benefit from our technique, since it allows to increase the SNR without the need for higher laser power.

Funding. Deutsche Forschungsgemeinschaft (Excellence PhoenixD (EXC 2122, Project ID 390833453), Excellence QuantumFrontiers (EXC 2123, Project ID 390837967)).

Acknowledgments. The authors wish to thank Charles Harb for productive discussions.

Disclosures. The authors declare no conflicts of interest.

References

1. B. P. T. D. e. a. Abbott, "Observation of Gravitational Waves from a Binary Black Hole Merger," *Phys. Rev. Lett.* **116**(6), 061102 (2016).
2. G. C. Bjorklund, "Frequency-modulation spectroscopy: a new method for measuring weak absorptions and dispersions," *Opt. Lett.* **5**(1), 15–17 (1980).
3. J. J. Scherer, D. Voelkel, D. J. Rakestraw, J. B. Paul, C. P. Collier, R. J. Saykally, and A. O'Keefe, "Infrared cavity ringdown laser absorption spectroscopy (IR-CRLAS)," *Chem. Phys. Lett.* **245**(2-3), 273–280 (1995).
4. P. Kwee, B. Willke, and K. Danzmann, "Shot-noise-limited laser power stabilization with a high-power photodiode array," *Opt. Lett.* **34**(19), 2912–2914 (2009).
5. J. Junker, P. Oppermann, and B. Willke, "Shot-noise-limited laser power stabilization for the AEI 10m Prototype interferometer," *Opt. Lett.* **42**(4), 755 (2017).
6. H. Vahlbruch, D. Wilken, M. Mehmet, and B. Willke, "Laser power stabilization beyond the shot noise limit using squeezed light," *Phys. Rev. Lett.* **121**(17), 173601 (2018).
7. C. Gardiner and P. Zoller, *Quantum Noise - A Handbook of Markovian and Non-Markovian Quantum Stochastic Methods with Applications to Quantum Optics* (Springer Science & Business Media, Berlin Heidelberg, 2004).
8. M. L. Denton, M. S. Foltz, L. E. Estlack, D. J. Stolarski, G. D. Noojin, R. J. Thomas, D. Eikum, and B. A. Rockwell, "Damage thresholds for exposure to NIR and blue lasers in an in vitro RPE cell system," *Invest. Ophthalmol. Visual Sci.* **47**(7), 3065–3073 (2006).
9. C. A. Casacio, L. S. Madsen, A. Terrasson, M. Waleed, K. Barnscheidt, B. Hage, M. A. Taylor, and W. P. Bowen, "Quantum correlations overcome the photodamage limits of light microscopy," arXiv:2004.00178 [physics.optics], <https://arxiv.org/abs/2004.00178> (2020).
10. R. A. e. a. J. Abadie and B. P. Abbott, "Predictions for the rates of compact binary coalescences observable by ground-based gravitational-wave detectors," *Classical Quantum Gravity* **27**(17), 173001 (2010).

11. H.-A. Bachor and T. C. Ralph, *A Guide to Experiments in Quantum Optics* (Wiley, New York, 2004).
12. U. L. Andersen, T. Gehring, C. Marquardt, and G. Leuchs, "30 years of squeezed light generation," *Phys. Scr.* **91**(5), 053001 (2016).
13. J. Lough, E. Schreiber, F. Bergamin, H. Grote, M. Mehmet, H. Vahlbruch, C. Affeldt, M. Brinkmann, A. Bisht, V. Kringsel, H. Luck, N. Mukund, S. Nadji, B. Sorazu, K. Strain, M. Weinert, and K. Danzmann, "First demonstration of 6 db quantum noise reduction in a kilometer scale gravitational wave observatory," arXiv:2005.10292 [physics.ins-det], <https://arxiv.org/abs/2005.10292> (2020).
14. A. L. e. a. Acernese F. and M. Agathos, "Increasing the astrophysical reach of the advanced virgo detector via the application of squeezed vacuum states of light," *Phys. Rev. Lett.* **123**(23), 231108 (2019).
15. K. N. e. a. Tse M. and Yu Haocun, "Quantum-enhanced advanced ligo detectors in the era of gravitational-wave astronomy," *Phys. Rev. Lett.* **123**(23), 231107 (2019).
16. R. E. Slusher, L. W. Hollberg, B. Yurke, J. C. Mertz, and J. F. Valley, "Observation of squeezed states generated by four-wave mixing in an optical cavity," *Phys. Rev. Lett.* **55**(22), 2409–2412 (1985).
17. H. Vahlbruch, M. Mehmet, K. Danzmann, and R. Schnabel, "Detection of 15 db squeezed states of light and their application for the absolute calibration of photoelectric quantum efficiency," *Phys. Rev. Lett.* **117**(11), 110801 (2016).
18. N. C. Menicucci, P. van Loock, M. Gu, C. Weedbrook, T. C. Ralph, and M. A. Nielsen, "Universal quantum computation with continuous-variable cluster states," *Phys. Rev. Lett.* **97**(11), 110501 (2006).
19. N. Treps, U. Andersen, B. Buchler, P. K. Lam, A. Maître, H.-A. Bachor, and C. Fabre, "Surpassing the standard quantum limit for optical imaging using nonclassical multimode light," *Phys. Rev. Lett.* **88**(20), 203601 (2002).
20. M. I. Kolobov and C. Fabre, "Quantum limits on optical resolution," *Phys. Rev. Lett.* **85**(18), 3789–3792 (2000).
21. S. L. Braunstein and H. J. Kimble, "Teleportation of continuous quantum variables," *Phys. Rev. Lett.* **80**(4), 869–872 (1998).
22. A. Furusawa, J. L. Sørensen, S. L. Braunstein, C. A. Fuchs, H. J. Kimble, and E. S. Polzik, "Unconditional quantum teleportation," *Science* **282**(5389), 706–709 (1998).
23. K. McKenzie, N. Grosse, W. P. Bowen, S. E. Whitcomb, M. B. Gray, D. E. McClelland, and P. K. Lam, "Squeezing in the audio gravitational-wave detection band," *Phys. Rev. Lett.* **93**(16), 161105 (2004).
24. H. Vahlbruch, S. Chelkowski, B. Hage, A. Franzen, K. Danzmann, and R. Schnabel, "Coherent control of vacuum squeezing in the gravitational-wave detection band," *Phys. Rev. Lett.* **97**(1), 011101 (2006).
25. A. E. Dunlop, E. H. Huntington, C. C. Harb, and T. C. Ralph, "Generation of a frequency comb of squeezing in an optical parametric oscillator," *Phys. Rev. A* **73**(1), 013817 (2006).
26. R. J. Senior, G. N. Milford, J. Janousek, A. E. Dunlop, K. Wagner, H.-A. Bachor, T. C. Ralph, E. H. Huntington, and C. C. Harb, "Observation of a comb of optical squeezing over many gigahertz of bandwidth," *Opt. Express* **15**(9), 5310 (2007).
27. M. Heurs, J. G. Webb, A. E. Dunlop, C. C. Harb, T. C. Ralph, and E. H. Huntington, "Multiplexed communication over a high-speed quantum channel," *Phys. Rev. A* **81**(3), 032325 (2010).
28. N. P. Georgiades, E. S. Polzik, K. Edamatsu, H. J. Kimble, and A. S. Parkins, "Nonclassical excitation for atoms in a squeezed vacuum," *Phys. Rev. Lett.* **75**(19), 3426–3429 (1995).
29. V. G. Lucivero, R. Jiménez-Martínez, J. Kong, and M. W. Mitchell, "Squeezed-light spin noise spectroscopy," *Phys. Rev. A* **93**(5), 053802 (2016).
30. E. S. Polzik, J. Carri, and H. J. Kimble, "Spectroscopy with squeezed light," *Phys. Rev. Lett.* **68**(20), 3020–3023 (1992).
31. R. B. de Andrade, H. Kerdoncuff, K. Berg-Sørensen, T. Gehring, M. Lassen, and U. L. Andersen, "Quantum-enhanced continuous-wave stimulated raman scattering spectroscopy," *Optica* **7**(5), 470–475 (2020).
32. J. Ye, L.-S. Ma, and J. L. Hall, "Ultrasensitive detections in atomic and molecular physics: demonstration in molecular overtone spectroscopy," *J. Opt. Soc. Am. B* **15**(1), 6 (1998).
33. B. Yurke and E. A. Whittaker, "Squeezed-state-enhanced frequency-modulation spectroscopy," *Opt. Lett.* **12**(4), 236–238 (1987).
34. S. S. Brown, H. Stark, and A. R. Ravishankara, "Cavity ring-down spectroscopy for atmospheric trace gas detection: Application to the nitrate radical (NO₃)," *Appl. Phys. B* **75**(2-3), 173–182 (2002).
35. B. A. Paldus, C. C. Harb, T. G. Spence, R. N. Zare, C. Gmachl, F. Capasso, D. L. Sivco, J. N. Baillargeon, A. L. Hutchinson, and A. Y. Cho, "Cavity ringdown spectroscopy using mid-infrared quantum-cascade lasers," *Opt. Lett.* **25**(9), 666 (2000).
36. M. J. Collett and C. W. Gardiner, "Squeezing of intracavity and traveling-wave light fields produced in parametric amplification," *Phys. Rev. A* **30**(3), 1386–1391 (1984).
37. R. J. Glauber, "The quantum theory of optical coherence," *Phys. Rev.* **130**(6), 2529–2539 (1963).
38. M. Mehmet, S. Ast, T. Eberle, S. Steinlechner, H. Vahlbruch, and R. Schnabel, "Squeezed light at 1550 nm with a quantum noise reduction of 12.3 db," *Opt. Express* **19**(25), 25763–25772 (2011).
39. R. W. P. Drever, J. L. Hall, F. V. Kowalski, J. Hough, G. M. Ford, A. J. Monley, and H. Ward, "Laser phase and frequency stabilization using an optical resonator," *Appl. Phys. B* **31**(2), 97–105 (1983).
40. Y. Takeno, M. Yukawa, H. Yonezawa, and A. Furusawa, "Observation of -9 dB quadrature squeezing with improvement of phase stability in homodyne measurement," *Opt. Express* **15**(7), 4321 (2007).
41. K. McKenzie, E. E. Mikhailov, K. Goda, P. K. Lam, N. Grosse, M. B. Gray, N. Mavalvala, and D. E. McClelland, "Quantum noise locking," *J. Opt. B: Quantum Semiclassical Opt.* **7**(10), S421–S428 (2005).

42. S. Chelkowski, H. Vahlbruch, B. Hage, A. Franzen, N. Lastzka, K. Danzmann, and R. Schnabel, "Experimental characterization of frequency-dependent squeezed light," *Phys. Rev. A* **71**(1), 013806 (2005).
43. R. Schnabel, W. Bowen, N. Treps, B. Buchler, T. Ralph, P. K. Lam, and H.-A. Bachor, "Optical experiments beyond the quantum limit: Squeezing, entanglement, and teleportation," *Opt. Spectrosc.* **94**(5), 651–665 (2003).
44. S. S. Y. Chua, M. S. Stefszky, C. M. Mow-Lowry, B. C. Buchler, S. Dwyer, D. A. Shaddock, P. K. Lam, and D. E. McClelland, "Backscatter tolerant squeezed light source for advanced gravitational-wave detectors," *Opt. Lett.* **36**(23), 4680–4682 (2011).
45. A. Foltynowicz, F. Schmidt, W. Ma, and O. Axner, "Noise-immune cavity-enhanced optical heterodyne molecular spectroscopy: Current status and future potential," *Appl. Phys. B* **92**(3), 313–326 (2008).
46. M. Heurs, I. R. Petersen, M. R. James, and E. H. Huntington, "Homodyne locking of a squeezer," *Opt. Lett.* **34**(16), 2465–2467 (2009).
47. S. Hild, H. Grote, J. Degallaix, S. Chelkowski, K. Danzmann, A. Freise, M. Hewitson, J. Hough, H. Luck, M. Prijatelj, K. A. Strain, J. R. Smith, and B. Willke, "DC-readout of a signal-recycled gravitational wave detector," *Classical Quantum Gravity* **26**(5), 055012 (2009).

3.3 Preparation of the required quantum state

For the method used in [P1], a phase-modulated and amplitude quadrature squeezed state is required. The experimental generation and characterisation of this particular quantum state is discussed in this section. Subsection 3.3.1 explains how the phase of the squeezed state is locked and modulated. Here, the focus is on the different electric fields required to ensure a stable operation. In [P1], the OPO was not characterised independently, and squeezing measurements were only shown behind the FP cavity. Therefore, Subsec. 3.3.2 is dedicated to investigating the squeezing performance of the OPO. A squeezing slope is presented that is well suited to get essential parameters characterising the OPO.

3.3.1 Phase-modulated amplitude quadrature squeezed state

We decided to modulate at a relatively large frequency of roughly 200 MHz so that the modulation sidebands are resonant in the OPO due to its free spectral range of also 200 MHz.¹¹ This subsection explains how the amplitude quadrature squeezed state is generated and how the phase modulation can be easily switched on/off by the function generator.

In the following, we distinguish between co- and counter-propagating travel direction in the OPO. The co-propagating mode is referred to the direction of generated squeezing. The counter-propagating mode is reversed and is thus ideally decoupled from the co-propagating mode.

The OPO, used for this experiment is described in Sec. 3.1 in [P1]¹² and in Sec. 2.4. It is locked on resonance for the fundamental field at 1064 nm. For the OPO length lock, a fundamental field is coupled through a high-reflective cavity mirror in counter-propagating direction (for simplicity not shown in Fig. 4 in [P1]). A piezoelectric transducer (PZT₂) is clamped between another high-reflective mirror and the cavity spacer. It is used to dither the mirror at 106 kHz to imprint a phase modulation on the locking field. Then, the locking field, leaking out at the input/output coupler, is measured on a photodetector. External demodulation with the dither frequency generates the error signal. It is applied on a proportional–integral–derivative (PID) controller, amplified and fed back to the PZT₂.

The squeezing angle must be locked to generate an amplitude quadrature squeezed state. We use a coherent field called *seed*, see Fig. 4 in [P1], which is coupled in the co-propagating direction through a high-reflective mirror into the OPO. Its amplitude is amplified or de-amplified, depending on its phase relation to the pump field.¹³ Thus, the power of the seed serves as an indicator of the actual squeezing angle. To actively control this angle, the phase of the seed is modulated with 73 kHz, by dithering PZT₁, as shown in Fig. 4 in [P1]. A fraction of 0.3 % of the seed's power is detected on the photodiode (PD₁) behind a partial-reflective mirror. Then, the detected signal is demodulated to generate an error signal which is sent back to PZT₃. If the loop is closed by a PID controller, an amplitude quadrature squeezed state is generated. After being reflected at the 99.7 % mirror in Fig. 4 in [P1], the seed is called *probe*.

¹¹Using smaller modulation frequencies at baseband (zeroth free spectral range) would also work in principle. However, then it would be beneficial to use shorter squeezers having linewidths in the order of 100 MHz as in [Vah+16].

¹²Note that for simplicity, the depicted OPO consists of four mirrors in Fig. 4 in [P1]. In reality, it consists of six mirrors as shown in 2.9a).

¹³A graphical presentation of how a fundamental input field is transformed in a OPO is given in [BWS13].

Now, the generated amplitude quadrature squeezed state must also be phase-modulated to be used for the spectroscopy experiment. Beneficially, the seed field already travels through the OPO to lock the squeezing angle. Hence, it can be used as a carrier field for the high-frequency phase modulation, which is applied before the seed couples into the OPO, as can be seen in Fig. 4 in [P1]. The modulation frequency of 199.733 MHz is switched on if it is needed for the spectroscopy. We switch it off to characterise the OPO independently. The characterisation of the squeezing generated by the OPO is covered in the next Subsec. 3.3.2.

3.3.2 Squeezing characterisation behind the OPO

The characterisation of the OPO was performed according to Subsec. 2.4.3. The intra-cavity loss was measured to be $\delta_x = 0.3\%$ as explained in Subsec. 2.1.2. This loss corresponds to a cavity escape efficiency of $\eta_{\text{esc}} = 97\%$. Knowing the escape efficiency and the reflectivity of the input coupler ($R_{\text{in}} = 90\%$), the linewidth of the unpumped OPO is determined to be $\delta\omega = 3.5\text{ MHz}$.¹⁴ The free spectral range of $\Delta\omega = 196.66\text{ MHz}$ is obtained from the frequency where maximum squeezing and anti-squeezing occur in a squeezing spectrum.¹⁵ It matches the expected free spectral range calculated from the optical path length according to the design dimensions of the OPO spacer.¹⁶

A homodyne detector measures the squeezing of the probe field from the OPO. It was set up directly after the squeezed beam is reflected from the 99.7% pick-off mirror (not shown in Fig. 4 in [P1]). Then, the propagation efficiency and the visibility efficiency were measured to $\eta_{\text{prop}} = 99.0\%$ and $\eta_{\text{vis}} = 98.5\%$.

Finally, a squeezing slope is measured. For this measurement, the squeezing angle is locked to generate an amplitude quadrature squeezed state. The phase modulation of the seed is switched off. Then, we can take a zero-span measurement at 199.66 MHz – the first free spectral range frequency of the OPO.¹⁷ The detection angle at the homodyne detector is continuously ramped to measure the maximal and minimal noise values in the signals quadrature. This procedure is done for different pump powers, as shown in Fig. 3.4. Squeezing is measured in the amplitude quadrature V^+ (blue) and anti-squeezing in the phase quadrature V^- (red). The maximal squeezing level of -8.6 dB was observed at 190 mW. The theoretical traces are created by fitting Eq. (2.96) to the measurement data, as explained in Subsec. 2.4.3. The fitting parameters are the pump threshold $P_{\text{th}} = 368\text{ mW}$, the total efficiency $\eta = 90.9\%$ and the phase noise $\Delta\phi = 30\text{ mrad}$. From the total loss η , we can infer the average quantum efficiency of the photodiodes, which is $\eta_{\text{qe}} = 96\%$.

A careful characterisation of the OPO and the generated squeezed state is important because it is injected into the FP cavity. With a previous characterisation, the influences of FP cavity on the squeezed state can be investigated and debugged. For instance, the increase in phase noise can be measured and attributed to the FP cavity. The following Sec. 3.4 focuses on our metrology experiment consisting of the FP cavity.

¹⁴In Table 1 in [P1], the value of 4.5 MHz is larger because it was obtained when the OPO was operated as second harmonic generation (SHG). Then the total cavity loss is larger due to frequency conversion, which is also expressed in the linewidth.

¹⁵The measurement of the squeezing spectrum behind the OPO is not shown here.

¹⁶The free spectral range can also be determined by observing destructively interfering modulation sidebands while ramping the cavity, see [Den16], Sec. 8.2.3.

¹⁷The measurement was taken with a spectrum analyser [Keysight, N9010B MXA].

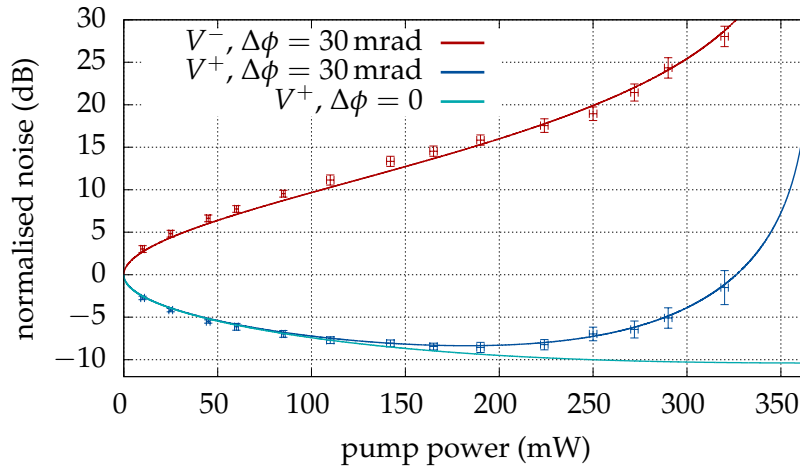


FIGURE 3.4: Squeezing and anti-squeezing generated by the OPO for different pump powers. The theoretical traces showing the squeezing slopes are created by using Eq. (2.96) with fitting parameters: $P_{\text{th}} = 368 \text{ mW}$, $\eta = 90.9\%$ and $\Delta\phi = 30 \text{ mrad}$. The maximal squeezing level of -8.6 dB was observed at 190 mW .

3.4 Fabry-Pérot cavity as spectroscopic device

This section discusses the design and the performance of the FP cavity. A former version of the FP cavity was already built in [Den16]. However, it turned out that this design exhibited several problems which needed to be tackled.

First, the new design of the FP cavity is presented in Subsec. 3.4.1. Then, Subsec. 3.4.2 gives a summary of the characterisation of the FP cavity. In particular, we attribute the amount of optical loss and phase noise that this system introduces. This section ends with Subsec. 3.4.3 where we discuss experimental problems that were faced while working with the FP cavity and the OPO.

3.4.1 Design of the Fabry-Pérot cavity

One important parameter is the optical length of the FP cavity. To use squeezing generated at the first free spectral range of the OPO, the FP cavity must be resonant at these frequencies. This is reached by choosing an equal free spectral range for the FP cavity as for the OPO.

An old design of the FP cavity for the spectroscopy experiment was already published in [Den16]. Since this design exhibited critical drawbacks, we decided to implement some modifications. Table 3.1 compares the relevant changes from the old to the new design. In the new design, we use a quasi-monolithic FP cavity consisting of an aluminium spacer,¹⁸ see Fig. 3.5. This increases the stability and decreases the susceptibility to air fluctuations in the beam path.

A crucial change is related to the quality of the mirrors. The two old mirrors¹⁹ exhibited a total optical loss of roughly 400 ppm, probably dominated by the scattering loss in the electron beam evaporation (EBE) coating (see Table 2.2). With the new mirrors,²⁰ the intra-cavity loss was reduced to 90 ppm. In a white light interferometer,

¹⁸The spacer is a $60 \text{ mm} \times 60 \text{ mm}$ profile [item Industrietechnik GmbH].

¹⁹These 99.5% reflective mirrors are from CVI Laser Optics with model type PR1-1064-99-1025-0.50CC.

²⁰These 99.69% reflective mirrors are from LASEROPTIK GmbH, with substrate type S-03975 and coating models B-08899 (AR) and B-00013-04 (PR).

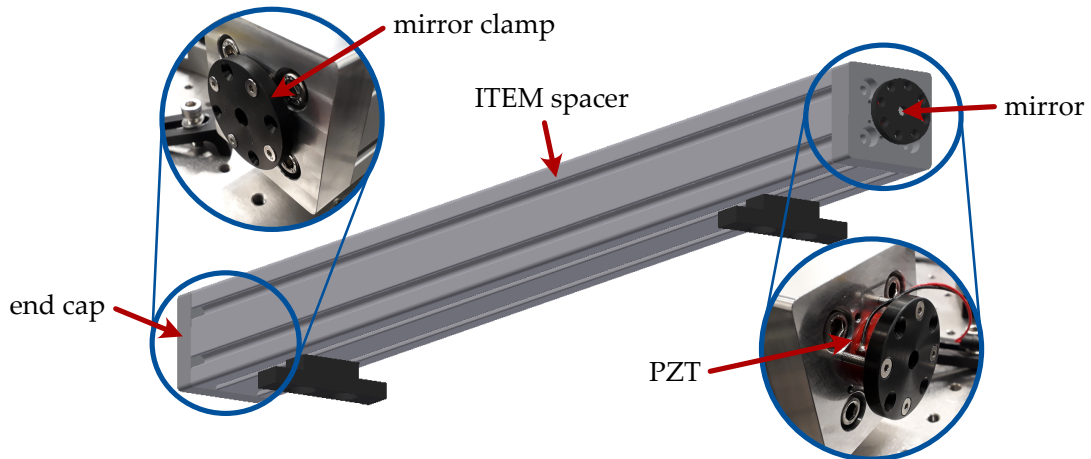


FIGURE 3.5: New design of the FP cavity. The mirrors are clamped with circular black clamps made of polyoxymethylene to the aluminium spacer.

the root mean square (RMS) roughness R_q was measured to be $R_q \approx 0.151 \text{ nm}$.²¹ Thus, according to Eq. (2.94), the scattering loss is expected to be in the order of 3 ppm per mirror. We assume that the limiting loss contribution comes most likely from insufficiently clean mirrors. However, the propagation efficiency increased from roughly $\eta_{\text{fp}} = 94\%$ to $\eta_{\text{fp}} = 97\%$.

Another important consideration is the higher-order mode suppression of the FP cavity which depends on the optical cavity length and the radius of curvature of the mirrors.²² For the old design, the round-trip Gouy phase of -119.8° led to a mode separation of 66.4 MHz. This mode separation is not optimal as it is approximately a third of the free spectral range of the FP cavity, meaning third-order modes are also partly resonant in the FP cavity. Due to the new cavity mirrors having radii of curvatures of 2000 mm, the mode separation reduces to 57 MHz, which significantly improves the effect of mode suppression in the FP cavity.

The free spectral range of the FP cavity must match with it from the OPO to ensure that no squeezing is lost. Hence, I accurately adjusted the optical cavity length of the FP cavity. Therefore, the length of the aluminium profile was measured with a coordinate measuring machine, and the two aluminium end caps were manufactured with a precision of $100 \mu\text{m}$ accordingly. Thus, the free spectral ranges of the two cavities distinguish only by roughly 73 kHz. The squeezing degradation because of this mismatch is expected to be 0.01 dB and thus negligible. Due to temperature drifts in the laboratory, the thermal expansion of the aluminium spacer causes a minimal change in the free spectral range. The effect of this change on the degradation in squeezing is even smaller and also negligible.²³

This subsection demonstrated the new design the FP cavity. The next subsection characterises the cavity, by investigating the squeezing performance behind it.

²¹The measurement was taken by LASEROPTIK GmbH.

²²See e.g. [KL66].

²³I estimated the change of free spectral range to be in the order of 19 kHz for temperature changes of 4°C at room temperature conditions according to the linear thermal expansion coefficient of aluminium [NM41].

TABLE 3.1: The main differences between the old FP design from [Den16] and the new FP cavity design.

	old design	new design
setup	free-space	quasi-monolithic
mirror coatings	EBE	IBS
intra-cavity loss	400 ppm	90 ppm
propagation efficiency η_{fp}	94 %	97 %
mirror power reflectivity	99.5 %	99.69 %
radius of curvature	500 mm	2000 mm
round-trip Gouy phase	-119.8°	102.7°
mode separation	66.4 MHz	57.0 MHz

3.4.2 Squeezing characterisation behind the Fabry-Pérot cavity

At the homodyne detector behind the FP cavity, the squeezed state has degraded due to optical loss, which has three main reasons. First, the squeezed state propagates along additional optical components as steering mirrors and two polarising beam splitters. This additional loss is included in the propagation efficiency $\eta_{\text{prop}} = 98\%$. Second, the FP cavity acts as a mode filter and transmits only the mode-matched content of the squeezed probe field. The effect of the mode-matching is represented by $\eta_{\text{mm}} = 99\%$. Third, the intra-cavity loss in the FP, investigated in Subsec. 3.4.1 leads to the efficiency $\eta_{\text{fp}} = 97\%$ for mode-matched light being transmitted through the FP cavity.

In analogy to Eq. (2.95), the total efficiency η is then

$$\eta = \eta_{\text{esc}}\eta_{\text{prop}}\eta_{\text{mm}}\eta_{\text{fp}}\eta_{\text{vis}}\eta_{\text{qe}}. \quad (3.11)$$

The visibility of the homodyne detection was measured as $\eta_{\text{vis}} = 98.5\%$. Assuming that the escape efficiency is the same $\eta_{\text{qe}} \approx 96\%$ as measured in Subsec. 3.3.2, we found the total efficiency to be $\eta = 86.3\%$, using Eq. (3.11). This is in agreement within the measurement uncertainties with the fitting parameter of $\eta = 86\%$ from Table 2 in [P1] used for the squeezing spectrum in Fig. 5 in [P1]. The total escape efficiency can be validated again by measuring a squeezing slope.

To measure the squeezing slope, first, the squeezing angle is locked so that an amplitude quadrature squeezed state is generated by the OPO. The high-frequency phase modulation of the seed is switched off, and the FP cavity is locked on resonance. The artificial spectroscopic signal is also turned off. Then, the detection angle is ramped by PZT₅ in Fig. 4 in [P1] to observe the noise in each readout quadrature. Now, the noise is measured at a zero-span at the free spectral range of the FP cavity, which is 199.733 MHz.

The measured squeezing slope can be seen in Fig. 3.6. Again, the blue trace shows squeezed and the red trace anti-squeezed noise. Now, the maximal squeezing of -6.8 dB was measured at 150 mW. The fit results in a total efficiency of $\eta = 86.6\%$. We see, that η is in the order as obtained from the fits shown Fig. 5 in [P1] or from the individual efficiencies from Eq. (3.11). Note, that the pump threshold has decreased from 368 mW in Fig. 3.4 to 297 mW in Fig. 3.6. This change can be explained by a better mode-matching of the green pump light into the OPO during the second measurement behind the FP cavity. Independent of the pump threshold change, we observe that the point of maximal squeezing has moved towards lower pump powers. This is explained by the increase of phase noise from 30 mrad to 40 mrad. A higher

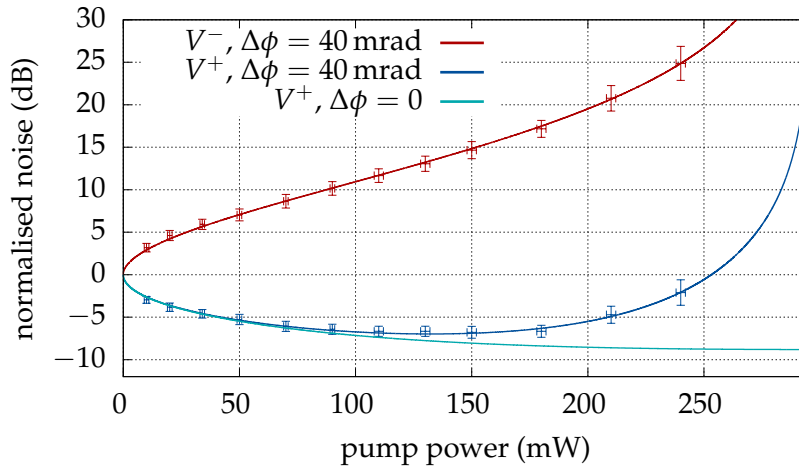


FIGURE 3.6: Squeezing and anti-squeezing of the state for different pump powers after being transmitted through the FP cavity. The theoretical traces show the squeezing slopes and are created by using Eq. (2.96) with fitting parameters: $P_{\text{th}} = 297$ mW, $\eta = 86.8\%$ and $\Delta\phi = 40$ mrad. The maximal squeezing of -6.8 dB was measured at 150 mW.

phase noise will cause the anti-squeezing to couple stronger into the squeezed noise measurement (visible in Eq. (2.96)). The larger the anti-squeezing, the more this effect is observable. Most likely the dominating reasons for the increased phase noise is due to a not perfectly stably locked OPO due to coupling between the cavities, as will be explicated in Subsec. 3.4.3.

When applying the intra-cavity length modulation, phase noise increases, as determined by our fits from Fig. 6 in [P1]. For the phase modulation at $\omega_{\text{sig}} = 20$ kHz the phase noise was $\Delta\phi = 49$ mrad and for $\omega_{\text{sig}} = 100$ Hz the phase noise was $\Delta\phi = 51$ mrad. An increase in phase noise is expected because the signal's intra-cavity phase modulation directly affects the detected detection angle.

3.4.3 Experimental challenges

This subsection is dedicated to polarisation couplings, an effect found to be critical for the spectroscopy experiment. The outcome of this study is that two perpendicular polarised light fields can not be treated as uncoupled in a realistic setup. Care has to be taken because all optical components might introduce polarisation-sensitive effects, creating polarisation coupling.

Often, the approach is to divide an experiment into individual subsystems and consider them separately. In the spectroscopy experiment, the OPO, the FP cavity and the detection scheme were first improved independently. However, it turned out that after the optimisation, the sequential combination of OPO and FP cavity involved serious coupling problems.

An overview of the situation between the three involved and competing laser fields is shown in Fig. 3.7. The figure shows the OPO on the left side and the FP cavity on the right side. Beams depicted by a solid line are s-polarised and dashed lines present p-polarised light fields. Apart from the pump field, three different laser beams are involved.

First, the orange beam presents the counter-propagating lock field used to lock the length of the OPO. It is detected on PD_1 to generate the Pound-Drever-Hall (PDH) error signal.

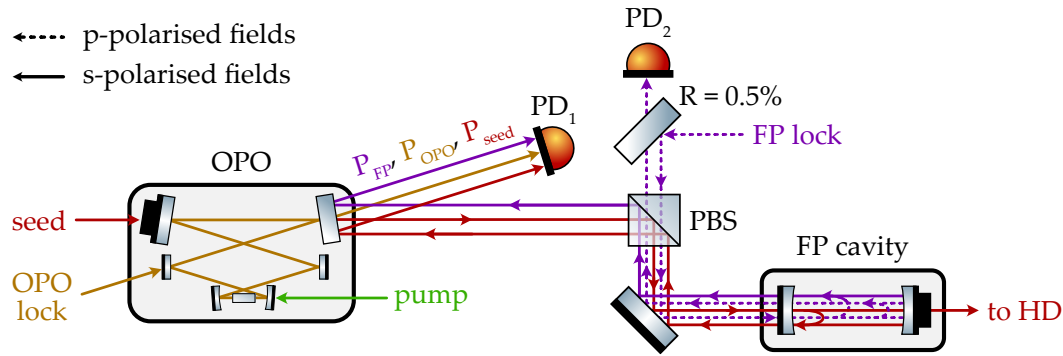


FIGURE 3.7: Experimental setup showing the dominating coupling effects between the OPO and the FP cavity. On PD_1 , not only the locking field (orange) is detected, generating the error signal for the OPO. In addition, the competing fields of the seed (red) and the FP locking field (purple) are interfering on PD_1 and distract the OPO lock. The FP locking field only appears on PD_1 because its polarisation is slightly rotated in the FP cavity, and its reflection has s-polarisation contributions reflected at the polarising beam splitter (PBS).

Second, the s-polarised seed²⁴ field shown in red is transmitted by the resonant OPO and sent to the FP cavity. Here, two situations can be distinguished. If the FP cavity is off-resonant, nearly all the light power is back-reflected into the counter-propagating mode of the OPO and beats with the OPO locking field on the PD_1 . Hence, a stable OPO lock is not possible anymore for that case. Otherwise, if the FP cavity is resonant, the seed will be transmitted to a large extent. Small residual reflections will still occur due to impedance mismatches of the cavity and will beat with the locking field in the same optical mode on PD_1 .

The third laser field is a p-polarised field used to lock the FP cavity (FP lock, purple beam). It is reflected on the FP cavity and detected on PD_2 . The detected signal is used to lock the FP cavity on resonance by applying the PDH technique. Nevertheless, we found that the FP cavity slightly rotates the polarisation of the intra-cavity locking field from p- to s-polarisation (purple dashed to solid line). Hence, a fraction of the locking field leaking out at the input mirror is reflected at the polarising beam splitter (PBS) and also beats on PD_1 with the two other fields. But why does the cavity rotate the polarisation?

We found that the effect of the polarisation rotation inside the FP cavity depends on how the mirrors are clamped onto the spacer. While screwing the clamp, the mirrors sit at the bottom of the clamps due to gravity. This procedure presumably applies asymmetric force to the mirror. The more the mirror is pressed, the stronger the effect of the polarisation rotation becomes. Therefore, we assume that induced stress causes the mirror to become birefringent.²⁵ To reduce this photoelastic problem, the two cavity mirrors are carefully clamped onto the spacer in a vertical orientation to distribute the load onto the clamp more evenly.

The influence of distracting fields beating with the seed on PD_1 should be minimised. Only then stable locks of the FP cavity *and* the OPO is possible. After the *couplings from technical imperfections*²⁶ had been minimised, we fine-tuned the coupling

²⁴Even though the seed transmitted through the FP cavity is called *probe*, only *seed* is used here.

²⁵Stress-induced birefringence has been already investigated in the context of gravitational wave detection. For more information, see, e.g. [Kr15; Web18].

²⁶Here, I mean coupling origins because of impedance mismatch of the FP cavity, polarisation rotation in the FP cavity or misalignments of polarisation bases.

magnitudes, namely the optical powers of the three beams. For the following consideration, all power values are rough measurements, and the exact values do not have a special meaning. However, these values should be understood more qualitatively in their order of magnitude. The power of the locking field was $P_{\text{OPO lock}} = 12 \mu\text{W}$ on PD₁. This is the benchmark for the competing powers of FP locking field $P_{\text{FP lock}}$ and the seed P_{seed} , seen in Fig. 3.7.

Looking at the role of the seed, its power reaching PD₁ was $P_{\text{seed}} = 4 \mu\text{W}$ for an off-resonant FP cavity.²⁷ Then, $P_{\text{OPO lock}} \approx P_{\text{seed}}$ and a stable lock of the OPO is not possible. However, when the FP cavity is resonant, the reflected seed is reduced and the power on PD₁ drops down to $P_{\text{seed}} = 4 \text{nW}$.

Next, we analyse the behaviour of the field locking the FP cavity. Due to the $R = 0.5\%$ mirror, a power of only $6 \mu\text{W}$ impinges on the FP cavity. Off-resonance, PD₁ detects $P_{\text{FP lock}} = 0.2 \text{nW}$ which originates from non-ideal polarisation optics. On resonance, this value increases to $P_{\text{FP lock}} = 4 \text{nW}$, which is potentially caused by the residual photoelastic polarisation rotation explained before. This power is only 4nW and scales with the reflectivity R of the partially reflective mirror in the path of FP locking field.²⁸ The value of $R = 0.5\%$ was used to reach a low $P_{\text{FP lock}}$.

Finally, the adjusted powers accomplished that $P_{\text{OPO lock}} \approx 3000 \times P_{\text{seed}}$ and $P_{\text{OPO lock}} \approx 3000 \times P_{\text{FP lock}}$ for a resonant FP cavity. Thus, a more stable lock of the OPO is ensured. However, we know that the beating effect of competing light fields is not fully suppressed. We assume this effect is a major contribution to our detected phase noise $\Delta\phi$.

3.5 Discussion and conclusion

In any high-precision measurement, defining the signal of interest is essential. In our approach, the signal is a tiny cavity length modulation at low frequencies (100 Hz and 20 kHz) applied in an optical FP cavity. This artificial signal is imprinted as a phase modulation on the intra-cavity probe field. We have studied that the signal can be resolved with the help of another phase modulation at high frequencies (200 MHz). It might be unintuitive, but the cavity length modulation can then be detected in the amplitude quadrature of the probe field. Frequency up-shifting the signal of interest is useful when the sensitivity is limited by low-frequency additive technical noise originating, e.g. from the detection electronics. Then this type of noise is circumvented; however, the sensitivity might still be limited by photon shot noise.

The effect of photon shot noise in a spectroscopic experiment can usually be decreased by increasing the laser power. However, some experiments work with small laser powers due to technical reasons such as damage thresholds of the probes. Here, the second feature of our tailored quantum probe field helps out. It is not only phase-modulated, but also an amplitude quadrature squeezed state. Then, the quantum noise is reduced, and since the cavity length modulation appears in the amplitude quadrature, the SNR is improved.

The OPO is seeded with a phase-modulated field, whose sidebands are resonant in the first free spectral range at 200 MHz. One experimental challenge is to precisely match the free spectral range of the FP cavity and OPO. Furthermore, a well-characterised experiment is preferable. We found that the total efficiency of the generated and detected squeezing coming from the OPO is $\eta = 90.9\%$ with an RMS

²⁷Here, for simplicity no pump is used and thus the gain is zero. The initial powers are as in Fig. 4 in [P1].

²⁸The PDH error signal used for the FP cavity lock is independent of the mirror reflectivity R .

phase noise of $\Delta\phi = 30$ mrad. When the squeezed state is transmitted through the FP cavity before the detection, the total escape efficiency drops by roughly 4% to $\eta = 86.6\%$. This degradation is caused by loss in the FP cavity and due to additional lossy optical components. In addition, the phase noise increases to 40 mrad, which might originate from the cross-talk between the two cavities. The cross-talk is caused by non-ideal optics, i.e. the polarising beam splitter and the FP cavity mirrors. The consequence is that the locking field used to stabilise the OPO needs to compete with distracting fields, provoking a slightly more unstable OPO lock. However, when the artificial signals are injected into the FP cavity, the phase noise increases anyway to roughly 50 mrad.

Finally, our measurements resolve small cavity length modulations on a squeezed noise floor of around 6 dB. The measurements are well confirmed by the theory presented in Sec. 2 in [P1]. In the following, I want to comment on a few points that were not addressed in the publication.

Our approach is particularly useful when the laser power cannot be increased arbitrarily. The signal from the cavity length modulation scales with the size of the high-frequency modulation sidebands at $\Omega = \pm 199.733$ MHz. Thus, the carrier field is not directly involved in detecting the signal at high-frequencies. It would be beneficial to prepare the probe field to contain only the phase modulation sidebands, not the carrier, which would also decrease the interacting laser power. A good solution would be to filter out the carrier of the phase-modulated seed, e.g. by a filter cavity before the seed is sent into the OPO. Another option could be the use of a frequency-shifted laser field.

Another remark also points to the direction of the laser power used. In [P1], we compared the case when the amplitude quadrature squeezed state is used and when a classical state is applied to sense the cavity length modulation. For both cases, the same parameters for the high-frequency phase modulation \bar{A}_{mod} and β were used (see Table 3 in [P1]). Importantly, this does not mean that the total power in the modulation sidebands is the same after the OPO, as can be seen in Eq. (21) in [P1]. For a pump phase adjusted to produce amplitude quadrature squeezing, the effective phase modulation of the seed will increase due to amplification. A fairer comparison has to use equal powers in the phase modulation sidebands at Ω . In principle, this could be investigated by measuring the height of the phase modulation sidebands visible in the phase quadrature (not shown in Fig. 6 in [P1]). However, this effect is only small and does not change anything about the usability and applicability of our approach.

Squeezing was already used to improve spectroscopic measurements at base-band frequencies [PCK92; Geo+95; Luc+16]. Recently, a quantum enhancement of the SNR of 3.6 dB relative to the shot noise limited SNR was demonstrated in stimulated Raman spectroscopy [And+20]. However, in our publication, we came up with a new approach. The combination of squeezing and modulation techniques at high frequencies has the potential to improve sensitivities in cavity spectroscopy.

Chapter 4

Detuning a squeezer to generate frequency-dependent squeezing

Squeezing can be applied to experiments dealing with opto-mechanical force measurements to increase their sensitivities. These kinds of experiments are limited by two types of noise depending on the measurement frequency. Photon shot noise arises in the phase quadrature and dominates at higher frequencies. Quantum-back action noise reveals in the amplitude quadrature and shows up at lower frequencies.¹ A *conventional*² squeezed state generated by an optical parametric oscillator (OPO) can only tackle either shot noise or quantum back-action noise, depending on its squeezing angle.

The straightforward solution seems to be a particularly tailored state with an optimised squeezing angle at each measurement frequency [Kim+01]. This state is called a frequency-dependent squeezed state and can reduce the quantum noise over a broad frequency band in opto-mechanical force measurements.

The most popular approach to generate frequency-dependent squeezing is to use conventional squeezing and reflect it from detuned filter cavities. The correlated quantum sidebands experience asymmetric phase responses when reflecting on a cavity. The result is that the reflected quantum state has a frequency-dependent squeezing angle.

In this chapter, a new way of generating frequency-dependent squeezing is presented. The chapter introduces the standard quantum limit of interferometry and shows how it is surpassed with frequency-dependent squeezed states in Sec. 4.1. The quantum sideband picture is used, showing the correlated quantum noise sidebands, to gain a better understanding of frequency-dependent squeezing. Next, Sec. 4.2 reprints the publication [P2] about the detuned squeezer. Section 4.3 gives an overview of quantum tomography since this is not covered in detail in [P2]. The following two Secs. 4.4 and 4.5 give more details and characterisations on the resonant and the detuned squeezer. Additional explanations and measurements support the concept of the detuned squeezer. Finally, this chapter ends with a discussion and conclusion in the last Sec. 4.6.

4.1 Introduction

This section introduces the problem of quantum noise in opto-mechanical force measurements. It starts with a description of the standard quantum limit of interferometry (SQL) in Subsec. 4.1.1. Squeezed states of light can be injected to beat the SQL. Moreover, a sophisticated, frequency-dependent squeezed state turns out to be

¹The *lower* and *higher* frequency regime will be determined in Subsec. 4.1.1.

²Or *frequency-independent*.

a better choice leading to a broad-band sensitivity improvement. In particular, this concept is applied to a gravitational wave detector. An intuitive explanation of how frequency-dependent squeezing is presented in a quantum sideband picture is given in Subsec. 4.1.2. With the help of the quantum noise phasors, the frequency-dependent behaviour becomes more visual.

4.1.1 The standard quantum limit of interferometry

Opto-mechanical force measurements are fundamentally limited by quantum noise, composed of photon shot noise and quantum back-action noise induced by radiation pressure noise. Both these types of noise are caused by the random appearance of photons in time following a Poissonian distribution. Photon shot noise directly arises when photons are detected on a photodetector, which manifests in an inconstant photocurrent over time. Shot noise is a white process increasing with the square root of the optical power. Contrarily, quantum back-action noise arises when the randomly distributed photons are reflected from a suspended mirror. On reflection, they randomly transfer their momentums and thus a fluctuating radiation pressure force. Thus, the mirror's position varies over time as well. Quantum radiation pressure noise goes with $1/\omega^2$ above the mirror's resonance frequency and scales with the square root of the power. Due to their frequency characteristics, the photon shot noise is dominant at higher frequencies, and quantum radiation pressure noise dominates at lower frequencies.³

In an interferometer, quantum noise consists of the uncorrelated sum of photon shot noise and quantum radiation pressure noise, see the blue trace in Fig. 4.1a). If the optical power is varied, the envelope of this sum results in the SQL (black dashed line). The SQL refers to the minimal amount of achievable quantum noise without using advanced techniques such as the injection of squeezing.⁴ Frequency-independent squeezing has already been injected into gravitational wave detectors. It leads to sensitivity improvements of 6 dB in GEO600 [Lou+21] and 3.2 dB in LIGO [Tse+19] and in VIRGO [Ace+19]. The next subsection links to one of the advanced techniques to beat the SQL, which is the injection of frequency-dependent squeezing.

4.1.2 Frequency-dependent squeezing

A quantum state is fully determined by its covariance matrix σ , as described in Subsec. 2.2.2. Generally, a state can be different for each measurement frequency ω . Then, the covariance matrix must be written in a frequency-dependent form $\sigma(\omega)$. In the case of $\sigma(\omega) = \sigma = \text{const.}$, the state is frequency-independent.

A loss-less single-mode squeezed state has a covariance matrix only depending on two parameters: the squeezing factor r and the squeezing angle θ , as shown by Eq. (2.43). In an accurate description, a squeezed state generated by an OPO is always frequency-dependent. The dependence is ascribed to the limited bandwidth of the down-conversion process and the limited linewidth of the OPO cavity. Consequently, the squeezing factor $r(\omega)$ has to be frequency-dependent. However, such a squeezed state is often attributed as frequency-independent because the frequencies of interest are in a region where the squeezing factor is constant in the first approximation.

³The SQL was covered in numerous publications, see e.g. [Cav81; WM08; Bas14; DKM19]. *Lower* and *higher* frequencies are determined with respect to the properties of the interferometer.

⁴There are numerous more advanced techniques as variational readout [VZ95; Kim+01], two-tone measurements [Her+10; Suh+14; Sho+19], stroboscopic measurements [BVT80; Vas+15], the optical spring effect [Che+11] or the use of Kerr media [Bon86].

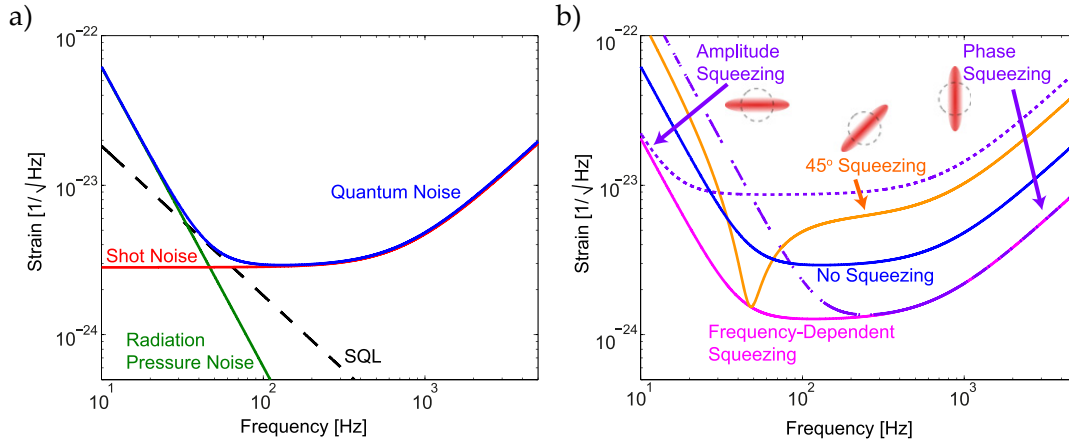


FIGURE 4.1: a) The quantum noise (blue line) in a gravitational wave detector is the uncorrelated sum of shot noise (red) and quantum radiation pressure noise (green). The point where the quantum noise touches the SQL depends on the optical power used. b) The injection of frequency-dependent squeezing reduces the quantum noise for all measurement frequencies (pink line). Frequency-independent squeezing leads to a high-frequency improvement (phase squeezing, dashed line) or a low-frequency improvement (amplitude squeezing, dotted line). The figure is taken from [Chu+14].

The definition of a frequency-dependent squeezed state is sometimes misleading. Often, the term *frequency-dependent squeezing* is used for a squeezed state that has a frequency-dependent covariance matrix $\sigma(\omega)$ arising from a frequency-dependent squeezing angle $\theta(\omega)$. Injecting such a state into a gravitational wave detector improves the strain sensitivity over the whole measurement band according to the pink trace of Fig. 4.1b). Due to the optimised squeezing angle for each frequency, there is a sensitivity improvement of e^r , with squeezing factor r , compared to the classical case depicted by the solid blue trace [Kim+01]. The injected state is squeezed along the amplitude quadrature for lower frequencies and rotates towards higher frequencies by approximately 90° such that it becomes phase quadrature squeezed. In particular, r remains constant for all frequencies. In the scope of this thesis, we call quantum states as *frequency-dependent squeezing* that have a frequency-dependent squeezing angle and/or a frequency-dependent squeezing factor.

Another opto-mechanical experiment, which calls for frequency-dependent squeezed states, is coherent quantum noise cancellation (CQNC) [TC10]. CQNC uses an anti-noise path coupled to the opto-mechanical meter cavity to destructively interfere with quantum back-action noise.⁵ The anti-noise path consists of an ancilla cavity, which generates a particularly frequency-dependent squeezed state reversing the effect of the ponderomotive squeezing of the opto-mechanical system.⁶ That is why the ancilla system is often called an effective negative-mass oscillator [PH14]. In the proposed all-optical realisation of CQNC [Wim+14; Ste19; Sch+22], the effective negative-mass oscillator is an optical cavity including a beam splitter and a two-mode down-conversion process.⁷

⁵Sometimes, radiation pressure noise and back-action noise are used as synonyms. In fact, the effect of (quantum) radiation pressure noise causes the opto-mechanical oscillator's position to fluctuate. Then, this displacement fluctuation is subject to (quantum) back-action noise.

⁶For a rotating ponderomotive squeezed state in phase space, see, e.g. [Ste19], Fig. 2.12.

⁷Also other realisations of this oscillator are conceivable to achieve back-action evasion. A spin ensemble in a magnetic field can act as an effective negative-mass oscillator [Ham+09] as demonstrated in [Møl+17; Koh+18]. Also, effective negative-mass characteristics were observed in

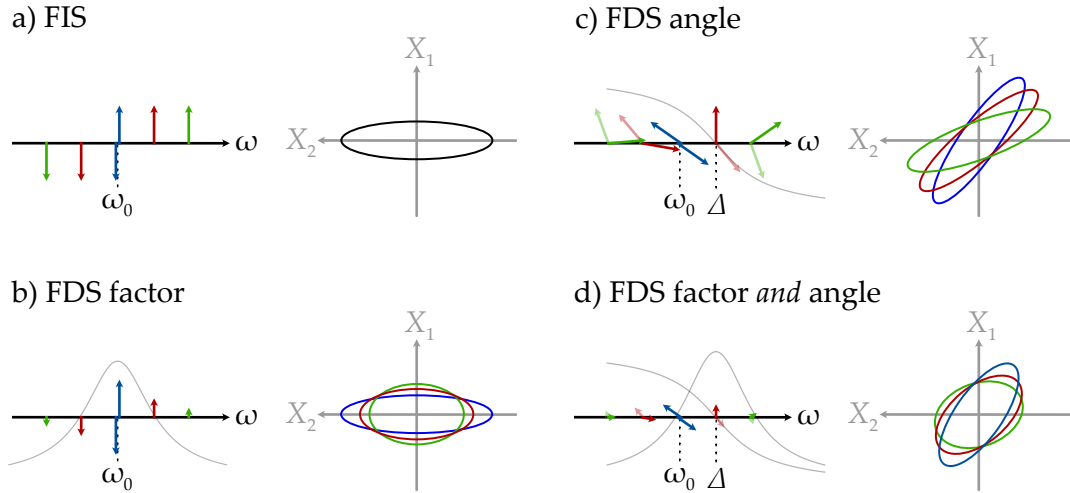


FIGURE 4.2: Quantum sideband representation for differently squeezed states. Arrows of the same colour correspond to a correlated sideband pair at a different frequency ω . a) Frequency-independent squeezing (FIS) leads to the same squeezing (black ellipse) at all frequencies. b) A frequency-dependent (FDS) squeezing factor creates ellipses that are differently squeezed in X_1 . c) A frequency-dependent squeezing angle creates ellipses that are differently rotated. d) State with a frequency-dependent squeezing factor *and* angle.

The effective negative-mass oscillator for the all-optical CQNC has to generate a particular frequency-dependent squeezed state. This state needs to have a frequency-dependent squeezing angle $\theta(\omega)$ *and* factor $r(\omega)$. The reason for this can be found in the susceptibility of the opto-mechanical oscillator, which has a frequency-dependent phase *and* amplitude behaviour. Using such a particular frequency-dependent squeezed state was already suggested in the context of gravitational wave detection [Kim+01]. Kimble et al. used the term *inversely input squeezed state* since it has the same Wigner function as an interferometer's ponderomotive squeezed state, but it is mirrored on either of the quadrature axes.⁸

Next, a brief, intuitive comparison is given on different frequency-dependent squeezed states. In Fig. 4.2, we use the quantum sideband picture introduced in Subsec. 2.3.3 and distinguish four cases.

Figure 4.2a) shows the correlated sideband pairs around ω_0 for a frequency-independent squeezed (FIS) state. The three presented sideband pairs (red, blue and green) represent three different frequencies, and they are only drawn at the specific time when they are aligned anti-parallel. Note that the phase of the individual phasors is not determined. However, phasor pairs always underlie correlations. Due to the destructive interference of sideband pairs, the squeezing ellipse is squeezed in the X_1 -quadrature in phase space.⁹ The ellipse is identical for all measurement frequencies ω , since all sidebands have the same length. With this picture, we can describe the output of an OPO, pumped with frequency $2\omega_0$, when we only consider frequencies much smaller than the OPO's linewidth.

Figure 4.2b) shows the squeezed state generated by an OPO pumped with the frequency $2\omega_0$. This state has a frequency-dependent squeezing (FDS) factor. Depending on the frequency, the sidebands experience the down-conversion process weaker or

the dispersion relation of matter waves propagating through an optical lattice [Eie+03] or for two-mode measurements [WC13; OK+16].

⁸See Figs. 5 and 8, and especially Sec. D in [Kim+01].

⁹Then, the orthogonal X_2 -axis is automatically anti-squeezed.

stronger, as indicated by the grey cavity amplitude transfer function. Consequently, the squeezing degree is largest close to ω_0 (blue phasors) and reduces towards higher frequencies (red and green phasors). In both pictures a) and b), the situation is fully symmetric around ω_0 .

To generate a state having a frequency-dependent squeezing angle, the symmetry between the upper and lower sidebands needs to be broken. This can be done, e.g. by reflecting a frequency-independent squeezed state shown in Fig. 4.2a) from a loss-less filter cavity detuned by Δ . This scenario is depicted in Fig. 4.2c). The quantum sidebands accumulate a phase change according to the phase transfer function of the cavity, shown by the grey graph. After reflection, each upper and lower phasor pair has a specific phase relation. There will be one timestamp where the phasors point parallel (or anti-parallel), indicated by the faded-out phasors.¹⁰ Parallel phasors indicate constructive and anti-parallel destructive interference. Thus, the squeezing ellipses are drawn for all three treated frequencies. Employing a detuned filter cavity is only one way to generate a state having a frequency-dependent squeezing angle. One alternative is injecting a two-mode squeezed state into the measurement cavity of a gravitational wave detector [Ma+17; Yap+20; Süd+20]. The signal recycling cavity must be resonant for the signal but detuned for the idler field whose sidebands accumulate a frequency-dependent phase shift [Süd+20]. After a spatial separation, the signal and idler sidebands are independently detected on homodyne detectors with matched local oscillator frequencies.¹¹ The electrical combination of the signals leads to frequency-dependent squeezing.

Figure 4.2d) shows a state that has a frequency-dependent squeezing factor *and* angle. This state is generated by a detuned OPO. The sidebands experience a phase response analogue to Fig. 4.2c). However, although the amplitude response is asymmetric for the red and the green phasor pair, they pairwise have the same length. The reason is that the down-conversion process only happens if *both* the upper and lower sideband can be correlated. Thus, the phasor corresponding to the smaller amplitude response value dictates the squeezing factor at that frequency. In the next section, the publication [P2] is reprinted, which shows how such a state is generated.

4.2 [P2]: Frequency-Dependent Squeezing from a Detuned Squeezer

This subsection reprints the following publication, which was accepted on 31 May 2022 and published on 14 July 2022 in Physical Review Letters. The author contributions and a short abstract can be found on Page iii.


[P2] J. Junker, D. Wilken, N. Johnny, D. Steinmeyer, and M. Heurs. “Frequency-Dependent Squeezing from a Detuned Squeezer”. In: *Phys. Rev. Lett.* 129 (3 July 2022), p. 033602. DOI: [10.1103/PhysRevLett.129.033602](https://doi.org/10.1103/PhysRevLett.129.033602)

¹⁰Note that the sideband pairs do not follow a predictable rotation as classical phasors would. Though their direction is entirely random, they will always occur correlated.

¹¹Similar as the dual homodyne detection scheme explained in Subsec. 5.3.1.

Frequency-Dependent Squeezing from a Detuned Squeezer

Jonas Junker¹,* Dennis Wilken¹, Nived Johny¹, Daniel Steinmeyer¹, and Michèle Heurs²
 Max Planck Institute for Gravitational Physics (Albert Einstein Institute), and Institute for Gravitational Physics,
 Leibniz Universität Hannover, Callinstraße 38, 30167 Hannover, Germany

 (Received 3 March 2022; accepted 31 May 2022; published 14 July 2022)

Frequency-dependent squeezing is a promising technique to overcome the standard quantum limit in optomechanical force measurements, e.g., gravitational wave detectors. For the first time, we show that frequency-dependent squeezing can be produced by detuning an optical parametric oscillator from resonance. Its frequency-dependent Wigner function is reconstructed quantum tomographically and exhibits a rotation by 39° , along which the noise is reduced by up to 5.5 dB. Our setup is suitable for realizing effective negative-mass oscillators required for coherent quantum noise cancellation.

DOI: [10.1103/PhysRevLett.129.033602](https://doi.org/10.1103/PhysRevLett.129.033602)

According to quantum mechanics, the continuous measurement of an object's position creates a random quantum backaction perturbation on its momentum. This backaction noise, together with the shot noise, fundamentally limits the precision in ultrasensitive force measurements, e.g., in cavity optomechanics [1] or gravitational wave detection [2–5]. The sensitivity limit imposed by backaction noise and shot noise is referred to as the standard quantum limit (SQL) of interferometry. Previous experiments measured mechanical motions with an imprecision below the SQL [6,7] observed quantum backaction [8–12] or demonstrated sensitivities near the SQL [10,13–15]. To reduce or even evade the effect of quantum backaction and to overcome the SQL, various quantum nondemolition techniques have been proposed, e.g., variational readout [16,17], two-tone measurements [18–20], stroboscopic measurements [21,22], the optical spring effect [23], or the use of Kerr media [24].

The SQL can also be beaten by the injection of frequency-dependent squeezing. For a lossless and non-detuned interferometer, the squeezing angle is optimized for each frequency ω with $\theta(\omega) = -\text{arccot}\mathcal{K}(\omega)$, and Kimble factor \mathcal{K} [16]. Then, the sensitivity can be improved by e^{-2r} with squeezing factor r in a broad frequency band [16]. Typically, frequency-dependent squeezing is generated by reflecting frequency-independent squeezed light off a detuned filter cavity [25–28]. However, frequency-dependent squeezing of this form cannot entirely evade quantum backaction noise because r is frequency-independent [16].

In contrast, the entire backaction noise can be evaded by using an effective negative-mass oscillator [29–31]. In the cascaded all-optical realization of coherent quantum noise cancellation [31,32], the optomechanical system and the effective negative-mass oscillator are independent subsystems [33]. There, the effective negative-mass oscillator produces a state that effectively exhibits frequency-dependent squeezing to counteract the effect of the disturbing ponderomotive squeezing of the optomechanical oscillator [33]. The squeezing, generated by this effective negative-mass oscillator, exhibits both a frequency-dependent rotation angle $\theta(\omega)$ and squeezing factor $r(\omega)$. Ideally, this state entirely evades backaction noise and is equal to the *inversely input squeezed* state [16]. To realize a well-matched effective negative-mass oscillator, a complicated coupled system, using a beam splitter process and a down-conversion interaction, has been studied in detail [32]. Instead of this complex system, in this Letter, we propose using a simpler and elegant alternative as an effective negative-mass oscillator.

We report on the generation of frequency-dependent squeezing using a detuned optical parametric oscillator (OPO). We show that the output state of this squeezer exhibits a frequency-dependent squeezing factor and rotation angle. We analyze the state by tomographically reconstructing its Wigner function at different measurement frequencies. The obtained Wigner functions agree well with our measured and simulated noise spectra. Our findings are relevant for optomechanical force measurements, e.g., gravitational wave detectors, limited by quantum backaction noise.

The system is described theoretically by applying the input-output formalism [34,35] on a linear lossless OPO, shown in Fig. 1. The interaction Hamiltonian for this nonclassical light source is

$$H = \frac{i\hbar g}{2} (\hat{a}^2 - \hat{a}^{\dagger 2}), \quad (1)$$

Published by the American Physical Society under the terms of the [Creative Commons Attribution 4.0 International license](https://creativecommons.org/licenses/by/4.0/). Further distribution of this work must maintain attribution to the author(s) and the published article's title, journal citation, and DOI. Open access publication funded by the Max Planck Society.

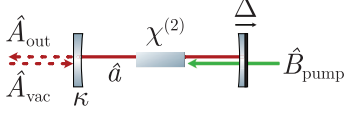


FIG. 1. Schematic of the optical parametric oscillator with decay rate κ and intracavity field \hat{a} . The $\chi^{(2)}$ medium is pumped with \hat{B}_{pump} . When the cavity is detuned by Δ from its resonance, the vacuum fluctuations \hat{A}_{vac} are converted into an output field \hat{A}_{out} exhibiting frequency-dependent squeezing.

where we assume an undepleted pump field \hat{B}_{pump} . The coupling strength of the down-conversion process is given by $g = 2\chi^{(2)}\hat{B}_{\text{pump}}$, where $\chi^{(2)}$ is the nonlinear coefficient of the down-conversion process. The pump oscillates with ω_p and does not exceed the threshold of the OPO. Vacuum fluctuations \hat{A}_{vac} couple to the intracavity field through the input coupling mirror. The derivative of the circulating intracavity field is

$$\dot{\hat{a}} = i\hat{a}\Delta - \hat{a}\kappa + \hat{a}^\dagger g + \hat{A}_{\text{vac}}\sqrt{2\kappa}. \quad (2)$$

We define the detuning Δ as the difference between cavity resonance frequency and fundamental frequency $\omega_0 = \omega_p/2$. The authors in [36] also considered the theory of a detuned but doubly resonant OPO (but they did not consider the frequency-dependent output state rotation). However, in many other publications [37–39], Δ is set to 0. The cavity has a decay rate κ , where $\kappa = 2\pi\nu/\mathcal{F}$ with finesse \mathcal{F} , free spectral range (FSR) $\nu = c/L$, and round-trip length L . We can decompose the field operators \hat{a} in a constant and a fluctuating term in the form $\hat{a} = \langle \hat{a} \rangle + \delta\hat{a}$. Then, Eq. (2) can be solved in the frequency domain as in [40,41] using the input-output theory [34,35] for the fluctuating terms $\delta\hat{a}(\omega)$ and $\delta\hat{a}^\dagger(\omega)$. After applying the cavity boundary condition [42], we can compute the fluctuating part of the output field $\delta\hat{A}_{\text{out}} = \sqrt{2\kappa}\delta\hat{a} - \delta\hat{A}_{\text{vac}}$. The fluctuations of the output amplitude and phase quadrature are $\delta\hat{X}_1 = \delta\hat{A}_{\text{out}} + \delta\hat{A}_{\text{out}}^\dagger$ and $\delta\hat{X}_2 = i(\delta\hat{A}_{\text{out}} - \delta\hat{A}_{\text{out}}^\dagger)$, respectively.

To characterize the output state, it is convenient to derive the symmetrized covariance matrix of the output state. It contains the spectral densities and is defined by $\sigma_{kl} = \frac{1}{2}(\langle \delta\hat{X}_k \delta\hat{X}_l + \delta\hat{X}_l \delta\hat{X}_k \rangle - \langle \delta\hat{X}_l \rangle \langle \delta\hat{X}_k \rangle)$, where $\delta\mathbf{X} = (\delta\hat{X}_1, \delta\hat{X}_2)$. When assuming an input variance for the vacuum field of $V_{\text{vac}} = 1$, the covariance matrix is

$$\begin{aligned} \sigma_{11} &= 1 + \frac{4g\kappa(|\chi^+|^2 - \Delta^2)}{|\Delta + \chi^+\chi^-|^2}, \\ \sigma_{22} &= 1 - \frac{4g\kappa(|\chi^-|^2 - \Delta^2)}{|\Delta + \chi^+\chi^-|^2}, \\ \sigma_{12} &= \sigma_{21} = -\frac{8g\kappa^2\Delta}{|\Delta + \chi^+\chi^-|^2}. \end{aligned} \quad (3)$$

Here, we have introduced $\chi^\pm = \kappa + i\omega \pm g$. For nonzero detuning $\Delta \neq 0$, we obtain nonvanishing off-diagonal elements of σ . These entries arise from the rotation of the output state in phase space. Hence, the rotation depends on the detuning Δ and the measurement sideband frequency ω .

The covariance matrix σ describes a pure state because we consider a lossless OPO. Passive optical losses will degrade the squeezed output state. When the state experiences power losses l , corresponding to an efficiency $\eta = 1 - l$, the lossy covariance is $\sigma_1 = \eta\sigma + (1 - \eta)\mathbf{I}_2$, with \mathbf{I}_2 being the 2×2 identity matrix.

This state can be phase sensitively detected with a balanced homodyne detector (HD), where it interferes with a local oscillator (LO) at frequency ω_0 . The phase difference ψ between LO and output state defines the detection angle and, accordingly, the projection axis for the measurement. The measurement result of the HD corresponds to $\tilde{\sigma}_{11}(\psi)$, with

$$\tilde{\sigma}(\psi) = \mathbf{R}^\top(\psi)\sigma_1\mathbf{R}(\psi), \quad (4)$$

with rotation matrix $\mathbf{R}(\psi)$.

At $\omega = 0$, a specific detection angle ψ_0 diagonalizes $\tilde{\sigma}(\psi_0)$ and maximized the measurable squeezing and antisqueezing values. This specific angle ψ_0 is

$$\psi_0 = -\frac{1}{2}\arctan\frac{2\kappa\Delta}{\Delta^2 - \kappa^2 - g^2}. \quad (5)$$

However, for measurement frequencies $\omega \neq 0$, $\tilde{\sigma}(\psi_0)$ is not diagonal anymore. It still can be diagonalized with a frequency-dependent detection angle ψ_ω . The rotation angle $\theta(\omega)$ of the quadrature distribution in phase space is

$$\theta(\omega) = \psi_0 - \psi_\omega = \psi_0 + \frac{1}{2}\arctan\frac{2\kappa\Delta}{\Delta^2 - \kappa^2 - g^2 - \omega^2}. \quad (6)$$

This shows again that the state rotation depends on the measurement frequency ω , indicating frequency-dependent squeezing. When changing the sign of Δ , the rotation direction flips because of the off-diagonal elements in Eq. (3). Thus, in the context of coherent quantum noise cancellation, the sign of Δ defines the positive or negative energy character of the oscillator.

A noisy detection angle ψ at the HD degrades the squeezing measurements. Assuming normally distributed fluctuations with a small standard deviation of $\delta\psi$ [38], the detected noise level is

$$\tilde{\sigma}_{11}^{\text{det}} = \tilde{\sigma}_{11}\cos^2(\delta\psi) + \tilde{\sigma}_{22}\sin^2(\delta\psi) + \tilde{\sigma}_{12}\sin(2\delta\psi). \quad (7)$$

To aid understanding, the detuned OPOs' essential features are shown in Fig. 2. Here, the output state's noise distribution is depicted by an ellipse in phase space.

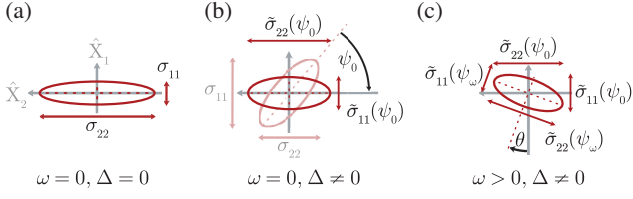


FIG. 2. The output state of the OPO is represented by the noise ellipse in phase space. In (a) the resonant OPO generates a noise ellipse with diagonal covariance matrix σ at baseband ($\omega = 0$). In (b) the OPO is detuned by Δ , generating a noise ellipse having a nondiagonal σ . According to Eq. (4), the covariance matrix can be rotated to $\tilde{\sigma}(\psi_0)$, which is diagonal. In (c) for a larger measurement frequency $\omega > 0$ the noise ellipse given by $\tilde{\sigma}(\psi_0)$ has rotated by θ . Now, the maximum squeezing and antisqueezing levels can be obtained from $\tilde{\sigma}_{11}(\psi_\omega)$ and $\tilde{\sigma}_{22}(\psi_\omega)$.

Figure 2(a) shows the ordinary case of a resonant OPO at a measurement frequency $\omega = 0$. The pump's phase is set to deamplification of $\delta\hat{X}_1$, and no state rotation can be seen. In (b), the OPO is detuned ($\Delta \neq 0$) but the measurement frequency is still at $\omega = 0$. The cavity phase response leads to a rotation of the ellipse by ψ_0 , represented by the whitened state with nondiagonal covariance matrix σ . After using Eq. (4), the diagonalized state $\tilde{\sigma}(\psi_0)$ is depicted, with main diagonal elements $\tilde{\sigma}_{11}(\psi_0)$ and $\tilde{\sigma}_{22}(\psi_0)$. Because of the detuning, the squeezing and antisqueezing levels $\tilde{\sigma}_{11}(\psi_0)$ and $\tilde{\sigma}_{22}(\psi_0)$ are reduced compared to (a). In (c), the OPO is still detuned but now the measurement frequency has changed. Depending on the actual measurement frequency ω , positive and negative sideband frequencies accumulate nonsymmetrical phases. The main consequence is a frequency-dependent squeezing angle θ . Additionally, the maximum squeezing and antisqueezing levels are also frequency-dependent and they are depicted by $\tilde{\sigma}_{11}(\psi_\omega)$ and $\tilde{\sigma}_{22}(\psi_\omega)$.

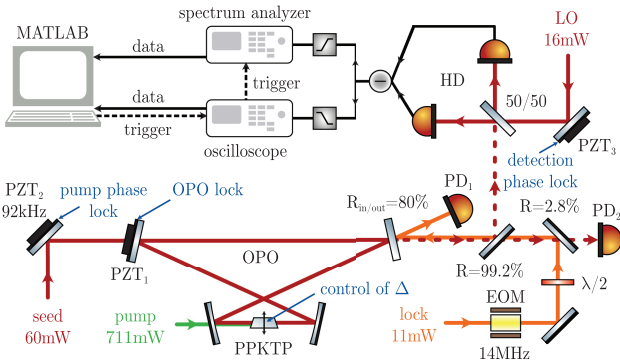


FIG. 3. Experimental setup consisting of the detuned OPO that generates a frequency-dependent squeezed state (bottom) and the HD with the data acquisition for reconstructing the state's Wigner function (top). The actuators of the locking loops are indicated in blue.

The schematic of our experimental setup is shown in Fig. 3. The core element of our free-space OPO is a $1 \text{ mm} \times 2 \text{ mm} \times 10 \text{ mm}$ nonlinear periodically poled potassium titanyl phosphate (PPKTP) type I crystal. It is temperature-controlled to 31°C to ensure phase matching for the s -polarized down-conversion process. The 0.5° trapezoidal-shaped crystal is placed in a four mirror cavity topology with an FSR of $\nu = 197 \text{ MHz}$. The plane input (front) mirror has a power reflectivity of $R_{\text{in/out}} = 80\%$. The plane rear mirror and the curved mirrors are highly reflective for the fundamental wavelength of 1064 nm and antireflective for the 532 nm green pump light.

We want to lock the OPO cavity to an arbitrary detuning Δ . This is realized by using perpendicularly polarized fields for locking and pumping using the cavity's adjustable birefringence. The refractive index of the PPKTP crystal is polarization- and temperature-dependent. Its trapezoidal shape allows us to change the crystal's effective length by shifting it perpendicular to the beam axis and parallel to the cavity plane. Thus, we can adjust the frequency difference between s -polarization and p -polarization resonances. Fine-tuning can be achieved by changing the crystal's temperature (a frequency difference of 1 MHz corresponds roughly to a temperature change of 0.1°C). Here, the effect on the nonlinear efficiency can be neglected. For the measurements presented in this Letter, the detuning was set to $\Delta = -2\pi \times 3.6 \text{ MHz}$.

We inject a p -polarized 14 MHz phase-modulated field into the cavity to stabilize to the chosen detuning via Pound-Drever-Hall locking. For locking on resonance, an s -polarized beam is used. The locking field is sent in counterpropagatingly to avoid cross-coupling and is detected in reflection of the OPO by photodetector PD_1 . After demodulation and filtering, the control signal is fed back to the piezoelectric transducer PZT_1 clamped onto the rear mirror.

The squeezing angle needs to be actively stabilized. Therefore, we inject a seed through the rear highly reflective mirror, which is phase-modulated at 92 kHz by PZT_2 . This field serves as a reference for the frequency-dependent squeezing. By detecting and demodulating a fraction of the seed field behind the $R = 99.2\%$ mirror on PD_2 , we are able to lock to the pump phase. The locking point is chosen such that the amplitude quadrature fluctuations are minimized. Technically, the seed displaces the squeezed vacuum converting it into a bright squeezed state.

The generated state is detected by a balanced HD scheme. Technical noise of the seed would dominate the measurement at baseband frequencies. Therefore, we take our measurements around the first FSR of the OPO at ν . The covariance matrix will be identical at frequencies corresponding to higher FSRs $\tilde{\sigma}(\psi, \omega) = \tilde{\sigma}(\psi, \omega + n\nu)$, $n \in \mathbb{Z}$, because of the spectral periodicity of the OPO's response. This approach has two advantages: First, measurement frequencies both above and below the resonance

frequency can be resolved, and second, experimental challenges of measuring squeezing at baseband can be avoided. The phase difference between the strong LO and the bright squeezed field determines the detection angle and can be changed with PZT₃. In order to measure the squeezing spectrum at a certain detection angle, the phase difference is usually stabilized at this angle. However, even with a swept LO, a full tomographic state reconstruction is possible, as can be seen in the following.

We record the homodyne projections for a measurement time of 1 s per measurement frequency while the LO phase is ramped for our tomographic reconstructions. The low-frequency output of the HD is recorded by an oscilloscope and shows the interference between seed and LO. The high-frequency output is demodulated at the measurement frequency around ω using a spectrum analyzer [Keysight, N9020A MXA] and recorded as amplitude time series on a computer. This signal exhibits the quadrature fluctuations of the squeezed state scaled with the amplitude of the LO. The data acquisition is realized with a MATLAB script that triggers and stores the measurement for each frequency bin.

The Wigner function is tomographically reconstructed in four steps. First, we use the low-frequency interference signal to map each voltage amplitude recorded by the spectrum analyzer to a detection angle between 0° and 180° . Second, the amplitudes are sorted into 180 angular bins depending on their detection angle. Third, for each angular bin, all amplitudes are distributed in a histogram with 201 bars. Now the data are stored in a 201×180 array. Fourth, the array is inversely Radon transformed by using the built-in MATLAB function *iradon*, leading to the filtered back-projected Wigner function [43]. This algorithm is repeated for a vacuum state measurement to normalize the Wigner function. The Wigner function is connected to the previously derived covariance matrix. Using the first moments $d_j = \langle\langle \hat{X}_1, \hat{X}_2 \rangle\rangle$ of the state, the Wigner function reads [44]

$$W(X) = \frac{1}{\pi \sqrt{\det(\sigma)}} e^{-(X-d)^\top \sigma^{-1} (X-d)}. \quad (8)$$

Before characterizing the detuned OPO, we analyze the performance of the resonant OPO. We generate an amplitude quadrature squeezed state by locking the pump's phase to the seed. From the measurements of the (squeezed) amplitude quadrature and the antisqueezed phase quadrature for different pump powers, we obtained $\delta\psi = 15$ mrad phase noise and a total efficiency $\eta = 92.8\%$ the same way as in [45]. At a pump power of 711 mW, we observed -9.8 dB of squeezing and 15.3 dB of antisqueezing at the first FSR, which corresponds to $g = -2\pi \times 2.3$ MHz. In separate measurements, we determined the OPO decay rate $\kappa = 2\pi \times 3.2$ MHz, the escape efficiency of the OPO $\eta_{\text{esc}} = 98.3\%$, the propagation efficiency $\eta_{\text{prop}} = 99.0\%$, and the homodyne efficiency

$\eta_{\text{hd}} = 97.6\%$. From these measurements, we estimated the quantum efficiency of the HD with $\eta_{\text{qe}} = \eta / (\eta_{\text{esc}} \eta_{\text{prop}} \eta_{\text{hd}}) > 97.6\%$ as in [46].

In a second step, we stabilized the OPO with a detuning of $\Delta = -2\pi \times 3.6$ MHz and again produced an amplitude quadrature squeezed state. We investigated the frequency behavior of the state with the tomographic reconstruction method described above. In the top row of Fig. 4, three examples for reconstructed Wigner functions are shown for the frequencies 194, 197, and 203 MHz. An animation showing the rotation over the entire spectrum can be found in the Supplemental Material [47]. In the middle row, we show the measured maximal and minimal noise levels, and the rotation angle (both with estimated absolute errors). These data points are obtained by fitting the reconstructed Wigner distribution to Eq. (8). Equation (6) yields the solid

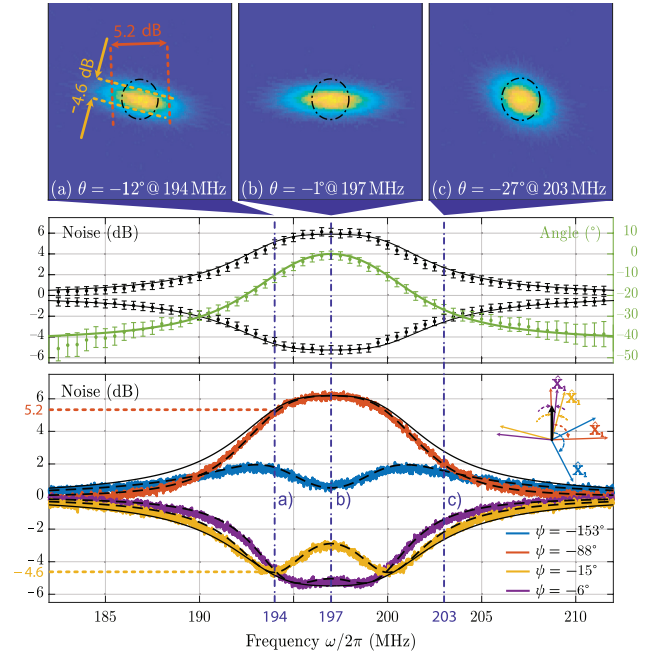


FIG. 4. Top row: Tomographically reconstructed Wigner functions for the frequencies (a) 194 MHz, (b) 197 MHz, and (c) 203 MHz; see Supplemental Material [47] for more reconstructions. The dashed circles indicate the shot noise levels as a reference. Middle row: Rotation angles, squeezing, and anti-squeezing values obtained from fitting a two-dimensional Gaussian function to our reconstructed distributions. The solid green trace was plotted using Eq. (6). The solid black traces show simulations when the detection angle is aligned to the maximum squeezing and antisqueezing axes at each measurement frequency, $\tilde{\sigma}_{11}(\psi_\omega)$ and $\tilde{\sigma}_{22}(\psi_\omega)$, respectively. Bottom row: The widths of the Wigner function are measured at four different detection angles of the HD shown by the colored traces with a spectrum analyzer ([Keysight, N9020A MXA]; resolution bandwidth (RBW), 100 kHz; video bandwidth (VBW), 100 Hz; sweep time, 5 s; average, 10). The black dashed traces are simulations of $\tilde{\sigma}_{11}(\psi - \psi_0)$ from Eq. (7) for these four specific angles.

curves for $\theta(\omega)$ and ψ_ω . Note that in the upper two rows, the coupling strength ($g = -2\pi \times 2.2$ MHz) was slightly reduced with respect to the measurements in the bottom row, as the measurements were taken at different times. In the bottom row, we show recorded spectra for different detection angles ψ . Here, each colored trace corresponds to a width of the Wigner function under a specified and stabilized detection phase ψ of the LO (0° corresponds to detecting the amplitude quadrature). The chosen angles represent four qualitatively different spectra. All measurements are normalized to shot noise. The electronic dark noise was 14.3 to 15.0 dB below the shot noise and was subtracted from the data. The angles are obtained from the fits (black dashed traces), which are based on Eq. (7). When choosing the optimal detection angle at all frequencies, we get the black solid envelop traces.

We observed frequency-dependent squeezing over the full measurement band of 30 MHz. At the first FSR at 197 MHz, the state rotates from $\theta = 0^\circ$ to $\theta = 39^\circ$ clockwise toward higher and lower frequencies (see Supplemental Material [47]). This rotation symmetry can only be seen at higher FSRs and was, to our knowledge, not observed before. The rotation angle θ agrees with the angle θ_0 determined to diagonalize the output covariance matrix at each measurement frequency; see Eq. (4). We detected a maximum squeezing of -5.5 dB and a maximum anti-squeezing of 6.2 dB at the first FSR. These noise values match the independently measured and reconstructed Wigner functions, which validates our tomographic reconstruction method. The detuned OPO requires larger coupling strengths than the resonant OPO to reach equivalent squeezing values. This does not imply any additional losses. Compared to the resonant case, the pump threshold changed from $g_{\text{thr}} = -2\pi \times 3.2$ MHz to $-2\pi \times 4.8$ MHz for the detuned case.

The relevant parameter defining the shape of the Wigner function of the output state is the relative detuning $\tilde{\Delta} = |\Delta|/\kappa$. In fact, when $\tilde{\Delta}$ increases, the maximum rotation angle increases as well. For a given pump power, the maximum squeezing level reduces for larger detunings. Our choice for $\tilde{\Delta} = |-3.6 \text{ MHz}|/3.2 \text{ MHz} = 1.125$ is a trade-off to achieve a state rotation of roughly 45° (required for the inversely input squeezed state [16]) and a decent squeezing level. For a large detuning $\tilde{\Delta} \gg 1$, the state experiences a rotation of 90° . However, the squeezing will vanish then.

Finally, we discuss the applicability of the detuned OPO to enhance sub-SQL measurement sensitivities. In gravitational wave detectors, the filter cavities require very low linewidths of hundreds of Hertz to rotate the squeezing over the detector's measurement band. Instead, building a detuned squeezer with equally low linewidth seems to be technically very challenging. Because of the residual parasitic reflections of the crystal, the detuned squeezer's cavity length would have to be even longer than that of

the filter cavities. Moreover, to ensure a sufficiently large escape efficiency, the cavity finesse would need to be reduced. However, using our detuned squeezer approach (instead of the usual resonant squeezer) can serve as a phase-rotation correction mechanism in addition to the filter cavities. This is especially relevant for systems dominantly limited by quantum backaction noise, such as the low-frequency Einstein Telescope [48,49]. Other experiments in the field of cavity optomechanics have begun to observe backaction noise due to quantum radiation pressure noise [8–10]. Using a detuned OPO could be an approximate but simple and promising approach to realize an effective negative-mass oscillator to cancel quantum backaction noise [32]. However, experimentally applying the detuned OPO to an optomechanical system requires sophisticated parameter matching. We plan to further investigate the detuned OPO as an effective negative-mass oscillator for coherent quantum noise cancellation in the future.

We have demonstrated the generation and quantum tomographic reconstruction of frequency-dependent squeezed states from a detuned OPO. The observed squeezed state rotates by 39° for increasing frequencies until it is amplitude quadrature squeezed at the first FSR of 197 MHz. For frequencies larger than the first FSR, the state rotates backward by -39° . The state exhibits maximum squeezing and antisqueezing levels of -5.5 and 6.2 dB, with a measurement efficiency of $\eta = 92.8\%$. The detuned OPO provides a simple realization for the required effective negative-mass oscillator in quantum backaction evasion schemes, such as coherent quantum noise cancellation.

We thank Klemens Hammerer for insightful discussions. This work was funded by the Deutsche Forschungsgemeinschaft (Excellence PhoenixD (EXC 2122, Project ID 390833453), Excellence QuantumFrontiers (EXC 2123, Project ID 390837967), GRK 1991, OE 177/ 10-1).

*Corresponding author.

jonas.junker@aei.mpg.de

- [1] M. Aspelmeyer, T. J. Kippenberg, and F. Marquardt, *Rev. Mod. Phys.* **86**, 1391 (2014).
- [2] C. M. Caves, *Phys. Rev. Lett.* **45**, 75 (1980).
- [3] A. A. Clerk, M. H. Devoret, S. M. Girvin, F. Marquardt, and R. J. Schoelkopf, *Rev. Mod. Phys.* **82**, 1155 (2010).
- [4] H. Yu *et al.* (LIGO Scientific Collaboration), *Nature (London)* **583**, 43 (2020).
- [5] F. Acernese *et al.* (The Virgo Collaboration), *Phys. Rev. Lett.* **125**, 131101 (2020).
- [6] J. D. Teufel, T. Donner, M. A. Castellanos-Beltran, J. W. Harlow, and K. W. Lehnert, *Nat. Nanotechnol.* **4**, 820 (2009).
- [7] G. Anetsberger, E. Gavartin, O. Arcizet, Q. P. Unterreithmeier, E. M. Weig, M. L. Gorodetsky, J. P.

- Kotthaus, and T. J. Kippenberg, *Phys. Rev. A* **82**, 061804(R) (2010).
- [8] K. W. Murch, K. L. Moore, S. Gupta, and D. M. Stamper-Kurn, *Nat. Phys.* **4**, 561 (2008).
- [9] T. P. Purdy, R. W. Peterson, and C. A. Regal, *Science* **339**, 801 (2013).
- [10] J. D. Teufel, F. Lecocq, and R. W. Simmonds, *Phys. Rev. Lett.* **116**, 013602 (2016).
- [11] J. Cripe, N. Aggarwal, R. Lanza, A. Libson, R. Singh, P. Heu, D. Follman, G. D. Cole, N. Mavalvala, and T. Corbitt, *Nature (London)* **568**, 364 (2019).
- [12] J. Cripe, T. Cullen, Y. Chen, P. Heu, D. Follman, G. D. Cole, and T. Corbitt, *Phys. Rev. X* **10**, 031065 (2020).
- [13] S. Schreppler, N. Spethmann, N. Brahms, T. Botter, M. Barrios, and D. M. Stamper-Kurn, *Science* **344**, 1486 (2014).
- [14] D. J. Wilson, V. Sudhir, N. Piro, R. Schilling, A. Ghadimi, and T. J. Kippenberg, *Nature (London)* **524**, 325 (2015).
- [15] M. Rossi, D. Mason, J. Chen, Y. Tsaturyan, and A. Schliesser, *Nature (London)* **563**, 53 (2018).
- [16] H. J. Kimble, Y. Levin, A. B. Matsko, K. S. Thorne, and S. P. Vyatchanin, *Phys. Rev. D* **65**, 022002 (2001).
- [17] S. Vyatchanin and E. Zubova, *Phys. Lett. A* **201**, 269 (1995).
- [18] J. B. Hertzberg, T. Rocheleau, T. Ndukum, M. Savva, A. A. Clerk, and K. C. Schwab, *Nat. Phys.* **6**, 213 (2010).
- [19] J. Suh, A. J. Weinstein, C. U. Lei, E. E. Wollman, S. K. Steinke, P. Meystre, A. A. Clerk, and K. C. Schwab, *Science* **344**, 1262 (2014).
- [20] I. Shomroni, L. Qiu, D. Malz, A. Nunnenkamp, and T. J. Kippenberg, *Nat. Commun.* **10**, 2086 (2019).
- [21] V. B. Braginsky, Y. I. Vorontsov, and K. S. Thorne, *Science* **209**, 547 (1980).
- [22] G. Vasilakis, H. Shen, K. Jensen, M. Balabas, D. Salart, B. Chen, and E. S. Polzik, *Nat. Phys.* **11**, 389 (2015).
- [23] Y. Chen, S. L. Danilishin, F. Y. Khalili, and H. Müller-Ebhardt, *Gen. Relativ. Gravit.* **43**, 671 (2011).
- [24] R. S. Bondurant, *Phys. Rev. A* **34**, 3927 (1986).
- [25] S. Chelkowski, H. Vahlbruch, B. Hage, A. Franzen, N. Lastzka, K. Danzmann, and R. Schnabel, *Phys. Rev. A* **71**, 013806 (2005).
- [26] E. Oelker, T. Isogai, J. Miller, M. Tse, L. Barsotti, N. Mavalvala, and M. Evans, *Phys. Rev. Lett.* **116**, 041102 (2016).
- [27] L. McCuller, C. Whittle, D. Ganapathy, K. Komori, M. Tse, A. Fernandez-Galiana, L. Barsotti, P. Fritschel, M. MacInnis, F. Matichard, K. Mason, N. Mavalvala, R. Mittleman, H. Yu, M. E. Zucker, and M. Evans, *Phys. Rev. Lett.* **124**, 171102 (2020).
- [28] Y. Zhao *et al.*, *Phys. Rev. Lett.* **124**, 171101 (2020).
- [29] E. S. Polzik and K. Hammerer, *Ann. Phys. (Berlin)* **527**, A15 (2015).
- [30] C. B. Møller, R. A. Thomas, G. Vasilakis, E. Zeuthen, Y. Tsaturyan, M. Balabas, K. Jensen, A. Schliesser, K. Hammerer, and E. S. Polzik, *Nature (London)* **547**, 191 (2017).
- [31] M. Tsang and C. M. Caves, *Phys. Rev. Lett.* **105**, 123601 (2010).
- [32] M. H. Wimmer, D. Steinmeyer, K. Hammerer, and M. Heurs, *Phys. Rev. A* **89**, 053836 (2014).
- [33] D. Steinmeyer, Subsystems for all-optical coherent quantum-noise cancellation, Ph.D. thesis, Gottfried Wilhelm Leibniz Universität Hannover, 2019.
- [34] M. J. Collett and C. W. Gardiner, *Phys. Rev. A* **30**, 1386 (1984).
- [35] C. W. Gardiner and C. M. Savage, *Opt. Commun.* **50**, 173 (1984).
- [36] C. Fabre, E. Giacobino, A. Heidmann, L. Lugiato, S. Reynaud, M. Vadacchino, and W. Kaige, *Quantum Opt.* **2**, 159 (1990).
- [37] L.-A. Wu, M. Xiao, and H. J. Kimble, *J. Opt. Soc. Am. B* **4**, 1465 (1987).
- [38] T. Aoki, G. Takahashi, and A. Furusawa, *Opt. Express* **14**, 6930 (2006).
- [39] S. Dwyer *et al.*, *Opt. Express* **21**, 19047 (2013).
- [40] J. Junker, D. Wilken, E. Huntington, and M. Heurs, *Opt. Express* **29**, 6053 (2021).
- [41] A. E. Dunlop, E. H. Huntington, C. C. Harb, and T. C. Ralph, *Phys. Rev. A* **73**, 013817 (2006).
- [42] C. W. Gardiner and M. J. Collett, *Phys. Rev. A* **31**, 3761 (1985).
- [43] U. Leonhardt, *Measuring the Quantum State of Light* (Cambridge University Press, Cambridge, England, 1997).
- [44] G. Adesso, S. Ragy, and A. Lee, *Open Syst. Inf. Dyn.* **21** (2014).
- [45] M. Mehmet, S. Ast, T. Eberle, S. Steinlechner, H. Vahlbruch, and R. Schnabel, *Opt. Express* **19**, 25763 (2011).
- [46] H. Vahlbruch, M. Mehmet, K. Danzmann, and R. Schnabel, *Phys. Rev. Lett.* **117**, 110801 (2016).
- [47] See Supplemental Material at <http://link.aps.org/supplemental/10.1103/PhysRevLett.129.033602> for animation showing the frequency-dependent rotation of the squeezed state.
- [48] ET Steering Committee Editorial Team, Technical Report No. ET-0007B-20, 2020.
- [49] M. Maggiore, C. V. D. Broeck, N. Bartolo, E. Belgacem, D. Bertacca, M. A. Bizouard, M. Branchesi, S. Clesse, S. Foffa, J. García-Bellido, S. Grimm, J. Harms, T. Hinderer, S. Matarrese, C. Palomba, M. Peloso, A. Ricciardone, and M. Sakellariadou, *J. Cosmol. Astropart. Phys.* **03** (2020) 050.

4.3 Quantum tomography

In [P2], we use quantum tomography to reconstruct the Wigner function of the frequency-dependent squeezed state. Because it is not treated comprehensively in the publication, it will be the subject of this section. It starts with a brief introduction to the concept of tomography in Subsec. 4.3.1. We will see that tomography is divided into *acquisition* and *reconstruction*. After the introduction, tomography is applied to quantum states, called *quantum tomography*. The goal is to reconstruct the Wigner function of the quantum state under investigation. Our quantum tomographic method is explained in Subsec. 4.3.2 and is performed after taking measurements with a homodyne detector. For the required measurements, we do not need to lock the detection phase of the local oscillator. Subsection 4.3.3 presents a roadmap with all the important steps required to convert the raw data into a Wigner function.

4.3.1 Tomography: imaging by sections

Tomography is a cross-sectional imaging procedure where an object is illuminated from different directions [KS01]. The transmitted or reflected rays are measured for different angular directions. These measurements form the *projections* of the object. The projections are required to create an image of the object using tomographic reconstruction. Computer-assisted tomography set the foundation for many modern revolutionary applications, e.g. in medicine [Rub14].¹² With the multi-directional method of tomography, it is e.g. possible to resolve the brain of a human [CPM87].

The tomographic acquisition and reconstruction are explained with the help of Fig. 4.3.

The tomographic acquisition yields in measured projections $p(s, \theta)$, which all depend on the projection angle θ and on the projection coordinate s . The object is defined by the function $f(x, y)$ in the object plane. The projections are calculated by using the *Radon transform* \mathcal{R} of the object, which is the line integral along the u coordinate

$$p(s, \theta) = \mathcal{R}\{f(x, y)\} \quad (4.1)$$

$$= \int_{L_{s, \theta}} f(x, y) du \quad (4.2)$$

$$= \int_{-\infty}^{\infty} f(s \cos \theta - u \sin \theta, s \sin \theta + u \cos \theta) du. \quad (4.3)$$

The projections $p(s, \theta)$ are concatenated and visualised in a so called sinogram.

In the experiment, usually, the projections are measured,¹³ and the object must be reconstructed. To solve this problem, the *inverse Radon transform* \mathcal{R}^{-1} is required, which is defined by [Leo97]

$$W(x, y) = \mathcal{R}^{-1}\{p(s, \theta)\} = -\frac{\mathcal{P}}{2\pi^2} \int_0^\pi \int_{-\infty}^{\infty} \frac{p(s, \theta) ds d\theta}{(x \cos \theta + y \sin \theta - s)^2}. \quad (4.4)$$

¹²The Nobel Prize in Physiology or Medicine 1979 was awarded jointly to Cormack, and Hounsfield for the development of computer-assisted tomography [N79].

¹³The projections are measured by either rotating the object or the projection plane, which is indicated by the dashed arrow in Fig. 4.3.

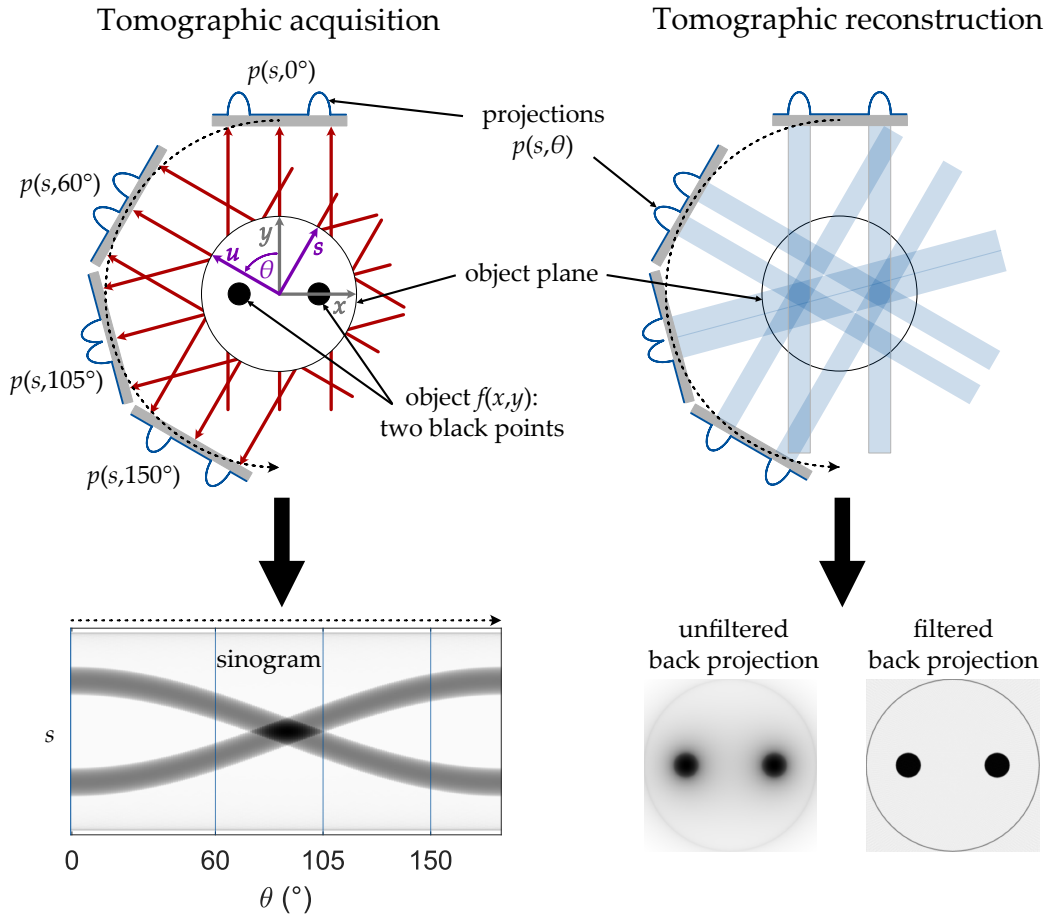


FIGURE 4.3: The basic principle of tomography. Left: The object consists of two solid black points in the object plane. The tomographic acquisition consists of the projections $p(s, \theta)$, which are obtained from measurements under different angles θ . They are all visualised in a sinogram. Right: The back projection leads to the tomographic reconstruction of the object, as indicated by the upper picture. For an unfiltered back projection, the object looks blurry. However, if the correct filters are applied, the original picture is reconstructed. The idea for this visualisation is taken from [Sei14].

The integral from Eq. (4.4)¹⁴ calculates the unfiltered back projection creating the picture of the object. However, it has a blurred appearance with less contrast; see bottom right of Fig. 4.3. Due to this problem, a filtered back projection is usually more appropriate to reconstruct the image. It consists of different high-pass filters applied in the Fourier plane [Rad17]. Overall, finding the reconstructed image $W(x, y)$ from Eq. (4.4) is the main goal of tomography.¹⁵

4.3.2 Locking-free tomographic acquisition of a squeezed state

Squeezing can be detected with a homodyne detector, but why do we need quantum tomography? Figure 4.4 visualises what is stated in Eq. (2.63): A homodyne detector measures a specific quadrature depending on the detection angle. In the figure, the detection angle is ramped over time, and the variance is monitored. For each

¹⁴The normalisation consists of \mathcal{P} that is defined as Cauchy's principal value of another integral from Eq. (5.5) from [Leo97].

¹⁵In comparison to the inverse Radon transform, other options are possible to reconstruct the image, such as the maximum likelihood reconstruction [Our+07; LR09; WF18].

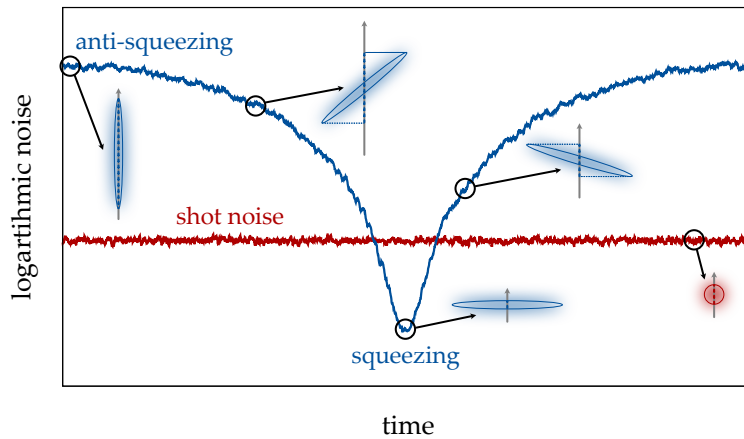


FIGURE 4.4: Homodyne measurement of a squeezed state while tracing over the detection angle. The projected noise on the vertical grey axis is measured for each detection angle.

detection angle, the squeezing ellipse has a particular orientation in phase space, and the measured noise is the state's projection onto the vertical grey axis. For instance, the maximum squeezing is observed when the ellipse is rotated perpendicular to the grey projection axis. However, it is not possible to *directly* generate the ellipse distribution from these measurements with the homodyne detector. Quantum tomography addresses the problem of reconstructing the squeezed ellipse *indirectly* from these projection measurements.

The first reconstruction of a squeezed state by applying quantum tomography was realised almost 30 years ago [Smi+93; BSM97]. From then, many experiments dealt with quantum tomography of various quantum states. In these experiments, two-mode squeezed states [D'A+09], Schrödinger cat states [Our+07], single-photon Fock states [ZVB04], or higher order Fock states [OTBG06; Coo+13] and frequency-dependent squeezed states [Che+05; Mil+22] were reconstructed.

First, we need to acquire the data, as mentioned in Subsec. 4.3.1. The standard approach is to take projection measurements with a homodyne detector for discrete detection phases $\theta \in [0, \pi)$. Usually, for each locked and thus defined detection phase θ_i , many noise measurements are taken.¹⁶ The noise data is sorted into a histogram to create a projection $p(s, \theta_i)$. For the histograms, parameters such as the bin size b and the number of bins n are chosen. The more data points N are monitored per detection angle, the higher the resolution of the reconstructed Wigner function.¹⁷ This procedure is repeated for n_θ different detection angles, resulting in an angular resolution of $\delta\theta = \pi/n_\theta$.

I used a slightly different approach to create the histograms in our tomographic acquisition. Instead of locking to fixed phase values, I continuously ramped the detection angle by changing the phase of the local oscillator (LO). For the setup, see again Fig. 3 in [P2]. Then, we beneficially do not need any active control for the detection angle, which could be unstable and noisy. The measured AC voltage U_{AC} (high-frequency noise amplitudes) and DC voltage U_{DC} (low-frequency interference signal) for a squeezed state being under tomographic acquisition are presented in

¹⁶Note that noise amplitudes are measured instead of variances.

¹⁷This is also true for the number of bins n , as long as enough data points N are taken, which is discussed in Sec. 4.6.

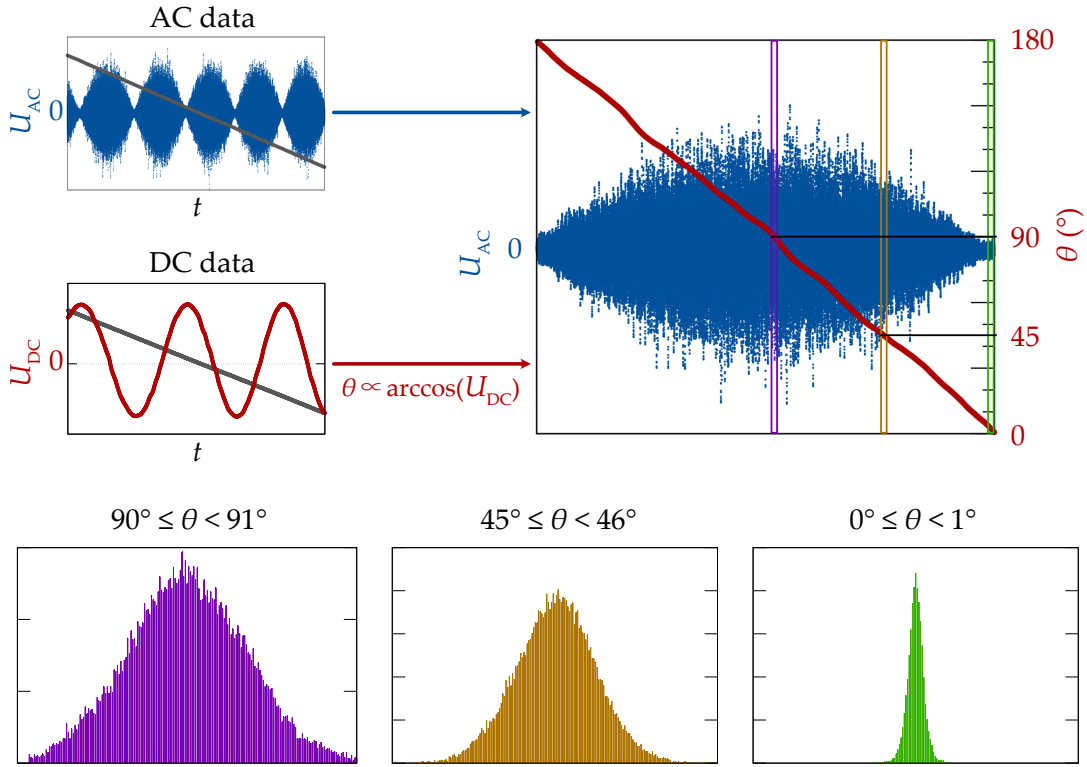


FIGURE 4.5: Tomographic acquisition. With the help of the DC voltages U_{DC} , each timestamp is connected to a specific detection angle θ . Then the AC voltage noise U_{AC} is sorted into $n_\theta = 180$ bins for the detection angle, e.g. $0^\circ \leq \theta < 1^\circ$. For each bin, a histogram is generated.

Fig. 4.5. From the DC trace, each timestamp is attributed to a detection angle by using the interference response $\theta \propto \arccos(U_{DC})$. Consequently, each AC noise voltage U_{AC} is connected to a specific detection angle θ_i . Then, the noise data is sorted into $n_\theta = 180$ angle bins with a bin size of $\delta\theta = 1^\circ$. For instance, the first bin is bounded by $0^\circ \leq \theta < 1^\circ$. The noise data is distributed in a histogram corresponding to our angle-dependent projections for each angle bin. In total, roughly 6 million data points are considered.

Experimentally, the detection phase is changed by a mirror clamped on a piezoelectric transducer (PZT). We applied a triangular voltage to the PZT.¹⁸ The movement of the PZT has a slightly non-linear behaviour. The non-linearity of the ramping function has no direct influence on our locking-free tomographic acquisition. Since each noise data point is always attributed to its actual detection angle, a ramp or a sine wave could also be used to change the phase via U_{DC} . Hence, our method is also not prone to any hysteresis or non-linear effects of our phase shifter.

Once the histograms are created, we reconstruct the Wigner function, which will be covered in the next subsection.

4.3.3 Quantum tomographic reconstruction

For the reconstructions, the following remarks are important. The projections are given by the obtained histograms. However, in general, each histogram can have a different number of data points due to the locking-free tomographic acquisition. Thus, the next step is to normalise all histograms and write them all in one matrix to

¹⁸A triangular ramp is used to get an equal number of data points per angle bin.

create the sinogram (matrix dimension: 201×180). I use the *iradon* command from MATLAB [Mat] to calculate the inverse Radon transform. Here, I first need to define the output size, which is the resolution of our image later. I chose an output size of $r = 140$. Namely, the resolution of the reconstructed Wigner function consists of $r^2 = 19600$ pixels. Then, the inverse Radon transform is computed, resulting in the reconstructed Wigner function. The last step includes two normalisations. First, the Wigner function is normalised on a vacuum state and independently reconstructed. It serves as a reference for our state under reconstruction. A two-dimensional, normalised Gaussian fit provides the widths of the two states. The actual squeezing and anti-squeezing values are obtained from the normalisation with a reconstructed vacuum state.

Finally, the Wigner function of a quantum state is reconstructed! Compared to the reconstruction procedure from Chapter 5, we do not have to assume a Gaussian state for quantum tomography. Since quantum tomography is a direct imaging procedure, it can also be applied to non-Gaussian states.¹⁹ Dealing with arbitrary quantum states is one big advantage of quantum tomography.

The choice of the parameters n , N , b and r was iteratively optimised. An indication of a good parameter choice is the visualised Wigner function, particularly its symmetry. For instance, the reason for a non-symmetric Wigner function can be in an even number of histogram bins²⁰ or if the histograms have an unequal number of data points.²¹

4.4 The single-mode resonant squeezer

This section starts with a characterisation of the setup in Subsec. 4.4.1. For the characterisation of the squeezer and the detection process, the same methods as in Subsec. 3.3.2 and Subsec. 5.4.1 are used. Then, parameters such as the total efficiency η are extracted, which later help to understand the detuned squeezer better. This section ends with Subsec. 4.4.2 where a 9 dB squeezed state reconstructed by quantum tomography is presented.

4.4.1 Characterisation

The resonant OPO is characterised in the same way as the similar²² OPO used for the spectroscopy experiment from Subsec. 3.3.2. A squeezing slope is measured to characterise the full system, presented in Fig. 4.6a). The curve fitting of the measurement data has the following parameters: pump threshold $P_{\text{th}} = 1.62 \text{ W}$, total efficiency $\eta = 92.8\%$ and phase noise $\Delta\phi = 15 \text{ mrad}$. From the individual efficiencies, the quantum efficiency of the homodyne detector $\eta_{\text{qe}} > 97.6\%$ is derived, as explained in Subsec. 2.4.3. In a separate measurement, the linewidth of the unpumped OPO was determined to 7.2 MHz. In the squeezing slope, the maximal anti-squeezing of 17.4 dB and squeezing of 9.8 dB were measured for a pump power of 920 mW, which is roughly 57% of the pump threshold.

The amplitude quadrature squeezed state is analysed at different frequencies when the OPO is pumped with 770 mW. The spectrum analyser [Keysight, N9020A

¹⁹An example of a non-Gaussian state reconstructed with tomography is a phase-diffused squeezed state [Fra+06], which was also reconstructed in our laboratory.

²⁰Then, there is no defined centre bin in the histograms. Hence, the rotation axis is not in the distribution centre.

²¹Then, the number needs to be normalised.

²²See Fig. 2.9 again.

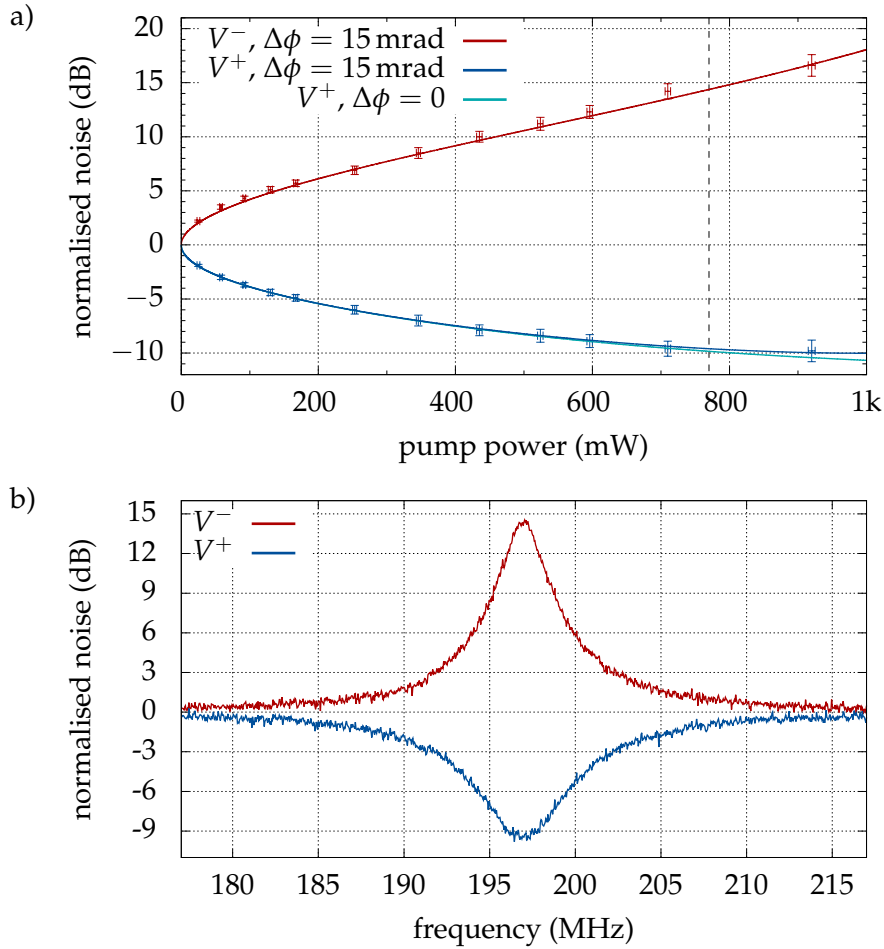


FIGURE 4.6: Top: Single-mode squeezing from a resonant OPO for different pump powers. The fitting parameters are $P_{\text{th}} = 1.62$ W, $\eta = 92.8\%$ and $\Delta\phi = 15$ mrad obtained from the theoretical traces by using Eq. (2.96). Bottom: The spectrum is measured with a pump power of roughly 770 mW (vertical dashed line in the top plot). It shows maximal squeezing in the amplitude quadrature $V^+ = -9.8$ dB (blue trace) and maximal anti-squeezing in the phase quadrature $V^- = 14.5$ dB (red trace) at 197 MHz. RBW 200 kHz, VBW 100 Hz. All traces are normalised to shot noise, and the electronic dark noise is subtracted.

MXA] measured a spectrum shown in Fig. 4.6b). This plot shows anti-squeezing again in the V^- variance (red trace) and squeezing in the V^+ variance (blue trace). The extreme values of the spectrum are observed at the first free spectral range frequency of $\delta\omega = 197$ MHz. There, the noise values are $V^- = 14.5$ dB and $V^+ = -9.8$ dB. They match the data from the squeezing slope. No better squeezing performance was published from our quantum control group before.²³

4.4.2 Wigner function of a 9 dB squeezed state

The squeezed state generated by the resonant OPO is tomographically reconstructed by applying the methodology from Sec. 4.3. The state under reconstruction is an amplitude quadrature squeezed state generated by the OPO pumped with $P = 700$ mW. For the reconstruction, 3.4 million data points are used. The angular resolution is

²³A previously locked squeezing spectrum revealed 1.96 dB of squeezing, see Fig. 7.6 from [Den16].

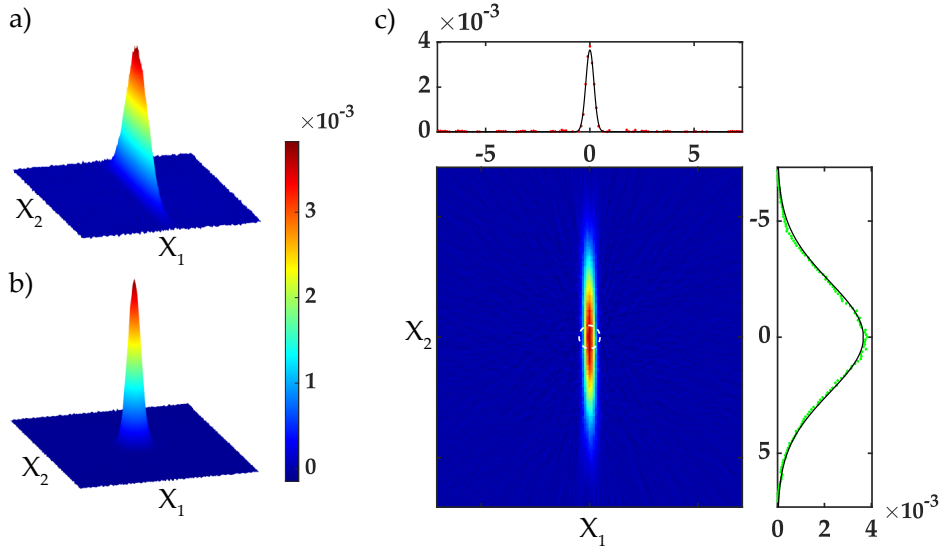


FIGURE 4.7: Shown are three-dimensional Wigner functions from a squeezed state in a) and a vacuum state in b). The vacuum state serves as a reference to calculate the widths and, thus, the squeezing factor of the squeezed state. In c), the calibrated Wigner function of the state is shown. It has linear widths of $\Delta X_1 = 0.34$ and $\Delta X_2 = 4.85$ at FWHM (the vacuum has $\Delta X_1 = \Delta X_2 = 1$). These values are already corrected for the electronic dark noise.

$\delta\theta = 0.5^\circ$, such that $n_\theta = 360$ histograms are created. The bin size of the $n = 201$ bins in the histograms is $b = 37 \mu\text{V}$.

The reconstructed Wigner function of the squeezed state is depicted in Fig. 4.7. The images a) and b) show three-dimensional Wigner functions of the squeezed state and a vacuum state used as a reference. In c), the squeezed Wigner function is visualised in a two-dimensional colour density plot. From the two-dimensional Gaussian fit, the widths of the minor (red data points) and major (green data points) axis are obtained. The dashed white circle gives the width of the reference vacuum state at full width at half maximum (FWHM). The variance of the amplitude quadrature is $\text{var } X_1 = -9.1 \text{ dB}$ and of the phase quadrature $\text{var } X_2 = 13.7 \text{ dB}$. The electronic dark noise undergoing the shot noise by 15 dB is already subtracted from these values.

The Wigner function of the squeezed state agrees with the previously presented characterisations from Subsec. 4.4.1 within the measurement uncertainties. The agreement indicates that the suggested quantum tomographic approach creates valuable results. It can be applied to any arbitrary Gaussian or non-Gaussian quantum state of interest. The next section deals with a frequency-dependent squeezed state generated by the detuned OPO.

4.5 The single-mode detuned squeezer

To generate frequency-dependent squeezing from the OPO, only one modification is required: The resonance frequency of the OPO needs to be detuned to the laser frequency. The first Subsec. 4.5.1 of this section is devoted to showing how the detuning in the OPO is realised experimentally. With a locked pump phase, a stabilised frequency-dependent squeezed state is generated. Subsection 4.5.2 deals with the effective pump threshold, which additionally helps to understand the concept of the detuned squeezer.

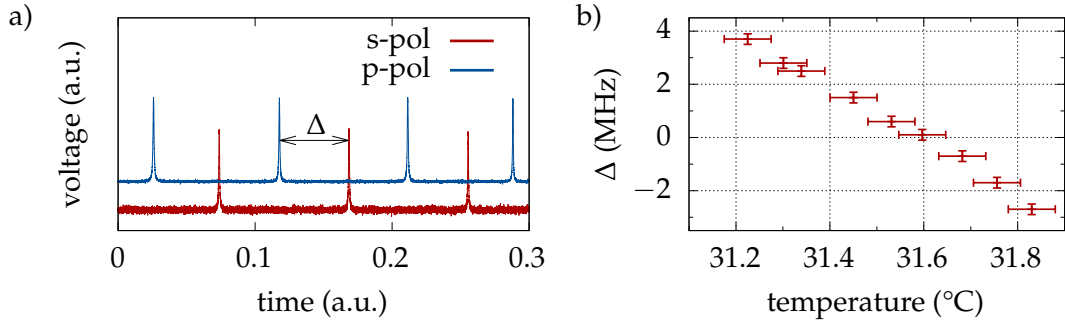


FIGURE 4.8: a) Polarisation modes in the OPO separated by frequency distance Δ of the s- and p-polarised modes. b) Plot of the detuning Δ depending on the polarisation degeneracy temperature T_{PD} of the small fraction of the PPKTP crystal.

4.5.1 Stabilising the detuned OPO

The OPO is in a detuned resonance condition when *frequency-degenerated* signal/idler sideband pairs do not see a resonant cavity. Multiple options are possible to lock the OPO in such a resonance condition detuned by Δ . For instance, the OPO can be locked on the resonance of an ancilla laser field frequency-shifted by Δ . Another option for locking is to use modulation sidebands located at $\pm\Delta$ with respect to the cavity frequency. Then, the Pound-Drever-Hall (PDH) error signal of the sideband can be taken. However, we apply a different approach in our publication [P2]. We exploit the effect of polarisation non-degeneracy in the cavity to detune the OPO because it is simple to realise and tune.

Since the down-conversion process takes place only in the s-polarisation, the cavity lock can be independently conducted with the orthogonal p-polarisation mode. In general, mainly due to the birefringent non-linear periodically-poled potassium titanyl phosphate (PPKTP) crystal, the OPO is non-degenerated for both polarisation contributions. The frequency distance is measured by detecting both modes on a polarisation selective detector in transmission of the OPO. The detector consists of a polarising beam splitter (PBS) followed by two photodiodes in the output ports.²⁴ When the OPO is ramped, both modes are monitored, as shown in Fig. 4.8a). The measured time between the two modes can be transformed into the frequency distance Δ by using the known free spectral range as a reference. The detuning is interpreted as the degree of polarisation non-degeneracy in the cavity. In the measurement in Fig. 4.8a), the frequency distance is relatively large and in the order of half the free spectral range. Note that the frequency distance can be either positive for a blue-detuned p-polarisation or negative for a red-detuned p-polarisation.

The OPO is locked on resonance for the p-polarisation. In general, the cavity phase for the s-polarisation and, thus, the detuning can be arbitrary. However, the detuning Δ is easily changed by increasing the optical path length in the birefringent wedged crystal or by the temperature T_{PD} .²⁵ The frequency distance Δ is measured for different temperatures T_{PD} to characterise the effect of polarisation non-degeneracy.

Figure 4.8b) shows the temperature sensitivity of the detuning in the OPO. Here, the frequency distance Δ is plotted over the temperature of the small fraction of the crystal T_{PD} . For a temperature of roughly $T_{\text{PD}} = 31.6^{\circ}\text{C}$, the OPO becomes polarisation-degenerate. Then, the OPO behaves as a resonant squeezer, even though

²⁴This detector is not depicted in Fig. 3 in [P2]

²⁵For detailed explanations, see again Subsec. 2.4.1 and Fig. 2.10b).

it is locked with the *wrong* polarisation mode. Of course, these exact values are only reproducible for a fixed crystal alignment position. Displacing the crystal will immediately change the polarisation non-degeneracy due to changing optical lengths in the birefringent crystal. In [P2], the detuning Δ was once adjusted before the tomographic acquisition was done.

4.5.2 The effective pump threshold

In the OPO, the pump threshold is the specific power where the round-trip losses are equal to the non-linear gain induced by the pump. For powers above the threshold, the OPO starts to lase and produces a bright squeezed state [Jin+06]. In this section, we discuss how the dynamics of the OPO change concerning the pump threshold when it is operated in a detuned resonance condition. The pump threshold is an important parameter to better understand the features of the frequency-dependent squeezed state generated by the detuned OPO.

First, we consider the situation in a resonant OPO. When a pump photon is converted into frequency-degenerate signal and an idler photons, the optical properties of the cavity define how long they circulate in the cavity before leaving. If the coupling strength threshold is exceeded, the OPO generates a bright field at the frequency of the signal/idler field. The squeezing effect is maximal for degenerate signal and idler pairs being resonant in the OPO (see Eq. (2.86)) or for non-degenerate signal and idler pairs being resonant at higher free spectral ranges (see squeezing spectrum from Fig. 4.6). Off-resonant frequency non-degenerate signal/idler pairs create a less squeezed state. Notwithstanding, the smaller squeezing is not due to more optical loss. Moreover, the cavity provides less power build-up for these frequencies away from resonance (see again Fig. 4.2a)), which can be interpreted as an effectively higher pump threshold.²⁶ Analogous considerations can be conducted for the detuned OPO.

In a detuned OPO, frequency-degenerated signal/idler pairs experience a lesser build-up due to the cavity amplitude transfer function, as indicated in Fig. 4.2d). This situation resembles non-degenerate pairs in a resonant OPO. That is why the pump threshold in a detuned OPO is larger compared to a resonant OPO.

For a resonant OPO, the pump threshold is defined according to Eq. (2.96). From the measurements presented in Fig. 4.6 we get a pump threshold of $P_{\text{thr}} = 1.62 \text{ W}$. This power can also be expressed in units of coupling strengths, see Eq. (2.89), which is done in the following.

Figure 4.9 shows simulated noise variances depending on the coupling strength. We distinguish between a resonant and detuned OPO by $\Delta = -2\pi \times 3.6 \text{ MHz}$. For the resonant OPO the lasing threshold is observed at $|g_{\text{thr}}^0| = \kappa = 2\pi \times 3.2 \text{ MHz}$. We also determine that for the detuned OPO the lasing threshold shifts to $|g_{\text{thr}}^\Delta| = 2\pi \times 4.8 \text{ MHz}$. The plot is created by using Eq. (7) in [P2] with the following parameters: $\omega = 0$, $\eta = 92.8\%$, $\delta\psi = 15 \text{ mrad}$, $\kappa = 2\pi \times 3.2 \text{ MHz}$. The two readout angles are chosen as $\psi_1 = \psi_0$ and $\psi_2 = \psi_0 + \pi/2$ to find the correct projection axis of squeezing and anti-squeezing.²⁷ Note that the minima of both squeezing curves (blue and orange traces) reach the same level of -10 dB . Hence, with the detuned OPO, the same squeezing levels can be reached as with the resonant one. The drawback is that more pump power is required in the detuned case. The benefit is that the generated state exhibits frequency-dependent squeezing.

²⁶Nevertheless, the state's purity for non-degenerate signal/idler pairs is usually larger because less squeezed states are less prone to the optical loss occurring, e.g. inside the cavity. The purity will be subject of Subsec. 5.1.2.

²⁷This is basically a matrix diagonalisation made for each measurement frequency.

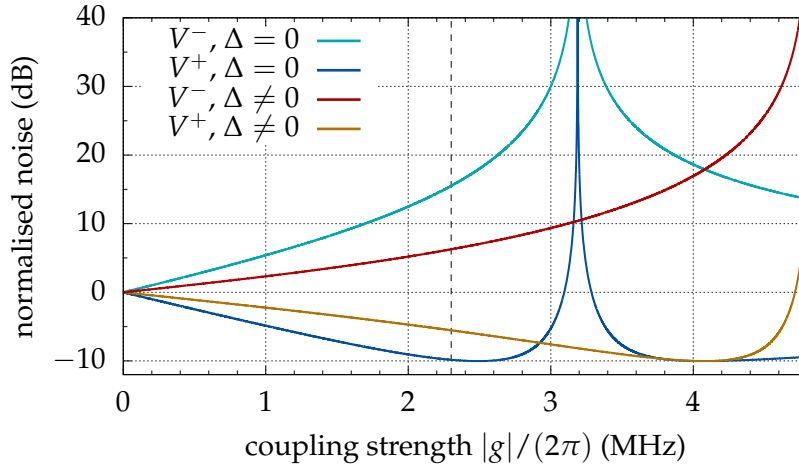


FIGURE 4.9: Maximal squeezed and anti-squeezed variances $V^+ = \bar{\sigma}_{22}(\psi_\omega)$ and $V^- = \bar{\sigma}_{11}(\psi_\omega)$ plotted over the coupling strength $|g|$ relative to shot noise. The resonant case with $\Delta = 0$ is visualised by the blue and turquoise traces. Here, the threshold coupling strength is $|g_{\text{thr}}^0| = \kappa = 2\pi \times 3.2$ MHz. For the detuned OPO with $\Delta = -2\pi \times 3.6$ MHz, the threshold coupling strength increases to $|g_{\text{thr}}^\Delta| = 2\pi \times 4.8$ MHz. The vertical dashed line indicates the coupling strength of $|g| = 2\pi \times 2.3$ MHz for which the measurements are taken in [P2].

Furthermore, the diagonalisation of the covariance matrix given by Eqs. (4) and (5) in [P2] is discussed next. Equation (5) in [P2] calculates the angle ψ_0 needed to diagonalise the covariance matrix σ . Here, ψ_0 always rotates σ onto the closest quadrature axis. For instance, for a squeezed state rotated by 40° , we find $\psi_0 = -40^\circ$. However, a squeezed state rotated by 55° has $\psi_0 = 35^\circ$. In Eq. (5) in [P2] this effect can be seen by looking at the denominator. If the absolute of the detuning is larger than the linewidth of the cavity ($|\Delta| > \kappa$),²⁸ the argument of the arctangent in Eq. (5) in [P2] flips its sign for increasing coupling strengths g . Apparently, Eq. (5) in [P2] works only for ($|\Delta| \leq \kappa$). A more general formulation of ψ_0 avoiding the sign flip can be written as

$$\psi_0 = \frac{1}{2} \arccos \left(\frac{\sigma_{11} - \sigma_{22}}{\sqrt{(\sigma_{11} - \sigma_{22})^2 + 4\sigma_{12}^2}} \right). \quad (4.5)$$

For creating the graphs in Fig. 4.9, this corrected and more general definition of ψ_0 is used.

4.6 Discussion and conclusion

This chapter closes with a discussion and conclusion on the detuned OPO. The discussion is split into a technical part mentioning challenges not presented in [P2]. In particular, it will point out suggestions for future setup improvements. Then, we dive deeper into implementing the frequency-dependent squeezed state in quantum optomechanical experiments. For CQNC, an inversely-input squeezed state is required to cancel quantum back-action noise. This section pinpoints that the frequency-dependent squeezed state generated by the detuned OPO does not fully match the needed inversely-input squeezed state.

²⁸In [P2], this relation is expressed in $\tilde{\Delta} = |\Delta|/\kappa$.

Reconstructing the Wigner function at multiple frequencies requires measuring millions of data points. The whole measurement procedure to create the Wigner functions shown in [Wig] is limited by the data storage time and roughly takes one hour. During that time, the detuned OPO runs in a steady condition generating a stable squeezed state. Nevertheless, the adjusted detuning Δ is not actively locked. Moreover, it is prone to any temperature changes, similar to our non-degenerate optical parametric oscillator (NDOPO), which will be subject to the next Chapter 5. Also, Subsec. 5.4.2 will elaborate on temperature stability. Temperature drifts in the crystal of the detuned OPO affect the detuning Δ . Our observations indicate that the detuning is not perfectly constant. During the measurements, we estimated a drift of roughly ± 100 kHz. However, in the future, I recommend studying the temperature dependence of the detuning in detail, especially since it is also relevant for our CQNC experiment [Ste19; Sch+22].

To reconstruct the frequency-dependent Wigner functions, quantum tomography was used. In our approach, each histogram's detection phase is rather ramped than locked. Consequently, a fundamental error occurs, which depends on the definition of the phase bin sizes $\delta\theta$. In our measurements, it was either 0.5° or 1° . Reducing the size also reduces the number of data points corresponding to the particular histogram. Thus, defining the bin size is always a trade-off between angular resolution and smoothness (number of data points) of the histograms.

Detuning an OPO enables the generation of a special quantum state. We have seen in Subsec. 4.5.2 that for a constant pump power, detuning the OPO will decrease the amount of generated squeezing. However, a different resonance condition does not influence the state's purity.²⁹ To generate a frequency-dependent squeezed state exhibiting squeezing values of up to 10 dB, the coupling strength of the down-conversion process must be increased. This can happen using more pump power or a higher-reflective input coupler to reduce the pump threshold (see Eq. (2.89)).³⁰ Another option is to use a cavity design that is doubly resonant for the fundamental and the harmonic field, as in [Vah+16]. In the following we discuss the potential applicability of a tailored squeezed state generated by the detuned OPO.

The reconstructed quantum state under investigation exhibits a frequency-dependent squeezing factor *and* angle. In CQNC, an inversely-input squeezed state is required to cancel the effect of the quantum back-action noise arising in an opto-mechanical system [TC10; Wim16; Ste19]. One example of an opto-mechanical system is a gravitational wave detector consisting of a Michelson interferometer with suspended optics. For a Michelson interferometer with arm cavities having bandwidths of 2γ , the required inversely-input squeezed state has a squeezing factor³¹

$$R(\Omega) = \operatorname{arcsinh} \left(\frac{\mathcal{K}}{2} \right), \quad (4.6)$$

and a squeezing angle

$$\phi(\Omega) = -\frac{1}{2} \operatorname{arccot} \left(\frac{\mathcal{K}}{2} \right), \quad (4.7)$$

with Kimble factor

$$\mathcal{K}(\Omega) \propto \frac{1}{\Omega^2(\gamma^2 + \Omega^2)}. \quad (4.8)$$

²⁹This is only true if the OPO cavity is lossless. With losses, the state generated by a detuned OPO is even purer since it is less prone to optical losses because of its smaller squeezing factor.

³⁰A higher-reflective input coupler will decrease also the escape efficiency.

³¹Expressions taken from [Kim+01], Eq. (18) and Eq. (31).

The frequency-dependent squeezed state generated by the detuned OPO needs to match with Eq. (4.6) and Eq. (4.7) to apply it as an inversely-input squeezed state. The matching is a non-trivial task since both the required squeezing angle and factor follow different mathematical functions. The squeezing angle of the state generated by the detuned OPO is according to Eq. (6) in [P2]

$$\theta(\Omega) = -\frac{1}{2} \arctan \left(\frac{2\kappa\Delta}{\Delta^2 - \kappa^2 - g^2} \right) + \frac{1}{2} \arctan \left(\frac{2\kappa\Delta}{\Delta^2 - \kappa^2 - g^2 - \omega^2} \right). \quad (4.9)$$

For the squeezing factor, the equation becomes much more cumbersome and is not printed here.³² If the detuned squeezer is considered as an effective negative-mass oscillator for CQNC, the next step seems to be a numeric optimisation of the parameters to best meet the requirements for $R(\omega)$ and $\phi(\omega)$. For instance, the parameters could be tuned only for a specific frequency band of interest. I have already conducted simulations showing a noise improvement in the context of CQNC if the detuned OPO is used as an effective negative-mass oscillator.

In conclusion, the detuned OPO is a simple way to generate a tailored quantum state exhibiting frequency-dependent squeezing. An orthogonally polarised additional light field locks the cavity. An arbitrary detuning is adjusted by slightly changing the crystal's temperature. Advantageously, the required temperature change is small, so the coupling strength is effectively not deteriorated. The generated frequency-dependent squeezed state is detected with a homodyne detector with a ramped detection angle. Taking many measurements allows us to reconstruct the state's Wigner functions at selected Fourier frequencies by applying quantum tomography. These reconstructions reveal that the state exhibits frequency-dependent squeezing. Additionally, different squeezing spectra, with each having a constant detection angle, are measured (Fig. 4 in [P2]). These spectra match the results from the quantum tomographic reconstruction. They show similar features as former publications demonstrating frequency-dependent squeezing [Che+05; Oel+16b; Zha+20; Yap+20; McC+20; Süd+20]. The detuned OPO turned out to be an exciting system worth continuing to study in the future, especially for systems limited by quantum back-action noise [Mag+20; Yu+20].

³²The squeezing factor is obtained from σ_{11} with optimised detection angle ψ_ω .

Chapter 5

Reconstruction of two-mode squeezed bipartite states

Many optical experiments use specific quantum states tailored to their needs. Some experiments use these states to reduce quantum noise, while others benefit from quantum entanglement, applicable, e.g. for quantum information. It is always relevant to ascertain the condition of the used quantum state to a high degree of accuracy. The goal of *quantum state reconstruction* is to find the full set of parameters describing a quantum state. The reconstruction of a quantum state can be arbitrarily difficult. Single-mode Gaussian¹ squeezed states, e.g., can be characterised by only a few parameters as the squeezing angle and factor. However, for Gaussian multi-mode squeezed states, the number of parameters drastically increases.

Compound systems can be divided into subsystems, and any subsystems can be combined into a composite system. In general, this statement is true for classical systems, e.g. for the solar system, including the planets and the sun as the subsystems. In quantum mechanics, the properties of composite systems can be completely different, e.g. when they exhibit quantum entanglement. However, local operations, e.g. state manipulations or measurements, can be performed for subsystems of composite systems [Aud07]. The simplest composite system is a *bipartite system* consisting of *two* subsystems. For instance, two simultaneously created, entangled photons form a bipartite system. Bipartite quantum states play a major role in quantum information theory, where the special features of these states are utilised.

This chapter deals with the reconstruction of bipartite states, studied in our publication [P3]. Section 5.1 starts with an introduction to bipartite states and their applications in quantum technologies. The section is dedicated to better understanding these kinds of states and relating them to polarisation two-mode squeezing. Section 5.2 reprints the publication [P3]. Section 5.3 again takes up the used detection schemes and expands [P3] with more details. It explains two ways of detecting two-mode squeezing: the conventionally used dual homodyne detection method and our polarisation-sensitive single homodyne detection. Next, the experimental generation of bipartite states with a two-mode squeezer will be considered in Sec. 5.4. In particular, more details are given on the stability of the non-degenerate optical parametric oscillator (NDOPO). Section 5.5 provides more information on preparing the polarisation-sensitive homodyne detector. It gives some missing data acquisition and statistical analysis information and shows all cross-sections of the reconstructed Wigner function. Finally, this chapter closes with a conclusion and a discussion.

¹In this chapter, we assume the state to be reconstructed as Gaussian, which is fully described by its covariance matrix.

5.1 Introduction

This section is devoted to bipartite states, which gained increasing importance in quantum optics. For instance, gravitational wave detectors or experiments related to quantum communication call for bipartite states. Subsection 5.1.1 gives an overview of different physics applications where bipartite states are employed. We take a closer look at the character of quantum optical bipartite states in Subsec. 5.1.2. We will define them and introduce some characteristics as quantum entanglement. Bipartite states are found in the regime of small photon numbers or for continuous waves. We will focus on the latter class and, in particular, discuss the two-mode squeezed state as an example of bipartite states.

5.1.1 Quantum technologies for entangled bipartite states

According to their name, quantum technologies use quantum effects – but what does this mean exactly? The properties of quantum mechanics, such as quantum entanglement or quantum tunnelling, form the basis for all applications in the field of quantum technologies [RV14]. Here, we want to focus on the manifold demand for entangled bipartite states.

Bipartite states are interesting for the detection of gravitational waves. Seven years after the first detection of gravitational waves [Abb+16a], gravitational wave detectors call for higher sensitivities than ever before. The standard quantum limit classically limits the sensitivity. However, it can be surpassed by using methods relying on quantum mechanics [GLM04]. For instance, single-mode squeezed states of light can be used to beat the standard quantum limit. However, producing the required frequency-dependent squeezed state to achieve perfect quantum noise cancellation is technically difficult. Another solution to surpass the standard quantum limit is the use of entangled bipartite states of light. By harnessing their mutual quantum correlations, the required frequency-dependent squeezed state can be produced [Ma+17; Süd+20].

Quantum entanglement also plays a role in quantum communication, particularly because of its non-locality [GT07; Zou21]. Quantum communication demands secure ways of exchanging information and therefore aims for channels protected against eavesdropping. One popular application is quantum key distribution [Sca+09]. Here, information is exchanged between two connected parties via a quantum channel and a classical channel. The quantum channel produces a secret quantum key, only shared by the two parties. It is required to encrypt and decrypt messages. Quantum key distribution can be performed with discrete variables [Lia+17], but also with continuous variables [Jou+13; Zha+19].

A particular way of quantum communication is quantum teleportation. Here, instead of physical objects as seen in science fiction, *quantum information* is teleported. Quantum teleportation works with discrete variables [Ben+93] and continuous variables [BK98; YAF04]. For instance, two entangled and spatially separated particles are required in quantum teleportation with discrete variables. Then, the state of a third particle can be instantly teleported from the first to the second particle, by including it to the entanglement.²

Bipartite entangled states are successfully used in quantum imaging [Tre+02]. By using quantum entanglement, the goal is to beat the limits of imaging resolution achievable with classical optics [KF00]. Quantum imaging is a growing field exhibiting many different methods. The resolution of an image can be improved,

²The third particle's state is not cloned but destroyed as shown in the no-cloning theorem in [WZ82].

e.g. by entangled states called NOON states³ for differential interference contrast microscopy [OOT13]. In quantum lithography, the so-called *quantum super resolution* can be obtained from two-photon interferences [DCS01]. These examples represent a range of different applications for entangled bipartite states.

5.1.2 Deciphering the covariance matrix of bipartite states

This subsection is devoted to understanding continuous variable bipartite states, also called two-mode states. In this chapter, all considered bipartite states are Gaussian,⁴ allowing us to fully describe their quantum noise with the covariance matrix. With few simple definitions, these states can be well explained and categorised. For instance, we can distinguish between pure and mixed states. An important property of bipartite states is their entanglement or separability. This subsection is not intended to include the full theory of bipartite states⁵ but rather summarises the properties and features most relevant to this thesis.

As already mentioned in Subsec. 2.2.2, two-mode quantum states are described by four canonical quadrature operators, which we call $\mathbf{X} = \{X_1^s, X_2^s, X_1^p, X_2^p\}$ in the following. Compared to the single-mode quantum states, the parameter space has doubled. Now, it is four-dimensional, which makes bipartite states harder to visualise, e.g. by using the Wigner function from Eq. (2.32).⁶ The covariance matrix from Eq. (2.30) now has a size of 4×4 containing the full information about the state's quantum noise. It provides the pureness of a state, the separability and entanglement character.

The covariance matrix gives insight into the pureness of the state. The presented minimum uncertainty states from Subsec. 2.2.3 are examples of pure states [NC12]. In Subsec. 2.2.3, we also have seen that optical loss can be understood as mixing these states with vacuum noise. Thus, states affected by optical loss are not pure anymore and are called *mixed states*. Analytically, pure and mixed states are distinguished by considering the determinant of the covariance matrix σ [ARL14]:

$$\det(\sigma) = \begin{cases} 1 & \implies \text{pure} \\ > 1 & \implies \text{mixed.} \end{cases} \quad (5.1)$$

With the determinant, the purity μ of an N -mode Gaussian state can be calculated by [ARL14]

$$\mu = \frac{1}{\sqrt{\det \sigma}}. \quad (5.2)$$

For any N -mode vacuum state with covariance matrix σ , we find $\mu = 1$. For instance, a single-mode squeezed state with initial squeezing of 10 dB (20 dB) suffering 10 % optical loss will turn into a mixed state with purity $\mu = 0.76$ (0.32). In comparison, a two-mode squeezed state with initial squeezing of 10 dB (20 dB) suffering 10 % optical loss will have a purity of $\mu = 0.58$ (0.10). Both squeezed states have squeezing factors of 7.2 dB (9.6 dB). We see that two-mode squeezed states are more prone to optical losses regarding their purity.

³NOON states are entangled states with a superposition of N particles in one mode and zero in the other and vice versa. NOON states, whose name was first used in [LKD02], can be created, e.g. from Hong-Ou-Mandel interference of two photons on a beam splitter [HOM87].

⁴We also assume our two-mode squeezed states as Gaussian. This is only an approximation because non-Gaussian phase noise will always be present.

⁵A good theoretical overview is given in [ARL14].

⁶The Wigner function of a bipartite state is usually visualised by projections onto two-dimensional subspaces, as will be done in Fig. 5 in [P3] and in Subsec. 5.5.3.

Entanglement and separability are fundamental concepts in quantum information theory. A state is *entangled* if it is impossible to describe the correlations between the canonical operators in classical terms. If possible, we call the state *separable*. Thus, entanglement is synonymous with the lack of separability [Wat18].

The concepts of entanglement and separability can be connected to the covariance matrix σ . Analysing the covariance matrix of a two-mode squeezed state, given in Eq. (2.48), discloses that the four individual quadratures have enhanced noise compared to a vacuum state. However, a proper combination of quadratures leads to a noise reduction, which is called two-mode squeezing. These combinations are defined in Chapter 2 in Eqs. (2.46a)–(2.47b). In principle, the pair (X_Σ, X_Λ) can be measured with arbitrary precision at the same time⁷ which demonstrates the Einstein-Podolsky-Rosen (EPR) paradox [EPR35; Ou+92]. Experimentally, $\text{var}(X_\Sigma)$ and $\text{var}(X_\Lambda)$ can be either measured directly or obtained from a reconstructed covariance matrix.⁸

With the variances $\text{var}(X_\Sigma)$ and $\text{var}(X_\Lambda)$, two famous criteria can be investigated. First, the Duan criterion for inseparability states that an inseparable state with EPR operators X_Σ and X_Λ fulfils [Dua+00]

$$\text{var}(X_\Sigma) + \text{var}(X_\Lambda) < 2. \quad (5.3)$$

Accordingly, if the inequality is not fulfilled and the left-hand side goes below 2, this is a sufficient condition for an inseparable state. Hence, the state is found to be entangled.⁹ Quantum entanglement is also analysed with the Reid criterium, which can be seen as an inferred Heisenberg uncertainty relation. If the inequality [Rei89]

$$\text{var}(X_\Sigma) \times \text{var}(X_\Lambda) < 1 \quad (5.4)$$

is fulfilled, this shows that X_Σ and X_Λ are EPR operators demonstrating the EPR paradox. Here we should emphasise again that a Gaussian (bipartite) EPR entangled state is also called a two-mode squeezed state to pinpoint the presence of quantum correlations in the two modes [HSS10]. The two-mode squeezed vacuum state is the quantum optical representative for bipartite continuous-variable entanglement [BL05; AMN08].

The paper [P3] is reprinted in the next section.

5.2 [P3]: Reconstructing Gaussian bipartite states with a single polarization-sensitive homodyne detector

This subsection reprints the following publication, which was accepted on 27 July 2022 and published on 31 August 2022 in Optics Express. The author contributions and a short abstract can be found on Page iii.

[P3] J. Junker, D. Wilken, D. Steinmeyer, and M. Heurs. “Reconstructing Gaussian bipartite states with a single polarization-sensitive homodyne detector”. In: *Opt. Express* 30.19 (Sept. 2022), pp. 33860–33868. DOI: [10.1364/OE.465186](https://doi.org/10.1364/OE.465186)

⁷Without loss of generality.

⁸This can be done by using Eq. (2) in [P3].

⁹For a maximally entangled state, the left-hand side is zero.



Reconstructing Gaussian bipartite states with a single polarization-sensitive homodyne detector

JONAS JUNKER,^{*}  DENNIS WILKEN,  DANIEL STEINMEYER, AND MICHÈLE HEURS 

Max Planck Institute for Gravitational Physics (Albert Einstein Institute), and Institute for Gravitational Physics, Leibniz Universität Hannover, Callinstraße 38, 30167 Hannover, Germany

**jonas.junker@aei.mpg.de*

Abstract: We present a novel method to fully estimate Gaussian bipartite polarization states using only a single homodyne detector. Our approach is based on [*Phys. Rev. Lett.* **102**, 020502 (2009)], but circumvents additional optics, and thereby losses, in the signal path. We provide an intuitive explanation of our scheme without needing to define auxiliary modes. With six independent measurements, we fully reconstruct the state's covariance matrix. We validate our method by comparing it to a conventional dual-homodyne measurement scheme.

© 2022 Optica Publishing Group under the terms of the [Optica Open Access Publishing Agreement](#)

1. Introduction

Bipartite Gaussian states increasingly gain importance as a reliable resource for numerous quantum technologies. The need for continuous-wave bipartite (entangled) states reaches from gravitational wave metrology [1,2] over quantum communication [3] including quantum teleportation [4,5] to quantum imaging [6,7]. For a full state characterization, the covariance matrix of the bipartite state needs to be measured. It contains the complete entanglement information and, therefore, allows to determine the quality of the state.

To reconstruct the covariance matrix of a bipartite Gaussian state, usually a homodyne measurement is performed. The measurement process destroys the optical quantum state and, in return, provides information needed to reconstruct the covariance matrix of the state. Any quantum decoherence arising before (e.g., due to lossy optics) or during the detection process (e.g., due to non-unitary detection efficiency) will degrade the reconstruction fidelity and should be avoided.

We consider Gaussian two-mode squeezed states where for specific combinations of quadratures the noise is reduced below the classical limit. Traditionally, these states are detected with a dual-homodyne scheme, which effectively measures both modes individually before the signals are electrically combined [8–11]. However, the full covariance matrix can also be obtained by using only a single homodyne detector (HD) [12,13]. The method demonstrated in [14] requires the measurement of additionally defined modes which need to be detected in a series of different measurements. In [14] the detection scheme itself inherently introduces decoherence. The two-mode squeezed state needs to pass through up to three additional optical components, introducing optical loss, even though on a small scale, degrading the bipartite state's quality before its detection.

In this letter, we present an advanced single-homodyne detection scheme to reconstruct the full covariance matrix of a two-mode squeezed state generated by a polarization-non-degenerate optical parametric oscillator (NDOPO). To measure variances of different combinations of quadratures, our technique requires six measurements with differently polarized local oscillators. We provide an intuitive explanation of our scheme. Compared to [14], the state under consideration does not pass three additional optics, typically introducing an optical loss of about 0.5%. Thus, our state deteriorates less on the way to the detection, avoiding decoherence. While this effect is small for currently achieved polarization bipartite states, it becomes relevant once two-mode

squeezing levels reach performance of the current single-mode squeezers [15]. In addition, we were able to reduce the number of required optical components. With our measurement, we show that the estimated two-mode squeezed state fulfills the Duan criterion [16] and the Reid criterion [17] demonstrating the Einstein-Podolsky-Rosen (EPR) paradox. To confirm our method, we compare our results to a measurement with a conventional dual-homodyne scheme.

2. Theoretical background

We consider bipartite two-mode squeezed Gaussian states with s- and p-polarized non-degenerate modes a_s and a_p . The state is described by a set of canonical operators $\mathbf{X} = (x_1^s, x_2^s, x_1^p, x_2^p)$, with amplitude quadratures $x_1^j = (a_j + a_j^\dagger)$ and phase quadratures $x_2^j = i(a_j - a_j^\dagger)$ with $j = \{s, p\}$. An arbitrary quadrature operator measured in a reference system rotated by α can be written as $x_\alpha^j = x_1^j \cos \alpha + x_2^j \sin \alpha$.

Gaussian states are fully characterized by their first and second moments [18]. The first moments \mathbf{d} are defined as $d_k = \langle X_k \rangle$ and vanish for undisplaced states, e.g. for squeezed vacuum. The second moments are represented in the covariance matrix σ and contain the full information about the (quantum) noise and the entanglement. The covariance matrix is a real symmetric positive matrix defined as

$$\sigma = \begin{pmatrix} \text{var } x_1^s & \text{cov } x_1^s, x_2^s & \text{cov } x_1^s, x_1^p & \text{cov } x_1^s, x_2^p \\ \text{cov } x_2^s, x_1^s & \text{var } x_2^s & \text{cov } x_2^s, x_1^p & \text{cov } x_2^s, x_2^p \\ \text{cov } x_1^p, x_1^s & \text{cov } x_1^p, x_2^s & \text{var } x_1^p & \text{cov } x_1^p, x_2^p \\ \text{cov } x_2^p, x_1^s & \text{cov } x_2^p, x_2^s & \text{cov } x_2^p, x_1^p & \text{var } x_2^p \end{pmatrix}. \quad (1)$$

For a coherent state all covariances (the off-diagonal elements) vanish and the covariance matrix has a diagonal form with $\sigma = \text{diag}(1, 1, 1, 1)$. For a polarization two-mode squeezed state the covariance matrix is not diagonal due to correlations between the quadratures. Instead of squeezing, an amplified noise will be visible when looking only at variances of single quadratures. However, we measure squeezing in the combined quadrature variances, e.g. $\text{var}(x_1^s \pm x_1^p)$ and $\text{var}(x_2^s \pm x_2^p)$. These combined variances are connected via the identity

$$\text{var } x_i \pm x_j = \text{var } x_i + \text{var } x_j \pm 2 \text{cov } x_i, x_j \quad (2)$$

to the covariance matrix with $\sigma_{i,k} = \text{cov } x_i, x_j$. The covariance matrix of any N-mode Gaussian state can be visualized by the Wigner function [19] defined as in [20]

$$W(\mathbf{X}) = \frac{1}{\pi^N \sqrt{\det(\sigma)}} e^{-(\mathbf{X}-\mathbf{d})^\top \sigma^{-1} (\mathbf{X}-\mathbf{d})}. \quad (3)$$

3. Reconstruction method

Homodyne detection is a standard technique to quantify the noise of a quantum state. In a balanced homodyne detection, see Fig. 1, the signal mode a is sent onto a 50/50 beam splitter where it interferes with a strong local oscillator (LO). The two output fields of the beam splitter are detected on two individual photodiodes. The photocurrents are subtracted and converted into a voltage Δu that is monitored on a spectrum analyzer. The part of mode a to be measured is selected by the specific mode characteristics of the LO b (such as spatial mode shape and polarization), as only the projection of a onto b interferes with b and is amplified by b to detectable powers. Changes in the local oscillator's characteristics thus lead to detecting different parts of mode a . This is an important insight towards understanding the detection scheme. Considering

single-mode fields, the detection phase determines the measured readout quadrature, e.g., phase or amplitude quadrature.

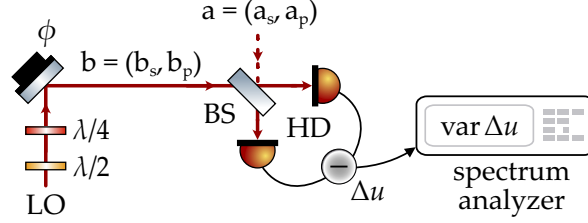


Fig. 1. Basic setup of our single HD reconstruction method. The LO is transmitted by a half-wave and a quarter-wave plate and experiences a phase shift ϕ . Then, the orthogonal polarization contributions of the LO b_s and b_p interfere with the corresponding fields of the signal a_s and a_p on a 50/50 beam splitter. The powers are measured on a HD where the difference voltage Δu is sent to a spectrum analyzer to quantify its variance. BS: 50/50 beam splitter, LO: local oscillator, HD: homodyne detector

For a polarization non-degenerate two-mode field, the readout quadrature combination can be determined by changing the magnitude and phase of the s-pol and p-polarization component of the LO, namely by adjusting its polarization. We now need to find the local oscillator's polarization states required to gain full knowledge of the covariance matrix described in (1). With a purely s-polarized LO $b = (b_s, 0)$, the detection scheme is only sensitive to the s-polarized part of the signal beam. A LO with s- and p- polarization components $b = (b_s, b_p)$ measures different linear combinations of the two modes a_s and a_p , depending on the phase difference of the LO modes b_s and b_p . In this sense, the single HD can also be interpreted as two independent HD detectors separated in polarization, sharing the same photodiodes.

As we will show in the following, six measurements with the below polarization states of the LO are sufficient to reconstruct the covariance matrix.

$$\text{linear p: } b_{1p} = (0, b) \quad \text{for var } x_\phi^p \quad (4a)$$

$$\text{linear s: } b_{1s} = (b, 0) \quad \text{for var } x_\phi^s \quad (4b)$$

$$\text{diagonal} + \pi/4 : b_{1r} = b/\sqrt{2} (1, 1) \quad \text{for var } (x_\phi^p + x_\phi^s) \quad (4c)$$

$$\text{diagonal} - \pi/4 : b_{1l} = b/\sqrt{2} (-1, 1) \quad \text{for var } (x_\phi^p - x_\phi^s) \quad (4d)$$

$$\text{left circular: } b_{cl} = b/\sqrt{2} (1, i) \quad \text{for var } (x_\phi^p - x_{\phi+\pi/2}^s) \quad (4e)$$

$$\text{right circular: } b_{cr} = b/\sqrt{2} (1, -i) \quad \text{for var } (x_\phi^p + x_{\phi+\pi/2}^s). \quad (4f)$$

For the calculation, we decompose the field operators a and b in a constant and a fluctuating term: $a = \langle a \rangle + \delta a$ and $b = \langle b \rangle + \delta b$. Since the LO is much more intense than the signal with $\langle b \rangle \gg \langle a \rangle$ we neglect $\langle a \rangle$ terms as well as all higher-order δ^2 terms. Finally, we compute the variance of the difference voltage $\text{var } \Delta u$ of the homodyne detection that is later monitored by a spectrum analyzer.

First, we consider the case when the LO is in a linear s- or p-polarized state, see Eqs. (4a, 4b). For a p-polarized LO we find $\text{var } \Delta u = \text{var } x_\phi^p$, and for an s-polarized LO, $\text{var } \Delta u = \text{var } x_\phi^s$. For the specific phases $\phi = 0$ and $\phi = \pi/2$, we obtain the four main diagonal elements $\sigma_{i,i}$ of the covariance matrix. When we set the local oscillators phase to $\phi = \pi/4$ and again measure $\text{var } \Delta u$,

we can compute the $\sigma_{1,2} = \sigma_{2,1}$ and $\sigma_{3,4} = \sigma_{4,3}$ entries of the covariance matrix by using our already reconstructed main diagonal entries of the covariance matrix and the identity [21]

$$\text{var } x_{\phi=\pi/4}^j = \frac{1}{2} (\text{var } x_1^j + \text{var } x_2^j + 2 \text{cov } x_1^j, x_2^j). \quad (5)$$

Following this procedure, the first six independent entries (in (1) in red dotted) of the covariance matrix can be obtained.

Second, we prepare the LO in a $\pm\pi/4$ linearly rotated polarization state, see Eqs. (4c, 4d). We measure the sum (difference) of amplitude or phase quadratures of both contributing modes, which is given by $\text{var } \Delta u = \text{var } x_{\phi}^p \pm x_{\phi}^s$. This is an elegant method to directly detect the sum (difference) of the same quadrature of modes with orthogonal polarizations. Now, the detector simultaneously detects the s- and p-polarized contributions and thus directly adds the quadratures. We can compute the $\sigma_{1,3} = \sigma_{3,1}$ and the $\sigma_{2,4} = \sigma_{4,2}$ entries by taking the main diagonal entries of the covariance matrix and (2). This procedure results in two more independent entries of the covariance matrix (in (1) in green solid).

Third and lastly, we prepare the LO in a right (left) circular polarized state, see Eqs. (4e, 4f). Now, mixing between quadratures and polarization modes occurs, which can be seen by $\text{var } \Delta u = \text{var } (x_{\phi}^p \pm x_{\phi+\pi/2}^s)$. To compute the missing $\sigma_{1,4} = \sigma_{4,1}$ and $\sigma_{2,3} = \sigma_{3,2}$ entries, we again use the main diagonal elements from the first part and the identity from (2). This way, the last two independent entries (in (1) in blue dashed) are obtained, leading to a fully reconstructed covariance matrix.

4. Experimental setup

The measured two-mode squeezed state is generated by a polarization non-degenerate optical parametric oscillator (NDOPO) as shown in Fig. 2. The NDOPO is similar to the (OPO) presented in [22]. It consists of an input/output mirror with power reflectivity of $R_{\text{in}} = 0.95$ and three highly-reflective mirrors for the fundamental wavelength 1064 nm. The cavity is kept on resonance for 1064 nm by applying the Pound-Drever-Hall technique (not shown in Fig. 2). We measured the cavity linewidth to be 1.7 MHz. The optical round-trip length of the cavity is 1.522 m, which leads to a free spectral range of 197.0 MHz.

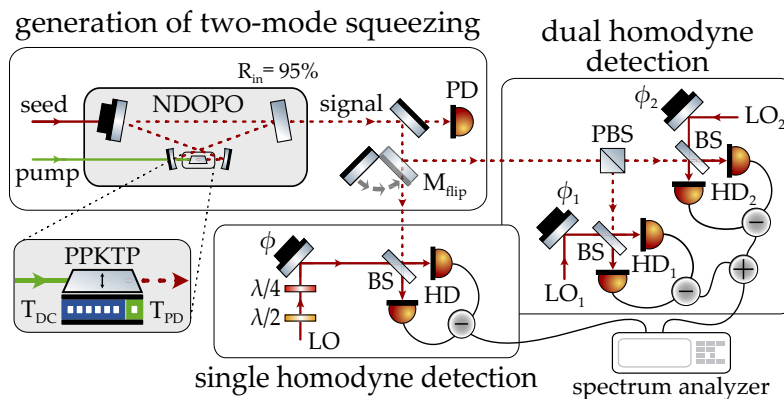


Fig. 2. Experimental setup consisting of generation and detection stage. We either detect the two-mode squeezed state with a single HD (bottom box) or, using the flipping mirror M_{flip} , with a dual HD. NDOPO: non-degenerate optical parametric oscillator, PD: photo detector, M: mirror, PBS: polarizing beam splitter, BS: 50/50 beam splitter, LO: local oscillator, HD: homodyne detector.

The core element of the NDOPO is a $1\text{ mm} \times 2\text{ mm} \times 10\text{ mm}$ (PPKTP) crystal for the non-linear type II down-conversion process, see Fig. 2. The optimal phase-matching condition for the down-conversion process is ensured by temperature controlling the larger left (8 mm) part of the crystal to $T_{\text{DC}} = 30^\circ\text{C}$. Since the birefringent crystal is wedged, we can roughly adjust the degeneracy point of the two polarization resonances by carefully shifting it perpendicularly to the cavity beam axis and thus changing the optical path length inside the crystal. Fine-tuning of the degree of degeneracy can be achieved by changing the temperature $T_{\text{PD}} \approx T_{\text{DC}}$ of the right (2 mm) part of the crystal by less than $\pm 1^\circ\text{C}$. We inject 650 mW of 532 nm pump light in a single-pass configuration. The pump phase can be locked to a seed field by detecting its de-amplification on the photodiode PD as in [23]. Also shown in Fig. 2 is the detection scheme for the two-mode squeezed state. To reconstruct the covariance matrix we can either use the conventional dual homodyne scheme or measure the state with our approach based on a single HD.

5. Reconstruction results

In this section, we explain how we have taken the measurements and present and discuss our reconstructed covariance matrices. We can employ the conventional dual-homodyne approach by using the flipping mirror M_{flip} in Fig. 2. In this case, the s- and p-polarization contributions of the signal are split by a polarising beam splitter (PBS) and are detected by the two individual homodyne detectors HD_1 and HD_2 . With mirrors clamped onto piezoelectric elements, we can change the two detection phases, respectively. By combining the voltages from both homodyne detectors for different phases ϕ_1 and ϕ_2 of the s-polarized LO_1 and the p-polarized LO_2 , the covariance matrix can be reconstructed [8,11].

To utilize the single HD approach, we send the signal beam directly onto the HD. Here, the signal interferes with the LO, whose particular polarization state is prepared with a half-wave and a quarter wave-plate. We use the six differently polarized local oscillator fields to take our measurements as explained in Section 3. The polarization states are generated by using motorized pre-calibrated rotation mounts for the two waveplates. By tuning the piezoelectric element (PZT), we change the relative phase ϕ between the local oscillator and the two-mode squeezed state (signal), as depicted in Fig. 2. The difference voltage Δu of the HD is measured with a spectrum analyzer [Keysight, N9020A MXA], and the trace is plotted in Fig. 3. We have taken the measurements over a zero span at 197 MHz, which is the first free spectral range frequency of the NDOPO. The measurements are normalized to shot noise and the electronic dark noise (which was roughly 15 dB below the shot noise) is subtracted. Each colored trace shows the signal's noise for a specific polarization state of the LO. For a purely s- or p-polarized LO, we observe the thermal noise characteristic of the state. The marginal dependence on the phase ϕ is probably due to a remaining mismatch between polarization bases of signal and local oscillator. For the other four polarizations we observed a squeezed noise of $-6.7(2)$ dB and an anti-squeezed noise of $12.8(2)$ dB. Here, we took up to six data points for each required variance. Thus, we average over the measurement time of 0.8 s, to get a higher precision for the entries in the covariance matrix.

When using the dual-homodyne scheme to analyze the two-mode squeezed state, we obtain measurements similar to those as shown in Fig. 3. We measured the s-pol and p-polarization thermal states by using only one of the two homodyne detectors. If we monitor the combined signal behind an electronic adder [Mini-Circuits, ZFSC-2-5-S+], we obtain variances of different quadrature combinations. For each measurement, we locked the detection phase of one HD (e.g. ϕ_1 on HD_1) and ramped the other detection phase (ϕ_2). Following this procedure, we can also reconstruct the full covariance matrix of the same two-mode squeezed state.

The reconstructed covariance matrices for the single HD and dual HD schemes are shown in Fig. 4. The entries are average values calculated over the full measurement time. We found both covariance matrices exhibiting well-matching entries within the statistical measurement

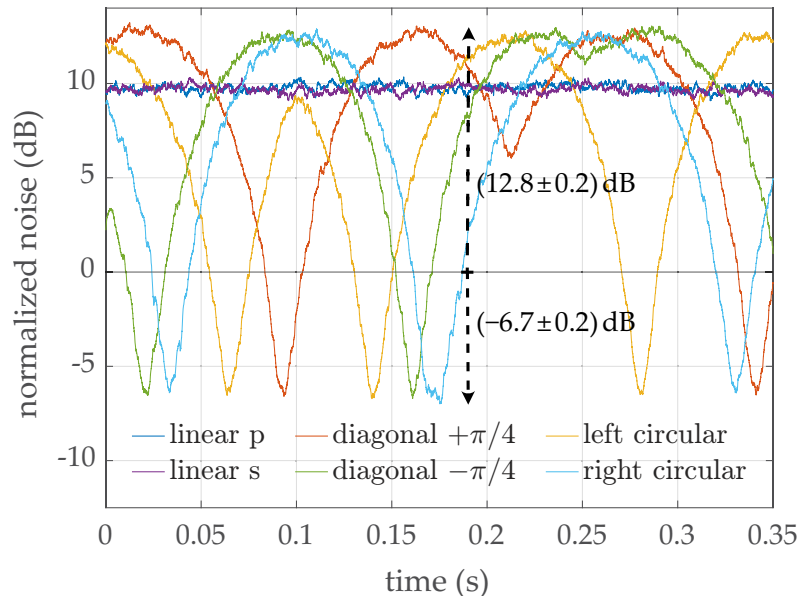


Fig. 3. Zero-span measurements taken with the single homodyne detector for six different polarization states of the local oscillator at 197 MHz, normalized on shot noise. We observe a squeezed level of -6.7 dB and an anti-squeezing level of 12.8 dB. Resolution bandwidth: 200 kHz, video bandwidth: 100 kHz.

uncertainties. For the main-diagonal entries, the standard deviation is at most 0.2, according to our statistics from taking several data points per trace. The uncertainty for the off-diagonal entries in the covariance matrix (CM) is up to a factor of 4 larger because they were indirectly obtained. In the following, we elaborate on the potential origins dominating the measurement uncertainties.

$$\begin{array}{cc}
 \text{single HD} & \text{dual HD} \\
 \sigma = \begin{pmatrix} 9.0 & 0.0 & -9.2 & 0.0 \\ 0.0 & 9.5 & 0.0 & 9.2 \\ -9.2 & 0.0 & 9.8 & 0.0 \\ 0.0 & 9.2 & 0.0 & 9.3 \end{pmatrix} & \sigma = \begin{pmatrix} 9.0 & -0.1 & -9.1 & -0.2 \\ -0.1 & 9.3 & -0.2 & 9.0 \\ -9.1 & -0.2 & 9.6 & 0.0 \\ -0.2 & 9.0 & 0.0 & 9.1 \end{pmatrix}
 \end{array}$$

Fig. 4. Comparison of the reconstructed covariance matrices obtained from measurements with the single homodyne detector (left) and the dual homodyne detector (right) approach. We observe nearly identical results for both approaches.

Since our single-homodyne measurements work with a polarization-sensitive local oscillator, they require reliable polarization optics. The beam splitter should have an equal splitting ratio of 50/50 for both polarizations for a precise reconstruction. Usually, this can be realized with the appropriate coating and careful alignment of the angle of incidence. In our experiment we could achieve $R_s \approx R_p \approx 50\%$ with a precision of $\pm 0.5\%$. Another important factor is the polarization accuracy of the LO and how well it matches the signal's polarization basis. The motorized rotations mounts [Thorlabs, ELL14] have an adjustment precision of $\pm 0.3\%$ to tune the ellipticity and rotation angle of the LO. The polarization was monitored by a polarimeter

[Thorlabs, PAX1000IR1]. However, these mentioned experimental uncertainties do not dominate the errors in the covariance matrix.

For the single-homodyne detection, the polarization state of the two-mode squeezed state is highly important when it interferes with the local oscillator at the beam splitter. Ideally, the two-mode squeezed state is diagonally linearly polarized. However, the polarization state changes due to any polarization non-degeneracy effects. One origin could be an asymmetric propagation phase for s- and p-polarization arising from mirror reflections, which is a static effect. Additionally, a slightly fluctuating resonance condition of the NDOPO for s- and p-polarization could also dynamically change their phase relation (the polarization state) but also their magnitudes (the squeezing degree). In our setup, this might be the case, most likely due to small temperature fluctuations in the crystal. This effect which originates from the NDOPO source and not from the detection scheme, dominates the uncertainties in the covariance matrices.

The comparison of both covariance matrices in Fig. 4 indicates that the state obtained by the dual HD method is slightly more squeezed. The main differences between the two detection setups are that, firstly, the propagation efficiencies for the three beam paths (to single HD vs. reflected at the PBS vs. transmitted at the PBS) are slightly different. Secondly, we measured slightly different visibilities (VIS) for the three homodyne detectors ($VIS_{1HD} = 99\%$, $VIS_{2HD,s} = 98\%$, $VIS_{2HD,p} = 99\%$). However, these differences do not explain why the state detected with the dual HD method is slightly more squeezed. A better explanation is that the two-mode squeezed state becomes slightly elliptical polarized when it travels to the detector, as explained in the previous paragraph. A non-degrading elliptical polarized two-mode squeezed state is only a problem when using the single HD method.

We visualize the covariance matrix obtained from the single HD method in Fig. 5 by plotting the Wigner functions using Eq. (3) with $N = 1$. The Wigner functions $W(x_1^s, x_1^p)$ and $W(x_2^s, x_2^p)$ show squeezed states representing anti-correlated quadratures x_1^s, x_1^p and correlated quadratures x_2^s, x_2^p . These two Wigner functions are squeezed by a factor of 0.20 and 0.21, respectively. We observe thermal states for $W(x_1^s, x_2^s)$ and $W(x_2^p, x_1^p)$. Due to the strong similarity of the two covariance matrices, the Wigner functions for the dual HD case look nearly identical and are omitted here.

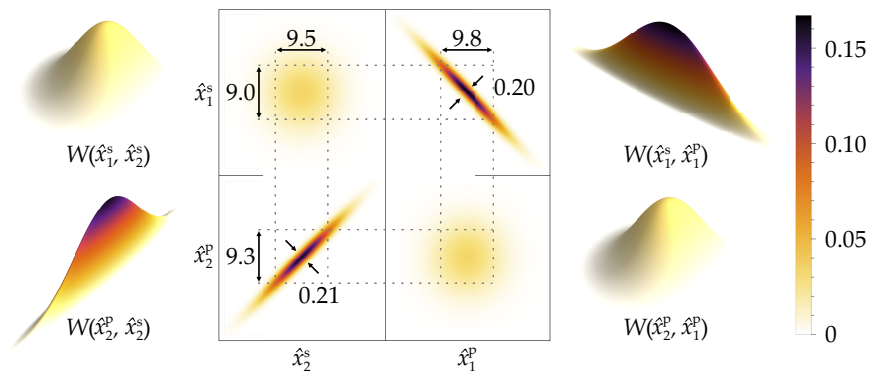


Fig. 5. Gaussian Wigner functions for different combinations of the four quadrature modes x_1^p, x_2^p, x_1^s and x_2^s . The distributions are plotted by using Eq. (1) and the reconstructed covariance matrix from our measurements with a single HD from Fig. 4.

To complete, we investigate our reconstructed two-mode squeezed state on inseparability and entanglement when we measure with a single HD. With our single HD approach, we can test these criteria directly, since we directly measure the required variances, see Section 3. We find a value of 0.42 ± 0.02 for the left hand side of the equation for the Duan

criterion $\text{var}(x_1^s + x_1^p) + \text{var}(x_2^s - x_2^p) < 2$ [16], falling a factor of roughly 4.8 below this criterion. The criterion from Reid can be seen as an inferred Heisenberg uncertainty relation with $\text{var}(x_1^s + x_1^p) \times \text{var}(x_2^s - x_2^p) < 1$ [17]. Using our reconstructed covariance matrix, the left hand side reads 0.044 ± 0.003 , surpassing the Reid criterion by a factor of roughly 23, which clearly demonstrates the EPR paradox.

6. Discussion and conclusion

Finally, we discuss the drawbacks and the advantages of using our demonstrated single HD approach. The technical drawback of the single HD reconstruction method is its susceptibility to polarization inaccuracies. This applies for the beam splitter, which has to be equally reflective for s- and p-polarization, but also the matching of the polarization bases of LO and signal. Moreover, our scheme is sensitive to the actual phase delay between both fields, which potentially explains the slightly reduced squeezing values for the single HD measurements compared to those measured with the dual HD. However, our demonstrated method has some advantages compared to [14]. With the motorized rotation mounts, our measurements can be taken very fast. The most significant benefit is that we do not send the state under estimation through components other than the beam splitter, as this would introduce additional and unwanted decoherence. Typically, these losses are in the order of 0.5% for three optical components in transmission. They are small with respect to the total losses shown here. However, with increasing performance these losses become a more significant contribution to the loss budget - [15] showed a total loss of 2.5% in a single-mode setup.

We have demonstrated a full Gaussian state estimation of a two-mode squeezed state by measurements with a single homodyne detector. Our detection scheme is similar to the method demonstrated in [14]. We use six different polarization states of the local oscillator, with each one measuring a particular combination of variances. These measurements allow us to fully reconstruct the covariance matrix of the two-mode squeezed state. The advantage of our method compared to [14] is that the state under estimation deteriorates less on the way to the homodyne detector because we avoid the transmission through of optical components (two waveplates and a polarising beam splitter), thereby retaining more coherence. To confirm our method, we compare our results to a measurement taken with a conventional dual-homodyne scheme. Our presented approach is an intuitive, low-loss alternative for characterizing bipartite polarization states.

Funding. Deutsche Forschungsgemeinschaft ((EXC 2122, Project ID 390833453), (EXC 2123, Project ID 390837967), (Project ID 239408513), Excellence PhoenixD, Excellence QuantumFrontiers, GRK 1991).

Disclosures. The authors declare no conflicts of interest.

Data availability. Data underlying the results presented in this paper are not publicly available at this time but may be obtained from the authors upon reasonable request.

References

1. Y. Ma, H. Miao, B. H. Pang, M. Evans, C. Zhao, J. Harms, R. Schnabel, and Y. Chen, "Proposal for gravitational-wave detection beyond the standard quantum limit through epr entanglement," *Nat. Phys.* **13**(8), 776–780 (2017).
2. J. Süßbeck, S. Steinlechner, M. Korobko, and R. Schnabel, "Demonstration of interferometer enhancement through einstein–podolsky–rosen entanglement," *Nat. Photonics* **14**(4), 240–244 (2020).
3. N. Gisin and R. Thew, "Quantum communication," *Nat. Photonics* **1**(3), 165–171 (2007).
4. S. L. Braunstein and H. J. Kimble, "Teleportation of continuous quantum variables," *Phys. Rev. Lett.* **80**(4), 869–872 (1998).
5. D. Bouwmeester, J.-W. Pan, K. Mattle, M. Eibl, H. Weinfurter, and A. Zeilinger, "Experimental quantum teleportation," *Nature* **390**(6660), 575–579 (1997).
6. N. Treps, U. Andersen, B. Buchler, P. K. Lam, A. Maître, H.-A. Bachor, and C. Fabre, "Surpassing the standard quantum limit for optical imaging using nonclassical multimode light," *Phys. Rev. Lett.* **88**(20), 203601 (2002).
7. M. I. Kolobov and C. Fabre, "Quantum limits on optical resolution," *Phys. Rev. Lett.* **85**(18), 3789–3792 (2000).
8. J. DiGuglielmo, B. Hage, A. Franzen, J. Fiurášek, and R. Schnabel, "Experimental characterization of gaussian quantum-communication channels," *Phys. Rev. A* **76**(1), 012323 (2007).

9. Z. Y. Ou, S. F. Pereira, H. J. Kimble, and K. C. Peng, "Realization of the einstein-podolsky-rosen paradox for continuous variables," *Phys. Rev. Lett.* **68**(25), 3663–3666 (1992).
10. J. Laurat, G. Keller, J. A. Oliveira-Huguenin, C. Fabre, T. Coudreau, A. Serafini, G. Adesso, and F. Illuminati, "Entanglement of two-mode gaussian states: characterization and experimental production and manipulation," *J. Opt. B: Quantum Semiclassical Opt.* **7**(12), S577–S587 (2005).
11. S. Steinlechner, J. Bauchrowitz, T. Eberle, and R. Schnabel, "Strong einstein-podolsky-rosen steering with unconditional entangled states," *Phys. Rev. A* **87**(2), 022104 (2013).
12. V. D'Auria, A. Porzio, S. Solimeno, S. Olivares, and M. G. A. Paris, "Characterization of bipartite states using a single homodyne detector," *J. Opt. B: Quantum Semiclassical Opt.* **7**(12), S750–S753 (2005).
13. D. Steinmeyer, "Subsystems for all-optical coherent quantum-noise cancellation," Ph.D. thesis, Gottfried Wilhelm Leibniz Universität Hannover (2019).
14. V. D'Auria, S. Fornaro, A. Porzio, S. Solimeno, S. Olivares, and M. G. A. Paris, "Full characterization of gaussian bipartite entangled states by a single homodyne detector," *Phys. Rev. Lett.* **102**(2), 020502 (2009).
15. H. Vahlbruch, M. Mehmet, K. Danzmann, and R. Schnabel, "Detection of 15 db squeezed states of light and their application for the absolute calibration of photoelectric quantum efficiency," *Phys. Rev. Lett.* **117**(11), 110801 (2016).
16. L.-M. Duan, G. Giedke, J. I. Cirac, and P. Zoller, "Inseparability criterion for continuous variable systems," *Phys. Rev. Lett.* **84**(12), 2722–2725 (2000).
17. M. D. Reid, "Demonstration of the einstein-podolsky-rosen paradox using nondegenerate parametric amplification," *Phys. Rev. A* **40**(2), 913–923 (1989).
18. R. Simon, N. Mukunda, and B. Dutta, "Quantum-noise matrix for multimode systems: U(n) invariance, squeezing, and normal forms," *Phys. Rev. A* **49**(3), 1567–1583 (1994).
19. E. Wigner, "On the quantum correction for thermodynamic equilibrium," *Phys. Rev.* **40**(5), 749–759 (1932).
20. G. Adesso, S. Ragy, and A. R. Lee, "Continuous variable quantum information: Gaussian states and beyond," *Open Syst. Inf. Dyn.* **21**(01n02), 1440001 (2014).
21. V. Händchen, "Experimental analysis of Einstein-Podolsky-Rosen steering for quantum information applications," Ph.D. thesis, Gottfried Wilhelm Leibniz Universität Hannover (2016).
22. J. Junker, D. Wilken, N. Johnny, D. Steinmeyer, and M. Heurs, "Frequency-dependent squeezing from a detuned squeezer," *Phys. Rev. Lett.* **129**, 033602 (2022).
23. J. Junker, D. Wilken, E. Huntington, and M. Heurs, "High-precision cavity spectroscopy using high-frequency squeezed light," *Opt. Express* **29**(4), 6053–6068 (2021).

5.3 Detection of two-mode squeezing

Before we illuminate how two-mode squeezed states are generated, we first discuss how they can be detected. The special feature of our two-mode squeezing is that the two modes of interest are distinguishable due to their orthogonal polarisations. A conventional (single-mode) homodyne detector, as described in Subsec. 2.2.4, cannot fully characterise the two-mode squeezed state. It can only measure either the s-polarisation *or* the p-polarisation contribution of the signal field. Thus, a more advanced detection scheme is required. This section discusses two possible detection schemes suitable for detecting two-mode squeezed states.

First, Subsec. 5.3.1 deals with the conventional dual homodyne detector. As the name suggests, it consists of two individual homodyne detectors. Here, each detector measures one orthogonal mode and the signal of both detectors is combined electronically. Second, Subsec. 5.3.2 complements the detection method used in [P3], namely the polarisation-sensitive single homodyne detection. This approach measures the two modes simultaneously by choosing specifically polarised local oscillators instead of splitting them. This subsection, in particular, discusses how the local oscillator is theoretically described and expounds the Eqs. (4a)–(4f) in [P3].

5.3.1 Dual balanced homodyne detection

The setup of the (balanced) dual homodyne detection scheme is shown in Fig. 5.1. First, the signal field $\mathbf{a} = (a_s, a_p)$ is split by a polarising beam splitter (PBS) into the orthogonal polarisation contributions a_s and a_p . Then, a_s and a_p are independently sent onto two conventional balanced homodyne detectors with individual local oscillators b_s and b_p . These homodyne detectors can be treated independently and each behaves as described in Subsec. 2.2.4. Depending on the relative phases ϕ_s and ϕ_p , arbitrary quadratures $\delta X_{\phi_s}^s, \delta X_{\phi_p}^p$ can be observed in the difference photocurrents Δi_s and Δi_p , analogously to Eq. (2.61). These photocurrents are converted into voltages Δu_s and Δu_p by the transimpedance amplifiers. Finally, the two voltages Δu_s and Δu_p are added ($\Sigma u = \Delta u_s + \Delta u_p$) or subtracted ($\Delta u = \Delta u_s - \Delta u_p$) and monitored on a spectrum analyser. They read as

$$\begin{aligned} \Sigma u = \Delta u_s + \Delta u_p &\propto 2\alpha_s\beta_{0,s}\cos(\phi_s) + \beta_{0,s}\delta X_{\phi_s}^s \\ &\quad + 2\alpha_p\beta_{0,p}\cos(\phi_p) + \beta_{0,p}\delta X_{\phi_p}^p, \end{aligned} \quad (5.5)$$

$$\begin{aligned} \Delta u = \Delta u_s - \Delta u_p &\propto 2\alpha_s\beta_{0,s}\cos(\phi_s) + \beta_{0,s}\delta X_{\phi_s}^s \\ &\quad - 2\alpha_p\beta_{0,p}\cos(\phi_p) - \beta_{0,p}\delta X_{\phi_p}^p. \end{aligned} \quad (5.6)$$

The phases ϕ_s and ϕ_p can be obtained from the DC terms. The variances are

$$\text{var}(\Sigma u) \propto \beta_{0,s}^2 \langle |\delta X_{\phi_s}^s|^2 \rangle + \beta_{0,p}^2 \langle |\delta X_{\phi_p}^p|^2 \rangle, \quad (5.7)$$

$$\text{var}(\Delta u) \propto \beta_{0,s}^2 \langle |\delta X_{\phi_s}^s|^2 \rangle - \beta_{0,p}^2 \langle |\delta X_{\phi_p}^p|^2 \rangle. \quad (5.8)$$

The local oscillators' powers need to be equal ($\beta_{0,s}^2 = \beta_{0,p}^2$), to achieve proper combinations of variances. Up to this point, we have assumed that both photodetectors are equal. However, it can be challenging in an experiment to create two perfectly identical photodetectors, particularly over a large frequency band up to the gigahertz regime.

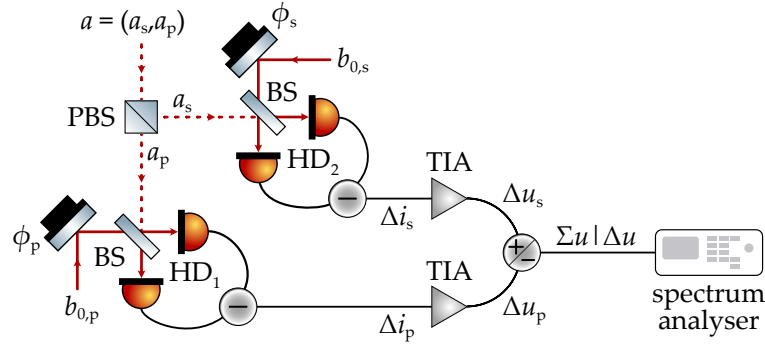


FIGURE 5.1: Schematic of a (balanced) dual homodyne detection scheme. The signal field a is split by a polarisation beam splitter (PBS) into the orthogonal polarisation contributions a_s and a_p . They are individually detected on balanced homodyne detectors HD₁ and HD₂ leading to differential photocurrents Δi_s and Δi_p . Transimpedance amplifiers (TIAs) convert the currents into voltages Δu_s and Δu_p that are added or subtracted to be monitored on a spectrum analyser. BS: 50/50 beam splitter.

For the experiment, we used two in-house manufactured homodyne detectors.¹⁰ Before using them for the actual detection, a noise characterisation was performed, which can be seen in Fig. 5.2.

The dark noise (turquoise graph for HD₁ and orange for HD₂) and the shot noise (blue for HD₁ and red for HD₂) are plotted in Fig. 5.2a). The shot noise measurement was taken with a local oscillator power of 9.5 mW for each of the two homodyne detectors. Hence, all four photodiodes each detected 4.75 mW of power. The measurement shows that the noise traces are similar for both homodyne detectors. Both detectors behave nearly equally at low frequencies up to 500 MHz. However, at higher frequencies, the dark and shot noise traces differ by up to 5 dB. It turned out that the dark noise level depends mainly on the high-frequency shielding and the mechanical forces of the connectors, potentially causing parasitic capacities. It was impossible to equalise the detectors' traces over the whole frequency band. However, at the desired measurement frequency of 200 MHz (indicated by the dashed vertical line in the figure), both detectors seem to work equally. At this frequency, the dark and shot noise traces indicate that the electrical transimpedance gains are equal. Contrarily, e.g. at 2 GHz the traces differ.

Figure 5.2b) shows the distance between dark noise and shot noise, which is called the dark noise *clearance*. Here, we also identify an equal clearance at most frequencies for the two homodyne detectors. In particular, at the measurement frequency of 200 MHz the two detectors show the same behaviour. In conclusion, the two homodyne detectors are suitable to take measurements at 200 MHz.

This subsection closes with a brief review on Fig. 5.1. Why do the calculations not consider that vacuum fluctuations couple into the detection scheme at the PBS? The PBS transmits vacuum fluctuations in p-polarisation and reflects those in s-polarisation. Hence, these fluctuations at the output ports are orthogonally polarised to the signal fields a_s and a_p and do not interfere with the local oscillators.

5.3.2 Polarisation-sensitive single homodyne detection

This subsection is devoted to giving some additional remarks to the reconstruction method described in Sec. 3 in [P3]. As long as we do not discriminate between the

¹⁰Labelled as e-GHzHDv8.2-1 and e-GHzHDv8.2-2.

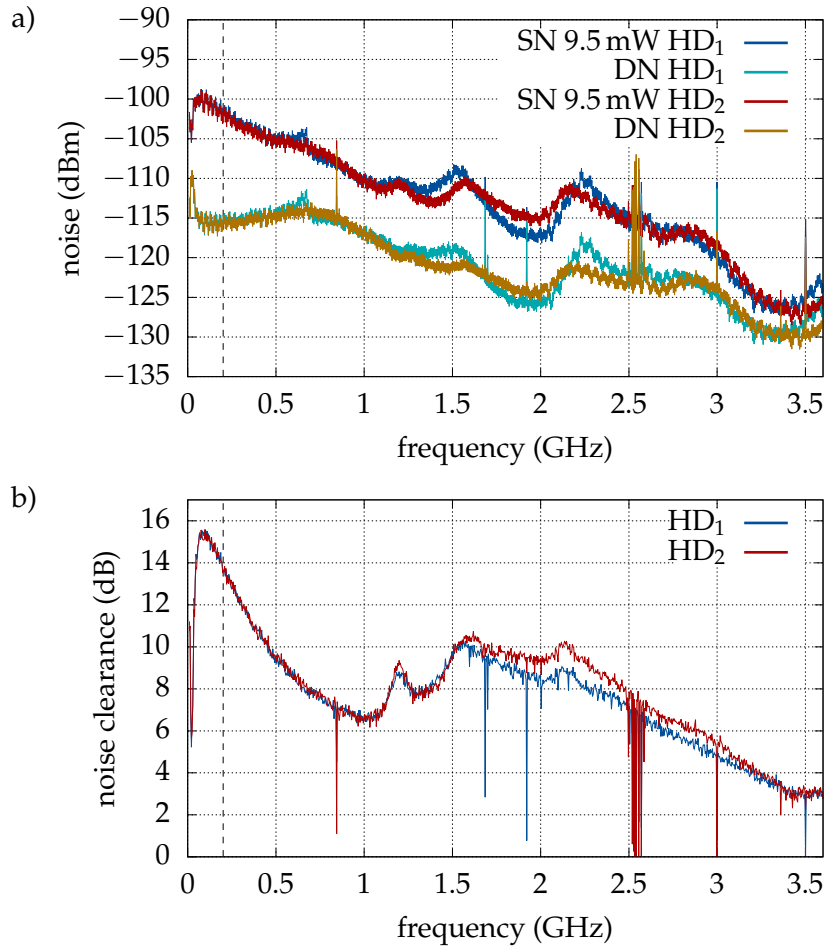


FIGURE 5.2: a) Shot noise (SN) and dark noise (DN) traces measured with the two homodyne detectors HD_1 and HD_2 . At the measurement frequency of 200 MHz (indicated by the dashed line), the two detectors show equal behaviour. b) Clearance between shot noise and dark noise of the two homodyne detectors. At 200 MHz, a clearance of roughly 14 dB was measured. Resolution bandwidth: 510 kHz, video bandwidth: 470 Hz.

two orthogonally polarised modes, we can treat two-mode squeezing as single-mode squeezing. This scenario can also be realised by a homodyne detector. The two-mode squeezed state is 45° linearly polarised. We can detect squeezing with a local oscillator having the same linearly 45° polarisation. Generally, the local oscillator can have arbitrary polarisation states, which all measure particular variances.¹¹

The required local oscillators' polarisations (according to Eqs. (4a)–(4f) in [P3]) are created by using two waveplates. For the theoretical description, the Jones calculus is used [Fow89]. In this formalism, polarised light is represented by a 2-dimensional vector and optical elements by 2×2 matrices. Here, I use the nomenclature from Fig. 1 in [P3]. The complex vector $\tilde{\mathbf{b}} = (\tilde{b}_s, \tilde{b}_p)$ describes the local oscillator, with entries representing the s- and p-polarisation. Its polarisation is adjusted with a half-wave

¹¹A similar idea of using one homodyne detector to measure *frequency* non-degenerated squeezed states was applied in [Süd+20]. There, a bichromatic balanced homodyne detection scheme is employed.

plate (HWP) and a quarter wave-plate (QWP) given by the Jones matrices¹²

$$\text{HWP}(\theta) = \begin{pmatrix} \cos(2\theta) & -\sin(2\theta) \\ -\sin(2\theta) & \cos(2\theta) \end{pmatrix}, \quad (5.9)$$

$$\text{QWP}(\theta) = \begin{pmatrix} i \cos^2(\theta) + \sin^2(\theta) & (i-1) \sin(\theta) \cos(\theta) \\ (i-1) \sin(\theta) \cos(\theta) & i \cos^2(\theta) + \sin^2(\theta) \end{pmatrix}. \quad (5.10)$$

After the transmission of the waveplates, the local oscillator is

$$\mathbf{b} = \begin{pmatrix} b_s \\ b_p \end{pmatrix} = \text{QWP}(\theta_1) \times \text{HWP}(\theta_2) \times \begin{pmatrix} \tilde{b}_s \\ \tilde{b}_p \end{pmatrix}. \quad (5.11)$$

Depending on θ_1 and θ_2 , the waveplates can arbitrarily polarise the local oscillator \mathbf{b} . In particular, we can achieve the six required polarisations states from Fig. 1 in [P3].¹³

The signal¹⁴ is described by the complex vector $\mathbf{a} = (a_s, a_p)$. It interferes with the local oscillator on a polarisation-insensitive 50/50 beam splitter.¹⁵ Before the interference, the local oscillator collects a polarisation-independent phase ϕ . Thus, the interfering fields on the beam splitter are

$$\text{the local oscillator } \begin{pmatrix} b_s \\ b_p \end{pmatrix} e^{i\phi} \quad (5.12)$$

$$\text{and the signal } \begin{pmatrix} a_s \\ a_p \end{pmatrix}. \quad (5.13)$$

At the beamsplitter, orthogonal polarisation contributions do not interfere with each other. Hence, up to the detection, s-polarisation and p-polarisation fields can be treated independently.¹⁶ Then, the difference current from the homodyne detector reads¹⁷

$$\Delta i \propto \frac{1}{2} \left(|b_s e^{i\phi} + a_s|^2 + |b_p e^{i\phi} + a_p|^2 - |b_s e^{i\phi} - a_s|^2 - |b_p e^{i\phi} - a_p|^2 \right). \quad (5.14)$$

As an example, the simple case of using a linear s-polarised local oscillator with $\mathbf{b} = (b_s, b_p) = (b, 0)$ is considered. To solve Eq. (5.14), we use the linearisations from Eq. (2.23). We again neglect higher-order terms going with δ^2 and find

$$\Delta i \propto 2\alpha_s \beta_s \cos(\phi) + \beta_s \delta X_{\phi, a_s} + \alpha_s \delta X_{-\phi, b_s} + \alpha_p \delta X_{-\phi, b_p}. \quad (5.15)$$

With fulfilled homodyne conditions from Eqs. (2.59) and (2.60),¹⁸ Eq. (5.15) simplifies to

$$\Delta i \propto 2\alpha_s \beta_s \cos(\phi) + \beta_s \delta X_{\phi, a_s}, \quad (5.16)$$

which is the equivalent result as in Eq. (2.61) for the single-mode detection scheme.

The difference current can be calculated for each of the six input polarisation states depending on the phase ϕ as shown in Table 5.1. The difference current is

¹²Jones matrices for different polarisation optics can be found in [TG13], Table 4.1.

¹³In the publication [P3], these states are labelled as b_{1p} , b_{1s} , b_{1r} , b_{1l} , b_{cl} and b_{cr} . They are all normalised and have an amplitude of $|\mathbf{b}| = b$.

¹⁴In [P3], the signal is a two-mode squeezed state.

¹⁵This beam splitter has a power reflectivity of $R = 50\%$ for both polarisations.

¹⁶However, the powers will add up at the detection.

¹⁷Again, we use the asymmetric beamsplitter convention as in Subsec. 2.2.4.

¹⁸This means that the local oscillator's amplitude is much stronger than the signal's amplitude and that the local oscillator's fluctuations are sufficiently low.

distributed into a DC mean term (middle column) and an AC fluctuations term (right column). The phase information ϕ can be obtained from the DC terms.

TABLE 5.1: Difference currents Δi of the polarisation-sensitive homodyne detector calculated by Eq. (5.14).

field operator	Δi DC (mean)	Δi AC (fluctuations)
$b_{1p} = (0, b)$	$2\alpha_p\beta \cos(\phi)$	$2\beta \delta X_\phi^p$
$b_{1s} = (b, 0)$	$2\alpha_s\beta \cos(\phi)$	$2\beta \delta X_\phi^s$
$b_{1r} = b/\sqrt{2} (1, 1)$	$\sqrt{2}\beta(\alpha_p + \alpha_s) \cos(\phi)$	$\sqrt{2}\beta(\delta X_\phi^p + \delta X_\phi^s)$
$b_{1l} = b/\sqrt{2} (-1, 1)$	$\sqrt{2}\beta(\alpha_p - \alpha_s) \cos(\phi)$	$\sqrt{2}\beta(\delta X_\phi^p - \delta X_\phi^s)$
$b_{cl} = b/\sqrt{2} (1, i)$	$\sqrt{2}\beta(\alpha_s \cos(\phi) - \alpha_p \sin(\phi))$	$\sqrt{2}\beta \left(\delta X_\phi^s + \delta X_{\phi+\pi/2}^p \right)$
$b_{cr} = b/\sqrt{2} (1, -i)$	$\sqrt{2}\beta(\alpha_s \cos(\phi) + \alpha_p \sin(\phi))$	$\sqrt{2}\beta \left(\delta X_\phi^s - \delta X_{\phi+\pi/2}^p \right)$

For the Gaussian state reconstruction presented in [P3], we need the variances of the individual quadrature operators and the combinations from the AC currents. They are all given in Table 5.1. The variances are obtained from normalised spectra measurements. The shot noise normalisation is done by repeating the measurement without a signal.

This section dealt with the electric fields involved in the polarisation-sensitive homodyne detection scheme. It presented the detected difference currents for the six different local oscillator polarisation states. It can be seen as a supplementary for Sec. 3 in [P3]. The next Section 5.4 dives more into the experiment and explains how bipartite states are generated with a two-mode squeezer.

5.4 Bipartite states generated with a two-mode squeezer

Two-mode squeezed states are bipartite states and can be generated by different methods. One prominent method is to use two single-mode squeezed states and interfere them on a 50/50 beam splitter [Fur+98; Bow+03a; Bow+03b; DiG+07; YBF07]. With this approach, a two-mode squeezing level of about 10 dB was achieved [EHS13]. Other approaches make use of the correlations of sidebands in single-mode squeezing. Quantum entanglement can be created by separating the quantum sidebands of a single spatial mode into two separate spatial beams. The separation is realised, e.g. by using unbalanced Mach-Zehnder interferometers [HR02; Zha03; Hun+05], or optical cavities [HSS10]. However, the most straightforward method to generate two-mode squeezing is the usage of an NDOPO which is also called a two-mode squeezer [Ou+92]. Many experiments use linear cavities [Lau+05; Vil+05; Su+07; Zho+15] as NDOPOs reaching up to 8.4 dB of two-mode squeezing [Zho+15]. These works use the dual homodyne detection scheme to detect the two-mode squeezed state.

This section deals with the generation of two-mode squeezed states with an NDOPO¹⁹ and their characterisations. First, Subsec. 5.4.1 focuses on the initial characterisation of the squeezer including a squeezing slope and a squeezing spectrum. Squeezing is measured by using a single polarisation-sensitive homodyne detector. This characterisation helps to understand the limitations of squeezing generation and detection. We found out that the used two-mode squeezer has stability problems in

¹⁹Subsection 2.4.2 instructs how the NDOPO is set up.

operation mode. Hence, we discuss determined problems and limitations regarding the stability in Subsec. 5.4.2.

5.4.1 First characterisation of the two-mode squeezer

Once the polarisation-sensitive homodyne detector was set up, the first characterisation of the two-mode squeezer was done. Using a local oscillator that is $+\pi/4$ linearly polarised, squeezing and anti-squeezing are detected, see Eq. (4c) in [P3]. I prepared a two-mode quantum state exhibiting squeezing in the amplitude quadrature $V^+ = \langle |\delta X_1^s + \delta X_1^p|^2 \rangle$ by locking the seed to de-amplification. Consequently, anti-squeezing was visible in the phase quadrature $V^- = \langle |\delta X_2^s + \delta X_2^p|^2 \rangle$. By changing the pump power, I observed the variances for different non-linear interaction strengths. Such a squeezing slope is seen in Fig. 5.3a). The measurement data is fitted by Eq. (2.96).²⁰ The fitting parameters are the pump threshold $P_{\text{th}} = 1.25 \text{ W}$, the total efficiency $\eta = 85.9 \%$ and the phase noise $\Delta\phi = 48 \text{ mrad}$.

The pump threshold was independently determined in a second measurement. Here, the two-mode periodically-poled potassium titanyl phosphate (PPKTP) crystal was pumped without the cavity with infrared light.²¹ Then, the non-linear efficiency is determined to $E_{\text{NL}} = P_{\text{green}}/P_{\text{IR}}^2 \approx 5.5 \times 10^{-4} \text{ W}^{-1}$, by using different fundamental P_{IR} and generated green P_{green} powers. The pump threshold is obtained from $P_{\text{th}} = (T_{\text{in}} + \delta_x)^2 / (4E_{\text{NL}}) = 1.23 \text{ W}$ [Ste19], where $T_{\text{in}} = 5 \%$ is the power transmission of the input coupler and $\delta_x \approx 0.2 \%$ the intra-cavity loss.

The detection efficiency is assumed as 97% ,²² the propagation efficiency is estimated to $\eta_{\text{prop}} = 99 \%$. The homodyne efficiency was measured to be $\eta_{\text{vis}} = 99 \%$ for both polarisations. The escape efficiency differed for both polarisations with $\eta_{\text{esc,s}} = 96.5 \%$ and $\eta_{\text{esc,p}} = 96 \%$. These escape efficiencies correspond to the cavity linewidths of roughly $\delta\omega = 1.7 \text{ MHz}$ neglecting the down-conversion process. For this consideration, I assumed an equal total efficiency for both polarisations ($\eta = \eta_s = \eta_p$). Note that this is only a simplification. I established the equation for the total efficiency by

$$\eta \equiv \eta_s = \eta_{\text{esc,s}} \eta_{\text{prop}} \eta_{\text{vis}} \eta_{\text{qe}} \eta_{x,s} = 85.9 \%, \quad (5.17)$$

$$\eta \equiv \eta_p = \eta_{\text{esc,p}} \eta_{\text{prop}} \eta_{\text{vis}} \eta_{\text{qe}} \eta_{x,p} = 85.9 \%. \quad (5.18)$$

It turned out that two undetermined loss channels of $\eta_{x,s} = 93.6 \%$ and $\eta_{x,p} = 94.1 \%$ need to be assumed. The missing loss channels will be discussed at the end of this subsection.

Squeezing is also observed in the frequency domain. I chose a pump power of roughly 500 mW to measure a squeezing spectrum at 197 MHz , which is the first free spectral range frequency of the NDOPO. The spectrum is displayed in Fig. 5.3b). It shows squeezing in the amplitude quadrature (blue trace) and anti-squeezing in the phase quadrature (red trace). Taking the average of 20 single traces has a strong smoothing effect, as shown by the orange and turquoise traces. In the spectrum, a maximum anti-squeezing of 12.3 dB and a maximal squeezing of 7.3 dB were measured.

²⁰Due to technical limitations in the pump power availability, the largest applied power was 695 mW . Further, for simplicity, we assumed equal losses for both polarisations, such that the two-mode squeezing can be treated like single-mode squeezing.

²¹Meaning the second harmonic generation (SHG) process was driven in the crystal.

²²Justified as a rough average of the quantum efficiency obtained in [P1] and in [P2].

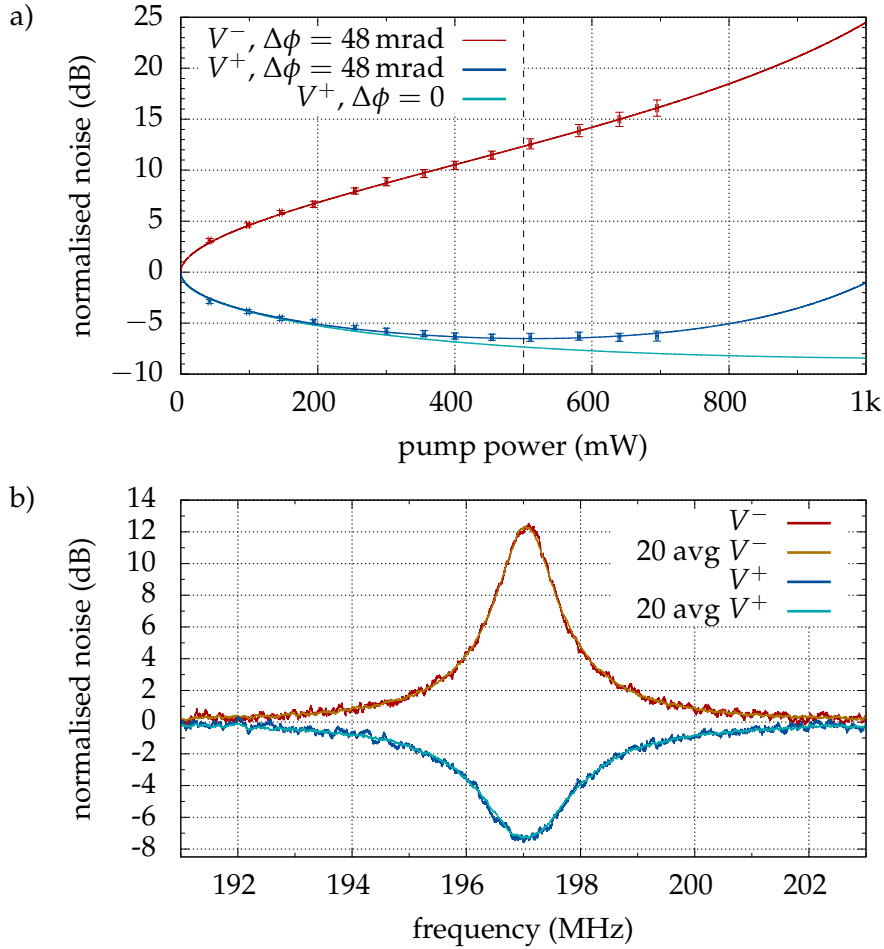


FIGURE 5.3: a) Two-mode squeezing was measured with a single homodyne detector for different pump powers. The parameters $P_{\text{th}} = 1.25 \text{ W}$, $\eta = 85.9\%$ and $\Delta\phi = 48 \text{ mrad}$ are fitting parameters from using Eq. (2.96). b) The spectrum was measured with a pump power of roughly 500 mW (vertical dashed line in the top plot) and shows squeezing in the amplitude quadrature $V^+ = \langle |\delta X_1^s + \delta X_1^p|^2 \rangle = -7.3 \text{ dB}$ (blue trace single measurement, turquoise with 20 averages) and anti-squeezing in the phase quadrature $V^- = \langle |\delta X_2^s + \delta X_2^p|^2 \rangle = 12.3 \text{ dB}$ (red trace single measurement, orange with 20 averages). Resolution bandwidth 200 kHz, video bandwidth 100 Hz. All traces are normalised to shot noise, and the electronic dark noise is subtracted.

Previous experiments in our group already utilised two-mode squeezers. One experiment reached locked squeezing values of 0.4 dB and 0.5 dB of anti-squeezing [Wim16]. Another experiment showed a locked squeezing level of 1.24 dB and anti-squeezing level of 2.03 dB (free running: 2.3 dB of squeezing, and 3.7 dB of anti-squeezing) [Ste19]. The reasons for this thesis's improved squeezing are many and related to better efficiencies. For instance, the escape efficiency η_{esc} increased from 93 % to 96 %, the quantum efficiency η_{qe} from 80 % (estimated) to 97 %, and the total efficiency η from 59 % to 86 % (old values taken from [Ste19]).

The best squeezing value measured in the squeezing slope in Fig. 5.3a) is around -6.4 dB, while -7.3 dB are measured in the spectrum in Fig. 5.3b). One assumption for causing this difference is that the squeezing slope measurement was taken when the NDOPO had a non-ideal cavity resonance condition, see Subsec. 5.4.2. The full slope measurement takes tens of minutes, and the crystal temperature needs to be manually optimised for each pump power again. This procedure can be prone to errors. For instance, the thermal equilibrium could not be reached for each pump power leading to a drifting and thus non-ideal resonance condition. Additionally, the unknown loss channels $\eta_{x,s} = 93.6$ % and $\eta_{x,p} = 94.1$ %, which are included in Eqs. (5.17) and (5.18), can cause trouble.

I suggest repeating the analysis of the individual loss channels in the future and remeasuring the squeezing slope with care. For the scope of [P3], this was not progressed because the priority was set on the novel detection scheme.

This subsection has shown that our NDOPO produces a two-mode squeezed state that exhibits a decent amount of squeezing. The quantum state can be reconstructed using the method from [P3]. The next subsection focuses on the experimental challenge of a barely stable cavity resonance.

5.4.2 Stability problems

We have observed that the squeezing and anti-squeezing levels are not constant on a timescale of minutes after optimisation. The reason for this degradation is a changing polarisation degeneracy point in the NDOPO induced by small temperature drifts in the crystal.

The PPKTP crystal inside the NDOPO is temperature controlled to roughly 30 °C, as explained in Subsec. 2.4.1. Figure 2.10 shows that both crystal sides are kept on independent temperatures T_{PD} and T_{DC} by two Peltier elements. Because the negative temperature coefficient thermistor (NTC) sensors are placed in the oven,²³ the temperatures are not directly measured at the crystal. Depending on the current resistances of the NTC, more or less current will flow to heat the Peltier elements. In general, the temperature of the crystal will be a little lower than the copper parts because heat dissipates to the environment. If the environment changes thermodynamically, e.g. due to a rise in the room temperature, the dissipation channels become less effective. The crystal increases its temperature before reaching thermal equilibrium again. Consequently, the polarisation degeneracy point can change despite constant temperature control loops.

The green pump light absorbed by the crystal has the largest influence on the heat dissipation of the crystal. I observed that the spectral distance between s- and p-polarisation modes changed by multiple linewidths ($\delta\omega \approx 1.7$ MHz), when increasing the pump from zero to hundreds of milliwatt. For an ideally constant pump power, the point of degeneracy should not change. However, the low-frequency pump power

²³See again Fig. 2.11.

fluctuations are causing the temperature drift. They are the reason for the change in polarisation degeneracy.

The changing resonance condition has two effects which cause the two-mode squeezing to degrade. Since the NDOPO is actively locked only on the resonance condition for the s-polarisation, the p-polarisation sees a detuned cavity. The detuning reduces the effective squeezing interaction strength because the p-polarisation is no longer resonant in the cavity.²⁴ Secondly, due to the temperature drift, the phase of the p-polarised field exiting the cavity is not constant, corresponding to a fluctuating output polarisation. The s- and p-polarised field are separately detected in a dual homodyne detector. There, a fluctuating output polarisation is not a problem because the detection angles' locks compensate for these fluctuations. However, our single homodyne detector is prone to the signal's polarisation fluctuations, as it is inherently polarisation-sensitive.

Despite the temperature drift, the two-mode squeezed state remained constant over the few seconds of the measurement. However, the temperature drifts are the largest limitation in demonstrating a more accurate reconstruction of the two-mode squeezed state using a single homodyne detector. Ideas for improving on that are discussed in Sec. 5.6.

5.5 From the measurement to the reconstruction of the Wigner function

The Wigner function cannot be measured directly but results from individual measurements that are post-processed and combined. The polarisation accuracy of the local oscillator is crucial for our proposed approach since this is the reference field for the detection. First, Subsec. 5.5.1 answers how the local oscillator is precisely adjusted. Once the required polarisation states are found, the data is taken in a series of automatic measurements, which will be the subject of Subsec. 5.5.2. This subsection also includes remarks on the statistical data analysis. It closes with a plot of all cross-sections of the reconstructed Wigner function in Subsec. 5.5.3.

5.5.1 Preparing the polarisation-sensitive homodyne detector

The local oscillator's polarisation state defines the detection's polarisation basis. Ideally, this basis matches the two-mode squeezed state's polarisation basis at the 50/50 beam splitter. Only then are the orthogonal s- and p-polarisation contributions decoupled and can be treated independently. Relying on accurate polarisation properties can cause problems, as we have already seen in Subsec. 3.4.3.

I use a polarimeter [Thorlabs, PAX1000IR1] to monitor the polarisation bases for the homodyne detection. The polarimeter senses a beam reflected on a high-reflective flipping mirror after the 50/50 beam splitter (not shown in Fig. 1 and 2 of [P3]). The polarisation basis of the polarimeter serves as a reference. The waveplates can arbitrarily modify the polarisation basis of the local oscillator, as seen in Subsec. 5.3.2. Hence, only the polarisation of a (classical) 45° linearly polarised beam transmitted by the NDOPO cavity needs to be adjusted. This beam's polarisation is determined by the NDOPO geometry and polarisation properties itself. Thus to prevent any polarisation misalignments, the cavity should be set up with care according to the explanations from Subsec. 2.4.2.

²⁴This effect is similar as in the case of the detuned OPO visualised in the quantum sideband picture in Fig. 4.2.

For the measurements required for the reconstruction, we need six accurately defined polarisation states of the local oscillator. Our half-wave and quarter waveplates are mounted on electronic rotation mounts [Thorlabs, ELL14] that are controlled by a MATLAB [Mat] script. Once the pairs of angles $(\theta_{\text{HWP}}^i, \theta_{\text{QWP}}^i)$, $i \in \{1, 2, 3, 4, 5, 6\}$ for the six polarisations are found, we can reproduce the local oscillators polarisations state on demand. Hence, all six measurements can be taken automatically in one measurement and also in a short acquisition time.

The six angle pairs are automatically found by another MATLAB script, calibrating the waveplates. The script behaves similarly to a conventional auto-alignment tool. For each of the six polarisation states of the local oscillator, two target values are defined: the polarisation ellipticity and the polarisation rotation angle. In each iteration, the current values for the ellipticity and the rotation angle are compared to the target values. If the ellipticity error is larger, the quarter waveplate is rotated into the direction where the ellipticity error is reduced.²⁵ If the error for the rotation angle is larger, the half waveplate is rotated into the direction where this error is reduced. The step size is continuously reduced to converge to a steady solution. The algorithm stops when a given accuracy for the ellipticity and the rotation angle is reached.

5.5.2 Data acquisition and statistical data analysis

A MATLAB script triggers the data acquisition on a computer for the measurements with a single homodyne detector. The computer is interfaced with a spectrum analyser [Keysight, N9020A MXA] and to the two electronic rotation mounts [Thorlabs, ELL14], where the waveplates are mounted. First, the waveplates are calibrated as described in the last two paragraphs of Subsec. 5.5.1. Then, the six required polarisation states can be instantaneously generated, initiated by the MATLAB script. For each polarisation state of the local oscillator, a zero-span spectrum was measured at a frequency of 197 MHz. The resolution bandwidth was set to 200 kHz and the video bandwidth was 100 Hz.²⁶

For the measurements with the dual homodyne detection scheme, all six measurements are started manually. The spectrum analyser's configurations are the same as for measuring with the single homodyne detector.

The statistical data analysis is performed with another MATLAB script. During the measurements shown in Fig. 1 of [P3], the detection phase (only a single detection phase for the dual homodyne detection) is ramped, and variances are measured. To extract the required variances given in Eqs. (4a)–(4f) in [P3], the data is smoothed and searched for minimal and maximal values. With the knowledge of the time stamps of these extrema variances, the detection phase is attributed to all other times. Then, the noise can be determined for a local oscillator phase of $\pi/4$, needed when applying Eqs. (5) in [P3].

5.5.3 Cross-sections of the Wigner function

The reconstructed Wigner function represents the two-mode squeezed state depending on the four quadratures. For a better visualisation of the covariance matrix, the Wigner function is partially plotted by two-dimensional cross-sections. In Fig. 5.4, each picture corresponds to an entry in the left covariance matrix from Fig. 4 in [P3]. All pictures are plotted using Eq. (2.32) with $N = 1$. The four variances on the diagonal define the projected widths of all other Wigner distributions. Moreover, the

²⁵The sign is found by trial and error.

²⁶In [P3], the video bandwidth was wrongly stated as 100 kHz.

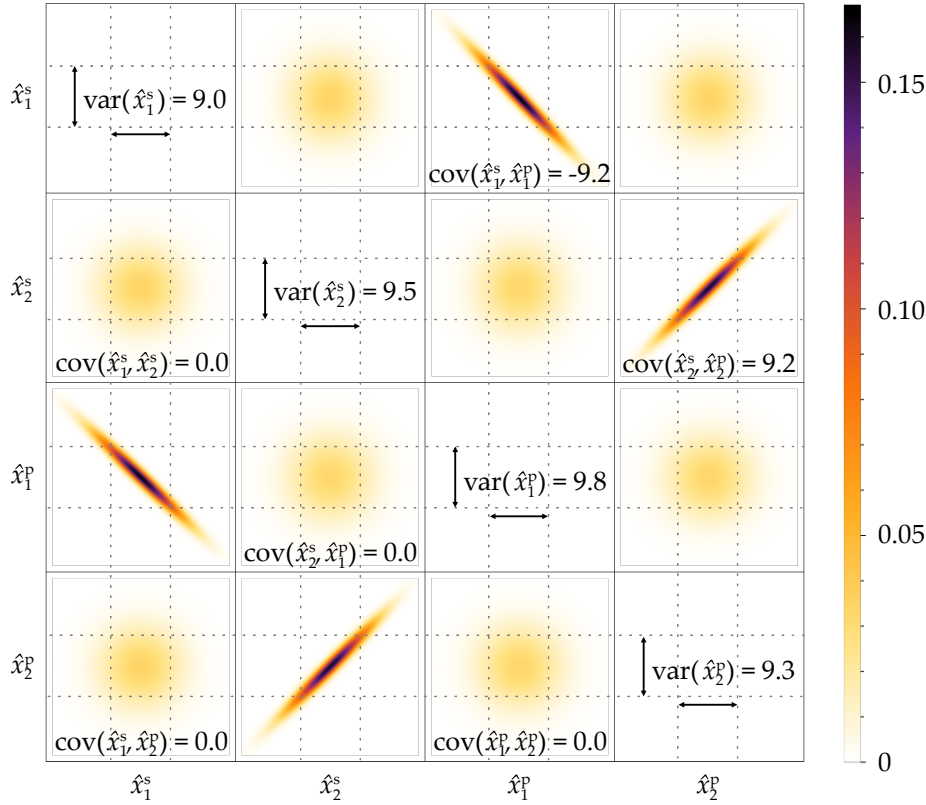


FIGURE 5.4: Cross-sections of the Wigner function obtained from measurements with a single homodyne detector for pairwise quadratures. The right upper plots are symmetric to the left bottom plots. They are plotted by using the left covariance matrix from Fig. 4 in [P3] and Eq. (2.32) with $N = 1$. The widths of the distributions are given by the four variances and the correlation by the covariances.

covariances show the pairwise correlations of quadrature combinations. Four Wigner distributions have shapes of squeezed ellipses. For the positive $\text{cov}(x_2^s, x_2^p) = 9.2$, the ellipse is distributed along the identity line $x_2^p = x_2^s$. Intuitively spoken, this means that when measuring a positive value for x_2^p , it is also likely that the value for x_2^s is also positive. In contrast, when the covariance is negative, as for $\text{cov}(x_1^s, x_1^p) = -9.2$, a positive value in x_1^p tends to imply a negative value for x_1^s . The other four distributions show nearly symmetric thermal states.

Thermal states have a larger uncertainty than vacuum or coherent states [BL04]. The reason for the increased width is that classical or thermal noise is added [SSL17]. Perfect thermal states obey $\text{var } x_1 = \text{var } x_2$. The blurry states in Fig. 5.4 are slightly asymmetric and show nearly ideal thermal states. Another way to create thermal states is by using a phase-insensitive amplifier.²⁷

This section presented supplemental information regarding the data acquisition and analysis for [P3]. It explained how the local oscillator's polarisation states are created using motorised waveplates. Further, it visualised the full reconstructed covariance matrix in a 4×4 plot showing different cross-sections of the Wigner function. The next section closes this chapter with a discussion and conclusion.

²⁷For a phase space picture, see, e.g. Fig. 5 of [Mar+14].

5.6 Discussion and conclusion

In our publication [P3], we reconstructed the covariance matrix of a two-mode squeezed state. The state shows quantum entanglement, which can be studied by the Reid criterium from Eq. (5.4) [Rei89]. From the covariance matrix, we can also infer the inseparability of the state by using the Duan criterium from Eq. (5.3) [Dua+00].²⁸ The bipartite two-mode squeezed state generated by our NDOPO is also characterised by the purity, as defined in Eq. (5.2). When detecting the two-mode squeezed state with the single homodyne detector, we find $\mu_{1\text{HD}} = 0.26$. For the dual homodyne detection, we find $\mu_{2\text{HD}} = 0.31$. These purity values might correspond to the fact that the state detected with a single homodyne detector experiences slightly more optical loss degrading the purity more.

Our reconstructed covariance matrix has relatively large uncertainties compared to other experiments that reconstructed bipartite states [Lau+05; D'A+09; Ste+13]. This should not be misinterpreted by assigning the uncertainties directly to the method of using only a polarisation-sensitive homodyne detector to reconstruct the state. The large uncertainties originate from the fluctuating polarisation of the output two-mode squeezed state, as explained in Subsec. 5.4.2. Thus, the locking stability of the NDOPO is the limitation for our obtained accuracy in the covariance matrix. However, the instability problem can be tackled by two approaches in the future.

First, we need to eliminate the temperature changes affecting the non-linear crystal. In operation mode, the temperature drifts originate from power fluctuations of the pump field. A power stabilisation for the green pump will create a much more stable thermal environment and equilibrium once the desired pump power is selected.²⁹ In our experiments, there are some potential approaches to stabilise the pump power using different actuators. As an actuator, we could use, e.g. a Mach-Zehnder interferometer [MV20], an acousto-optic modulator (AOM) [JOW17], the current of the laser diode³⁰ or even the resonance point in the SHG cavity could be possible.

The second option to tackle the drifting polarisation degeneracy is to actively control it. Here, the task is to optically generate an error signal that can be fed back to the oven temperature of the crystal. The error signal can be generated, e.g. with a polarisation-sensitive homodyne lock [HC80; Heu+09], as shown in Fig. 5.5. From the right, the counter-propagating locking field, which is 45° linearly polarised, is coupled into the NDOPO. The reflected field is sent to a 50/50 beam splitter where it is equally distributed. One fraction is detected behind an s-polarisation filter on a photodiode to create the Pound-Drever-Hall (PDH) error signal to lock the NDOPO. With this control loop, the NDOPO is kept resonant for the s-polarisation field. The other fraction is sent through a quarter waveplate on a PBS to let both polarisation contributions interfere. The two output fields are then measured with a homodyne detector to generate the error signal.

The error signal for the polarisation degeneracy lock is investigated, as seen in Fig. 5.6. First, the polarisation degeneracy was ramped by changing the temperature of the small part of the crystal (a schematic of the crystal is shown in Fig. 2.10). The temperature is proportional to the voltage shown by the blue trace in Fig. 5.6. During the temperature change, the homodyne detector monitored the error signal shown by the red trace, which looks like a typical PDH error signal. This can be explained

²⁸The verification of these two criteria is done in the last paragraph of Sec. 5 in [P3].

²⁹A power stabilisation for the pump was also realised in [MV18], to reach co-resonance for the pump and the fundamental field in a doubly resonant OPO.

³⁰To already stabilise the fundamental power.

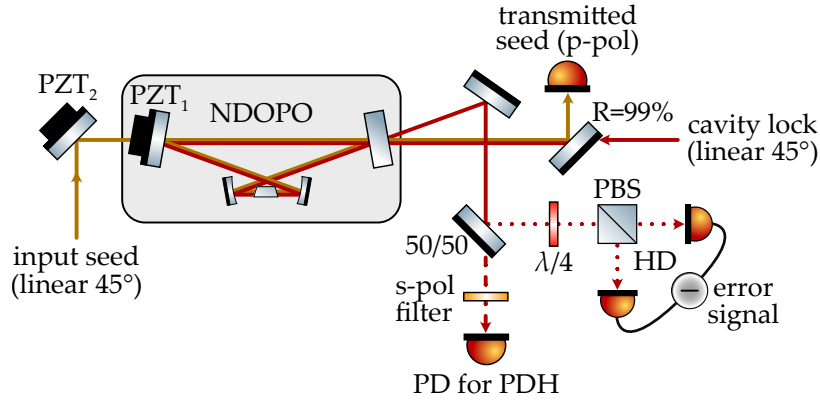


FIGURE 5.5: Setup of the polarisation degeneracy lock, including the seed field propagating from the left (orange arrow) and the locking field from the right (red arrow). The NDOPO is kept on resonance by detecting the s-polarisation contribution of the locking field for the PDH lock (red dashed arrow). The error signal for the polarisation degeneracy lock is obtained on the homodyne detector (HD) from self-interference of the 45° linearly polarised locking field at the PBS (red dotted arrow).

by the 12 MHz phase modulation of the locking field. The two small error signals are created by the beat of the resonant phase modulation sidebands with the input seed. The measurements from Fig. 5.6 show that an active lock for the polarisation degeneracy in the NDOPO seems possible.

The suggested lock was not fully realised due to technical difficulties at the time of writing. Optimally, the lock uses a servo, which is interfaced with the temperature controller. Slowly changing the current heating the Peltier element would be beneficial to conveniently resolve the error signal. Additionally, a variable gain and offset would be beneficial, making debugging simpler and locking less complicated. Then, the locking bandwidth can be analysed, which will be strongly limited by the heat flow from the Peltier element to the crystal, which is measured to happen at sub-hertz frequencies. Using a digital loop could simplify the realisation of the lock. An optimised oven design with shorter heat flows and better thermal shielding potentially improves the control bandwidth.

In conclusion, I recommend continuing to develop a lock for the polarisation degeneracy when working with two-mode squeezers³¹ in the future.³² Stabilising the pump power would help to minimise the temperature drifts in the first place.

Once the NDOPO generates a more stable two-mode squeezed state, we can reconstruct the covariance matrix with higher accuracy using only a single homodyne detector. Then, the statistical errors are presumably reduced, and longer measurement durations with more data points are realisable.³³ In particular, more data points are relevant when applying quantum tomography to reconstruct the squeezed state, as done in [P2].

A two-mode squeezed state can be generated by various methods as mentioned in Sec. 5.4. During the work with two-mode squeezed states, another potential method evolved. It seems conceivable to use two single-mode squeezed states, but instead of interfering them on a 50/50 beam splitter, they are superimposed on a PBS. Then a

³¹These can be normal two-mode squeezers or all-optical effective negative-mass oscillators used for coherent quantum noise cancellation (CQNC) [Ste19].

³²The suggested lock is only one option. Another possibility to generate an error signal for the p-polarisation resonance is to use modulation techniques [Dre+83].

³³More data points require longer storage times to process the data.

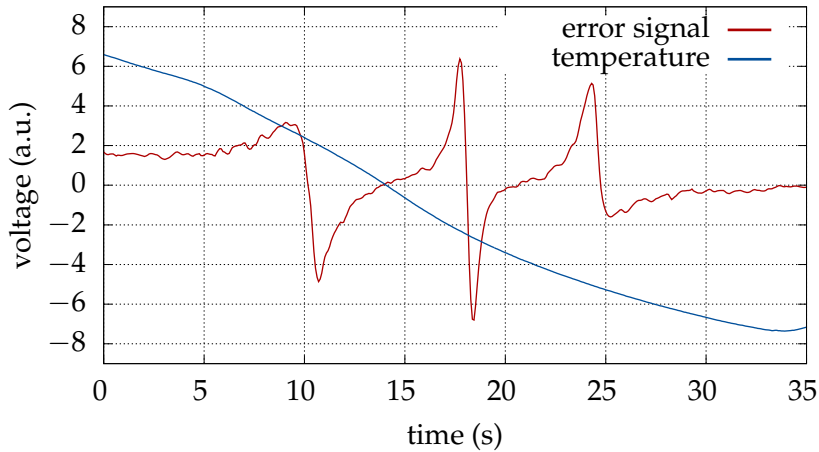


FIGURE 5.6: Error signal of the polarisation degeneracy lock for a two-mode squeezer. The blue trace shows the ramped temperature of the small part of the oven, which changes the polarisation degeneracy in the NDOPO. The red trace depicts the error signal measured at the homodyne detector.

polarisation two-mode squeezed state should be created at the output ports of the PBS. It seems to be interesting to elaborate on this idea in the future.

The measured squeezing and anti-squeezing from Fig. 5.3 can be used to calculate the coupling strength for the down-conversion process g_{DC} . Taking the obtained parameters of the linewidth $\delta\omega = 1.7$ MHz and the threshold power of 1.25 W, the coupling strength only depends on the used green pump power P and reads as³⁴

$$g_{\text{DC}} = \frac{2\pi \times 1.7 \text{ MHz}}{2} \sqrt{\frac{P}{1.25 \text{ W}}} = 2\pi \times 240 \text{ kHz} \sqrt{\frac{P}{100 \text{ mW}}}. \quad (5.19)$$

For the all-optical cascaded CQNC we aim for $g_{\text{DC}} = 2\pi \times 250$ kHz [Sch+22]. This value can be reached with the new two-mode squeezer for a pump power of only $P = 108$ mW, according to Eq. (5.19). The old two-mode squeezer required $P = 137$ mW of pump power to reach the same coupling strength of $g_{\text{DC}} = 2\pi \times 250$ kHz [Ste19].

In conclusion, entangled Gaussian bipartite states can be used in numerous applications. They reach from gravitational wave detectors, over quantum communication, to quantum imaging. The bipartite state is also called a two-mode squeezed state indicating quantum correlations in the two spatial modes. Usually, the covariance matrix is determined to characterise these two-mode squeezed states. It exhibits the full information about the quantum noise distributions. In particular, the covariance matrix discloses the degree of entanglement and the purity of the investigated state.

Conventionally, the two-mode squeezed states are detected by dual homodyne detection schemes, where each of the two homodyne detectors measures the quadratures of a single mode. The quadrature combinations are obtained by electronically adding or subtracting the signals from the homodyne detectors. Our publication [P3] demonstrated that a polarisation-sensitive single homodyne detector takes all measurements needed to reconstruct the covariance matrix. We use six different polarisation states of the local oscillator, each measuring a particular combination of variances. The advantage of our method compared to [D'A+05; D'A+09] is that the state under estimation deteriorates less on the way to the homodyne detector. This

³⁴Compare with Eq. (4.75) from [Ste19].

is because we avoid the transmission through optical components (two waveplates and a PBS), thereby retaining more coherence. Our intuitive method does not require to define new auxiliary modes [D'A+05; D'A+09]. Compared to the conventional dual homodyne detection method, we are not dependent on two equal homodyne detectors, which might be technically difficult at high frequencies in the hundreds of megahertz regime. The reconstructed state fulfils the criteria from Reid [Rei89] and Duan [Dua+00], clearly showing its inseparability and quantum entanglement character.

The generated two-mode squeezed state has a reduced squeezed uncertainty of up to -7.3 dB, which is a squeezing improvement of around 5 dB compared to previous experiments in our working group [Wim16; Ste19]. Finally, the derived down-conversion coupling strength g_{DC} fulfils the requirements for the all-optical cascaded CQNC experiment for a pump power of roughly 108 mW. For the future, I recommend optimising the temperature stability of the PPKTP crystal in the NDOPO to reach a more stable polarisation non-degeneracy.

Chapter 6

Discussion

This chapter discusses the findings of this thesis first from a technical perspective. It starts with a list of new developments and improvements compared to former experiments. Then, this chapter links the previous Chapters 3, 4 and 5. In particular, the discussion includes insights gained from working with these experiments. Also, relevant suggestions for future investigations and potential improvements are given.

Throughout this thesis, the squeezer (optical parametric oscillator (OPO) or non-degenerate optical parametric oscillator (NDOPO)) forms the heart of our experiments. At the time when the thesis was started, the maximum measured squeezing in our group was only a few decibels [Den16; Wim16]. The progress in the last years led to significant improvements in the squeezers. They can be ascribed to reducing optical losses and developing new control architectures.

Compared to the former, the new squeezers consist of a full set of new optical components. These are better polished and coated optics, i.e. cavity mirrors and periodically-poled potassium titanyl phosphate (PPKTP) crystals. Thus, the intracavity loss was reduced to roughly 0.2%. The new experiments are conducted in a cleaner laboratory environment. Consequently, they are less exposed to dust particles, distributing on mirrors and causing optical loss. One significant milestone was the substitution of the old homodyne detector with a new one with high-quantum efficiency (> 96%). This innovation reduced the loss because of inefficient detection by more than 15%. In the scope of this thesis, a new second harmonic generation (SHG) cavity design was created. Since it is roughly 1.5 times more efficient than the old SHG [Den16], more pump power is available for the OPO. Thus, I could decrease the finesse of the OPO by reducing the input/output coupler's reflectivity. This is beneficial because a lower reflectivity improves the cavity escape efficiency (see Eqs. (2.11) and (2.87)).

In this thesis, new methods were developed when working with the squeezers. Here, I want to list the four most relevant changes. First, the old squeezer was only stable when the PPKTP crystal was inserted [Den16; Wim16; Ste19]. This old design was adopted in [P1]. I changed the optical design of the squeezer such that it is stable even without the crystal, which significantly helps to align the cavity. Second, in [P2] and [P3], I placed a wedged crystal in an oven where two temperatures can be controlled. Previously, a rectangular-shaped crystal was used in a single-temperature oven. With the wedged crystal, adjusting the polarisation phase degeneracy was possible, increasing the performance of the NDOPO from roughly 2 dB to 7 dB of squeezing compared to [Ste19]. Third, instead of using the front beam as the seed [Den16], I only operate with a seed coupling via a high-reflective mirror into the squeezer. Thus, it is ensured that the seed coming from the squeezer represents the pure eigenmode of the cavity, which can then be used to optimise the contrast of the homodyne detection. Fourth, one change in the locking topology significantly enlarged the signal-to-noise ratio of the error signal. In the previous designs, the

squeezers were locked with an error signal obtained by the locking beam reflected from a high-reflective cavity mirror [Ste19]. In the new topology, I instead used the beam exiting the squeezer at the input/output mirror, which has a higher power leading to a better resolvable error signal.

It turned out that the squeezer used in [P1] has serious problems with phase noise which is mainly caused by two contributions. First, due to the rectangular crystal geometry, coupling can occur between co- and counter-propagating cavity modes. Depending on the coupling dynamics, the error signal suffers and the locking point of the squeezer can change, which created phase noise. Second, the intra-cavity modulation is used to imprint a phase modulation on the locking field to generate an error signal created phase noise. For the new iteration of the squeezers, these two details are modified. In [P2] and in [P3], a wedged crystal is installed, and the locking field is externally modulated. In particular, the OPO from [P2] benefits from this change. For this squeezer, the amount of phase noise is reduced from $\Delta\phi = 30$ mrad to $\Delta\phi = 15$ mrad (see Subsecs. 3.3.2 and 4.4.1).

Nevertheless, phase noise is still a problem in our squeezers. In principle, phase noise values of 1.7 mrad [Vah+16] or 1.3 mrad [Oel+16a] can be achieved. To reduce phase noise in future experiments, I recommend a detailed investigation of channels where phase noise couples. These involve, e.g. the locking stability of OPO and SHG cavities or phase noise occurring due to control sidebands of seed and local oscillator. A reduced phase noise would increase the squeezing level and brings us closer to the current squeezing record of 15 dB [Vah+16].

Another problem in our setups is potential noise from scattered light, originating mainly from three different fields. The squeezed state's amplitude consists only of the seed field, which co-propagates in the OPO. However, fractions of the counter-propagating locking field are reflected at the crystal surfaces and scatter into the co-propagating squeezing mode. Also, the seed itself and the local oscillator field are reflected at the homodyne detector and scatter in the counter-propagating mode of the OPO. Hence, three fields interfere, which distorts the set point of the cavity length control.

The squeezers used in the experiments [Vah+16; Oel+16a] exhibit two major differences to our setups. First, they do not require a locking field at the fundamental wavelength but rather control the cavity length with the green pump field. This is possible because their squeezers are resonant for both the infrared fundamental *and* the green pump light. Additionally, they use a coherent, frequency-shifted seed to lock the squeezing ellipse [Vah+06; Che+07]. For future work, I suggest implementing the mentioned two features to reduce phase noise, potentially caused by cavity length noise and noisy locked squeezing and detection angles. At the time of writing, the setup of a doubly resonant OPO cavity has already begun in our laboratories.

The experiments from [P2] and [P3] fully reconstruct the quantum state by using homodyne measurements. The main difference between the two approaches is that the reconstruction from [P3] assumes a Gaussian state. Thus, the full covariance matrix can be obtained by taking only a few measurements. Contrarily, in [P2], we applied quantum tomography, an imaging method that reconstructs the state as it is. Hence, this more elaborate reconstruction method can reveal any non-Gaussian quantum behaviour.

Chapter 7

Conclusion

In this conclusion, the main findings from this thesis are brought into a broader scientific context. The aim of this thesis was to develop different quantum systems generating tailored squeezed states and demonstrate their respective applicability. Here, the question is answered how the collected knowledge from this thesis is applicable in quantum optics.

In conclusion, this thesis developed novel quantum optical methods employing different, tailored non-classical light sources. It gives relevant theoretical descriptions for understanding these quantum systems. The quantum states are stably controlled, detected with least decoherence on different homodyne detector schemes and characterised resulting in the degree of squeezing or potential quantum entanglement. Each considered quantum system has specific features. This thesis explored high-frequency squeezed states for high-precision spectroscopy, frequency-dependent squeezed states from a detuned squeezer, and the reconstruction of a two-mode squeezed state. The publications [P1], [P2] and [P3] show that the results are of interest to the scientific community in the fields calling for particular squeezed states.

[P1] High-precision cavity spectroscopy using high-frequency squeezed light

In high-precision spectroscopy, the measurement sensitivity is often limited by technical noise at low frequencies, e.g. from the electronics. If technical noise is sufficiently reduced or circumvented, quantum shot noise will be visible and act as a fundamentally classical limitation. Shot noise can be passed with squeezed states of light. Even though squeezing was already implemented decades ago [PCK92], non-classical light is a rather unexplored topic for spectroscopy.

In publication [P1], a high-frequency phase modulated and amplitude quadrature squeezed state is generated to improve the sensitivity of measuring low-frequency phase signals. To be limited by shot noise, we shift our signal to larger measurement frequencies using a modulation technique. We demonstrated that sub-shot-noise signals at 100 Hz and 200 kHz are resolved in a reduced noise floor, squeezed by 6 dB. Recent publications showed the potential of using quantum correlations for microscopy [TG+20] and spectroscopy [Whi+17; And+20; MT22].

[P2] Frequency-dependent squeezing from a detuned squeezer

One of the most prominent examples of squeezed states' application in high-precision metrology is gravitational wave detectors. These instruments have been achieving unprecedented sensitivities near the standard quantum limit of interferometry, which can be beaten by non-classical methods. For instance, a state with a frequency-dependent squeezing angle can be utilised, realised by a conventional squeezer and reflected on filter cavities having low linewidths of hundreds of hertz.

The publication [P2] shows that a detuned optical parametric oscillator (OPO) produces a quantum state exhibiting frequency-dependent squeezing. Our generated state is reconstructed by quantum tomography. It rotates over megahertz frequencies and has a rotation angle of 39° and a maximal squeezing degree of 5.5 dB. Generating a squeezed state rotating over hundreds of hertz requires a long and lossless detuned OPO, which is technically challenging to realise. However, using our detuned squeezer approach (instead of the resonant squeezer) could potentially serve as a phase-rotation correction mechanism in addition to the filter cavities.

In opto-mechanical force measurements, coherent quantum noise cancellation (CQNC) is one way to beat the standard quantum limit [TC10; Wim+14; Sch+22]. Here, a particularly frequency-dependent squeezed state is required to cancel quantum back-action noise. This particular state can be generated by an effective negative-mass oscillator. The oscillator can be realised by a complicated combination of a two-mode squeezer and a coupled cavity [Ste19; Sch+22]. Instead, a detuned OPO could be an approximate but simple and promising approach to realise an effective negative-mass oscillator to cancel quantum back-action noise. First simulations show that e.g. the parameters could be numerically optimised, cancelling quantum noise only in a specific frequency band of interest.

[P3] Reconstructing Gaussian bipartite states with a single polarization-sensitive homodyne detector

Two-mode squeezed states require careful generation and handling since they are even more fragile than single-mode squeezed states. Asymmetries in the two modes cause degradations of the bipartite state. However, these states are required in many applications. For instance, they are considered to be applied in gravitational wave detectors [Ma+17; Yap+20; Süd+20] to beat the standard quantum limit. Two-mode squeezing relates to continuous-variable entanglement, a fundamental resource for numerous tasks. They range from quantum teleportation [BK98], continuous variable quantum computing [YAF04; Men+06], quantum imaging [Tre+02], quantum cryptography [Gis+02] and communication [GT07] or for measurements of biological samples [Tay+13]. Furthermore, they form a resource for fundamental tests of quantum mechanics, such as the Einstein-Podolsky-Rosen paradox [EPR35; Ou+92; Rei+09].

Publication [P3] deals with two-mode squeezed states generated by a non-degenerate optical parametric oscillator. It shows that the covariance matrix of a 7 dB squeezed state can be fully determined by taking measurements with a single polarisation-sensitive homodyne detector. This detection scheme does not require two equal homodyne detectors and will simplify the characterisations needed for the experiments mentioned above. Moreover, it introduces less loss than a previously demonstrated approach using a single homodyne detector [D'A+05; D'A+09].

With quantum states, violations of the Bell inequalities [AGR82; Wei+98] or tests of local hidden-variable theories [Cla+69; FC72] are shown. The implications of quantum physics are more relevant than ever. For instance, quantum physics is discussed in the context of machine learning [Sch+20; KZ20]. The actuality is also underlined by the award of this year's Nobel prize in physics to Aspect, Clauser and Zeilinger, *for experiments with entangled photons, establishing the violation of Bell inequalities and pioneering quantum information science* [N22]. The fundamental methods and concepts developed in this thesis can be applied to modern experiments using non-classical quantum states.

Bibliography

- [Abb+17] B. P. Abbott et al. “Multi-messenger Observations of a Binary Neutron Star Merger^{*}”. In: *The Astrophysical Journal Letters* 848.2 (2017), p. L12. DOI: [10.3847/2041-8213/aa91c9](https://doi.org/10.3847/2041-8213/aa91c9).
- [Abb+16a] B. P. Abbott et al. “Observation of Gravitational Waves from a Binary Black Hole Merger”. In: *Phys. Rev. Lett.* 116 (6 Feb. 2016), p. 061102. DOI: [10.1103/PhysRevLett.116.061102](https://doi.org/10.1103/PhysRevLett.116.061102).
- [Abb+16b] B. P. Abbott et al. “Observing gravitational-wave transient GW150914 with minimal assumptions”. In: *Phys. Rev. D* 93 (12 June 2016), p. 122004. DOI: [10.1103/PhysRevD.93.122004](https://doi.org/10.1103/PhysRevD.93.122004).
- [Abb+16c] B. P. Abbott et al. “Properties of the Binary Black Hole Merger GW150914”. In: *Phys. Rev. Lett.* 116 (24 June 2016), p. 241102. DOI: [10.1103/PhysRevLett.116.241102](https://doi.org/10.1103/PhysRevLett.116.241102).
- [AMMIL12] Y. S. Abu-Mostafa, M. Magdon-Ismail, and H.-T. Lin. *Learning From Data*. AMLBook, 2012. ISBN: 1600490069.
- [Ace+19] F. Acernese et al. “Increasing the Astrophysical Reach of the Advanced Virgo Detector via the Application of Squeezed Vacuum States of Light”. In: *Phys. Rev. Lett.* 123 (23 Dec. 2019), p. 231108. DOI: [10.1103/PhysRevLett.123.231108](https://doi.org/10.1103/PhysRevLett.123.231108).
- [ARL14] G. Adesso, S. Ragy, and A. R. Lee. “Continuous Variable Quantum Information: Gaussian States and Beyond”. In: *Open Systems & Information Dynamics* 21.01n02 (Mar. 2014), p. 1440001. DOI: [10.1142/s1230161214400010](https://doi.org/10.1142/s1230161214400010).
- [ASI04] G. Adesso, A. Serafini, and F. Illuminati. “Extremal entanglement and mixedness in continuous variable systems”. In: *Phys. Rev. A* 70 (2 Aug. 2004), p. 022318. DOI: [10.1103/PhysRevA.70.022318](https://doi.org/10.1103/PhysRevA.70.022318).
- [AMN08] S. Adhikari, A. S. Majumdar, and N. Nayak. “Broadcasting of continuous-variable entanglement”. In: *Phys. Rev. A* 77 (4 2008), p. 042301. DOI: [10.1103/PhysRevA.77.042301](https://doi.org/10.1103/PhysRevA.77.042301).
- [Agg+20] N. Aggarwal et al. “Room-temperature optomechanical squeezing”. In: *Nature Physics* 16.7 (2020), pp. 784–788.
- [And+20] R. B. de Andrade et al. “Quantum-enhanced continuous-wave stimulated Raman scattering spectroscopy”. In: *Optica* 7.5 (May 2020), pp. 470–475. DOI: [10.1364/OPTICA.386584](https://doi.org/10.1364/OPTICA.386584).
- [ATF06] T. Aoki, G. Takahashi, and A. Furusawa. “Squeezing at 946nm with periodically poled KTiOPO₄”. In: *Opt. Express* 14.15 (July 2006), pp. 6930–6935. DOI: [10.1364/OE.14.006930](https://doi.org/10.1364/OE.14.006930).
- [Ari+98] A. Arie et al. “Efficient resonant frequency doubling of a cw Nd:YAG laser in bulk periodically poled KTiOPO₄”. In: *Opt. Lett.* 23.1 (Jan. 1998), pp. 28–30. DOI: [10.1364/OL.23.000028](https://doi.org/10.1364/OL.23.000028).

- [Ari+97] A. Arie et al. "Green and ultraviolet quasi-phase-matched second harmonic generation in bulk periodically-poled KTiOPO₄". In: *Optics Communications* 142.4 (1997), pp. 265–268. ISSN: 0030-4018. DOI: [10.1016/S0030-4018\(97\)00338-6](https://doi.org/10.1016/S0030-4018(97)00338-6).
- [AGR82] A. Aspect, P. Grangier, and G. Roger. "Experimental Realization of Einstein-Podolsky-Rosen-Bohm Gedankenexperiment: A New Violation of Bell's Inequalities". In: *Phys. Rev. Lett.* 49 (2 July 1982), pp. 91–94. DOI: [10.1103/PhysRevLett.49.91](https://doi.org/10.1103/PhysRevLett.49.91).
- [Aud07] J. Audretsch. *Entangled Systems*. Wiley, Feb. 2007. DOI: [10.1002/9783527619153](https://doi.org/10.1002/9783527619153).
- [BR19] H.-A. Bachor and T. C. Ralph. *A Guide to Experiments in Quantum Optics*. Wiley, July 2019. DOI: [10.1002/9783527695805](https://doi.org/10.1002/9783527695805).
- [Bar20] T. Bartelsmeier. "Efficient Resonant Second Harmonic Generation Using a Precision Crystal Aligner". Bachelor's Thesis. Gottfried Wilhelm Leibniz Universität Hannover, 2020.
- [BE+19] S. Basiri-Esfahani, A. Armin, S. Forstner, and W. P. Bowen. "Precision ultrasound sensing on a chip". In: *Nature Communications* 10.1 (Jan. 2019), p. 132. DOI: [10.1038/s41467-018-08038-4](https://doi.org/10.1038/s41467-018-08038-4).
- [Bas14] M. Bassan, ed. *Advanced Interferometers and the Search for Gravitational Waves*. Springer International Publishing, 2014. DOI: [10.1007/978-3-319-03792-9](https://doi.org/10.1007/978-3-319-03792-9).
- [BWS13] J. Bauchrowitz, T. Westphal, and R. Schnabel. "A graphical description of optical parametric generation of squeezed states of light". In: *American Journal of Physics* 81.10 (2013), pp. 767–771. DOI: [10.1119/1.4819195](https://doi.org/10.1119/1.4819195).
- [Ben+93] C. H. Bennett et al. "Teleporting an unknown quantum state via dual classical and Einstein-Podolsky-Rosen channels". In: *Phys. Rev. Lett.* 70 (13 Mar. 1993), pp. 1895–1899. DOI: [10.1103/PhysRevLett.70.1895](https://doi.org/10.1103/PhysRevLett.70.1895).
- [BP61] H. E. Bennett and J. O. Porteus. "Relation Between Surface Roughness and Specular Reflectance at Normal Incidence". In: *J. Opt. Soc. Am.* 51.2 (1961), pp. 123–129. DOI: [10.1364/JOSA.51.000123](https://doi.org/10.1364/JOSA.51.000123).
- [Bla01] E. D. Black. "An introduction to Pound–Drever–Hall laser frequency stabilization". In: *American Journal of Physics* 69.1 (2001), pp. 79–87. DOI: [10.1119/1.1286663](https://doi.org/10.1119/1.1286663).
- [Boh13] N. Bohr. "I. On the constitution of atoms and molecules". In: *The London, Edinburgh, and Dublin Philosophical Magazine and Journal of Science* 26.151 (1913), pp. 1–25. DOI: [10.1080/14786441308634955](https://doi.org/10.1080/14786441308634955).
- [Bon+17] C. Bond, D. Brown, A. Freise, and K. A. Strain. "Interferometer techniques for gravitational-wave detection". In: *Living Reviews in Relativity* 19.1 (Feb. 2017), p. 3. ISSN: 1433-8351. DOI: [10.1007/s41114-016-0002-8](https://doi.org/10.1007/s41114-016-0002-8).
- [Bon86] R. S. Bondurant. "Reduction of radiation-pressure-induced fluctuations in interferometric gravity-wave detectors". In: *Phys. Rev. A* 34 (5 Nov. 1986), pp. 3927–3931. DOI: [10.1103/PhysRevA.34.3927](https://doi.org/10.1103/PhysRevA.34.3927).
- [BS84] R. S. Bondurant and J. H. Shapiro. "Squeezed states in phase-sensing interferometers". In: *Phys. Rev. D* 30 (12 Dec. 1984), pp. 2548–2556. DOI: [10.1103/PhysRevD.30.2548](https://doi.org/10.1103/PhysRevD.30.2548).

- [Bou+99] B. Boulanger et al. "Optical studies of laser-induced gray-tracking in KTP". In: *IEEE Journal of Quantum Electronics* 35.3 (1999), pp. 281–286. DOI: [10.1109/3.748831](https://doi.org/10.1109/3.748831).
- [Bow+03a] W. P. Bowen, R. Schnabel, P. K. Lam, and T. C. Ralph. "Experimental Investigation of Criteria for Continuous Variable Entanglement". In: *Phys. Rev. Lett.* 90 (4 Jan. 2003), p. 043601. DOI: [10.1103/PhysRevLett.90.043601](https://doi.org/10.1103/PhysRevLett.90.043601).
- [Bow+03b] W. P. Bowen et al. "Experimental investigation of continuous-variable quantum teleportation". In: *Phys. Rev. A* 67 (3 Mar. 2003), p. 032302. DOI: [10.1103/PhysRevA.67.032302](https://doi.org/10.1103/PhysRevA.67.032302).
- [BK68] G. D. Boyd and D. A. Kleinman. "Parametric Interaction of Focused Gaussian Light Beams". In: *Journal of Applied Physics* 39.8 (1968), pp. 3597–3639. DOI: [10.1063/1.1656831](https://doi.org/10.1063/1.1656831).
- [Boy20] R. W. Boyd. *Nonlinear Optics*. Elsevier, 2020. DOI: [10.1016/c2015-0-05510-1](https://doi.org/10.1016/c2015-0-05510-1).
- [BLZ19] R. W. Boyd, S. G. Lukishova, and V. N. Zadkov, eds. *Quantum Photonics: Pioneering Advances and Emerging Applications*. Springer International Publishing, 2019. DOI: [10.1007/978-3-319-98402-5](https://doi.org/10.1007/978-3-319-98402-5).
- [BVT80] V. B. Braginsky, Y. I. Vorontsov, and K. S. Thorne. "Quantum Nondestruction Measurements". In: *Science* 209.4456 (1980), pp. 547–557. DOI: [10.1126/science.209.4456.547](https://doi.org/10.1126/science.209.4456.547).
- [BL04] S. Braunstein and P. Loock. "Quantum Information with Continuous Variables". In: *Reviews of Modern Physics* 77 (Oct. 2004). DOI: [10.1103/RevModPhys.77.513](https://doi.org/10.1103/RevModPhys.77.513).
- [BK98] S. L. Braunstein and H. J. Kimble. "Teleportation of Continuous Quantum Variables". In: *Phys. Rev. Lett.* 80 (4 Jan. 1998), pp. 869–872. DOI: [10.1103/PhysRevLett.80.869](https://doi.org/10.1103/PhysRevLett.80.869).
- [BL05] S. L. Braunstein and P. van Loock. "Quantum information with continuous variables". In: *Rev. Mod. Phys.* 77 (2 June 2005), pp. 513–577. DOI: [10.1103/RevModPhys.77.513](https://doi.org/10.1103/RevModPhys.77.513).
- [BSM97] G. Breitenbach, S. Schiller, and J. Mlynek. "Measurement of the quantum states of squeezed light". In: *Nature* 387.6632 (May 1997), pp. 471–475. ISSN: 1476-4687. DOI: [10.1038/387471a0](https://doi.org/10.1038/387471a0).
- [BTW20] S. D. Brown, R. Tauler, and B. Walczak. *Comprehensive chemometrics: chemical and biochemical data analysis*. Elsevier, 2020.
- [Cam+06] M. Campanelli, C. O. Lousto, P. Marronetti, and Y. Zlochower. "Accurate Evolutions of Orbiting Black-Hole Binaries without Excision". In: *Phys. Rev. Lett.* 96 (11 Mar. 2006), p. 111101. DOI: [10.1103/PhysRevLett.96.111101](https://doi.org/10.1103/PhysRevLett.96.111101).
- [Cas+20] C. A. Casacio et al. "Quantum correlations overcome the photo-damage limits of light microscopy". In: *arXiv e-prints* (Mar. 2020), arXiv:2004.00178. DOI: [10.48550/arXiv.2004.00178](https://doi.org/10.48550/arXiv.2004.00178).
- [Cav81] C. M. Caves. "Quantum-mechanical noise in an interferometer". In: *Phys. Rev. D* 23 (8 Apr. 1981), pp. 1693–1708. DOI: [10.1103/PhysRevD.23.1693](https://doi.org/10.1103/PhysRevD.23.1693).

- [Cav80] C. M. Caves. "Quantum-Mechanical Radiation-Pressure Fluctuations in an Interferometer". In: *Phys. Rev. Lett.* 45 (2 July 1980), pp. 75–79. DOI: [10.1103/PhysRevLett.45.75](https://doi.org/10.1103/PhysRevLett.45.75).
- [Cav+80] C. M. Caves, K. S. Thorne, R. W. P. Drever, V. D. Sandberg, and M. Zimmermann. "On the measurement of a weak classical force coupled to a quantum-mechanical oscillator. I. Issues of principle". In: *Rev. Mod. Phys.* 52 (2 Apr. 1980), pp. 341–392. DOI: [10.1103/RevModPhys.52.341](https://doi.org/10.1103/RevModPhys.52.341).
- [Che07] S. Chelkowski. "Squeezed light and laser interferometric gravitational wave detectors". PhD thesis. Hannover: Gottfried Wilhelm Leibniz Universität Hannover, 2007.
- [Che+07] S. Chelkowski, H. Vahlbruch, K. Danzmann, and R. Schnabel. "Coherent control of broadband vacuum squeezing". In: *Phys. Rev. A* 75 (4 Apr. 2007), p. 043814. DOI: [10.1103/PhysRevA.75.043814](https://doi.org/10.1103/PhysRevA.75.043814).
- [Che+05] S. Chelkowski et al. "Experimental characterization of frequency-dependent squeezed light". In: *Phys. Rev. A* 71 (1 Jan. 2005), p. 013806. DOI: [10.1103/PhysRevA.71.013806](https://doi.org/10.1103/PhysRevA.71.013806).
- [Che+11] Y. Chen, S. L. Danilishin, F. Y. Khalili, and H. Müller-Ebhardt. "QND measurements for future gravitational-wave detectors". In: *General Relativity and Gravitation* 43.2 (Feb. 2011), pp. 671–694. ISSN: 1572-9532. DOI: [10.1007/s10714-010-1060-y](https://doi.org/10.1007/s10714-010-1060-y).
- [Chu+14] S. S. Y. Chua, B. J. J. Slagmolen, D. A. Shaddock, and D. E. McClelland. "Quantum squeezed light in gravitational-wave detectors". In: *Classical and Quantum Gravity* 31.18 (Sept. 2014), p. 183001. DOI: [10.1088/0264-9381/31/18/183001](https://doi.org/10.1088/0264-9381/31/18/183001).
- [CPM87] H. T. Chugani, M. E. Phelps, and J. C. Mazziotta. "Positron emission tomography study of human brain functional development". In: *Annals of Neurology* 22.4 (Oct. 1987), pp. 487–497. DOI: [10.1002/ana.410220408](https://doi.org/10.1002/ana.410220408).
- [Cla+16] J. B. Clark, F. Lecocq, R. W. Simmonds, J. Aumentado, and J. D. Teufel. "Observation of strong radiation pressure forces from squeezed light on a mechanical oscillator". In: *Nature Physics* 12.7 (July 2016), pp. 683–687. ISSN: 1745-2481. DOI: [10.1038/nphys3701](https://doi.org/10.1038/nphys3701).
- [Cla+69] J. F. Clauser, M. A. Horne, A. Shimony, and R. A. Holt. "Proposed Experiment to Test Local Hidden-Variable Theories". In: *Phys. Rev. Lett.* 23 (15 Oct. 1969), pp. 880–884. DOI: [10.1103/PhysRevLett.23.880](https://doi.org/10.1103/PhysRevLett.23.880).
- [CG84] M. J. Collett and C. W. Gardiner. "Squeezing of intracavity and traveling-wave light fields produced in parametric amplification". In: *Phys. Rev. A* 30 (3 Sept. 1984), pp. 1386–1391. DOI: [10.1103/PhysRevA.30.1386](https://doi.org/10.1103/PhysRevA.30.1386).
- [Coo+13] M. Cooper, L. J. Wright, C. Söller, and B. J. Smith. "Experimental generation of multi-photon Fock states". In: *Opt. Express* 21.5 (Mar. 2013), pp. 5309–5317. DOI: [10.1364/OE.21.005309](https://doi.org/10.1364/OE.21.005309).
- [CHH61] A. B. Crawford, D. C. Hogg, and L. E. Hunt. "A horn-reflector antenna for space communication". In: *The Bell System Technical Journal* 40.4 (1961), pp. 1095–1116. DOI: [10.1002/j.1538-7305.1961.tb01639.x](https://doi.org/10.1002/j.1538-7305.1961.tb01639.x).
- [Czy18] D. E. Czyzyk. "Nature of Sideband Generation". In: *IEEE Potentials* 37.1 (2018), pp. 19–22. DOI: [10.1109/MPOT.2016.2550014](https://doi.org/10.1109/MPOT.2016.2550014).

- [DCS01] M. D'Angelo, M. V. Chekhova, and Y. Shih. "Two-Photon Diffraction and Quantum Lithography". In: *Phys. Rev. Lett.* 87 (1 June 2001), p. 013602. DOI: [10.1103/PhysRevLett.87.013602](https://doi.org/10.1103/PhysRevLett.87.013602).
- [DKM19] S. L. Danilishin, F. Y. Khalili, and H. Miao. "Advanced quantum techniques for future gravitational-wave detectors". In: *Living Reviews in Relativity* 22.1 (Apr. 2019), p. 2. ISSN: 1433-8351. DOI: [10.1007/s41114-019-0018-y](https://doi.org/10.1007/s41114-019-0018-y).
- [DLPP01] G. M. D'Ariano, P. Lo Presti, and M. G. A. Paris. "Using Entanglement Improves the Precision of Quantum Measurements". In: *Phys. Rev. Lett.* 87 (27 Dec. 2001), p. 270404. DOI: [10.1103/PhysRevLett.87.270404](https://doi.org/10.1103/PhysRevLett.87.270404).
- [D'A+09] V. D'Auria et al. "Full Characterization of Gaussian Bipartite Entangled States by a Single Homodyne Detector". In: *Phys. Rev. Lett.* 102 (2 Jan. 2009), p. 020502. DOI: [10.1103/PhysRevLett.102.020502](https://doi.org/10.1103/PhysRevLett.102.020502).
- [D'A+05] V. D'Auria, A. Porzio, S. Solimeno, S. Olivares, and M. G. A. Paris. "Characterization of bipartite states using a single homodyne detector". In: *Journal of Optics B: Quantum and Semiclassical Optics* 7.12 (Nov. 2005), S750–S753. DOI: [10.1088/1464-4266/7/12/044](https://doi.org/10.1088/1464-4266/7/12/044).
- [Den16] T. Denker. "High-precision metrology with high-frequency nonclassical light sources". PhD thesis. Gottfried Wilhelm Leibniz Universität Hannover, 2016. DOI: [10.15488/8661](https://doi.org/10.15488/8661).
- [Den+06] M. L. Denton et al. "Damage thresholds for exposure to NIR and blue lasers in an in vitro RPE cell system". In: *Investig. Ophthalmol. Vis. Sci.* 47.7 (July 2006), pp. 3065–3073. ISSN: 01460404. DOI: [10.1167/iovs.05-1066](https://doi.org/10.1167/iovs.05-1066).
- [DK87] M. R. Dickinson and T. A. King. "Polarization Frequency Splitting in Non-planar Ring Laser Resonators". In: *Journal of Modern Optics* 34.8 (1987), pp. 1045–1055. DOI: [10.1080/09500348714550941](https://doi.org/10.1080/09500348714550941).
- [DiG+07] J. DiGuglielmo, B. Hage, A. Franzen, J. Fiurášek, and R. Schnabel. "Experimental characterization of Gaussian quantum-communication channels". In: *Phys. Rev. A* 76 (1 July 2007), p. 012323. DOI: [10.1103/PhysRevA.76.012323](https://doi.org/10.1103/PhysRevA.76.012323).
- [Dou+99] A. Douillet, J.-J. Zondy, A. Yelisseyev, S. Lobanov, and L. Isaenko. "Stability and frequency tuning of thermally loaded continuous-wave AgGaS₂ optical parametric oscillators". In: *J. Opt. Soc. Am. B* 16.9 (Sept. 1999), pp. 1481–1498. DOI: [10.1364/JOSAB.16.001481](https://doi.org/10.1364/JOSAB.16.001481).
- [Dre+83] R. W. P. Drever et al. "Laser phase and frequency stabilization using an optical resonator". In: *Applied Physics B* 31.2 (June 1983), pp. 97–105. ISSN: 1432-0649. DOI: [10.1007/BF00702605](https://doi.org/10.1007/BF00702605).
- [DMW81] P. Drummond, K. McNeil, and D. Walls. "Non-equilibrium Transitions in Sub/second Harmonic Generation". In: *Optica Acta: International Journal of Optics* 28.2 (1981), pp. 211–225. DOI: [10.1080/713820531](https://doi.org/10.1080/713820531).
- [Dua+00] L.-M. Duan, G. Giedke, J. I. Cirac, and P. Zoller. "Inseparability Criterion for Continuous Variable Systems". In: *Phys. Rev. Lett.* 84 (12 Mar. 2000), pp. 2722–2725. DOI: [10.1103/PhysRevLett.84.2722](https://doi.org/10.1103/PhysRevLett.84.2722).
- [EHS13] T. Eberle, V. Händchen, and R. Schnabel. "Stable control of 10 dB two-mode squeezed vacuum states of light". In: *Opt. Express* 21.9 (May 2013), pp. 11546–11553. DOI: [10.1364/OE.21.011546](https://doi.org/10.1364/OE.21.011546).

- [Eie+03] B. Eiermann et al. "Dispersion Management for Atomic Matter Waves". In: *Phys. Rev. Lett.* 91 (6 Aug. 2003), p. 060402. DOI: [10.1103/PhysRevLett.91.060402](https://doi.org/10.1103/PhysRevLett.91.060402).
- [EPR35] A. Einstein, B. Podolsky, and N. Rosen. "Can Quantum-Mechanical Description of Physical Reality Be Considered Complete?" In: *Phys. Rev.* 47 (10 May 1935), pp. 777–780. DOI: [10.1103/PhysRev.47.777](https://doi.org/10.1103/PhysRev.47.777).
- [Ein05] A. Einstein. "The photoelectric effect". In: *Ann. Phys* 17.132 (1905), p. 4.
- [ERB83] J. M. Elson, J. P. Rahn, and J. M. Bennett. "Relationship of the total integrated scattering from multilayer-coated optics to angle of incidence, polarization, correlation length, and roughness cross-correlation properties". In: *Appl. Opt.* 22.20 (Oct. 1983), pp. 3207–3219. DOI: [10.1364/AO.22.003207](https://doi.org/10.1364/AO.22.003207).
- [EBB79] J. Elson, H. Bennett, and J. Bennett. "Scattering from optical surfaces". In: vol. 7. *Applied Optics and Optical Engineering*. Elsevier, 1979, pp. 191–244. DOI: [10.1016/B978-0-12-408607-4.50014-1](https://doi.org/10.1016/B978-0-12-408607-4.50014-1).
- [Eng+97] A. Englander et al. "Highly efficient doubling of a high-repetition-rate diode-pumped laser with bulk periodically poled KTP". In: *Opt. Lett.* 22.21 (Nov. 1997), pp. 1598–1599. DOI: [10.1364/OL.22.001598](https://doi.org/10.1364/OL.22.001598).
- [FOP05] A. Ferraro, S. Olivares, and M. G. A. Paris. "Gaussian states in continuous variable quantum information". In: (2005). DOI: [10.48550/ARXIV.QUANT-PH/0503237](https://doi.org/10.48550/ARXIV.QUANT-PH/0503237).
- [Fow89] G. R. Fowles. *Introduction to modern optics*. Courier Corporation, 1989.
- [Fra+06] A. Franzen, B. Hage, J. DiGuglielmo, J. Fiurášek, and R. Schnabel. "Experimental Demonstration of Continuous Variable Purification of Squeezed States". In: *Phys. Rev. Lett.* 97 (15 Oct. 2006), p. 150505. DOI: [10.1103/PhysRevLett.97.150505](https://doi.org/10.1103/PhysRevLett.97.150505).
- [FC72] S. J. Freedman and J. F. Clauser. "Experimental Test of Local Hidden-Variable Theories". In: *Phys. Rev. Lett.* 28 (14 Apr. 1972), pp. 938–941. DOI: [10.1103/PhysRevLett.28.938](https://doi.org/10.1103/PhysRevLett.28.938).
- [Fur+98] A. Furusawa et al. "Unconditional Quantum Teleportation". In: *Science* 282.5389 (1998), pp. 706–709. DOI: [10.1126/science.282.5389.706](https://doi.org/10.1126/science.282.5389.706).
- [GK97] E. J. Galvez and P. M. Koch. "Use of four mirrors to rotate linear polarization but preserve input–output collinearity. II." In: *J. Opt. Soc. Am. A* 14.12 (Dec. 1997), pp. 3410–3414. DOI: [10.1364/JOSAA.14.003410](https://doi.org/10.1364/JOSAA.14.003410).
- [GC85] C. W. Gardiner and M. J. Collett. "Input and output in damped quantum systems: Quantum stochastic differential equations and the master equation". In: *Phys. Rev. A* 31 (6 June 1985), pp. 3761–3774. DOI: [10.1103/PhysRevA.31.3761](https://doi.org/10.1103/PhysRevA.31.3761).
- [Geo+95] N. P. Georgiades, E. S. Polzik, K. Edamatsu, H. J. Kimble, and A. S. Parkins. "Nonclassical excitation for atoms in a squeezed vacuum". In: *Phys. Rev. Lett.* 75.19 (1995), pp. 3426–3429. ISSN: 00319007. DOI: [10.1103/PhysRevLett.75.3426](https://doi.org/10.1103/PhysRevLett.75.3426).
- [GK04] C. Gerry and P. Knight. *Introductory Quantum Optics*. Cambridge University Press, Oct. 2004. DOI: [10.1017/cbo9780511791239](https://doi.org/10.1017/cbo9780511791239).
- [GLM04] V. Giovannetti, S. Lloyd, and L. Maccone. "Quantum-Enhanced Measurements: Beating the Standard Quantum Limit". In: *Science* 306.5700 (2004), pp. 1330–1336. DOI: [10.1126/science.1104149](https://doi.org/10.1126/science.1104149).

- [Gis+02] N. Gisin, G. Ribordy, W. Tittel, and H. Zbinden. “Quantum cryptography”. In: *Rev. Mod. Phys.* 74 (1 Mar. 2002), pp. 145–195. DOI: [10.1103/RevModPhys.74.145](https://doi.org/10.1103/RevModPhys.74.145).
- [GT07] N. Gisin and R. Thew. “Quantum communication”. In: *Nature Photonics* 1.3 (Mar. 2007), pp. 165–171. ISSN: 1749-4893. DOI: [10.1038/nphoton.2007.22](https://doi.org/10.1038/nphoton.2007.22).
- [Gla63a] R. J. Glauber. “Coherent and Incoherent States of the Radiation Field”. In: *Phys. Rev.* 131 (6 Sept. 1963), pp. 2766–2788. DOI: [10.1103/PhysRev.131.2766](https://doi.org/10.1103/PhysRev.131.2766).
- [Gla63b] R. J. Glauber. “The Quantum Theory of Optical Coherence”. In: *Phys. Rev.* 130 (6 June 1963), pp. 2529–2539. DOI: [10.1103/PhysRev.130.2529](https://doi.org/10.1103/PhysRev.130.2529).
- [Gra+87] P. Grangier, R. E. Slusher, B. Yurke, and A. LaPorta. “Squeezed-light-enhanced polarization interferometer”. In: *Phys. Rev. Lett.* 59 (19 Nov. 1987), pp. 2153–2156. DOI: [10.1103/PhysRevLett.59.2153](https://doi.org/10.1103/PhysRevLett.59.2153).
- [Gro46] H. Groenewold. “On the principles of elementary quantum mechanics”. In: *Physica* 12.7 (1946), pp. 405–460. ISSN: 0031-8914. DOI: [10.1016/S0031-8914\(46\)80059-4](https://doi.org/10.1016/S0031-8914(46)80059-4).
- [HSS10] B. Hage, A. Samblowski, and R. Schnabel. “Towards Einstein-Podolsky-Rosen quantum channel multiplexing”. In: *Phys. Rev. A* 81 (6 June 2010), p. 062301. DOI: [10.1103/PhysRevA.81.062301](https://doi.org/10.1103/PhysRevA.81.062301).
- [Ham+09] K. Hammerer, M. Aspelmeyer, E. S. Polzik, and P. Zoller. “Establishing Einstein-Poldosky-Rosen Channels between Nanomechanics and Atomic Ensembles”. In: *Phys. Rev. Lett.* 102 (2 Jan. 2009), p. 020501. DOI: [10.1103/PhysRevLett.102.020501](https://doi.org/10.1103/PhysRevLett.102.020501).
- [HC80] T. Hansch and B. Couillaud. “Laser frequency stabilization by polarization spectroscopy of a reflecting reference cavity”. In: *Optics Communications* 35.3 (1980), pp. 441–444. ISSN: 0030-4018. DOI: [10.1016/0030-4018\(80\)90069-3](https://doi.org/10.1016/0030-4018(80)90069-3).
- [He+19] Y. He, Y. Ma, Y. Tong, X. Yu, and F. K. Tittel. “Ultra-high sensitive light-induced thermoelastic spectroscopy sensor with a high Q-factor quartz tuning fork and a multipass cell”. In: *Opt. Lett.* 44.8 (Apr. 2019), pp. 1904–1907. DOI: [10.1364/OL.44.001904](https://doi.org/10.1364/OL.44.001904).
- [Hei27] W. Heisenberg. “Über den anschaulichen Inhalt der quantentheoretischen Kinematik und Mechanik”. In: *Zeitschrift für Physik* 43.3 (Mar. 1927), pp. 172–198. ISSN: 0044-3328. DOI: [10.1007/BF01397280](https://doi.org/10.1007/BF01397280).
- [HK96] C. H. Henry and R. F. Kazarinov. “Quantum noise in photonics”. In: *Rev. Mod. Phys.* 68 (3 July 1996), pp. 801–853. DOI: [10.1103/RevModPhys.68.801](https://doi.org/10.1103/RevModPhys.68.801).
- [Her+10] J. B. Hertzberg et al. “Back-action-evading measurements of nanomechanical motion”. In: *Nature Physics* 6.3 (Mar. 2010), pp. 213–217. ISSN: 1745-2481. DOI: [10.1038/nphys1479](https://doi.org/10.1038/nphys1479).
- [Her+06] F. Herzog, K. Kudielka, D. Erni, and W. Bachtold. “Optical Phase Locking by Local Oscillator Phase Dithering”. In: *IEEE Journal of Quantum Electronics* 42.10 (Oct. 2006), pp. 973–985. DOI: [10.1109/jqe.2006.881413](https://doi.org/10.1109/jqe.2006.881413).

- [Heu18] M. Heurs. “Gravitational wave detection using laser interferometry beyond the standard quantum limit”. In: *Philosophical Transactions of the Royal Society A: Mathematical, Physical and Engineering Sciences* 376.2120 (2018), p. 20170289. DOI: [10.1098/rsta.2017.0289](https://doi.org/10.1098/rsta.2017.0289).
- [Heu+09] M. Heurs, I. R. Petersen, M. R. James, and E. H. Huntington. “Homodyne locking of a squeezer”. In: *Opt. Lett.* 34.16 (Aug. 2009), pp. 2465–2467. DOI: [10.1364/OL.34.002465](https://doi.org/10.1364/OL.34.002465).
- [HOM87] C. K. Hong, Z. Y. Ou, and L. Mandel. “Measurement of subpicosecond time intervals between two photons by interference”. In: *Phys. Rev. Lett.* 59 (18 Nov. 1987), pp. 2044–2046. DOI: [10.1103/PhysRevLett.59.2044](https://doi.org/10.1103/PhysRevLett.59.2044).
- [Hoo65] R. Hooke. *Micrographia*. History of microscopy series. Science Heritage, 1665. ISBN: 9780940095076.
- [Hor84] W. Horsthemke. “Noise induced transitions”. In: *Non-equilibrium dynamics in chemical systems*. Springer, 1984, pp. 150–160.
- [HR02] E. H. Huntington and T. C. Ralph. “Separating the quantum sidebands of an optical field”. In: *Journal of Optics B: Quantum and Semiclassical Optics* 4.2 (Feb. 2002), pp. 123–128. DOI: [10.1088/1464-4266/4/2/307](https://doi.org/10.1088/1464-4266/4/2/307).
- [Hun+05] E. H. Huntington et al. “Demonstration of the spatial separation of the entangled quantum sidebands of an optical field”. In: *Phys. Rev. A* 71 (4 Apr. 2005), p. 041802. DOI: [10.1103/PhysRevA.71.041802](https://doi.org/10.1103/PhysRevA.71.041802).
- [JR90] M. T. Jaekel and S. Reynaud. “Quantum Limits in Interferometric Measurements”. In: *Europhysics Letters* 13.4 (Oct. 1990), p. 301. DOI: [10.1209/0295-5075/13/4/003](https://doi.org/10.1209/0295-5075/13/4/003).
- [Jin+06] J. Jing, S. Feng, R. Bloomer, and O. Pfister. “Experimental continuous-variable entanglement from a phase-difference-locked optical parametric oscillator”. In: *Phys. Rev. A* 74 (4 Oct. 2006), p. 041804. DOI: [10.1103/PhysRevA.74.041804](https://doi.org/10.1103/PhysRevA.74.041804).
- [Jou+13] P. Jouguet, S. Kunz-Jacques, A. Leverrier, P. Grangier, and E. Diamanti. “Experimental demonstration of long-distance continuous-variable quantum key distribution”. In: *Nature Photonics* 7.5 (May 2013), pp. 378–381. ISSN: 1749-4893. DOI: [10.1038/nphoton.2013.63](https://doi.org/10.1038/nphoton.2013.63).
- [JOW17] J. Junker, P. Oppermann, and B. Willke. “Shot-noise-limited laser power stabilization for the AEI 10 m Prototype interferometer”. In: *Opt. Lett.* 42.4 (Feb. 2017), pp. 755–758. DOI: [10.1364/OL.42.000755](https://doi.org/10.1364/OL.42.000755).
- [Jun+21] J. Junker, D. Wilken, E. Huntington, and M. Heurs. “High-precision cavity spectroscopy using high-frequency squeezed light”. In: *Opt. Express* 29.4 (Feb. 2021), pp. 6053–6068. DOI: [10.1364/OE.416713](https://doi.org/10.1364/OE.416713).
- [Jun+22a] J. Junker, D. Wilken, N. Johny, D. Steinmeyer, and M. Heurs. “Frequency-Dependent Squeezing from a Detuned Squeezer”. In: *Phys. Rev. Lett.* 129 (3 July 2022), p. 033602. DOI: [10.1103/PhysRevLett.129.033602](https://doi.org/10.1103/PhysRevLett.129.033602).
- [Jun+22b] J. Junker, D. Wilken, D. Steinmeyer, and M. Heurs. “Reconstructing Gaussian bipartite states with a single polarization-sensitive homodyne detector”. In: *Opt. Express* 30.19 (Sept. 2022), pp. 33860–33868. DOI: [10.1364/OE.465186](https://doi.org/10.1364/OE.465186).

- [KS01] A. C. Kak and M. Slaney. *Principles of Computerized Tomographic Imaging*. Society for Industrial and Applied Mathematics, Jan. 2001. DOI: [10.1137/1.9780898719277](https://doi.org/10.1137/1.9780898719277).
- [Kam+17] N. S. Kampel et al. “Improving Broadband Displacement Detection with Quantum Correlations”. In: *Phys. Rev. X* 7 (2 Apr. 2017), p. 021008. DOI: [10.1103/PhysRevX.7.021008](https://doi.org/10.1103/PhysRevX.7.021008).
- [Kar+04] J. P. Karr, A. Baas, R. Houdré, and E. Giacobino. “Squeezing in semiconductor microcavities in the strong-coupling regime”. In: *Phys. Rev. A* 69 (3 Mar. 2004), p. 031802. DOI: [10.1103/PhysRevA.69.031802](https://doi.org/10.1103/PhysRevA.69.031802).
- [KT02] K. Kato and E. Takaoka. “Sellmeier and thermo-optic dispersion formulas for KTP”. In: *Appl. Opt.* 41.24 (Aug. 2002), pp. 5040–5044. DOI: [10.1364/AO.41.005040](https://doi.org/10.1364/AO.41.005040).
- [Kau18] S. Kaufer. “Optical AC coupling in the gravitational wave detection band”. PhD thesis. Gottfried Wilhelm Leibniz Universität Hannover, 2018. DOI: [10.15488/3138](https://doi.org/10.15488/3138).
- [KDM77] H. J. Kimble, M. Dagenais, and L. Mandel. “Photon Antibunching in Resonance Fluorescence”. In: *Phys. Rev. Lett.* 39 (11 Sept. 1977), pp. 691–695. DOI: [10.1103/PhysRevLett.39.691](https://doi.org/10.1103/PhysRevLett.39.691).
- [Kim+01] H. J. Kimble, Y. Levin, A. B. Matsko, K. S. Thorne, and S. P. Vyatchanin. “Conversion of conventional gravitational-wave interferometers into quantum nondemolition interferometers by modifying their input and/or output optics”. In: *Phys. Rev. D* 65 (2 Dec. 2001), p. 022002. DOI: [10.1103/PhysRevD.65.022002](https://doi.org/10.1103/PhysRevD.65.022002).
- [KL66] H. Kogelnik and T. Li. “Laser Beams and Resonators”. In: *Appl. Opt.* 5.10 (Oct. 1966), pp. 1550–1567. DOI: [10.1364/AO.5.001550](https://doi.org/10.1364/AO.5.001550).
- [Koh+18] J. Kohler, J. A. Gerber, E. Dowd, and D. M. Stamper-Kurn. “Negative-Mass Instability of the Spin and Motion of an Atomic Gas Driven by Optical Cavity Backaction”. In: *Phys. Rev. Lett.* 120 (1 Jan. 2018), p. 013601. DOI: [10.1103/PhysRevLett.120.013601](https://doi.org/10.1103/PhysRevLett.120.013601).
- [KF00] M. I. Kolobov and C. Fabre. “Quantum Limits on Optical Resolution”. In: *Phys. Rev. Lett.* 85 (18 Oct. 2000), pp. 3789–3792. DOI: [10.1103/PhysRevLett.85.3789](https://doi.org/10.1103/PhysRevLett.85.3789).
- [Kra+12] A. G. Krause, M. Winger, T. D. Blasius, Q. Lin, and O. Painter. “A high-resolution microchip optomechanical accelerometer”. In: *Nature Photonics* 6.11 (Nov. 2012), pp. 768–772. ISSN: 1749-4893. DOI: [10.1038/nphoton.2012.245](https://doi.org/10.1038/nphoton.2012.245).
- [KZ20] M. Krenn and A. Zeilinger. “Predicting research trends with semantic and neural networks with an application in quantum physics”. In: *Proceedings of the National Academy of Sciences* 117.4 (Jan. 2020), pp. 1910–1916. DOI: [10.1073/pnas.1914370116](https://doi.org/10.1073/pnas.1914370116).
- [Kr15] C. Krüger et al. “Birefringence measurements on crystalline silicon”. In: *Classical and Quantum Gravity* 33.1 (Dec. 2015), p. 015012. DOI: [10.1088/0264-9381/33/1/015012](https://doi.org/10.1088/0264-9381/33/1/015012).
- [Kub62] R. Kubo. “A stochastic theory of line-shape and relaxation”. In: *Fluctuation, Relaxation and Resonance in Magnetic Systems* 23 (1962).

- [Kwe10] P. Kwee. “Laser characterization and stabilization for precision interferometry”. PhD thesis. Gottfried Wilhelm Leibniz Universität Hannover, 2010. DOI: [10.15488/7443](https://doi.org/10.15488/7443).
- [Lam98] P. K. Lam. “Applications of quantum electro-optic control and squeezed light”. PhD thesis. The Australian National University, 1998.
- [Lan08] P. Langevin. “Sur la théorie du mouvement brownien”. In: *Compt. Rendus* 146 (1908), pp. 530–533.
- [Lau+05] J. Laurat et al. “Entanglement of two-mode Gaussian states: characterization and experimental production and manipulation”. In: *Journal of Optics B: Quantum and Semiclassical Optics* 7.12 (Nov. 2005), S577–S587. DOI: [10.1088/1464-4266/7/12/021](https://doi.org/10.1088/1464-4266/7/12/021).
- [LKD02] H. Lee, P. Kok, and J. P. Dowling. “A quantum Rosetta stone for interferometry”. In: *Journal of Modern Optics* 49.14-15 (2002), pp. 2325–2338. DOI: [10.1080/0950034021000011536](https://doi.org/10.1080/0950034021000011536).
- [LG97] D. S. Lemons and A. Gythiel. “Paul Langevin’s 1908 paper “On the Theory of Brownian Motion” [“Sur la théorie du mouvement brownien,” C. R. Acad. Sci. (Paris) 146, 530–533 (1908)]”. In: *American Journal of Physics* 65.11 (1997), pp. 1079–1081. DOI: [10.1119/1.18725](https://doi.org/10.1119/1.18725).
- [Leo97] U. Leonhardt. *Measuring the Quantum State of Light*. Cambridge: Cambridge University Press, 1997. ISBN: 978-0-521-49730-5.
- [LK94] R.-D. Li and P. Kumar. “Quantum-noise reduction in traveling-wave second-harmonic generation”. In: *Phys. Rev. A* 49 (3 Mar. 1994), pp. 2157–2166. DOI: [10.1103/PhysRevA.49.2157](https://doi.org/10.1103/PhysRevA.49.2157).
- [Lia+17] S.-K. Liao et al. “Satellite-to-ground quantum key distribution”. In: *Nature* 549.7670 (Sept. 2017), pp. 43–47. ISSN: 1476-4687. DOI: [10.1038/nature23655](https://doi.org/10.1038/nature23655).
- [Liu+19] S. Liu, B. Liu, J. Wang, T. Sun, and W.-X. Yang. “Realization of a highly sensitive mass sensor in a quadratically coupled optomechanical system”. In: *Phys. Rev. A* 99 (3 Mar. 2019), p. 033822. DOI: [10.1103/PhysRevA.99.033822](https://doi.org/10.1103/PhysRevA.99.033822).
- [Lou+21] J. Lough et al. “First Demonstration of 6 dB Quantum Noise Reduction in a Kilometer Scale Gravitational Wave Observatory”. In: *Phys. Rev. Lett.* 126 (4 Jan. 2021), p. 041102. DOI: [10.1103/PhysRevLett.126.041102](https://doi.org/10.1103/PhysRevLett.126.041102).
- [Luc+16] V. G. Lucivero, R. Jiménez-Martínez, J. Kong, and M. W. Mitchell. “Squeezed-light spin noise spectroscopy”. In: *Phys. Rev. A* 93 (5 May 2016), p. 053802. DOI: [10.1103/PhysRevA.93.053802](https://doi.org/10.1103/PhysRevA.93.053802).
- [LR09] A. I. Lvovsky and M. G. Raymer. “Continuous-variable optical quantum-state tomography”. In: *Rev. Mod. Phys.* 81 (1 Mar. 2009), pp. 299–332. DOI: [10.1103/RevModPhys.81.299](https://doi.org/10.1103/RevModPhys.81.299).
- [Lya16] F. Lyall. *International Communications*. Routledge, Apr. 2016. DOI: [10.4324/9781315589336](https://doi.org/10.4324/9781315589336).
- [Ma+17] Y. Ma et al. “Proposal for gravitational-wave detection beyond the standard quantum limit through EPR entanglement”. In: *Nature Physics* 13.8 (Aug. 2017), pp. 776–780. ISSN: 1745-2481. DOI: [10.1038/nphys4118](https://doi.org/10.1038/nphys4118).

- [Ma+20] Y. Ma et al. “Ultra-high sensitive trace gas detection based on light-induced thermoelastic spectroscopy and a custom quartz tuning fork”. In: *Applied Physics Letters* 116.1 (Jan. 2020), p. 011103. DOI: [10.1063/1.5129014](https://doi.org/10.1063/1.5129014).
- [MYI87] S. Machida, Y. Yamamoto, and Y. Itaya. “Observation of amplitude squeezing in a constant-current-driven semiconductor laser”. In: *Phys. Rev. Lett.* 58 (10 Mar. 1987), pp. 1000–1003. DOI: [10.1103/PhysRevLett.58.1000](https://doi.org/10.1103/PhysRevLett.58.1000).
- [Mag+20] M. Maggiore et al. “Science case for the Einstein telescope”. In: *Journal of Cosmology and Astroparticle Physics* 2020.03 (Mar. 2020), p. 050. DOI: [10.1088/1475-7516/2020/03/050](https://doi.org/10.1088/1475-7516/2020/03/050).
- [Mai60] T. H. Maiman. “Stimulated Optical Radiation in Ruby”. In: *Nature* 187.4736 (Aug. 1960), pp. 493–494. ISSN: 1476-4687. DOI: [10.1038/187493a0](https://doi.org/10.1038/187493a0).
- [Mal06] M. Malec. “Commissioning of advanced, dual-recycled gravitational-wave detectors: simulations of complex optical systems guided by the phasor picture”. PhD thesis. 2006.
- [Mam+18] A. Mamrashev et al. “Optical Properties of KTP Crystals and Their Potential for Terahertz Generation”. In: *Crystals* 8.8 (2018). ISSN: 2073-4352. DOI: [10.3390/cryst8080310](https://doi.org/10.3390/cryst8080310).
- [Mar+14] M. E. Marhic et al. “Fiber optical parametric amplifiers in optical communication systems”. In: *Laser & Photonics Reviews* 9.1 (Sept. 2014), pp. 50–74. DOI: [10.1002/lpor.201400087](https://doi.org/10.1002/lpor.201400087).
- [Mas+19] D. Mason, J. Chen, M. Rossi, Y. Tsaturyan, and A. Schliesser. “Continuous force and displacement measurement below the standard quantum limit”. In: *Nature Physics* 15.8 (Aug. 2019), pp. 745–749. ISSN: 1745-2481. DOI: [10.1038/s41567-019-0533-5](https://doi.org/10.1038/s41567-019-0533-5).
- [Mat] *MATLAB version 9.8.0.1323502 (R2020a)*. The Mathworks, Inc. Natick, Massachusetts, 2020.
- [MT22] K. Matsuzaki and T. Tahara. “Superresolution concentration measurement realized by sub-shot-noise absorption spectroscopy”. In: *Nature Communications* 13.1 (Feb. 2022), p. 953. ISSN: 2041-1723. DOI: [10.1038/s41467-022-28617-w](https://doi.org/10.1038/s41467-022-28617-w).
- [Max65] J. C. Maxwell. “VIII. A dynamical theory of the electromagnetic field”. In: *Philosophical Transactions of the Royal Society of London* 155 (Dec. 1865), pp. 459–512. DOI: [10.1098/rstl.1865.0008](https://doi.org/10.1098/rstl.1865.0008).
- [McC+20] L. McCuller et al. “Frequency-Dependent Squeezing for Advanced LIGO”. In: *Phys. Rev. Lett.* 124 (17 Apr. 2020), p. 171102. DOI: [10.1103/PhysRevLett.124.171102](https://doi.org/10.1103/PhysRevLett.124.171102).
- [MV18] M. Mehmet and H. Vahlbruch. “High-efficiency squeezed light generation for gravitational wave detectors”. In: *Classical and Quantum Gravity* 36.1 (Dec. 2018), p. 015014. DOI: [10.1088/1361-6382/aaf448](https://doi.org/10.1088/1361-6382/aaf448).
- [MV20] M. Mehmet and H. Vahlbruch. “The Squeezed Light Source for the Advanced Virgo Detector in the Observation Run O3”. In: *Galaxies* 8.4 (2020). ISSN: 2075-4434. DOI: [10.3390/galaxies8040079](https://doi.org/10.3390/galaxies8040079).

- [Men+06] N. C. Menicucci et al. “Universal Quantum Computation with Continuous-Variable Cluster States”. In: *Phys. Rev. Lett.* 97 (11 Sept. 2006), p. 110501. DOI: [10.1103/PhysRevLett.97.110501](https://doi.org/10.1103/PhysRevLett.97.110501).
- [MM87a] A. A. Michelson and E. W. Morley. “On a method of making the wavelength of sodium light the actual and practical standard of length”. In: *American Journal of Science* s3-34.204 (1887), pp. 427–430. ISSN: 0002-9599. DOI: [10.2475/ajs.s3-34.204.427](https://doi.org/10.2475/ajs.s3-34.204.427).
- [MM87b] A. A. Michelson and E. W. Morley. “On the relative motion of the Earth and the luminiferous ether”. In: *American Journal of Science* s3-34.203 (1887), pp. 333–345. ISSN: 0002-9599. DOI: [10.2475/ajs.s3-34.203.333](https://doi.org/10.2475/ajs.s3-34.203.333).
- [Mil+22] A. Militaru et al. “Ponderomotive Squeezing of Light by a Levitated Nanoparticle in Free Space”. In: *Physical Review Letters* 129.5 (July 2022). DOI: [10.1103/physrevlett.129.053602](https://doi.org/10.1103/physrevlett.129.053602).
- [Møl+17] C. B. Møller et al. “Quantum back-action-evading measurement of motion in a negative mass reference frame”. In: *Nature* 547.7662 (July 2017), pp. 191–195. ISSN: 1476-4687. DOI: [10.1038/nature22980](https://doi.org/10.1038/nature22980).
- [Mot+16] A. Motazedifard, F. Bemani, M. Naderi, R. Roknizadeh, and D. Vitali. “Force sensing based on coherent quantum noise cancellation in a hybrid optomechanical cavity with squeezed-vacuum injection”. In: *New Journal of Physics* 18.7 (2016), p. 073040. DOI: [10.1088/1367-2630/18/7/073040](https://doi.org/10.1088/1367-2630/18/7/073040).
- [Mot+19] A. Motazedifard, A. Dalafi, F. Bemani, and M. H. Naderi. “Force sensing in hybrid Bose-Einstein-condensate optomechanics based on parametric amplification”. In: *Phys. Rev. A* 100 (2 Aug. 2019), p. 023815. DOI: [10.1103/PhysRevA.100.023815](https://doi.org/10.1103/PhysRevA.100.023815).
- [Wig] *Movie of the frequency-dependent rotating Wigner function*. URL: https://journals.aps.org/prl/supplemental/10.1103/PhysRevLett.129.033602/wigers_over_frequency.gif (visited on 10/13/2022).
- [Moy49] J. E. Moyal. “Quantum mechanics as a statistical theory”. In: *Mathematical Proceedings of the Cambridge Philosophical Society* 45.1 (1949), 99–124. DOI: [10.1017/S0305004100000487](https://doi.org/10.1017/S0305004100000487).
- [Myu03] I. J. Myung. “Tutorial on maximum likelihood estimation”. In: *Journal of Mathematical Psychology* 47.1 (2003), pp. 90–100. ISSN: 0022-2496. DOI: [10.1016/S0022-2496\(02\)00028-7](https://doi.org/10.1016/S0022-2496(02)00028-7).
- [Na04] I. Newton and G. H. and. *Opticks: or, A treatise of the reflections, refractions, inflexions and colours of light : also two treatises of the species and magnitude of curvilinear figures*. Printed for Sam. Smith, and Benj. Walford, 1704. DOI: [10.5479/sil.302475.39088000644674](https://doi.org/10.5479/sil.302475.39088000644674).
- [NC12] M. A. Nielsen and I. L. Chuang. *Quantum Computation and Quantum Information*. Cambridge University Press, June 2012. DOI: [10.1017/cbo9780511976667](https://doi.org/10.1017/cbo9780511976667).
- [NM41] F. C. Nix and D. MacNair. “The Thermal Expansion of Pure Metals: Copper, Gold, Aluminum, Nickel, and Iron”. In: *Phys. Rev.* 60 (8 Oct. 1941), pp. 597–605. DOI: [10.1103/PhysRev.60.597](https://doi.org/10.1103/PhysRev.60.597).

- [OK+16] C. F. Ockeloen-Korppi et al. “Quantum Backaction Evading Measurement of Collective Mechanical Modes”. In: *Phys. Rev. Lett.* 117 (14 Sept. 2016), p. 140401. DOI: [10.1103/PhysRevLett.117.140401](https://doi.org/10.1103/PhysRevLett.117.140401).
- [Oel+16a] E. Oelker et al. “Ultra-low phase noise squeezed vacuum source for gravitational wave detectors”. In: *Optica* 3.7 (July 2016), pp. 682–685. DOI: [10.1364/OPTICA.3.000682](https://doi.org/10.1364/OPTICA.3.000682).
- [Oel+16b] E. Oelker et al. “Audio-Band Frequency-Dependent Squeezing for Gravitational-Wave Detectors”. In: *Phys. Rev. Lett.* 116 (4 Jan. 2016), p. 041102. DOI: [10.1103/PhysRevLett.116.041102](https://doi.org/10.1103/PhysRevLett.116.041102).
- [OOT13] T. Ono, R. Okamoto, and S. Takeuchi. “An entanglement-enhanced microscope”. In: *Nature Communications* 4.1 (Sept. 2013), p. 2426. ISSN: 2041-1723. DOI: [10.1038/ncomms3426](https://doi.org/10.1038/ncomms3426).
- [Ou+92] Z. Y. Ou, S. F. Pereira, H. J. Kimble, and K. C. Peng. “Realization of the Einstein-Podolsky-Rosen paradox for continuous variables”. In: *Phys. Rev. Lett.* 68 (25 June 1992), pp. 3663–3666. DOI: [10.1103/PhysRevLett.68.3663](https://doi.org/10.1103/PhysRevLett.68.3663).
- [Our+07] A. Ourjoumtsev, H. Jeong, R. Tualle-Brouri, and P. Grangier. “Generation of optical ‘Schrödinger cats’ from photon number states”. In: *Nature* 448.7155 (Aug. 2007), pp. 784–786. ISSN: 1476-4687. DOI: [10.1038/nature06054](https://doi.org/10.1038/nature06054).
- [OTBG06] A. Ourjoumtsev, R. Tualle-Brouri, and P. Grangier. “Quantum Homodyne Tomography of a Two-Photon Fock State”. In: *Phys. Rev. Lett.* 96 (21 June 2006), p. 213601. DOI: [10.1103/PhysRevLett.96.213601](https://doi.org/10.1103/PhysRevLett.96.213601).
- [Pas+94] R. Paschotta et al. “Bright squeezed light from a singly resonant frequency doubler”. In: *Phys. Rev. Lett.* 72 (24 June 1994), pp. 3807–3810. DOI: [10.1103/PhysRevLett.72.3807](https://doi.org/10.1103/PhysRevLett.72.3807).
- [PW65] A. A. Penzias and R. W. Wilson. “A Measurement of Excess Antenna Temperature at 4080 Mc/s.” In: *The Astrophysical Journal* 142 (July 1965), p. 419. DOI: [10.1086/148307](https://doi.org/10.1086/148307).
- [Per+88] S. F. Pereira, M. Xiao, H. J. Kimble, and J. L. Hall. “Generation of squeezed light by intracavity frequency doubling”. In: *Phys. Rev. A* 38 (9 Nov. 1988), pp. 4931–4934. DOI: [10.1103/PhysRevA.38.4931](https://doi.org/10.1103/PhysRevA.38.4931).
- [Pla01] M. Planck. “On the law of distribution of energy in the normal spectrum”. In: *Annalen der physik* 4.553 (1901), p. 1.
- [Pla00] M. Planck. “On the theory of the energy distribution law of the normal spectrum”. In: *Verh. Deut. Phys. Ges* 2 (1900), pp. 237–245.
- [PCK92] E. S. Polzik, J. Carri, and H. J. Kimble. “Atomic spectroscopy with squeezed light for sensitivity beyond the vacuum-state limit”. In: *Applied Physics B* 55.3 (Sept. 1992), pp. 279–290. ISSN: 1432-0649. DOI: [10.1007/BF00325016](https://doi.org/10.1007/BF00325016).
- [PH14] E. S. Polzik and K. Hammerer. “Trajectories without quantum uncertainties”. In: *Annalen der Physik* 527.1-2 (Nov. 2014), A15–A20. DOI: [10.1002/andp.201400099](https://doi.org/10.1002/andp.201400099).
- [Pun+10] M. Punturo et al. “The Einstein Telescope: a third-generation gravitational wave observatory”. In: *Classical and Quantum Gravity* 27.19 (Sept. 2010), p. 194002. DOI: [10.1088/0264-9381/27/19/194002](https://doi.org/10.1088/0264-9381/27/19/194002).

- [Pur+13] T. P. Purdy, P.-L. Yu, R. W. Peterson, N. S. Kampel, and C. A. Regal. “Strong Optomechanical Squeezing of Light”. In: *Phys. Rev. X* 3 (3 Sept. 2013), p. 031012. DOI: [10.1103/PhysRevX.3.031012](https://doi.org/10.1103/PhysRevX.3.031012).
- [Qva+18] S. Qvarfort, A. Serafini, P. F. Barker, and S. Bose. “Gravimetry through non-linear optomechanics”. In: *Nature Communications* 9.1 (Sept. 2018), p. 3690. ISSN: 2041-1723. DOI: [10.1038/s41467-018-06037-z](https://doi.org/10.1038/s41467-018-06037-z).
- [Rad17] J. Radon. “Über die Bestimmung von Funktionen durch ihre Integralwerte längs gewisser Mannigfaltigkeiten”. In: *Berichte über die Verhandlungen der Sächsische Akademie der Wissenschaften* 69 (1917). 00000, pp. 262–277.
- [RV14] S. Rajasekar and R. Velusamy. *Quantum Mechanics II: Advanced Topics*. CRC Press, 2014.
- [Rei89] M. D. Reid. “Demonstration of the Einstein-Podolsky-Rosen paradox using nondegenerate parametric amplification”. In: *Phys. Rev. A* 40 (2 July 1989), pp. 913–923. DOI: [10.1103/PhysRevA.40.913](https://doi.org/10.1103/PhysRevA.40.913).
- [Rei+09] M. D. Reid et al. “Colloquium: The Einstein-Podolsky-Rosen paradox: From concepts to applications”. In: *Rev. Mod. Phys.* 81 (4 Dec. 2009), pp. 1727–1751. DOI: [10.1103/RevModPhys.81.1727](https://doi.org/10.1103/RevModPhys.81.1727).
- [Rei+19] D. Reitze et al. “Cosmic Explorer: The U.S. Contribution to Gravitational-Wave Astronomy beyond LIGO”. In: *Bulletin of the AAS* 51.7 (Sept. 2019). URL: <https://baas.aas.org/pub/2020n7i035>.
- [Ros+18] M. Rossi, D. Mason, J. Chen, Y. Tsaturyan, and A. Schliesser. “Measurement-based quantum control of mechanical motion”. In: *Nature* 563.7729 (Nov. 2018), pp. 53–58. ISSN: 1476-4687. DOI: [10.1038/s41586-018-0643-8](https://doi.org/10.1038/s41586-018-0643-8).
- [Rub14] G. D. Rubin. “Computed Tomography: Revolutionizing the Practice of Medicine for 40 Years”. In: *Radiology* 273.2S (Nov. 2014), S45–S74. DOI: [10.1148/radiol.14141356](https://doi.org/10.1148/radiol.14141356).
- [ST19] B. Saleh and M. Teich. *Fundamentals of Photonics*. Fundamentals of Photonics: Optics. Wiley, 2019. ISBN: 9781119506867.
- [Sca+09] V. Scarani et al. “The security of practical quantum key distribution”. In: *Rev. Mod. Phys.* 81 (3 Sept. 2009), pp. 1301–1350. DOI: [10.1103/RevModPhys.81.1301](https://doi.org/10.1103/RevModPhys.81.1301).
- [Sch17] R. Schnabel. “Squeezed states of light and their applications in laser interferometers”. In: *Physics Reports* 684 (2017). Squeezed states of light and their applications in laser interferometers, pp. 1–51. ISSN: 0370-1573. DOI: [10.1016/j.physrep.2017.04.001](https://doi.org/10.1016/j.physrep.2017.04.001).
- [Sch18] E. Schreiber. “Gravitational-wave detection beyond the quantum shot-noise limit: the integration of squeezed light in GEO 600”. PhD thesis. Gottfried Wilhelm Leibniz Universität Hannover, 2018. DOI: [10.15488/3773](https://doi.org/10.15488/3773).
- [Sch+14] S. Schreppler et al. “Optically measuring force near the standard quantum limit”. In: *Science* 344.6191 (2014), pp. 1486–1489. DOI: [10.1126/science.1249850](https://doi.org/10.1126/science.1249850).
- [Sch+20] K. T. Schütt et al., eds. *Machine Learning Meets Quantum Physics*. Springer International Publishing, 2020. DOI: [10.1007/978-3-030-40245-7](https://doi.org/10.1007/978-3-030-40245-7).

- [Sch+22] J. Schweer, D. Steinmeyer, K. Hammerer, and M. Heurs. “All-optical coherent quantum-noise cancellation in cascaded optomechanical systems”. In: *Phys. Rev. A* 106 (3 Sept. 2022), p. 033520. DOI: [10.1103/PhysRevA.106.033520](https://doi.org/10.1103/PhysRevA.106.033520).
- [Sei14] J. A. Seibert. “Iterative reconstruction: how it works, how to apply it”. In: *Pediatric Radiology* 44.S3 (Oct. 2014), pp. 431–439. DOI: [10.1007/s00247-014-3102-1](https://doi.org/10.1007/s00247-014-3102-1).
- [Sei+06] F. Seifert, P. Kwee, M. Heurs, B. Willke, and K. Danzmann. “Laser power stabilization for second-generation gravitational wave detectors”. In: *Opt. Lett.* 31.13 (July 2006), pp. 2000–2002. DOI: [10.1364/OL.31.002000](https://doi.org/10.1364/OL.31.002000).
- [Sho+19] I. Shomroni, L. Qiu, D. Malz, A. Nunnenkamp, and T. J. Kippenberg. “Optical backaction-evading measurement of a mechanical oscillator”. In: *Nature Communications* 10.1 (May 2019), p. 2086. ISSN: 2041-1723. DOI: [10.1038/s41467-019-10024-3](https://doi.org/10.1038/s41467-019-10024-3).
- [Sie86] A. Siegman. *Lasers*. University Science Books, 1986. ISBN: 9780685055953.
- [SSM87] R. Simon, E. C. G. Sudarshan, and N. Mukunda. “Gaussian-Wigner distributions in quantum mechanics and optics”. In: *Phys. Rev. A* 36 (8 Oct. 1987), pp. 3868–3880. DOI: [10.1103/PhysRevA.36.3868](https://doi.org/10.1103/PhysRevA.36.3868).
- [Siz+90] A. Sizmann, R. Horowicz, G. Wagner, and G. Leuchs. “Observation of amplitude squeezing of the up-converted mode in second harmonic generation”. In: *Optics Communications* 80.2 (1990), pp. 138–142. ISSN: 0030-4018. DOI: [10.1016/0030-4018\(90\)90375-4](https://doi.org/10.1016/0030-4018(90)90375-4).
- [SL99] A. Sizmann and G. Leuchs. “V The Optical Kerr Effect and Quantum Optics in Fibers”. In: *Progress in Optics*. Elsevier, 1999, pp. 373–469. DOI: [10.1016/s0079-6638\(08\)70392-5](https://doi.org/10.1016/s0079-6638(08)70392-5).
- [Slu+85] R. E. Slusher, L. W. Hollberg, B. Yurke, J. C. Mertz, and J. F. Valley. “Observation of Squeezed States Generated by Four-Wave Mixing in an Optical Cavity”. In: *Phys. Rev. Lett.* 55 (22 Nov. 1985), pp. 2409–2412. DOI: [10.1103/PhysRevLett.55.2409](https://doi.org/10.1103/PhysRevLett.55.2409).
- [SK96] L. L. Smith and P. M. Koch. “Use of four mirrors to rotate linear polarization but preserve input–output collinearity”. In: *J. Opt. Soc. Am. A* 13.10 (Oct. 1996), pp. 2102–2105. DOI: [10.1364/JOSAA.13.002102](https://doi.org/10.1364/JOSAA.13.002102).
- [Smi+93] D. T. Smithey, M. Beck, M. G. Raymer, and A. Faridani. “Measurement of the Wigner distribution and the density matrix of a light mode using optical homodyne tomography: Application to squeezed states and the vacuum”. In: *Phys. Rev. Lett.* 70 (9 Mar. 1993), pp. 1244–1247. DOI: [10.1103/PhysRevLett.70.1244](https://doi.org/10.1103/PhysRevLett.70.1244).
- [Ste+13] S. Steinlechner, J. Bauchowitz, T. Eberle, and R. Schnabel. “Strong Einstein-Podolsky-Rosen steering with unconditional entangled states”. In: *Phys. Rev. A* 87 (2 Feb. 2013), p. 022104. DOI: [10.1103/PhysRevA.87.022104](https://doi.org/10.1103/PhysRevA.87.022104).
- [Ste19] D. Steinmeyer. “Subsystems for all-optical coherent quantum-noise cancellation”. PhD thesis. Gottfried Wilhelm Leibniz Universität Hannover, 2019. DOI: [10.15488/9179](https://doi.org/10.15488/9179).

- [SSL17] B. Stiller, U. Seyfarth, and G. Leuchs. “Temporal and spectral properties of quantum light”. In: *Quantum Optics and Nanophotonics*. Oxford University Press Oxford, May 2017, pp. 169–228. DOI: [10.1093/oso/9780198768609.003.0004](https://doi.org/10.1093/oso/9780198768609.003.0004).
- [SM05] P. Stoica and R. Moses. *Spectral Analysis of Signals*. Pearson Prentice Hall, 2005. ISBN: 9780131139565.
- [Su+07] X. Su et al. “Experimental Preparation of Quadripartite Cluster and Greenberger-Horne-Zeilinger Entangled States for Continuous Variables”. In: *Phys. Rev. Lett.* 98 (7 Feb. 2007), p. 070502. DOI: [10.1103/PhysRevLett.98.070502](https://doi.org/10.1103/PhysRevLett.98.070502).
- [Sud63] E. C. G. Sudarshan. “Equivalence of Semiclassical and Quantum Mechanical Descriptions of Statistical Light Beams”. In: *Phys. Rev. Lett.* 10 (7 Apr. 1963), pp. 277–279. DOI: [10.1103/PhysRevLett.10.277](https://doi.org/10.1103/PhysRevLett.10.277).
- [Süd+20] J. Südbeck, S. Steinlechner, M. Korobko, and R. Schnabel. “Demonstration of interferometer enhancement through Einstein–Podolsky–Rosen entanglement”. In: *Nature Photonics* 14.4 (Apr. 2020), pp. 240–244. ISSN: 1749-4893. DOI: [10.1038/s41566-019-0583-3](https://doi.org/10.1038/s41566-019-0583-3).
- [Sud+17] V. Sudhir et al. “Quantum Correlations of Light from a Room-Temperature Mechanical Oscillator”. In: *Phys. Rev. X* 7 (3 Sept. 2017), p. 031055. DOI: [10.1103/PhysRevX.7.031055](https://doi.org/10.1103/PhysRevX.7.031055).
- [Suh+14] J. Suh et al. “Mechanically detecting and avoiding the quantum fluctuations of a microwave field”. In: *Science* 344.6189 (2014), pp. 1262–1265. DOI: [10.1126/science.1253258](https://doi.org/10.1126/science.1253258).
- [TZL05] R. L. Targat, J.-J. Zondy, and P. Lemonde. “75%-Efficiency blue generation from an intracavity PPKTP frequency doubler”. In: *Optics Communications* 247.4-6 (Mar. 2005), pp. 471–481. DOI: [10.1016/j.optcom.2004.11.081](https://doi.org/10.1016/j.optcom.2004.11.081).
- [Tay+13] M. A. Taylor et al. “Biological measurement beyond the quantum limit”. In: *Nature Photonics* 7.3 (Mar. 2013), pp. 229–233. ISSN: 1749-4893. DOI: [10.1038/nphoton.2012.346](https://doi.org/10.1038/nphoton.2012.346).
- [N07] *The Nobel Prize in Physics 1907*. URL: <https://www.nobelprize.org/prizes/physics/1907/summary/> (visited on 10/17/2022).
- [N18] *The Nobel Prize in Physics 1918*. URL: <https://www.nobelprize.org/prizes/physics/1918/summary/> (visited on 12/03/2022).
- [N21] *The Nobel Prize in Physics 1921*. URL: <https://www.nobelprize.org/prizes/physics/1921/summary/> (visited on 10/17/2022).
- [N78] *The Nobel Prize in Physics 1978*. URL: <https://www.nobelprize.org/prizes/physics/1978/summary/> (visited on 10/14/2022).
- [N79] *The Nobel Prize in Physics 1979*. URL: <https://www.nobelprize.org/prizes/physics/1979/summary/> (visited on 10/22/2022).
- [N05] *The Nobel Prize in Physics 2005*. URL: <https://www.nobelprize.org/prizes/physics/2005/summary/> (visited on 10/18/2022).
- [N17] *The Nobel Prize in Physics 2017*. URL: <https://www.nobelprize.org/prizes/physics/2017/summary/> (visited on 10/18/2022).
- [N22] *The Nobel Prize in Physics 2022*. URL: <https://www.nobelprize.org/prizes/physics/2022/summary/> (visited on 10/13/2022).

- [TG13] P. S. Theocaris and E. E. Gdoutos. *Matrix theory of photoelasticity*. Vol. 11. Springer, 2013.
- [Pow] *Thorlabs Photodiode Power Sensors*. URL: https://www.thorlabs.com/newgrouppage9.cfm?objectgroup_id=3328 (visited on 11/06/2022).
- [Thü09] A. Thüring. “Investigations of coupled and Kerr non-linear optical resonators”. PhD thesis. Gottfried Wilhelm Leibniz Universität Hannover, 2009. DOI: [10.15488/7324](https://doi.org/10.15488/7324).
- [T12] G. Tóth. “Multipartite entanglement and high-precision metrology”. In: *Phys. Rev. A* 85 (2 Feb. 2012), p. 022322. DOI: [10.1103/PhysRevA.85.022322](https://doi.org/10.1103/PhysRevA.85.022322).
- [Tre+02] N. Treps et al. “Surpassing the Standard Quantum Limit for Optical Imaging Using Nonclassical Multimode Light”. In: *Phys. Rev. Lett.* 88 (20 May 2002), p. 203601. DOI: [10.1103/PhysRevLett.88.203601](https://doi.org/10.1103/PhysRevLett.88.203601).
- [TG+20] G. Triginer Garces et al. “Quantum-enhanced stimulated emission detection for label-free microscopy”. In: *Applied Physics Letters* 117.2 (2020), p. 024002. DOI: [10.1063/5.0009681](https://doi.org/10.1063/5.0009681).
- [TC10] M. Tsang and C. M. Caves. “Coherent Quantum-Noise Cancellation for Optomechanical Sensors”. In: *Phys. Rev. Lett.* 105 (12 Sept. 2010), p. 123601. DOI: [10.1103/PhysRevLett.105.123601](https://doi.org/10.1103/PhysRevLett.105.123601).
- [Tse+19] M. Tse et al. “Quantum-Enhanced Advanced LIGO Detectors in the Era of Gravitational-Wave Astronomy”. In: *Phys. Rev. Lett.* 123 (23 Dec. 2019), p. 231107. DOI: [10.1103/PhysRevLett.123.231107](https://doi.org/10.1103/PhysRevLett.123.231107).
- [Unr83] W. G. Unruh. “Quantum Noise in the Interferometer Detector”. In: *Quantum Optics, Experimental Gravity, and Measurement Theory*. Ed. by P. Meystre and M. O. Scully. Boston, MA: Springer US, 1983, pp. 647–660. ISBN: 978-1-4613-3712-6. DOI: [10.1007/978-1-4613-3712-6_28](https://doi.org/10.1007/978-1-4613-3712-6_28).
- [Vah+16] H. Vahlbruch, M. Mehmet, K. Danzmann, and R. Schnabel. “Detection of 15 dB Squeezed States of Light and their Application for the Absolute Calibration of Photoelectric Quantum Efficiency”. In: *Phys. Rev. Lett.* 117 (11 Sept. 2016), p. 110801. DOI: [10.1103/PhysRevLett.117.110801](https://doi.org/10.1103/PhysRevLett.117.110801).
- [Vah+06] H. Vahlbruch et al. “Coherent Control of Vacuum Squeezing in the Gravitational-Wave Detection Band”. In: *Phys. Rev. Lett.* 97 (1 July 2006), p. 011101. DOI: [10.1103/PhysRevLett.97.011101](https://doi.org/10.1103/PhysRevLett.97.011101).
- [VE06] W. C. Van Etten. *Introduction to random signals and noise*. John Wiley & Sons, 2006.
- [Vas+15] G. Vasilakis et al. “Generation of a squeezed state of an oscillator by stroboscopic back-action-evading measurement”. In: *Nature Physics* 11.5 (May 2015), pp. 389–392. ISSN: 1745-2481. DOI: [10.1038/nphys3280](https://doi.org/10.1038/nphys3280).
- [Vil+05] A. S. Villar, L. S. Cruz, K. N. Cassemiro, M. Martinelli, and P. Nussenzweig. “Generation of Bright Two-Color Continuous Variable Entanglement”. In: *Phys. Rev. Lett.* 95 (24 Dec. 2005), p. 243603. DOI: [10.1103/PhysRevLett.95.243603](https://doi.org/10.1103/PhysRevLett.95.243603).
- [VZ95] S. Vyatchanin and E. Zubova. “Quantum variation measurement of a force”. In: *Physics Letters A* 201.4 (1995), pp. 269–274. ISSN: 0375-9601. DOI: [10.1016/0375-9601\(95\)00280-G](https://doi.org/10.1016/0375-9601(95)00280-G).

- [Wal83] D. F. Walls. "Squeezed states of light". In: *Nature* 306.5939 (Nov. 1983), pp. 141–146. ISSN: 1476-4687. DOI: [10.1038/306141a0](https://doi.org/10.1038/306141a0).
- [WM08] D. Walls and G. Milburn. *Quantum Optics*. Springer Berlin Heidelberg, 2008. ISBN: 9783540285731.
- [Wan+17] Y. Wang, Z. Li, Y. Zheng, and J. Su. "Determination of the Thermal Lens of a PPKTP Crystal Based on Thermally Induced Mode-Mismatching". In: *IEEE Journal of Quantum Electronics* 53.1 (2017), pp. 1–7. DOI: [10.1109/JQE.2016.2640229](https://doi.org/10.1109/JQE.2016.2640229).
- [Wat18] J. Watrous. *The Theory of Quantum Information*. Cambridge University Press, 2018. DOI: [10.1017/9781316848142](https://doi.org/10.1017/9781316848142).
- [Web18] M. J. Weber. *Handbook of optical materials*. CRC press, 2018.
- [Wei+98] G. Weihs, T. Jennewein, C. Simon, H. Weinfurter, and A. Zeilinger. "Violation of Bell's Inequality under Strict Einstein Locality Conditions". In: *Phys. Rev. Lett.* 81 (23 Dec. 1998), pp. 5039–5043. DOI: [10.1103/PhysRevLett.81.5039](https://doi.org/10.1103/PhysRevLett.81.5039).
- [WF18] J. Weinbub and D. K. Ferry. "Recent advances in Wigner function approaches". In: *Applied Physics Reviews* 5.4 (2018), p. 041104. DOI: [10.1063/1.5046663](https://doi.org/10.1063/1.5046663).
- [Wei72] R. Weiss. *Electromagnetically coupled broadband gravitational antenna*. Quarterly Report of the Research Laboratory for Electronics, MIT Report No. 105. 1972.
- [Wey27] H. Weyl. "Quantenmechanik und Gruppentheorie". In: *Zeitschrift für Physik* 46.1 (Nov. 1927), pp. 1–46. ISSN: 0044-3328. DOI: [10.1007/BF02055756](https://doi.org/10.1007/BF02055756).
- [Whe16] T. Wheatley. "To the standard quantum limit and beyond: Experimental quantum parameter estimation using adaptive quantum smoothing". PhD thesis. UNSW Sydney, 2016.
- [Whi97] A. G. White. "Classical and quantum dynamics of optical frequency conversion". PhD thesis. 1997.
- [Whi+00] A. G. White, P. K. Lam, D. E. McClelland, H.-A. Bachor, and W. J. Munro. "Kerr noise reduction and squeezing". In: *Journal of Optics B: Quantum and Semiclassical Optics* 2.4 (Aug. 2000), p. 553. DOI: [10.1088/1464-4266/2/4/315](https://doi.org/10.1088/1464-4266/2/4/315).
- [Whi02] D. Whitehouse. "Foreword". In: *Surfaces and Their Measurement*. Ed. by D. Whitehouse. Oxford: Kogan Page Science, 2002, pp. ix–xi. ISBN: 978-1-903996-01-0. DOI: [10.1016/B978-190399601-0/50000-1](https://doi.org/10.1016/B978-190399601-0/50000-1).
- [Whi+17] R Whittaker et al. "Absorption spectroscopy at the ultimate quantum limit from single-photon states". In: *New Journal of Physics* 19.2 (Feb. 2017), p. 023013. DOI: [10.1088/1367-2630/aa5512](https://doi.org/10.1088/1367-2630/aa5512).
- [Wig32] E. Wigner. "On the Quantum Correction For Thermodynamic Equilibrium". In: *Phys. Rev.* 40 (5 June 1932), pp. 749–759. DOI: [10.1103/PhysRev.40.749](https://doi.org/10.1103/PhysRev.40.749).
- [Wil+98] B. Willke et al. "Spatial and temporal filtering of a 10-W Nd:YAG laser with a Fabry–Perot ring-cavity premode cleaner". In: *Opt. Lett.* 23.21 (Nov. 1998), pp. 1704–1706. DOI: [10.1364/OL.23.001704](https://doi.org/10.1364/OL.23.001704).

- [Wil+15] D. J. Wilson et al. “Measurement-based control of a mechanical oscillator at its thermal decoherence rate”. In: *Nature* 524.7565 (Aug. 2015), pp. 325–329. ISSN: 1476-4687. DOI: [10.1038/nature14672](https://doi.org/10.1038/nature14672).
- [Wim16] M. Wimmer. “Coupled nonclassical systems for coherent backaction noise cancellation”. PhD thesis. Gottfried Wilhelm Leibniz Universität Hannover, 2016. DOI: [10.15488/8904](https://doi.org/10.15488/8904).
- [Wim+14] M. H. Wimmer, D. Steinmeyer, K. Hammerer, and M. Heurs. “Coherent cancellation of backaction noise in optomechanical force measurements”. In: *Phys. Rev. A* 89 (5 May 2014), p. 053836. DOI: [10.1103/PhysRevA.89.053836](https://doi.org/10.1103/PhysRevA.89.053836).
- [Wol] Wolfram Research Inc. *Mathematica, Version 12.0*. Champaign, IL, 2019.
- [WC13] M. J. Woolley and A. A. Clerk. “Two-mode back-action-evading measurements in cavity optomechanics”. In: *Phys. Rev. A* 87 (6 June 2013), p. 063846. DOI: [10.1103/PhysRevA.87.063846](https://doi.org/10.1103/PhysRevA.87.063846).
- [WZ82] W. K. Wootters and W. H. Zurek. “A single quantum cannot be cloned”. In: *Nature* 299.5886 (Oct. 1982), pp. 802–803. ISSN: 1476-4687. DOI: [10.1038/299802a0](https://doi.org/10.1038/299802a0).
- [XWK87] M. Xiao, L.-A. Wu, and H. J. Kimble. “Precision measurement beyond the shot-noise limit”. In: *Phys. Rev. Lett.* 59 (3 July 1987), pp. 278–281. DOI: [10.1103/PhysRevLett.59.278](https://doi.org/10.1103/PhysRevLett.59.278).
- [XT14] X. Xu and J. M. Taylor. “Squeezing in a coupled two-mode optomechanical system for force sensing below the standard quantum limit”. In: *Phys. Rev. A* 90 (4 Oct. 2014), p. 043848. DOI: [10.1103/PhysRevA.90.043848](https://doi.org/10.1103/PhysRevA.90.043848).
- [YIM86] Y. Yamamoto, N. Imoto, and S. Machida. “Amplitude squeezing in a semiconductor laser using quantum nondemolition measurement and negative feedback”. In: *Phys. Rev. A* 33 (5 May 1986), pp. 3243–3261. DOI: [10.1103/PhysRevA.33.3243](https://doi.org/10.1103/PhysRevA.33.3243).
- [Yam+87] Y. Yamamoto, S. Machida, N. Imoto, M. Kitagawa, and G. Björk. “Generation of number-phase minimum-uncertainty states and number states”. In: *J. Opt. Soc. Am. B* 4.10 (Oct. 1987), pp. 1645–1662. DOI: [10.1364/JOSAB.4.001645](https://doi.org/10.1364/JOSAB.4.001645).
- [Yap+20] M. J. Yap et al. “Generation and control of frequency-dependent squeezing via Einstein–Podolsky–Rosen entanglement”. In: *Nature Photonics* 14.4 (Apr. 2020), pp. 223–226. ISSN: 1749-4893. DOI: [10.1038/s41566-019-0582-4](https://doi.org/10.1038/s41566-019-0582-4).
- [YAF04] H. Yonezawa, T. Aoki, and A. Furusawa. “Demonstration of a quantum teleportation network for continuous variables”. In: *Nature* 431.7007 (Sept. 2004), pp. 430–433. ISSN: 1476-4687. DOI: [10.1038/nature02858](https://doi.org/10.1038/nature02858).
- [YBF07] H. Yonezawa, S. L. Braunstein, and A. Furusawa. “Experimental Demonstration of Quantum Teleportation of Broadband Squeezing”. In: *Phys. Rev. Lett.* 99 (11 Sept. 2007), p. 110503. DOI: [10.1103/PhysRevLett.99.110503](https://doi.org/10.1103/PhysRevLett.99.110503).
- [YS88] M. R. Young and S. Singh. “Effects of multiplicative white noise on laser light fluctuations”. In: *Phys. Rev. A* 38 (1 July 1988), pp. 238–244. DOI: [10.1103/PhysRevA.38.238](https://doi.org/10.1103/PhysRevA.38.238).

- [YAR89] A. W. Yu, G. P. Agrawal, and R. Roy. "Power spectra and spatial pattern dynamics of a ring laser". In: *Journal of Statistical Physics* 54.5 (Mar. 1989), pp. 1223–1241. ISSN: 1572-9613. DOI: [10.1007/BF01044714](https://doi.org/10.1007/BF01044714).
- [Yu+20] H. Yu et al. "Quantum correlations between light and the kilogram-mass mirrors of LIGO". In: *Nature* 583.7814 (2020), pp. 43–47. ISSN: 1476-4687. DOI: [10.1038/s41586-020-2420-8](https://doi.org/10.1038/s41586-020-2420-8).
- [ZVB04] A. Zavatta, S. Viciani, and M. Bellini. "Quantum-to-Classical Transition with Single-Photon-Added Coherent States of Light". In: *Science* 306.5696 (2004), pp. 660–662. DOI: [10.1126/science.1103190](https://doi.org/10.1126/science.1103190).
- [Zha03] J. Zhang. "Einstein-Podolsky-Rosen sideband entanglement in broadband squeezed light". In: *Phys. Rev. A* 67 (5 May 2003), p. 054302. DOI: [10.1103/PhysRevA.67.054302](https://doi.org/10.1103/PhysRevA.67.054302).
- [Zha+19] Y. Zhang et al. "Continuous-variable QKD over 50 km commercial fiber". In: *Quantum Science and Technology* 4.3 (May 2019), p. 035006. DOI: [10.1088/2058-9565/ab19d1](https://doi.org/10.1088/2058-9565/ab19d1).
- [Zha+20] Y. Zhao et al. "Frequency-Dependent Squeezed Vacuum Source for Broadband Quantum Noise Reduction in Advanced Gravitational-Wave Detectors". In: *Phys. Rev. Lett.* 124 (17 Apr. 2020), p. 171101. DOI: [10.1103/PhysRevLett.124.171101](https://doi.org/10.1103/PhysRevLett.124.171101).
- [Zho+15] Y. Zhou, X. Jia, F. Li, C. Xie, and K. Peng. "Experimental generation of 8.4 dB entangled state with an optical cavity involving a wedged type-II nonlinear crystal". In: *Opt. Express* 23.4 (Feb. 2015), pp. 4952–4959. DOI: [10.1364/OE.23.004952](https://doi.org/10.1364/OE.23.004952).
- [Zou21] N. Zou. "Quantum Entanglement and Its Application in Quantum Communication". In: *Journal of Physics: Conference Series*. Vol. 1827. 1. IOP Publishing. 2021, p. 012120. DOI: [10.1088/1742-6596/1827/1/012120](https://doi.org/10.1088/1742-6596/1827/1/012120).

Acknowledgements

I acknowledge my privileges which brought me to the situation that I can write a PhD thesis. I could always concentrate on my scientific work without being distracted by acts beyond my control as wars or catastrophes because of the climate crisis. I have a great social environment, friends and family who emotionally support me and go with my decisions.

I want to thank everyone who made my time in the institute unforgettable.

First, I want to thank you, Michèle, for giving me a position in this awesome working group. You always stand behind me and trustfully opened many doors to pursue. I could speak to you anytime about literally anything, which was very valuable for me. Thank you for your scientific support and much advice beyond. I am very pleased about the skills I learned in your group. I am very happy about all the workshops and travels you have sent me on.

My time in this institute started in your group, Benno. I am very thankful that I could learn from you, especially about things like the phasor picture. I really appreciated working with you, for instance, for the scope of your lecture on laser interferometry, in which I learnt a lot.

My gratitude also goes to you, Georgia, for agreeing to examine my thesis on a super short time scale.

When I started my PhD, I expected to like the scientific work, but I was wrong. I was not expecting that I would like it passionately *that much!* This has to do with the numerous and diverse challenges I faced while growing for myself. Moreover, I enjoyed working with my colleagues from the "quantum control" group.

In particular, I want to emphasise Dennis. I remember the time when we started in an empty lab, and I had no clue about squeezing experiments. I wouldn't have done it without this teamwork! A special thank also goes to Daniel, Bernd and Johnny for the time and all the valuable discussions, and to all other members of the "quantum control" working group. I have had so much fun and enjoy working with you together!

I want to acknowledge all my co-authors who helped me write the publications that are now used for this cumulative thesis. Thank you especially for your input when writing up the papers! I benefited from the nice infrastructure in the institute. Thanks to all employees ranging from the workshops to the excellent baker Kirsten!

This thesis significantly improved over the last weeks because of proofreads from many people. A special thank you for constructive comments goes to Lina, Dennis, Daniel, Bernd, Johnny, Anni and Michèle.

Finally, I want to thank my beloved family, my parents, my sister and my grandmother, for their boundless emotional support. And to Lina, for Everything.

Keywords of memories: Tablettenwizzard, Schifoan, Marathons, Flunkindenmai, Honig, Alignmentisgone, Kochstudio, Kristallbruch, Stetteritz, Ankersalat, Wombats, Endederwochegrün, Napoleon

Curriculum Vitae

Personal information

Jonas Junker

born on 11 January 1991 in Hameln, Germany

University studies

12/2016 – 02/2023

Doctoral studies in Physics
Max Planck Institute for Gravitational Physics and
Institute for Gravitational Physics,
Leibniz Universität Hannover, Germany

03/2014 – 05/2016

Master of Science
Master thesis: *Laser Power Stabilization for the AEI 10m
Prototype*,
Leibniz Universität Hannover, Germany

10/2010 – 03/2014

Bachelor of Science
Bachelor thesis: *Entwicklung eines Lasersystems für die
Interferometrie mit ultrakalten Rubidium-Ensembles*,
Leibniz Universität Hannover, Germany

Education

08/2003 – 06/2010

Abitur
Viktoria-Luise-Gymnasium Hameln, Germany